Electrochemical charge transfer at a metallic electrode: a simulation study

Michael A. Pounds

Doctor of Philosophy

University of Edinburgh

2010

The work in this thesis is entirely my own, except where I have *either* acknowledged help from a named person *or* given a reference to a published source or a thesis. I have not submitted this work for another degree or professional qualification.

Signature **Date**

To my parents

Abstract

Part I Electrochemical charge transfer at a metallic electrode: a simulation study

The factors which affect the rate of heterogeneous electron transfer at a metallic electrode in the context of Marcus theory are investigated through molecular dynamics simulations. The system consists of the ionic melt $K_3Eu^{2+}_{0.5}Eu^{3+}_{0.5}Cl_{5.5}$ sandwiched between two parallel plate platinum electrodes held at a preset electrical potential. The charges on the electrode atoms are variationally obtained through the method of Siepmann and Sprik [J. Chem. Phys. **102**, 511 (1995)] which models the polarization of the electrode by the melt and maintains the condition of constant potential. A two-dimensional Ewald summation is employed to ensure that the *absolute* value of the potential is known, and the expressions derived by Kawata and Mikami [Chem. Phys. Lett. **340**, 157 (2001)] are extended to allow for induced dipoles on the melt ions by their mutual interaction and the interaction with the electrode surface.

The Marcus free energy curves are calculated for electron transfer events between a europium ion and the metallic electrode, and their dependence on the position of the redox ion and the applied potential examined. The system is consistently found to be in accord with the linear response régime. A moderately-ranged oscillatory character in the mean electrical (Poisson) potential is observed extending into the fluid, which is in marked disagreement with the predictions of existing mean-field (Gouy-Chapman) predictions. These oscillations are found not to be reflected in the calculated Helmholtz reaction free energy, which indicates that the Poisson potential is not the appropriate potential for discussions of the kinetics of electrode processes. The strong dependence of the reorganization energy on the position of the redox ion is traced to the image charge effect, and appears insensitive to the polarizability of the anion. Following the evolution of the Eu–Cl radial distribution function throughout a redox process reveals that the bond length in the transition complex is exactly in between those of the ground state reactant and product complexes. The potentials of mean force for the approach of a Eu^{2+} and Eu^{3+} ion to the electrode calculated through umbrella sampling are found to be in quantitative agreement with those calculated through the position-dependence of the respective concentration profiles.

A method to parameterize a model of the interactions between the melt ions and the electrode surface from *ab initio* density functional theory calculations is described. The method is used to obtain a suitable interaction model for a system consisting of a LiCl liquid electrolyte and a solid aluminium electrode. The electrolyte is found to exhibit a potential-driven phase transition which involves the commensurate ordering of the electrolyte ions with the electrode surface; this leads to a maximum in the differential capacitance as a function of applied potential. Away from the phase transition the capacitance was found to be independent of the applied potential.

Part II Are dipolar liquids ferroelectric?

The observation of a very sharp low frequency spike in the *hyper*-Rayleigh spectrum (HRS) of strongly dipolar fluids, such as acetonitrile and water, has been interpreted as reflecting a very slowly relaxing component in the transverse dipole density. This suggestion is at variance with the expectation of dielectric theory for an isotropic fluid and has led to the speculation that the slow relaxation is associated with the reorganization of ferroelectric domains. Very large-scale molecular dynamics simulation ($\sim$ 28000 molecules) have been carried out using a 3-site potential model of acetonitrile. The simulated fluid shows no suggestion of strong dipole correlations and domain structure. The dipole density correlations behave as predicted by normal dielectric theory and their spectra do not show the low-frequency feature seen in the HRS. In order to examine the characteristics of the spectra which would be seen in a ferroelectric domain, the acetontrile model was transmuted to more closely resemble a Stockmayer-like fluid with the same dipole density and a ferroelectric phase was observed. In this phase the dielectric spectra show (i) a high-frequency spectral feature due to librational motion of the molecules within a domain, and (ii) slowly-relaxing longitudinal *and* transverse polar modes, again at variance from the experimental HRS characteristics.

Acknowledgements

I should like to thank my supervisor, Prof. Paul Madden, for proposing a workable and enjoyable project, and for being a trusty fingerpost throughout. My initiation into the Madden crowd was led by Lindsay Foy and Robert Heaton, who have been tireless mentors ever since, and have almost cured me of my Luddism. I am grateful to Stewart Reed for *inter alia* acting as an antidote to my mathematical illiteracy, and Dario Marochelli for being a sane and light-hearted colleague (although we will always disagree on the Hawaiian pizza question). And I must not forget the *formidable* Carmen for her rôle as Madden group historian and psychologist. *Gracias!*

I should paradoxically thank Alex Chremos for upbraiding me for my ignorance of Bergman and Antonioni (on 30 June 2007), as a result of which I have become an avant-gardist. Mention must go to Jason the Greek, sorry *Spartan*, for our highfalutin chitchats, and for teaching me how to make a chiton and a himation from haberdasheries. And the other two members of that unholy trinity: Amy for the mental penetration, and Sebastian for all that dandyish hosting.

Lindsay went out to recce the streets of Morningside and found me a super flat and a superlative landlady, Mary, who acted *in loco parentis*. I was very lucky to have my friend Tai Lin as a flatmate, whose greatest legacy may be his Sino-Swedish meatballs recipe: I regularly make a hash of it.

Finally, my acknowledgement of the Inner Circle, who have supported me unwaveringly from the beginning to the much-delayed chugging-out from the printer of these pages: Mum, Dad, Jen, and A.

Contents

List of Figures

List of Tables

Major symbols

Roman symbols

Symbol	Meaning	Usual units	Section
A	area	cm^2	1.2
A_M	Helmholtz free energy of species M	eV	4.3
$A_\mathrm{M}(x)$	Helmholtz free energy of species M at reaction coordinate x	eV	4.3
ΔA	Helmholtz free energy change in a reaction	eV	1.6.4
$\Delta A^\dagger$	Helmholtz free energy of activation	eV	1.5
$\Delta A_a^\dagger$	Helmholtz free energy of activation for an oxidation process	eV	1.5
$\Delta A_c^\dagger$	Helmholtz free energy of activation for a reduction process	eV	1.5
$\Delta A_a^\dagger(0)$	Helmholtz free energy of activation for an oxidation process under equilibrium (zero current) conditions	eV	1.5
$\Delta A_c^\dagger(0)$	Helmholtz free energy of activation for a reduction process under equilibrium (zero current) conditions	eV	1.5
a_{ij}	parameter in the Born Mayer description of the short-range repulsive interaction due to overlapping electron densities	a_0^{-1}	2.1.2
B	frequency factor in a first-order heterogeneous rate expression	$\mathrm{cm\,s}^{-1}$	1.5
B_a	frequency factor in a first-order heterogeneous rate expression for the anodic current	$\mathrm{cm\,s}^{-1}$	1.5
B_c	frequency factor in a first-order heterogeneous rate expression for the cathodic current	$\mathrm{cm\,s}^{-1}$	1.5
B_{ij}	parameter in the Born Mayer description of the short-range repulsive interaction due to overlapping electron densities	$\mathrm{E_h}$	2.1.2
b_{ij}	parameter used in the representation of short-range corrections to the charge–dipole interaction energy	a_0^{-1}	2.1.3
C	differential capacitance of the double layer	$\mu\mathrm{F\,cm}^{-2}$	1.3.1
C_{ij}^6	parameter in the Born Mayer description of the short-range dipole–dipole dispersion interactions	$\mathrm{E_h}\,a_0^6$	2.1.2
C_{ij}^8	parameter in the Born Mayer description of the dipole–quadrupole dispersion interactions	$\mathrm{E_h}\,a_0^8$	2.1.2
c_+	concentration of cations	$\mathrm{mol\,cm}^{-3}$	1.4.2
c_-	concentration of anions	$\mathrm{mol\,cm}^{-3}$	1.4.2
c_{ij}	parameter used in the representation of short-range corrections to the charge–dipole interaction energy	none	2.1.3
c_max	maximum allowed local concentration of ions (both cations and anions)	$\mathrm{mol\,cm}^{-3}$	1.4.2
D_M	diffusion coefficient of species M	$\mathrm{cm}^2\,\mathrm{s}^{-1}$	1.2
E	potential of an electrode	V	1.2
E^0	standard potential of an electrode or a couple	V	1.5
E'^0	formal potential of an electrode or a couple	V	1.2
ΔE	vertical potential energy gap for a charge transfer process	eV	4.2
$\mathbf{E}$	electric field strength vector	$e(4\pi\epsilon_0 a_0^2)^{-1}$	2.1.3
e	electronic charge	C	1.3.2
F	Faraday constant	$\mathrm{C\,mol}^{-1}$	1.2

Symbol	Meaning	Usual units	Section
$\mathbf{F}$	force vector	$E_h\, a_0^{-1}$	2.2
f	F/RT	V^{-1}	1.5
f_{ij}^6	Tang-Toennies dispersion damping function	none	2.1.2
f_{ij}^8	Tang-Toennies dispersion damping function	none	2.1.2
f_0	Ewald screening function	none	3.4.1.1
f_1	Ewald screening function	none	3.4.1.1
f_2	Ewald screening function	none	3.4.1.1
g_{ij}	parameter used in the representation of short-range corrections to the charge–dipole interaction energy	none	2.1.3
I	ionization energy	eV	4.5
i_p	peak current	mA	1.2
J	molar flux	mol cm^{-2} s^{-1}	1.2
j	current density	A cm^{-2}	1.5
j_a	anodic current density	A cm^{-2}	1.5
j_c	cathodic current density	A cm^{-2}	1.5
j_0	exchange current density	A cm^{-2}	1.5
k_B	Boltzmann constant	$J\,K^{-1}$	1.3.2
k_a	first-order heterogeneous rate constant for oxidation	cm s^{-1}	1.5
k_c	first-order heterogeneous rate constant for reduction	cm s^{-1}	1.5
n_g	total number of electrode atoms in simulation	none	2.1.2
n_i	number concentration of ion i in an electrolyte	cm^{-3}	1.3.2
n_i^0	number concentration of ion i in the bulk electrolyte	cm^{-3}	1.3.2
n^0	number concentration of each ion in a symmetrical electrolyte	cm^{-3}	1.3.2
n_p	total number of melt ions in simulation	none	2.1.2
Ox	oxidized form of the system Ox + ne ⇌ Red		1.5
p_{max}	parameter used in the representation of short-range corrections to the charge–dipole interaction energy	none	2.1.3
R	gas constant	J K^{-1} mol^{-1}	1.5
Red	reduced form of the system Ox + ne ⇌ Red		1.5
T	temperature	K	1.3.2
T_{ij}	interaction tensor	$(4\pi\epsilon_0)^{-1}a_0^{-1}$	2.1.2
T_{ij}^{α}	interaction tensor	$(4\pi\epsilon_0)^{-1}a_0^{-2}$	2.1.3
$T_{ij}^{\alpha\beta}$	interaction tensor	$(4\pi\epsilon_0)^{-1}a_0^{-3}$	2.1.3
$T_{ij}^{\alpha\beta\gamma}$	interaction tensor	$(4\pi\epsilon_0)^{-1}a_0^{-4}$	3.4.1.2
t	time	s	2.2
U^{q-q}	charge–charge interaction potential energy	E_h	2.1.2
$U^{q-\mu}$	charge–dipole interaction potential energy	E_h	2.1.3
$U^{\mu-\mu}$	dipole–dipole interaction potential energy	E_h	2.1.3
U^{DIPPIM}	total potential energy appropriate to the DIPPIM	E_h	2.1.3
U^{RIM}	total potential energy appropriate to the RIM	E_h	2.1.2
U^{disp}	Born Mayer short-range dispersion energy	E_h	2.1.2
U^{pol}	energy cost of deforming electron densities of ions to create induced dipoles	E_h	2.1.3
U^{rep}	Born Mayer short-range repulsion energy	E_h	2.1.2
V	Madelung potential	$e(4\pi\epsilon_0 a_0)^{-1}$	3.4.1.4
W	work function of a metal	eV	1.6.3
x_2	distance of the OHP from the electrode surface	Å	1.3.3

Greek symbols

Symbol	Meaning	Usual units	Section
α	(a) transfer coefficient	none	1.5
	(b) Ewald screening parameter	a_0^{-1}	3.2
	(c) dipole polarizability	$4\pi\epsilon_0 a_0^3$	2.1.3
β	(a) distance factor for extended charge transfer	Å^{-1}	1.6.3
	(b) $1/k_\text{B}T$	eV^{-1}	4.3
	(c) $\kappa\alpha(\kappa^2+2\alpha^2)^{-1/2}$	a_0^{-1}	3.2
Γ	defined by equation 1.30	none	1.4.2
γ	(a) activity coefficient	none	2.1.1.2
	(b) $\kappa\alpha(\kappa^2+\alpha^2)^{-1/2}$	a_0^{-1}	3.2
	(c) electronic coupling matrix element	none	1.6.3
γ^0	value of the electronic coupling matrix element at the electrode surface	none	1.6.3
ϵ_s	total (static) dielectric constant	none	1.6.4
ϵ_0	permittivity of free space	$\text{C}^2\,\text{N}^{-1}\,\text{m}^{-2}$	1.3.1
ϵ_∞	infinite-frequency dielectric constant	none	1.6.4
η	overpotential, $E-E^0$	V	1.5
κ	fixed width of electrode Gaussian charge distributions	a_0^{-1}	2.3
λ	reorganization energy for electron transfer	eV	1.6.4
λ_i	inner component of the reorganization energy	eV	1.6.4
λ_o	outer component of the reorganization energy	eV	1.6.4
$\boldsymbol{\mu}$	induced dipole vector	ea_0	2.1.3
σ^M	excess charge density on phase M	C cm^{-2}	1.3.2
τ	double layer thickness parameter	cm^{-1}	1.3.2
υ_n	nuclear frequency factor	s^{-1}	1.6.3
υ_s	applied potential sweeping rate	V s^{-1}	1.2
υ_Ox	rate of reduction of Ox	$\text{mol cm}^{-2}\,\text{s}^{-1}$	1.5
υ_Red	rate of oxidation of Red	$\text{mol cm}^{-2}\,\text{s}^{-1}$	1.5
Ψ^PZC	potential of zero charge	V	1.3.2
Ψ^bulk	Poisson potential in the bulk	V	5.4
Ψ_2	Poisson potential at the OHP	V	1.3.3
Ψ^+	(externally applied) potential at the anode	V	1.3.2
Ψ^-	(externally applied) potential at the cathode	V	3.5
Ψ^0	(externally applied) potential at an electrode	V	2.3
$\Delta\Psi_1$	$\Psi^+-\Psi^\text{bulk}$	V	5.4
$\Delta\Psi_2$	$\Psi^--\Psi^\text{bulk}$	V	5.4

Standard abbreviations

Symbol	Meaning	Section
DIPPIM	dipole polarizable ion model	2.1
OHP	outer Helmholtz plane	1.3.1
PES	potential energy surface	4.2
PZC	potential of zero charge	1.3.2
RIM	rigid ion model	2.1
RTIL	room temperature ionic liquid	7.5.2
VBC	vacuum boundary conditions	3.2

Part I

Charge transfer at a metallic electrode

1 Ionic melt electrochemistry

1.1 Introduction

The economic consequences of electron transfer reactions are immense. The world produces energy inefficiently to produce goods that then corrode. This waste can only be reduced by an intimate understanding of electrode kinetics. The development of fuel cells, for instance, could revolutionize our energy production. And numerous industrial applications depend on electrochemical phenomena, ranging from organic and inorganic electrosynthesis to the large-scale production of aluminium and chlorine. But there are imperatives other than the financial. Countries throughout the world are currently investigating pyroprocessing as the preferred method for dealing with nuclear waste to minimize environmental impact and proliferation risk.

The rate of an electron transfer reaction between an electrolyte and a metallic electrode can be affected by:

- the electrode potential;
- the inherent reactivity (ease of oxidation or reduction) of the redox species;
- the structure at the interface between the electrolyte and the metal;
- the nature of the electrode surface;

- transport of the redox species between the electrode and bulk solution.

The kinetics of a faradaic (charge transfer) process at a metallic surface are significantly affected by the **potential of the electrode.** Copper dissolves in aqueous solution within a certain potential range, but will be a stable metal sample outside that range. Hydrogen evolves rapidly at some potentials, but not at others. It would be useful therefore to be able to predict how the electrochemical rate constant depends on the electrode potential. In Section 1.5 we describe the phenomenological Butler Volmer model which underpins the majority of current interpretations of electrode kinetics, notwithstanding its inherent limitations. Section 1.6 details the more modern Marcus model which is based on a microscopic perspective, and which will be employed extensively throughout this work. It is instructive to compare the phenomenological and microscopic models to appreciate their points of contact, and therefore what can potentially be learnt about the former method through simulations based on the latter.

The Marcus theory of electron transfer seeks to understand the observed rates of reaction at the molecular level, and can therefore predict how the kinetics are affected by the **fundamental structural and environmental factors** causing reactions to be facile or sluggish. Marcus obtained an expression for the activation free energy of a redox process as a function of structural parameters of the reactant, which enables the rate constant to be written in a form inspired by transition state theory. The activation free energy will be greater the more gross the difference in reactant structure between the reactant and product species, and the rate of electron transfer slower. The term "reactant structure" is understood to embrace bond angles, bond lengths, degree of solvation, orientation and position of local solvent dipole moments, *etc.*

The forces which govern the behaviour of the liquid electrolyte are interrupted by the **structure at the electrode/electrolyte interface.** The electrode atoms carry charges which will interact electrostatically with the charges on the electrolyte ions. The electrode atoms may also interact with the dipole moments of polarizable ions in solution. The objective of this work is a representation of the *microscopic* phenomena through a realistic computer simulation. However, the existing theoretical models of the interfacial structure (described in Section 1.3) employ a *mean-field* approximation. Furthermore, the theories arise from a *dilute solution*

approximation, whereas our system consists of a *molten salt* electrolyte in order to generate better statistics through higher concentrations of redox species close to the electrodes. The extent of the realism of the mean-field descriptions can be assessed experimentally: electrocapillary measurements determine the variation of the interfacial surface tension as a function of the electrode potential; and A.C. impedance spectroscopy measures the variation in the differential capacitance of the interface with the applied potential. The deficiencies in the mean-field descriptions of the interfacial structure as highlighted by experiment are discussed (Section 1.4.2), along with results from recent computer simulations which provide a microscopic perspective not contained within the existing theories (Section 1.4.1).

The remaining two factors which can affect the rate of heterogeneous electron transfer will not be investigated in this work, but are mentioned here because of their significance when comparing electrochemical data and maximizing the efficiency of industrial processes.

The rate of electrodeposition can vary significantly depending on the **nature of the electrode.** Consider a metal/hydrogen electrode at the zero-current electrode potential. If the electrode is made of either lead or mercury, it will take approximately five years to replace a monolayer of atoms, and consequently a large overpotential is required to induce significant hydrogen evolution. In contrast, a monolayer of platinum is replaced in 0.1 seconds [1]. A related but more subtle effect is the nature of the crystallographic face exposed to the electrolyte. For the deposition of copper on copper, the (100) face grows at 2.5 times the rate of the (111) face at the same applied potential [1].

1.2 Mass transport *vs.* electrode kinetics

In order for electrolysis to proceed, the reactant species must be transported from the bulk solution to the vicinity of the electrode, and the reaction products will themselves diffuse away from the electrode. The overall reaction rate will be limited by the slowest step. A particular reaction might therefore be controlled by the electron transfer kinetics, or the rate at which the redox species can diffuse to and from the electrode/solution interface.

This competition between electrode kinetics and diffusion governs the shape of cyclic voltam-

mograms. Figure 1.1 shows the cyclic voltammogram at a glassy carbon electrode in the NaCl-KCl-$EuCl_3$ melt at 973 K, which is similar to the melt that is modelled in this thesis (KCl-$EuCl_3$). The ordinate is the *anodic* (oxidation) current measured in mA, and the abscissa is the applied potential measured in V. Assume that at the beginning of the experiment all the europium ions are in their +2 oxidation state. The potential of the electrode starts at a value E_1 (about -1.1 V in Figure 1.1) at which Eu^{2+} cannot oxidize. The applied potential is then swept at a constant rate (υ_s) to a value E_2 (about -0.3 V in the figure) at which the electron transfer is driven rapidly. The direction of the voltage scan is then reversed until the electrode obtains its original potential value E_1. Initially there is negligible current because the applied potential is too negative to induce oxidation of the europium ions. As E reaches more positive values, the heterogeneous electrochemical rate constant for the oxidation of the reduced species, k_{Red}, becomes greater (as suggested by Equation 1.41 below). Consequently, the current increases approximately exponentially with time (or applied potential). The rate constant will continue to increase as the potential is swept to E_2, but it is clear that the current reaches a maximum (i_p) and then starts to fall. As the anodic current converts Eu^{2+} to Eu^{3+}, the concentration of Eu^{2+} at the electrode surface steadily decreases.

It is helpful to express the rate of a heterogeneous reaction as the 'flux' of products, J, which is the quantity of material reacting in the electrode area per second (units: mol cm^{-2} s^{-1}). The current, i, is then given by $i = AFJ$ (where A is the electrode area and F is the Faraday constant). By analogy with first-order homogeneous kinetics, we can describe the rate of reaction by the rate law

$$J = k\,[\mathrm{Eu}^{2+}], \tag{1.1}$$

where k is the first-order heterogeneous rate constant for the electron transfer reaction and $[Eu^{2+}]$ is the *surface* concentration of the reactant. The depletion of Eu^{2+} is *partially* replaced by diffusion of fresh Eu^{2+} from the bulk according to Fick's second law [2]:

$$\frac{\partial[\mathrm{Eu}^{2+}]}{\partial t} = D_{\mathrm{Eu}^{2+}} \frac{\partial^2[\mathrm{Eu}^{2+}]}{\partial x^2}, \tag{1.2}$$

where $D_{Eu^{2+}}$ is the diffusion coefficient of Eu^{2+}. The observation of a maximum in the voltammogram therefore reflects a balance between an increasing heterogeneous rate constant and a decreasing reactant concentration. The current then falls as the electrolysis proceeds because the region around the electrode in which Eu^{2+} is depleted (the 'diffusion layer') is constantly expanding, and so Eu^{2+} from the bulk has to diffuse further to the electrode. Algebraically this can be understood using Equation 1.2: once the electrode potential has reached a value at which the surface concentration of Eu^{2+} is close to zero, the concentration gradient will decrease steadily with increasing diffusion layer thickness[1]. We can say that the section of the voltammogram at potentials more negative than that corresponding to the peak current is dominated by electrode kinetics, whereas the section at more positive potentials reflects the rate at which the reactant can diffuse in solution.

As the potential is swept back from E_2 to E_1, a cathodic (reduction) current is observed due to reduction of Eu^{3+} to Eu^{2+}. This current can increase initially because a high concentration of Eu^{3+} has built up in the diffusion layer. The kinetics for the reduction process become increasingly favourable as the potential becomes more negative, until this current also becomes diffusion controlled. The values of potential associated with the peak anodic and cathodic currents, along with diffusion coefficients for the Eu^{2+} and Eu^{3+} species, allow the calculation of the formal standard potential of the redox couple, $E'^{0}_{Eu^{3+}/Eu^{2+}}$. Kuznetsov *et al.* [3] in this way obtain $E'^{0}_{Eu^{3+}/Eu^{2+}} = -0.735\,V$ for $EuCl_3$ in pure KCl at 1300 K, which is the system modelled in this thesis.

To rationalise the observed increase of i_p with v_s in Figure 1.1 we first recall that this area of the voltammogram is primarily controlled by the rate of diffusion of the reactant R. Fick's first law of diffusion indicates that the flux J of a reactant R at a particular position is proportional to the concentration gradient at that position [2]:

$$J = -D_R \frac{\partial [R]}{\partial x}. \tag{1.3}$$

[1] If the transport effects were *purely* diffusional, then the diffusion layer would grow until all the reactant in the cell was exhausted. In reality the concentration profile evolves to a steady state diffusion layer thickness maintained by natural convection in the bulk.

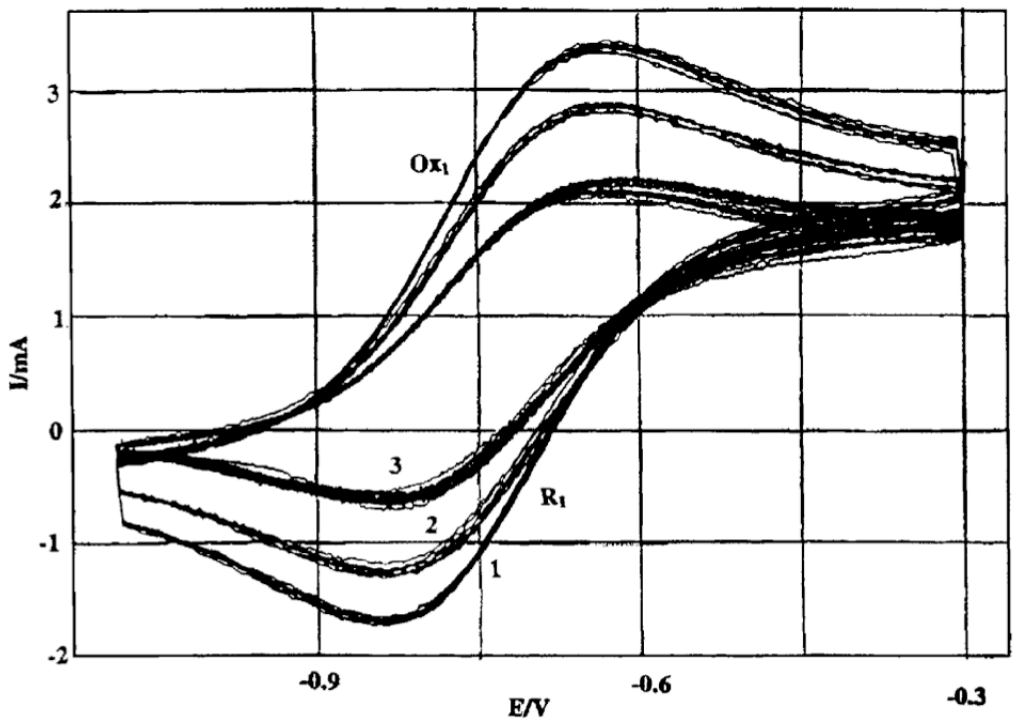

Figure 1.1: A series of cyclic voltammograms at a glassy carbon electrode in NaCl-KCl-$EuCl_3$ melt for various scan rates. Area: $0.19\,\mathrm{cm}^2$; temperature: $973\,\mathrm{K}$; concentration of $EuCl_3$: $9.0\times10^{-5}\,\mathrm{mol\,cm}^{-3}$; reference electrode: Cl_2/Cl^-; scan rate: $0.1\,\mathrm{Vs}^{-1}$(1), $0.075\,\mathrm{Vs}^{-1}$(2), $0.05\,\mathrm{Vs}^{-1}$(3). Taken from reference [3].

When the electrode potential is swept more rapidly, relatively less time is available for electrolysis and the depletion of R near the electrode is less marked, resulting in a thinner diffusion layer and a steeper concentration gradient. The consequent larger flux effects an enhanced i_p.

One of the primary aims of this work is to use our simulation method to connect with the Marcus theory of electrode kinetics, and therefore all our results are appropriate to the fast diffusion limit, where the electron transfer is the rate-determining step of the overall electrochemical process. As will become apparent in Chapter 4, our model electrochemical system is capable of sustaining an electrical current, which will in future allow us to model a working electrode where diffusion competes with the kinetics of electron transfer.

1.3 The electrical double layer

1.3.1 The Helmholtz model

It follows from Gauss's law [4] that a metallic conductor supports no electric fields within itself at equilibrium, and so any excess charge is located at its surface. Helmholtz [5, 6, 7] used this concept to posit that the counter charge in a conducting solution would likewise reside at the surface. There would thus be two sheets of charge, one on the electrode and the other in solution, as shown in Figure 1.2 (a). The charge densities on the two sheets are equal in magnitude and opposite in sign, and so the structure is equivalent to a parallel plate capacitor, and the potential therefore drops linearly across the interface. The charge density, σ, can be related to the voltage drop, $\Delta\Psi$, between the plates through

$$\sigma = \frac{\epsilon\epsilon_0}{d}\Delta\Psi, \tag{1.4}$$

where d is the distance between the plates, ϵ is the dielectric constant of the medium, and ϵ_0 is the permittivity of free space.

The variation of this charge density with applied potential results in the differential capacitance, C, of the interface:

$$\frac{\partial\sigma}{\partial\Delta\Psi} = C = \frac{\epsilon\epsilon_0}{d}. \tag{1.5}$$

The Helmholtz model therefore predicts a constant capacitance.

1.3.2 The Gouy-Chapman Theory

Gouy [8, 9] and Chapman [10] model the counter charge in solution as a *diffuse layer*, as illustrated in Figure 1.2 (b). The finite thickness of counter charge arises from an interplay between the tendency of the charge on the metal to attract or repel ions according to their polarity, and the tendency of thermal processes to randomize them.

The electrostatic forces arising from the metal charge have a greater propensity for overcom-

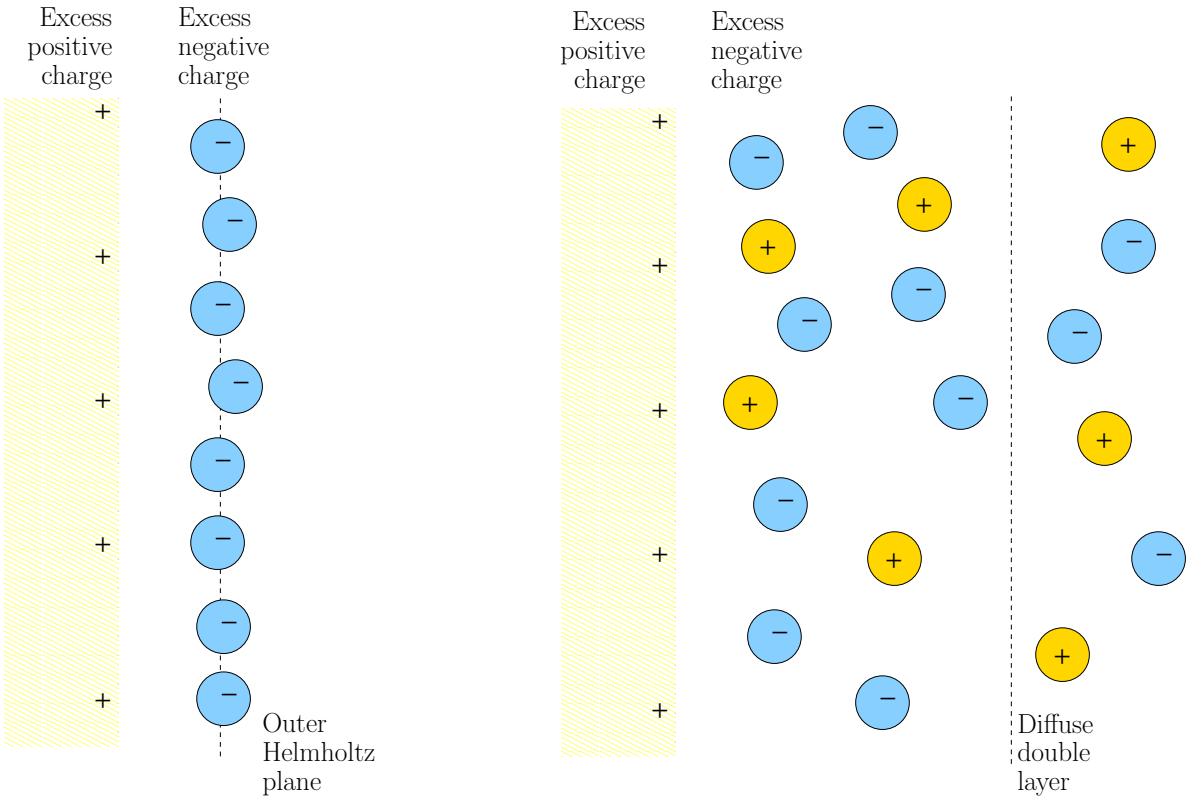

Figure 1.2: (a) *Left:* A simple model of the electrode–solution interface treats it as two rigid planes of charge. One plane, the outer Helmholtz plane (OHP), is due to the ions with their solvating molecules and the other plane is that of the electrode itself. (b) *Right:* The Gouy-Chapman model of the electrical double layer treats the outer region as an atmosphere of counter charge, similar to the Debye-Hückel theory of ion atmospheres.

ing thermal motions as an ion approaches the interface. Consequently the greatest concentration of counter charge resides adjacent to the electrode, whilst progressively lesser concentrations are found at greater distances where thermal motions have increasing influence. The bulk concentration is achieved at a distance from the electrode where the net charge density is zero (*i.e.* positive and negative ions have equal local densities), and the dynamics are controlled exclusively by thermal motion.

The Gouy-Chapman model describes the diffuse layer through statistical mechanics. The solution is divided into laminae arranged parallel to the electrode surface. The laminae are all in thermal equilibrium with each other, but the ions of any species i will have different energies in the various laminae because the electrostatic potential varies. The number concentrations of species in two laminae have a ratio determined by the Boltzmann factor. The reference lamina is chosen to be far from the electrode, where every ion is at its bulk concentration n_i^0. The population in any other lamina, n_i, is then given by

$$n_i = n_i^0 \exp\left(\frac{-z_i e\Psi}{k_\mathrm{B}T}\right), \tag{1.6}$$

where Ψ is the electrical potential measured with respect to the bulk solution, and z_i is the (signed) charge on ion i.

The corresponding charge density of a lamina is

$$\begin{aligned}\rho(x) &= \sum_i n_i z_i e \\ &= \sum_i n_i^0 z_i e \exp\left(\frac{-z_i e\Psi}{k_\mathrm{B}T}\right).\end{aligned} \tag{1.7}$$

The charge density is then related to the potential through the Poisson equation

$$\rho(x) = -\epsilon\epsilon_0 \frac{\mathrm{d}^2\Psi}{\mathrm{d}x^2}. \tag{1.8}$$

Combining Equations 1.7 and 1.8 gives

$$\frac{\mathrm{d}^2\Psi}{\mathrm{d}x^2} = -\frac{e}{\epsilon\epsilon_0}\sum_i n_i^0 z_i \exp\left(\frac{-z_i e\Psi}{k_\mathrm{B}T}\right). \tag{1.9}$$

We note that

$$\frac{\mathrm{d}^2\Psi}{\mathrm{d}x^2} = \frac{1}{2}\frac{\mathrm{d}}{\mathrm{d}\Psi}\left(\frac{\mathrm{d}\Psi}{\mathrm{d}x}\right)^2, \tag{1.10}$$

and hence

$$\mathrm{d}\left(\frac{\mathrm{d}\Psi}{\mathrm{d}x}\right)^2 = -\frac{2e}{\epsilon\epsilon_0}\sum_i n_i^0 z_i \exp\left(\frac{-z_i e\Psi}{k_\mathrm{B}T}\right)\mathrm{d}\Psi. \tag{1.11}$$

Integrating yields

$$\left(\frac{\mathrm{d}\Psi}{\mathrm{d}x}\right)^2 = \frac{2k_\mathrm{B}T}{\epsilon\epsilon_0}\sum_i n_i^0\left[\exp\left(\frac{-z_i e\Psi}{k_\mathrm{B}T}\right) - 1\right], \tag{1.12}$$

where we required that at distances far from the electrode $\Psi = 0$ and $(\mathrm{d}\Psi/\mathrm{d}x = 0)$. For a symmetrical electrolyte[1], Equation 1.12 simplifies to [11]

$$\frac{\mathrm{d}\Psi}{\mathrm{d}x} = -\left(\frac{8k_\mathrm{B}Tn^0}{\epsilon\epsilon_0}\right)^{1/2}\sinh\left(\frac{ze\Psi}{2k_\mathrm{B}T}\right), \tag{1.13}$$

where n^0 is the number concentration of each ion in the bulk, and z is now the *magnitude* of the charge on the ions. Rearranging Equation 1.13 results in

$$\int_{\Psi^+}^{\Psi}\frac{\mathrm{d}\Psi}{\sinh(ze\Psi/2k_\mathrm{B}T)} = -\left(\frac{8k_\mathrm{B}Tn^0}{\epsilon\epsilon_0}\right)^{1/2}\int_0^x \mathrm{d}x, \tag{1.14}$$

where Ψ^+ is the electrical potential of the anode relative to the bulk solution. Integrating gives the final result

$$\frac{\tanh\left(ze\Psi/4k_\mathrm{B}T\right)}{\tanh\left(ze\Psi^+/4k_\mathrm{B}T\right)} = \exp\left(-\tau x\right), \tag{1.15}$$

where

$$\tau = \left(\frac{2n^0z^2e^2}{\epsilon\epsilon_0 k_\mathrm{B}T}\right)^{1/2}. \tag{1.16}$$

The potential profile is exponential in the limit of small Ψ^+. If $(ze\Psi^+/4k_\mathrm{B}T) < 0.5$ it follows

[1]That is, an electrolyte having only one cationic and one anionic species, both with charge magnitude z.

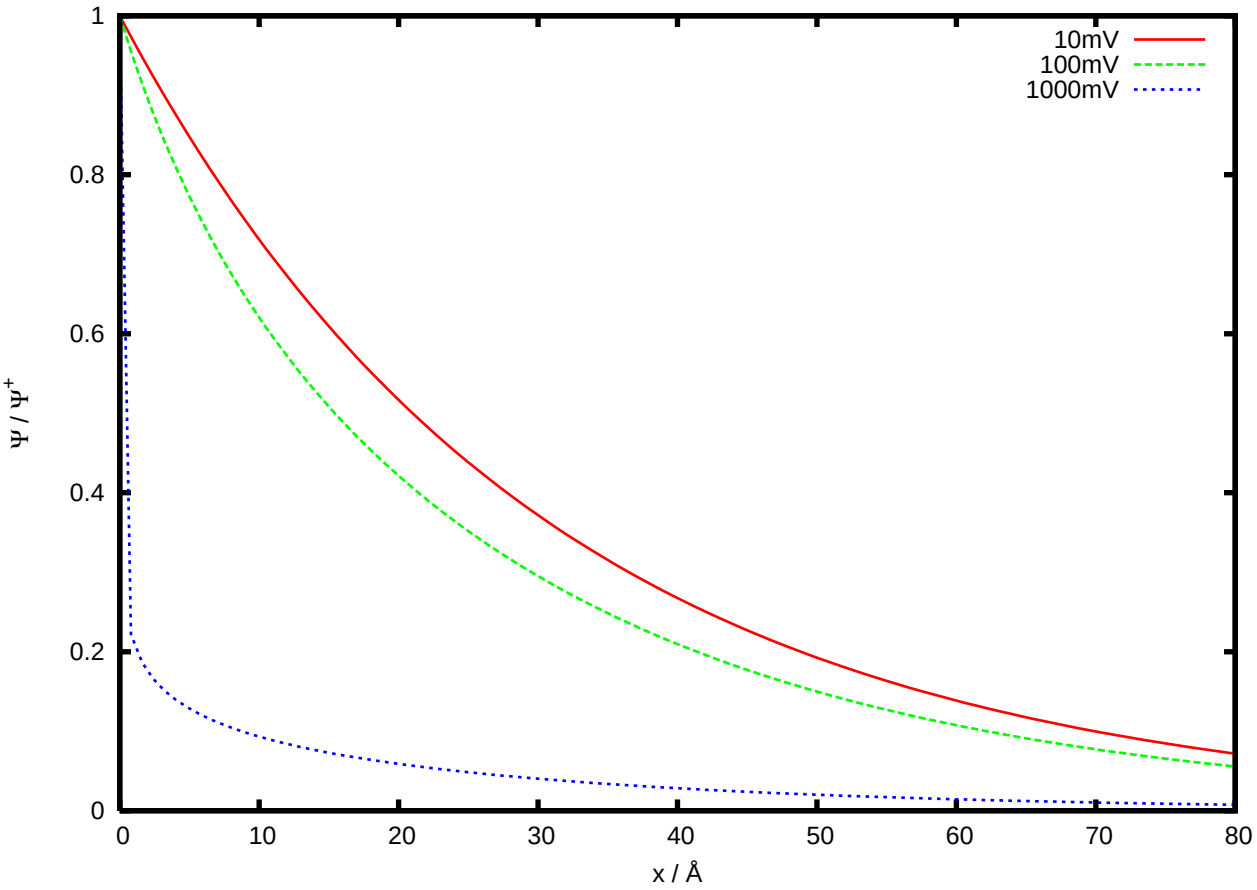

Figure 1.3: The potential across the double layer in the Gouy-Chapman model (see Equation 1.15). Calculated for a 10^{-2} M solution of a 1:1 electrolyte at 25°C. $\epsilon = 78.49$ and $1/\tau = 30.4$ Å. The curve corresponding to $\Psi^+ = 10$ mV is the limiting exponential form.

that $\tanh(ze\Psi/4k_BT) \approx ze\Psi/4k_BT$ everywhere, and

$$\Psi = \Psi^+ \exp(-\tau x). \tag{1.17}$$

Equation 1.15 is used to plot the potential profile across the diffuse layer for several values of Ψ^+ in Figure 1.3. When the electrode is highly charged (large Ψ^+), the interfacial potential drop is very steep because the double layer is relatively compact. As the electrode becomes less highly charged, the drop becomes more gradual until the exponential limiting form is reached.

In order to calculate the differential capacitance we need to first determine the total diffuse

charge in the solution. According to Gauss's law this is

$$q = \epsilon\epsilon_0 A \left(\frac{\mathrm{d}\Psi}{\mathrm{d}x}\right)_{x=0}, \tag{1.18}$$

where A is the area of the electrode surface. We now denote the excess charge density on the metal as σ^{M}, and the equal but opposite counter charge density in the solution as σ^{S}. Substituting 1.13 into Equation 1.18, and noting that $q/A = \sigma^{\mathrm{S}}$, we obtain

$$\sigma^{\mathrm{M}} = -\sigma^{\mathrm{S}} = (8k_{\mathrm{B}}T\epsilon\epsilon_0 n^0)^{1/2} \sinh\left(\frac{ze\Psi^+}{2k_{\mathrm{B}}T}\right). \tag{1.19}$$

Consequently the differential capacitance is

$$C = \frac{\mathrm{d}\sigma^{\mathrm{M}}}{\mathrm{d}\Psi^+} = \left(\frac{2z^2e^2\epsilon\epsilon_0 n^0}{k_{\mathrm{B}}T}\right)^{1/2} \cosh\left(\frac{ze\Psi^+}{2k_{\mathrm{B}}T}\right). \tag{1.20}$$

The minimum capacitance is obtained at the *potential of zero charge* (PZC) where $\sigma^{\mathrm{M}} = \sigma^{\mathrm{S}} = 0$. Equation 1.20 is graphed in Figure 1.4, in which the abscissa $\Psi - \Psi^{\mathrm{PZC}}$ is the potential relative to the PZC.

1.3.3 Stern's modification

Stern [12] took a Hegelian dialectic approach. He synthesised the Helmholtz thesis of a rigid layer of ions adjacent to the electrode with the Gouy-Chapman antithesis of the ions being scattered in a diffuse layer. This is schematized in Figure 1.5. The modification is in essence twofold:

- A *plane of closest approach* is fixed at a certain distance x_2 from the electrode.
- Part of the charge is immobilized close to the electrode, and the remainder is diffusely spread out in the solution.

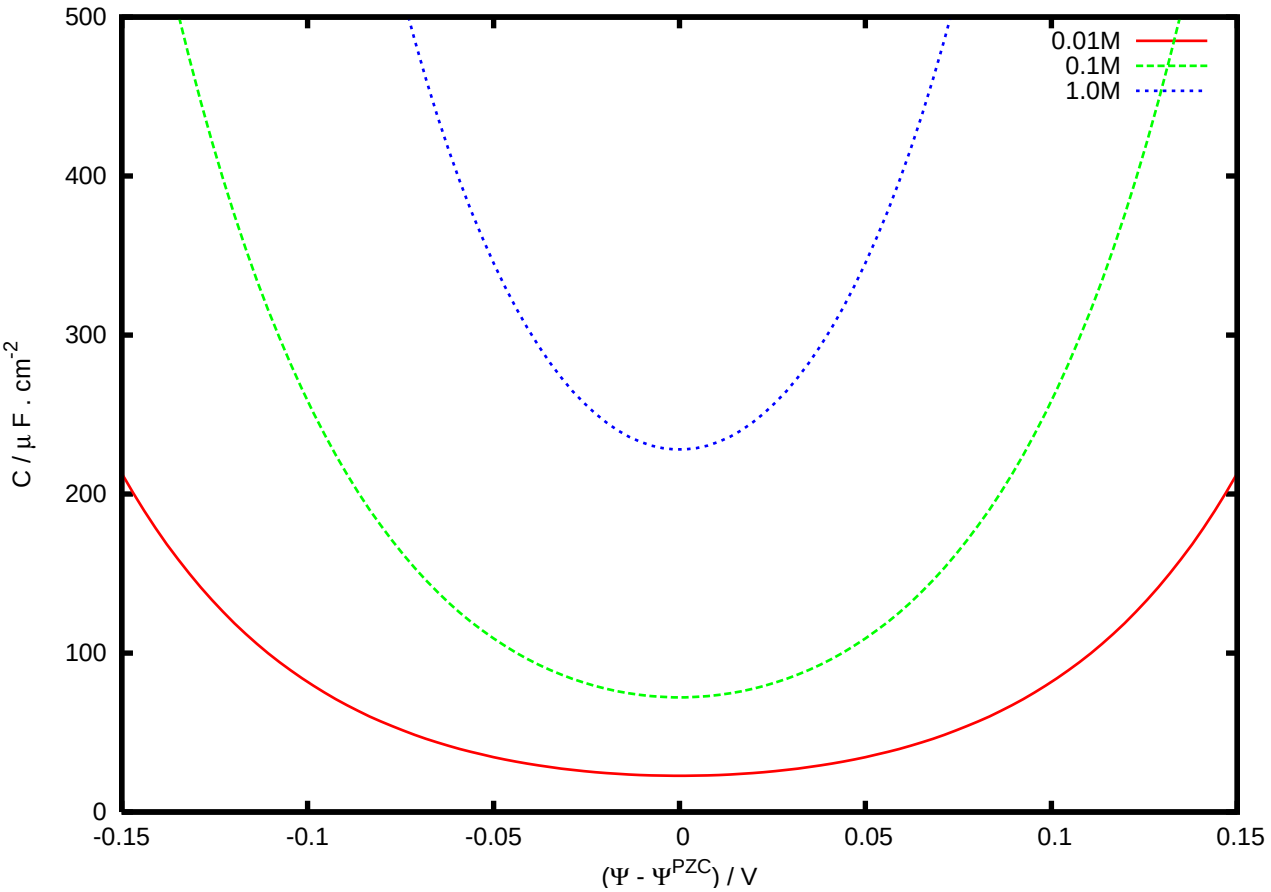

Figure 1.4: The differential capacitance of the interface as predicted by Gouy-Chapman theory (see Equation 1.20). The cosh functions associated with three different concentrations of a 1:1 electrolyte in water at 25°C are plotted.

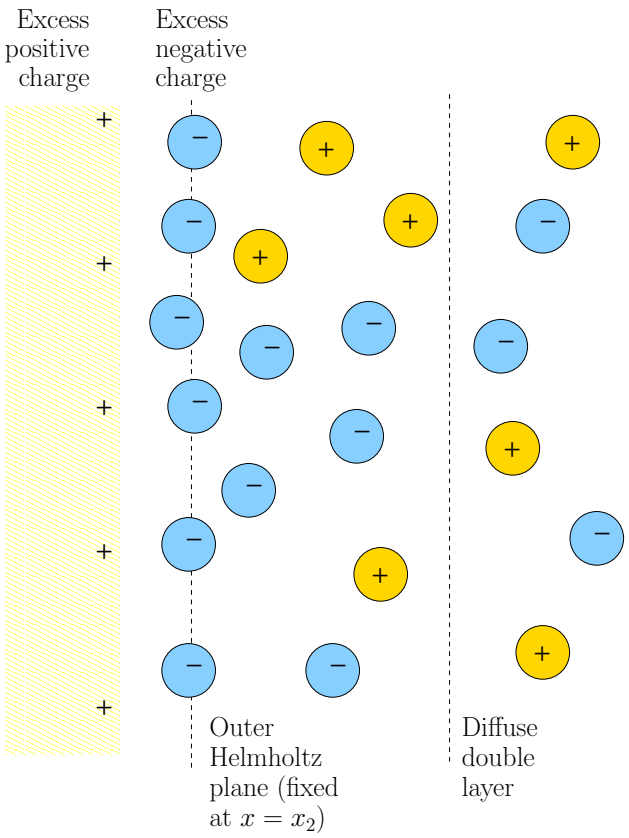

Figure 1.5: A representation of the Stern model of the electrode–solution interface. The model incorporates the idea of an outer Helmholtz plane near the surface and of a diffuse double layer further away from the surface.

Equation 1.9 still applies at distance $x \geq x_2$. So we have

$$\int_{\Psi_2}^{\Psi} \frac{\mathrm{d}\Psi}{\sinh(ze\Psi/2k_\mathrm{B}T)} = -\left(\frac{8k_\mathrm{B}Tn^0}{\epsilon\epsilon_0}\right)^{1/2} \int_{x_2}^{x} \mathrm{d}x, \tag{1.21}$$

or

$$\frac{\tanh\left(ze\Psi/4k_\mathrm{B}T\right)}{\tanh\left(ze\Psi_2/4k_\mathrm{B}T\right)} = \exp\left(-\tau(x-x_2)\right), \tag{1.22}$$

where Ψ_2 is the potential at the OHP ($x = x_2$). We can use Equation 1.13 to write down the field strength at x_2:

$$\left(\frac{\mathrm{d}\Psi}{\mathrm{d}x}\right)_{x=x_2} = -\left(\frac{8k_\mathrm{B}Tn^0}{\epsilon\epsilon_0}\right)^{1/2} \sinh\left(\frac{ze\Psi_2}{2k_\mathrm{B}T}\right). \tag{1.23}$$

Equation 1.8 reveals that the potential profile in the region $0 < x > x_2$ is linear, since there is no charge density there. The total potential drop across the double layer is

$$\Psi^+ = \Psi_2 - \left(\frac{\mathrm{d}\Psi}{\mathrm{d}x}\right)_{x=x_2} x_2. \tag{1.24}$$

The potential profile is plotted in Figure 1.6 using Equations 1.22 and 1.23. The vertical green line at $x = x_2$ marks the position of the plane of closest approach.

Following again the procedure which led to Equation 1.19 above, we obtain the charge density:

$$\sigma^\mathrm{M} = -\sigma^\mathrm{S} = -\epsilon\epsilon_0 \left(\frac{\mathrm{d}\Psi}{\mathrm{d}x}\right)_{x=x_2} = (8k_\mathrm{B}T\epsilon\epsilon_0 n^0)^{1/2} \sinh\left(\frac{ze\Psi_2}{2k_\mathrm{B}T}\right). \tag{1.25}$$

To derive the differential capacitance we substitute Equation 1.24 into Equation 1.25 to give

$$\sigma^\mathrm{M} = (8k_\mathrm{B}T\epsilon\epsilon_0 n^0)^{1/2} \sinh\left[\frac{ze}{2k_\mathrm{B}T}\left(\Psi^+ - \frac{\sigma^\mathrm{M}x_2}{\epsilon\epsilon_0}\right)\right]. \tag{1.26}$$

Differentiation and rearrangement [11] results in

$$\frac{1}{C} = \frac{x_2}{\epsilon\epsilon_0} + \frac{1}{(2\epsilon\epsilon_0 z^2e^2n^0/k_\mathrm{B}T)^{1/2}\cosh\left(ze\Psi_2/2k_\mathrm{B}T\right)}. \tag{1.27}$$

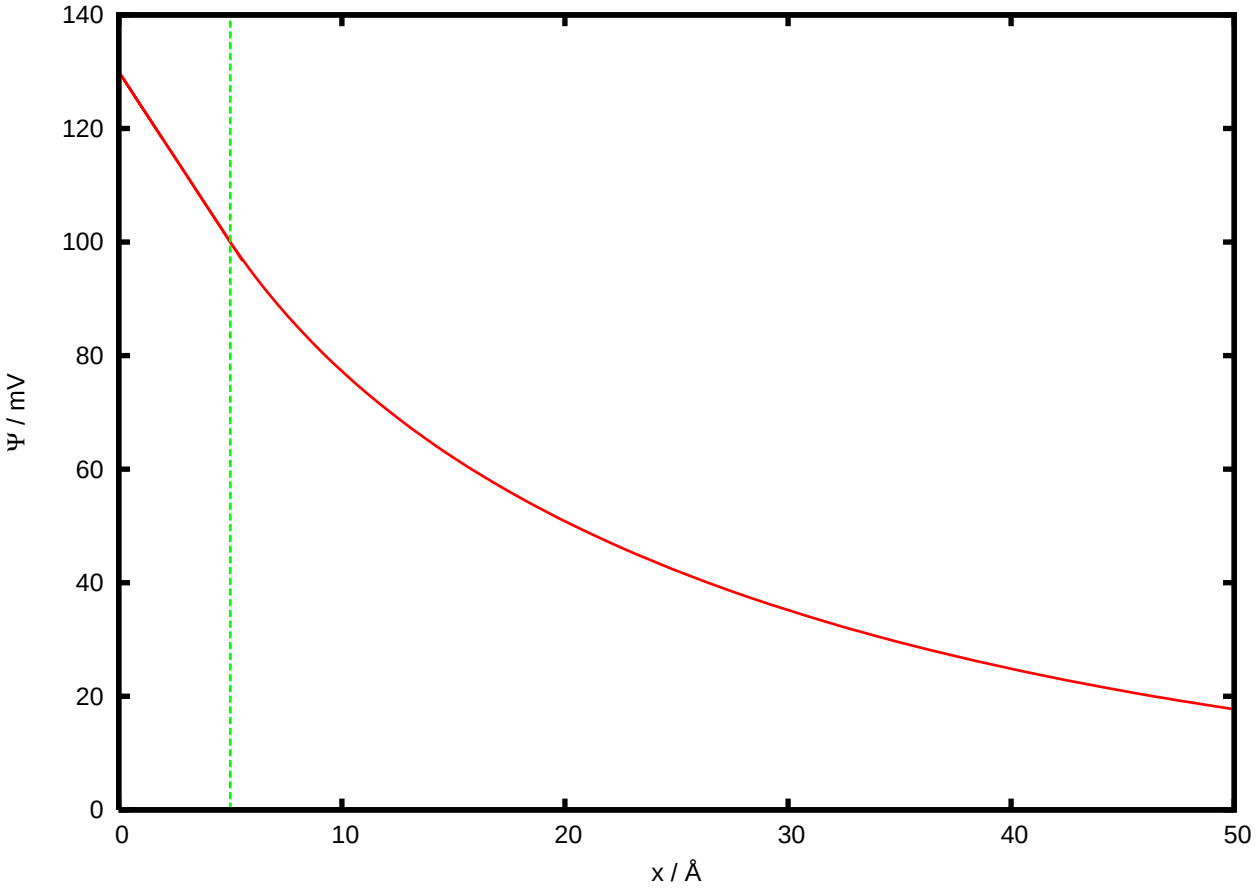

Figure 1.6: The potential across the double layer in the Stern model. Calculated for a 10^{-2} M solution of a 1:1 electrolyte at 25°C. $\epsilon = 78.49$ and $1/\tau = 30.4$ Å. The vertical green line at $x_2 = 5$ Å represents the position of the Helmholtz layer. The potential is linear in the region $0 < x > x_2$ (see Equation 1.23). The potential at $x > x_2$ is calculated using Equation 1.22.

Each term represents the reciprocal of a differential capacity, and we can write

$$\frac{1}{C} = \frac{1}{C_{\mathrm{H}}} + \frac{1}{C_{\mathrm{D}}}, \tag{1.28}$$

where C is the total capacity of the interface, C_{H} is the Helmholtz capacity, and C_{D} is the Gouy-Chapman capacity. This result is the same as the expression for the total capacity of two capacitors linked in series. Figure 1.7 is a schematic of the differential capacitance for different electrolyte concentrations. The value of C_{H} is independent of potential, but C_{D} is V-shaped.

Figure 1.7 can be rationalized in a simplistic physical way. At low concentrations of electrolyte and potentials close to the PZC, the thickness of the diffuse layer is large. This is due both to the weak electric fields arising from the electrode charges, and the low concentration of electrolyte. The total capacitance is dominated by the C_{D} term, and is therefore small. As the potential is shifted away from the PZC, the electric fields arising from the electrode charges become larger, and the centre of mass of the counter charge is drawn closer to the electrode. This leads to an increase in the capacitance. At potentials sufficiently far from the PZC, the value of C_{D} becomes so large that the total capacitance is dominated by the C_{H} component. This explains why the capacitance reaches a plateau at extreme positive and negative values of the potential, because C_{H} is independent of potential (see Equation 1.5).

At high concentrations the dip in the capacitance at the PZC due to the diffuse layer is absent. There is now an abundance of counter charges in the vicinity of the electrode, the value of C_{D} is consequently very large, and the total capacitance is dominated by C_{H}.

1.4 Limitations of the double layer model

1.4.1 Previous particle-based simulations

The earliest computational studies designed to test the Poisson-Boltzmann equation were carried out by Torrie and Valleau [13, 14] in the 1980s. They performed Monte Carlo simulations using the Restricted Primitive Model, which represents the ions as charged spheres of diameter

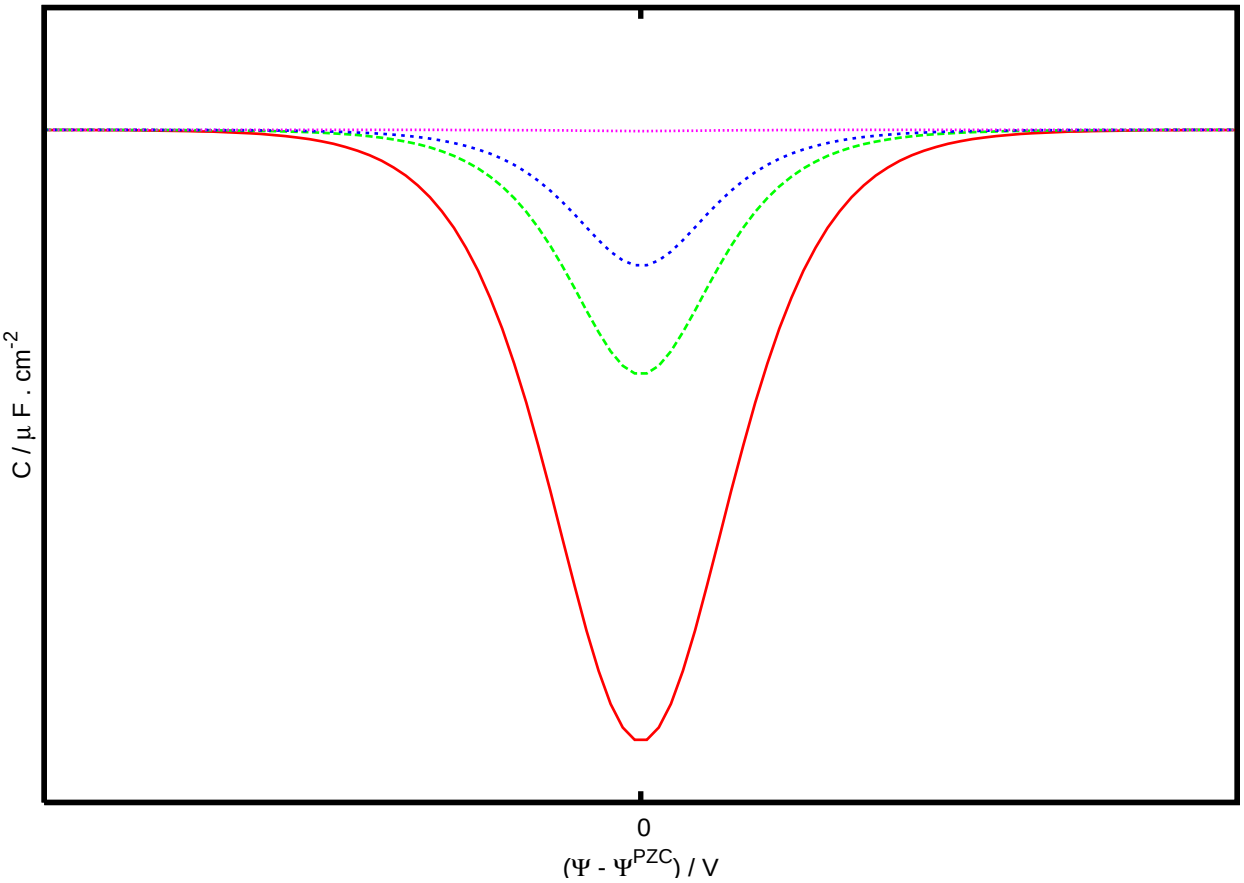

Figure 1.7: The differential capacitance across the interface according to the Stern model. All the curves have their minima at $\Psi - \Psi^{\mathrm{PZC}} = 0$. The red curve represents the lowest electrolyte concentration, and the purple line represents the most concentrated electrolyte. The value of the capacitance at the plateau at the highest and lowest overpotentials corresponds to C_{H} of Equation 1.28. C_{D} varies in a V-shaped fashion.

d in a solvent with dielectric constant ϵ. The results suggested that the Stern model is a good approximation for 1:1 electrolytes up to concentrations of 0.1 M, and for surface charges up to 30 μC/cm^2. However, they found that the Stern model greatly overestimated the diffuse layer potential for 2:2 and 2:1 electrolytes. These oft-quoted results were carried out with an electrode held at constant charge; more recently, Boda *et al.* [15] have shown that the Stern model predicts the double layer to be too broad when the electrode *charge* is specified, but too narrow when the electrode *potential* is specified. They suggest that the inaccuracies of the Stern model in the case of divalent ions is part of a general failure for electrolytes with a high coupling constant (small diameter, low temperature, high valence, low solvent dielectric constant).

The Stern model fails to predict the so-called anomalous temperature effect of the capacitance, namely the positive temperature derivative of the capacitance of molten salts [16] and some frozen electrolytes [17]. Henderson and Boda [18] have demonstrated that for strongly coupled liquids and a small electrode charge, the counterions are more strongly attracted to coions than to the electrode, and so the ions are pulled away from the electrode. This contrasts with weakly coupled liquids which, even at low electrode charge, are pushed against the electrode by the osmotic pressure. The depletion of ions adjacent to the electrode effects an increase in the width and potential of the double layer, and a consequent decrease in the capacitance.

Indeed, the ability of the Primitive Model to explain various experimental phenomena has engendered its renaissance in the last decade. The volume exclusion effects and ionic correlations not captured in the mean-field Poisson-Boltzmann description play important roles in DNA condensation [19, 20], cement cohesion [21], and the attractive force between like-charged particles [22, 23].

Recent simulations [24, 25, 26, 27, 28] have examined the microscopic structure of ionic liquids at a metal interface and found standing *charge density waves* formed by collective rearrangement of the ions. Spatial integration of the Poisson equation then results in a potential which rapidly oscillates in the vicinity of the walls, in contrast to the monotonic behaviour

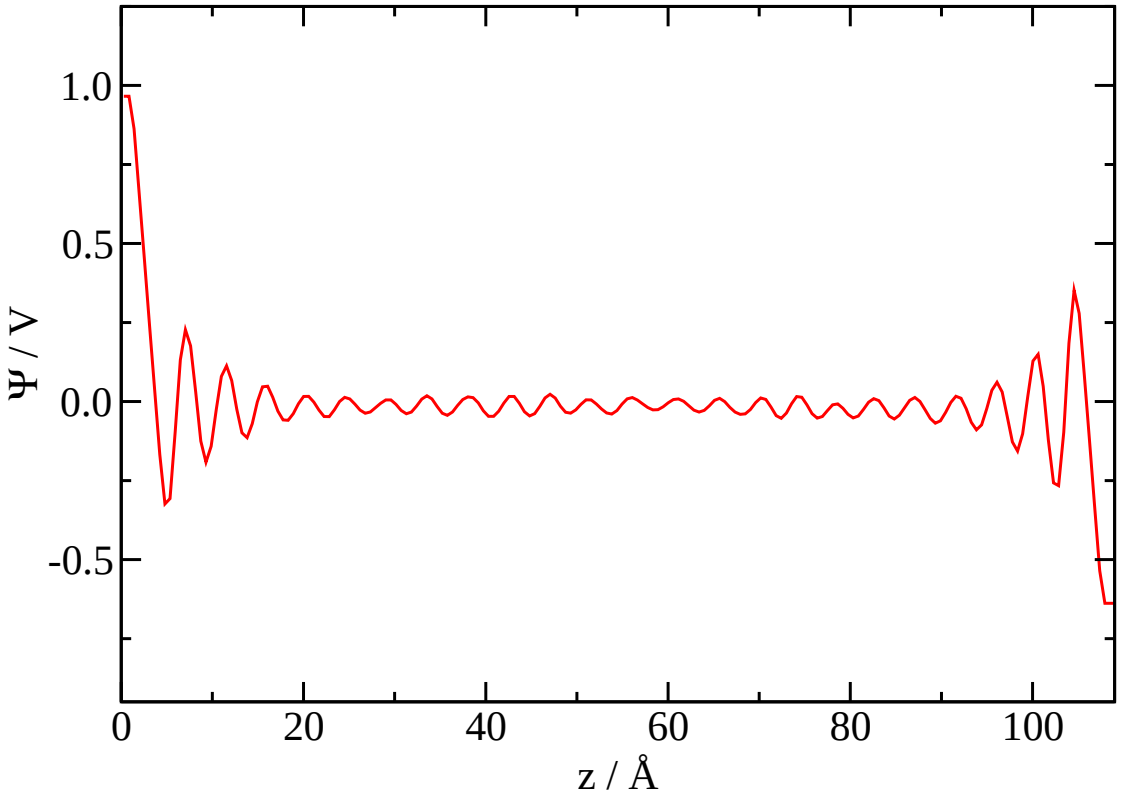

Figure 1.8: Poisson potential across the cell for KCl at a temperature of 1300 K sandwiched between two electrodes held at a constant charge density of $3.242\,\mu\mathrm{C\,cm^{-2}}$. The left-hand electrode is positively charged and the right-hand electrode negatively charged. The potential profile is obtained *via* spatial integration of the Poisson equation. Taken from reference [24].

predicted by the Stern model. See, for example, Figure 1.8. Such oscillatory profiles have been corroborated by experiment [29, 30], and more data in this area would be welcome: experiments usually yield integral quantities, such as the interfacial capacitance, whereas electrochemical charge transfer is determined by the interfacial profiles.

1.4.2 An extended mean-field theory

We noted in Section 1.3.1 that the Helmholtz model predicts that the capacitance is independent of the applied potential (see Equation 1.5). Experimental measurements of the differential

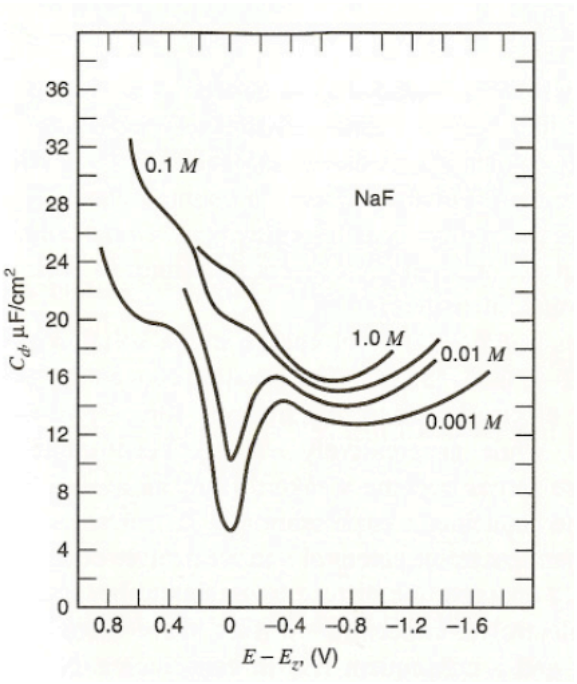

Figure 1.9: Differential capacitance *vs.* potential for NaF solutions in contact with mercury at 25°C. Taken from reference [31].

capacitance, however, show variation with potential and concentration. A particularly striking example is provided by Figure 1.9, in which is plot the capacitance appropriate to the interface between mercury and sodium fluoride solutions of various concentrations. It would appear that an electrified interface does not behave as a simple double layer; the Helmholtz model is too naïve an approach.

The Gouy-Chapman theory predicts that the interfacial capacitance will have an inverted parabola dependence on the applied potential (see Equation 1.20 and Figure 1.4). This resembles the experimental capacitance curves for NaF in Figure 1.9 only at very low concentrations and at potentials near the PZC. The failures of the model are obvious: the experimental capacitance flattens at higher potentials, the valley at the PZC disappears at high electrolyte concentration, and the values are much lower than the Gouy-Chapman predictions.

There are obvious reasons why the model lacks verisimilitude. First, it neglects ion-ion correlations which become increasingly important as the concentration increases. Second, it assumes that the ions are point charges. Third, it assumes an invariant dielectric constant in the region between the electrode and the bulk of the solution.

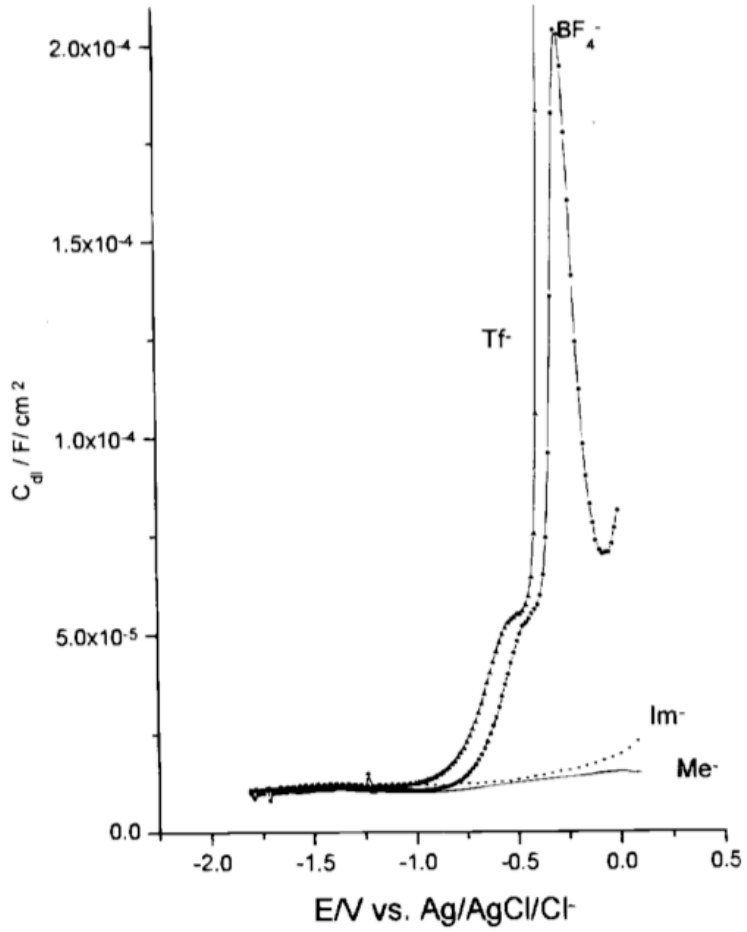

Figure 1.10: Differential capacitance *vs.* potential for ionic liquids with EMI^+ cation and indicated anions in contact with a saturated calomel electrode. EMI^+ = 1-ethyl-3-methyl imidazolium, $Me^- = (CF_3SO_2)C^-$, $Im^- = (CF_3SO_2)_2N^-$, $Tf^- = CF_3SO_3^-$. Taken from reference [33].

The Stern model is certainly the most consistent with the experimental NaF results. An obvious discrepancy, however, is that the value of C_H (the capacitance of the charges held in the compact layer) is not actually independent of potential. Furthermore, the theory neglects differences in x_2 for anions and cations, the oscillating charge density profiles found in computer simulation, and the possibility of specific adsorption of ions to the electrode.

Most experimental molten salt capacitance curves are parabolic around a capacitance minimum at the PZC [32]. There are fewer data, however, for capacitance curves of ionic liquids, and indeed some experiments [33, 34] seem to generate a *maximum* in the capacitance at the PZC. An example of such behaviour is illustrated by the mercury electrode curves in Figure 1.10, obtained by Nanjundiah *et al.* [33].

Kornyshev [27, 28, 35] has extended the Gouy-Chapman theory to derive an analytical statistical mechanics expression for the double layer capacitance which reflects the fact that a local concentration of counter charge cannot increase indefinitely with electrode potential, but rather reaches a limiting value due to the finite sizes of the ions. The model casts the ionic concentrations as Fermi-like distributions (compare with the Boltzmann distributions in Equation 1.6) in the context of the mean-field lattice-gas model of concentrated electrolytes. This means that, however the system is polarized, there is a maximum allowed local concentration: $c_+(\Psi \to -\infty) = c_{\max}$ and $c_-(\Psi \to +\infty) = c_{\max}$, where c_+ and c_- denote respectively the cationic and anionic concentrations. The derivation [35] proceeds through the Poisson-Boltzmann equation, or rather a "Poisson-Fermi" equation, and casts the final result for the double layer capacitance as

$$C = C_0 \cdot \frac{\cosh\left(\frac{e\Psi}{2k_{\mathrm{B}}T}\right)}{1 + 2\Gamma \sinh^2\left(\frac{e\Psi}{2k_{\mathrm{B}}T}\right)} \cdot \sqrt{\frac{2\Gamma \sinh^2\left(\frac{e\Psi}{2k_{\mathrm{B}}T}\right)}{\ln\left[1 + 2\Gamma \sinh^2\left(\frac{e\Psi}{2k_{\mathrm{B}}T}\right)\right]}}. \tag{1.29}$$

The capacitance is written here in terms of the parameter Γ, which reflects the compressibility of the liquid:

$$\Gamma = \overline{N}/N, \tag{1.30}$$

where $\overline{N}$ is the total number of cations and anions in the bulk, and N is the total number of sites available for them. Alternatively Γ can be written as[1]

$$\Gamma = 2c_0/c_{\max}, \tag{1.31}$$

where in the bulk, $c_+ = c_- = c_0$, and $c_{\max}$ is again the maximum allowed local concentration of ions (both cations and anions). C_0 is the minimum value of the capacitance as predicted by the Gouy-Chapman theory (see Equation 1.20). There are suggestions that ionic liquids have $\Gamma < 1$. Experiments indicate a swelling of some 15% upon melting, without a corresponding increase in the average interionic distances measured by spectroscopy [36]. And molecular

[1] We assume here that the total volume of the system is independent of the applied potential.

simulations have indicated the presence of vacuum cavities within ionic liquids [37], suggesting that they are not incompressible.

Equation 1.29 gives the Gouy-Chapman result as $\Gamma \to 0$, which serves as a reminder that this earlier theory arises from a dilute solution approximation. Figure 1.11 displays the capacitance curves obtained through Equation 1.29 for three finite values of Γ. When $0 < \Gamma < 1/3$, the function is camel-shaped: instead of growing exponentially at large potentials, the capacitance decreases according to an inverse square law which is a signature of the lattice saturation. Kornyshev posits that most experimental capacitance curves for *high temperature molten salts* are V-shaped because: (i) upon melting the salt acquires a large number of free voids (holes) whose net volume increases with temperature [38] as $\propto T^{3/2}$; (ii) the high temperature of molten salts (compared to room temperature ionic liquids) will serve to push the decaying wings of the capacitance out to higher potentials.

The demarcation line between a camel-shape and bell-shape capacitance occurs at $\Gamma = 1/3$. Kornyshev suggests that most *room temperature ionic liquids* will have $\Gamma > 1/3$, and therefore exhibit a bell-shaped capacitance curve with a maximum capacitance at the PZC. It should be noted that the Kornyshev model is still based upon a mean-field approximation, and therefore cannot account for microscopic effects such as the oscillations in the concentration profiles that we reported in Section 1.4.1. Kornyshev has carried out some molecular dynamics (MD) simulations of model ionic liquids sandwiched between two metal plates to facilitate a comparison with his mean-field theory (see in particular [27, 28]). It would appear that the methodology therein employed uses a modification of the Ewald summation appropriate to a slab geometry, and consequently *the potential at their simulated electrodes is unknown.* This point will be taken up more fully in Chapter 3, in which we develop a solution to this problem for our simulations.

1.5 Butler Volmer kinetics

It is convenient to express the rate of heterogeneous electron transfer as the flux of products, *i.e.* the amount of product formed over a region of the electrode surface in an interval of time

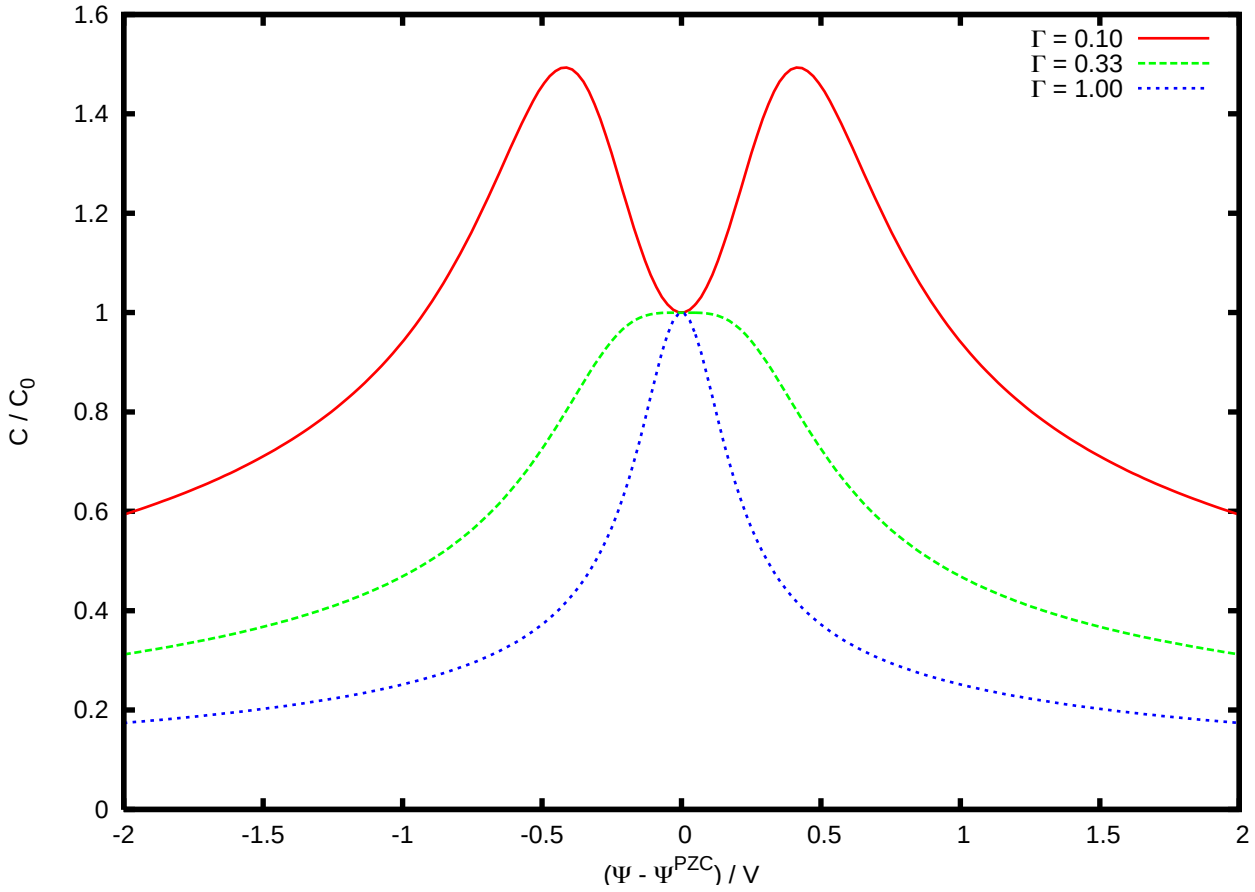

Figure 1.11: The differential capacitance across the interface according to the Kornyshev model. Plotted using equation 20 from reference [35] with $T = 1300\,\mathrm{K}$.

divided by the area of the region and the duration of the interval. The first-order rate law has the form

$$J = k\,[\text{species}] \tag{1.32}$$

where k is the first-order heterogeneous rate constant and [species] is the surface concentration of reactant (in $\text{mol}\,\text{cm}^{-3}$), namely that within the critical electron tunnelling distance. The first-order heterogeneous rate constant has the dimensions of velocity, unlike the analogous homogeneous rate constant where the unit is 1/time. Note that the relevant concentration term in Equation 1.32 is that adjacent to the electrode[1]. The surface concentration will evolve temporally, since the passage of current through the interface will lead to the depletion of reactants local to the electrode surface. As will become fully evident in Chapter 5, there is a pronounced spatial variation in the reactant concentration even at equilibrium, with no current passing through the interface. The heterogeneous rate constant will depend on temperature and pressure, as is the case for the homogeneous rate constant. However the heterogeneous (electrochemical) rate constant is extremely sensitive to the potential drop across the interface ($\Psi^{\pm} - \Psi^{\text{bulk}}$). For a typical reaction at 1300 K, a change in ($\Psi^{\pm} - \Psi^{\text{bulk}}$) of 1 V will effect a corresponding change in k of the order of 10^2.

The rate of reduction of Ox is given by

$$\upsilon_{\text{Ox}} = k_c[\text{Ox}], \tag{1.33}$$

where [Ox] is the surface concentration of the oxidised species. Analogously, the rate of oxidation of Red is

$$\upsilon_{\text{Red}} = k_a[\text{Red}], \tag{1.34}$$

with [Red] the surface concentration of the reduced species[1]. Consider the simplest possible electrode process, wherein species Ox and Red engage in a rate-determining one electron transfer

[1]The physical truth is that the rate constant will be proportional to the *surface* concentration of the reactant; the associated phenomenology, however, uses the *bulk* concentration.

[1]The "c" and "a" subscripts on the rate constants denote respectively the cathodic (reduction) and anodic (oxidation) processes.

at the interface:

$$\mathrm{Ox} + e^- \rightleftharpoons \mathrm{Red}. \tag{1.35}$$

The net current density at the electrode is the difference between the current density due to the reduction of Ox and the oxidation of Red. Because the redox processes at the electrode involve the transfer of *one* electron per reaction event, the current densities, j, arising from the redox processes are the rates (as expressed through Equations 1.33 and 1.34) multiplied by Faraday's constant. As such, the cathodic current density is

$$j_c = Fk_c\,[\mathrm{Ox}], \tag{1.36}$$

and the opposing anodic current density is

$$j_a = Fk_a\,[\mathrm{Red}]. \tag{1.37}$$

The net current density is the difference

$$j = j_a - j_c = Fk_a\,[\mathrm{Red}] - Fk_c\,[\mathrm{Ox}]. \tag{1.38}$$

When $j_a > j_c$, the net current is anodic, and the oxidation process predominates; this will be the case at the anode. When $j_c > j_a$, the net current is cathodic, and the reduction process predominates; this will be the case at the cathode. We next recall the Arrhenius expression which relates the rate constant to the Helmholtz energy of activation,

$$k = B\,\mathrm{e}^{-\Delta A^\dagger/RT}, \tag{1.39}$$

and substitute Equation 1.39 into Equation 1.38 to give

$$j = FB_a\,[\mathrm{Red}]\,\mathrm{e}^{-\Delta A_a^\dagger/RT} - FB_c\,[\mathrm{Ox}]\,\mathrm{e}^{-\Delta A_c^\dagger/RT}. \tag{1.40}$$

Suppose that the Helmholtz free energy profiles along the reaction coordinate have the parabolic

shapes shown in Figure 1.12. The upper curve on the Ox side of the figure applies when the electrode potential takes its equilibrium value E^0. The cathodic and anodic activation energies are then $\Delta A_c^\dagger(0)$ and $\Delta A_a^\dagger(0)$ respectively. If the potential is changed by ΔE to a new value, E, the relative energy of the electron resident on the electrode changes by $-nF\Delta E = -F(E-E^0)$; hence the Ox curve moves up or down by that amount[1]. The lower curve on the left hand side of Figure 1.12 shows this effect for a positive ΔE. It is obvious that the barrier for oxidation $\Delta A_a^\dagger$ has become less than $\Delta A_a^\dagger(0)$ by a fraction of the total energy change. We denote this fraction by $1-\alpha$, where α, the transfer coefficient, can range from zero to unity. Thus we have

$$\Delta A_a^\dagger = \Delta A_a^\dagger(0) - (1-\alpha)F(E-E^0). \tag{1.41}$$

Similarly we notice that at the potential E the cathodic barrier $\Delta A_c^\dagger$ is higher than $\Delta A_c^\dagger(0)$ by $\alpha F(E-E^0)$. Consequently,

$$\Delta A_c^\dagger = \Delta A_c^\dagger(0) + \alpha F(E-E^0). \tag{1.42}$$

The two activation energies in Equations 1.41 and 1.42 can now be inserted into Equation 1.40 to obtain

$$j = FB_a\,[\mathrm{Red}]\,\mathrm{e}^{-\Delta A_a^\dagger(0)/RT}\,\mathrm{e}^{(1-\alpha)F(E-E^0)/RT} - FB_c\,[\mathrm{Ox}]\,\mathrm{e}^{-\Delta A_c^\dagger(0)/RT}\mathrm{e}^{-\alpha F(E-E^0)/RT}. \tag{1.43}$$

When the electrode is at the equilibrium potential E^0 there is no net current, and so the anodic and cathodic current densities must be equal:

$$j_a = j_c = j_0, \tag{1.44}$$

[1]In Figure 1.12 the Helmholtz reaction free energy ΔA is equal to $-nF(E-E^0)$ for an applied overpotential of $E-E^0$, which assumes that the change in ΔA with applied potential is due *solely* to the change in energy of the electron on the electrode, *i.e.* that the redox ions Ox and Red are perfectly screened from the electrode charges. We will test this assumption in Chapter 6 where we calculate the Marcus free energy surfaces of the Ox and Red species in our ionic melt for different values of the applied potential difference. In anticipation of that result, in Chapter 5 we investigate how the electrostatic potential varies across the cell.

where j_0 is called the exchange current density. We now for cosmetic purposes write $f = \frac{F}{RT}$, and the overpotential $\eta = E - E^0$ to obtain the Butler Volmer equation

$$j = j_0 \{ \mathrm{e}^{(1-\alpha)f\eta} - \mathrm{e}^{-\alpha f\eta} \}. \tag{1.45}$$

For large values of η (either negative or positive), one of the exponential terms in Equation 1.45 becomes neglible. At large negative overpotentials the first exponential may be neglected. This gives

$$j = -j_0 \, \mathrm{e}^{-\alpha f\eta}, \tag{1.46}$$

so

$$\ln(-j) = \ln j_0 - \alpha f\eta. \tag{1.47}$$

At large positive overpotentials it is the second exponential which may be neglected, giving

$$j = j_0 \, \mathrm{e}^{(1-\alpha)f\eta}, \tag{1.48}$$

so

$$\ln j = \ln j_0 + (1-\alpha)f\eta. \tag{1.49}$$

It helps to understand the transfer coefficient α as a measure of the symmetry of the energy barrier. Figure 1.13 shows the geometry of the region where the free energy curves intersect. From the figure we can define α:

$$\tan\theta = \alpha F \Delta E / x, \tag{1.50}$$

$$\tan\phi = (1-\alpha) F \Delta E / x, \tag{1.51}$$

$$\alpha = \frac{\tan\theta}{\tan\phi + \tan\theta}. \tag{1.52}$$

Only if the intersection is symmetrical is $\alpha = 1/2$. Because the free energy profiles are not likely to be linear over large ranges of the reaction coordinate, the geometry of the inter-

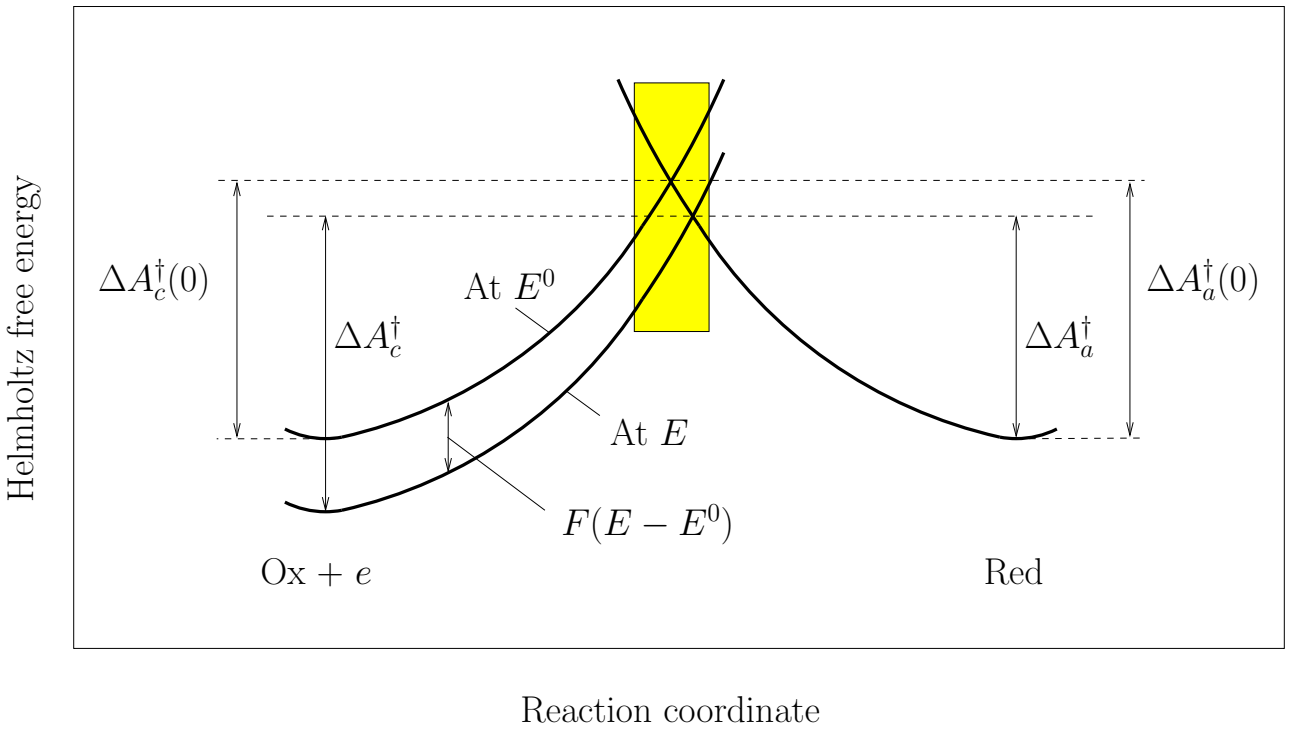

Figure 1.12: Effects of a potential change on the Helmholtz free energies of activation for oxidation and reduction. The boxed area is magnified in Figure 1.13.

section of the free energy profiles will change with potential. Consequently α ought to be a potential-dependent factor. The classical Butler Volmer formalism, however, considers α to be independent of the applied potential.

1.6 Marcus kinetics

1.6.1 Introduction

The Butler Volmer theory of heterogeneous electron transfer kinetics is based on macroscopic concepts, and the rate of reaction is written in terms of the phenomenological parameters j_0 and α (see Equation 1.45). The model is useful for analysing experimental results and providing insight into reaction mechanisms, but it cannot elucidate how the kinetics are affected by such factors as the nature and structure of the reacting species, the solvent, and the electrode material. For such information a microscopic theory is required. The Marcus theory is now ubiquitous in electrochemical fields, and can predict with accuracy and simplicity the effects of

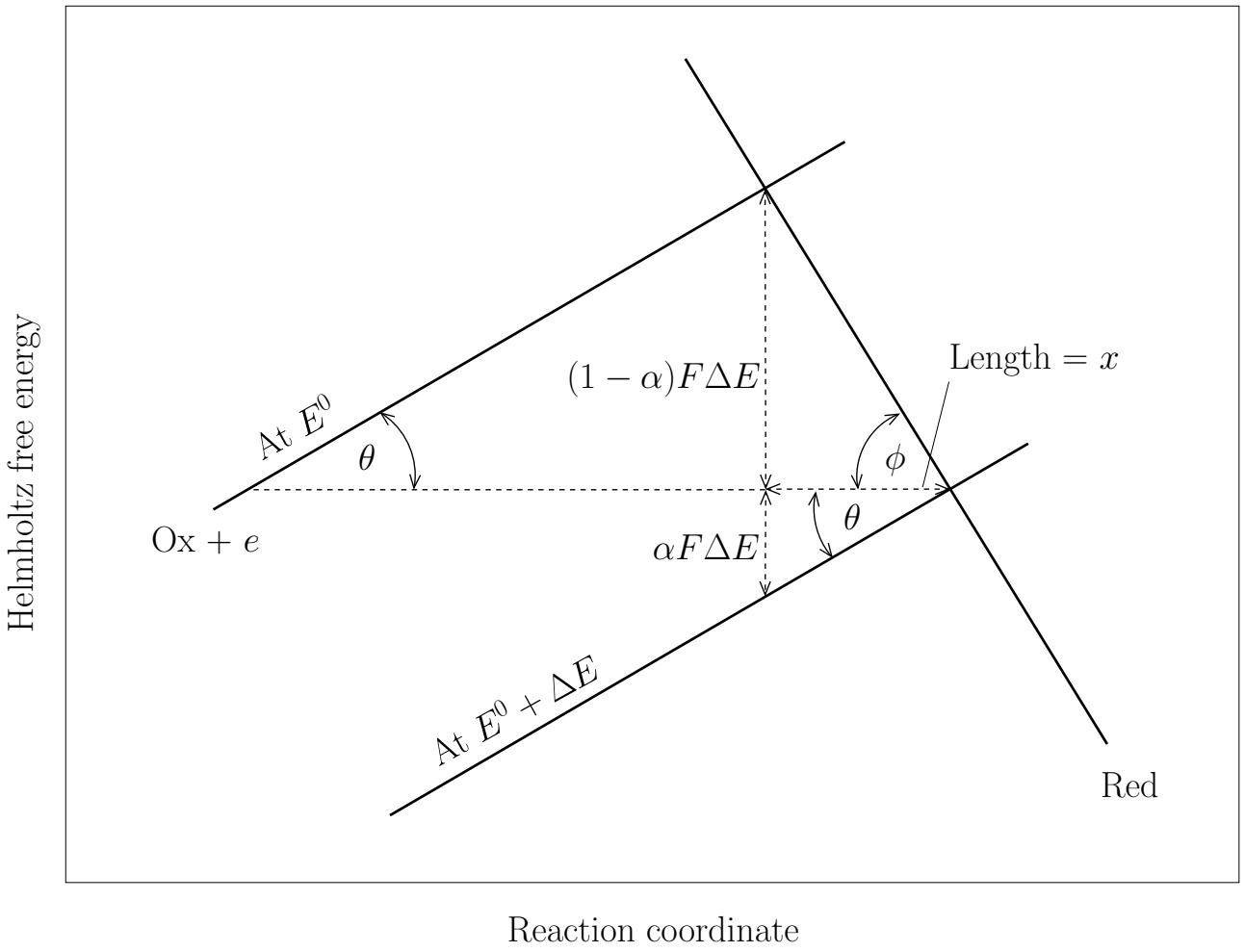

Figure 1.13: Relationship of the transfer coefficient to the angles of intersection of the free energy curves.

structure on kinetics.

Consider a single electron transfer from Eu^{2+} to an electrode, to form the product Eu^{3+}, where both ions have a primary solvation shell consisting of an octahedral arrangement of six chlorine ligands:

$$[EuCl_6]^{2+} \rightleftharpoons [EuCl_6]^{3+} + e^{-}. \tag{1.53}$$

We illustrate in Figure 1.14 the free energy curves of the reactants (Red = Eu^{2+}) and products (Ox = Eu^{3+}) as a function of the reaction coordinate. In a democratic society there is a choice of reaction coordinate; for pedagogic reasons we choose for this discussion simply the Eu–Cl bond length within the octahedral complex. We anticipate that the $Eu^{3+}-Cl$ bond is shorter than the $Eu^{2+}-Cl$ bond, which accounts for the relative positioning of the two free energy curves in Figure 1.14.

It is important to clarify why there is in fact an activation barrier to electron transfer from the Eu^{2+} species to the electrode. The explanation is twofold. First, the transfer is radiationless such that the electron must move from a reactant to a product of the same energy. In other words, before the electron transfer can take place, the Eu^{2+} ion must be thermally activated to an energy corresponding to the crossover of the free energy curves. Such thermal activation will arise when the bond lengths and angles of the reactant change, and the solvent shells are distorted. Second, the Frank Condon principle relates that the transfer of an electron occurs on a significantly shorter timescale ($\sim 10^{-15}$ s) than the timescale of the change in nuclear coordinates ($\sim 10^{-13}$ s). Consequently, the electron transfer corresponds to a 'vertical' transition between the energy curves in Figure 1.14, because the nuclei remain immobile on this timescale.

The demand for isoenergetic electron transfer in conjunction with the Frank Condon principle necessitates that the electron tunelling takes place at the transition state (at reaction coordinate $x^{\dagger}$ in Figure 1.14), where the reactants and products have the same configuration. Rapid thermal deactivation of the excited product $(Eu^{3+})^{\dagger}$ then occurs *via* collision with other ions, until its ground state is attained.

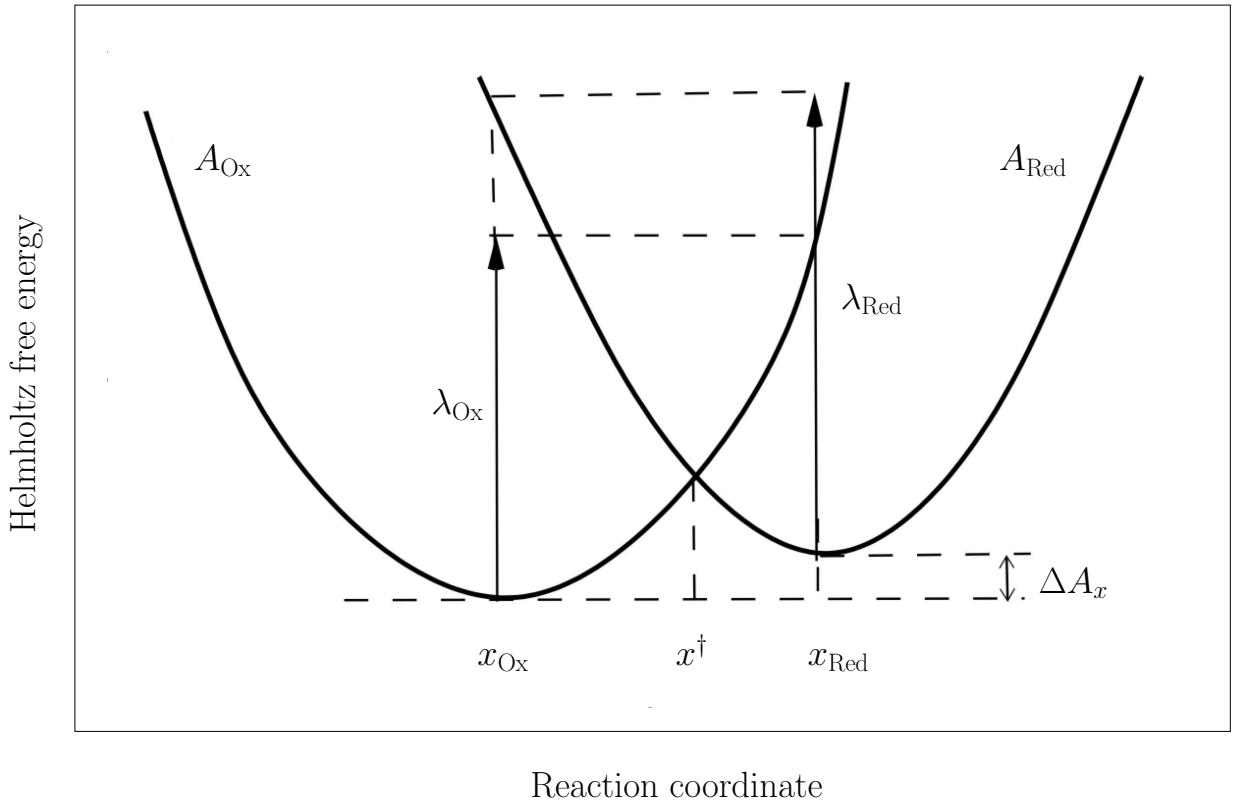

Figure 1.14: The intersecting diabatic free energy surfaces A_{Ox} and A_{Red}. The reorganization free energies λ_{Ox} and λ_{Red} are defined by Equations 4.20 and 4.21. The reaction free energy change ΔA is defined by Equation 4.22. Note the distinction between this representation of free energies and Figure 4.1 which shows the potential energy surfaces E_{M} and vertical energy gaps ΔE.

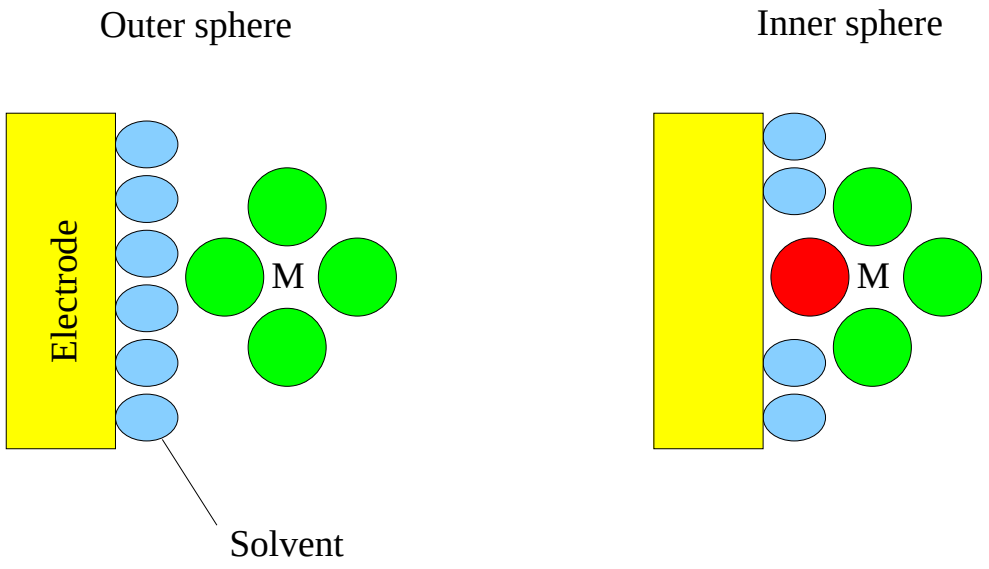

Figure 1.15: Inner sphere and outer sphere charge transfer at an electrode. Both panels show a metal atom (M) surrounded by ligands adjacent to a metallic electrode. In the outer sphere mechanism (left hand panel) there is little interaction of the reactant, intermediate, or product with the electrode. In contrast, the inner sphere mechanism (right hand panel) pertains when there is a strong interaction between the reactant, intermediate, or product with the electrode. One of the ligands (shaded in red) specifically adsorbs onto the electrode.

1.6.2 Inner and outer sphere reactions

The inner and outer sphere mechanisms for heterogeneous electron transfer derive from the work of Taube [39] on the homogeneous electron transfer of coordination compounds. The outer sphere mechanism (left hand panel in Figure 1.15) is characterized by a weak interaction between the electrode and the reactive species, with the inner coordination sphere remaining intact during the electron transfer. In contrast, the inner sphere mechanism (right hand panel in Figure 1.15) procedes through a bridging ligand which is specificially adsorbed onto the electrode. The kinetics are as such strongly dependent on the chemical nature of the electrode surface.

1.6.3 Adiabatic and non-adiabatic reactions

Figure 1.16 shows the free energy surfaces for a system moving from reactants, Ox, to products, Red. In the intersection region there is a splitting of the energy levels due to the interaction or electronic coupling between the reactant and the electrode. If the splitting is strong ($> k_{\mathrm{B}}T$),

there is a significant perturbation of the isolated Ox and Red curves and the reaction proceeds along a well-defined, continuous energy surface connecting Ox with Red. This is the *adiabatic* limit illustrated in the left hand panel. Alternatively, if the splitting is small ($< k_{\mathrm{B}}T$), the system will tend to cross from the ground state Ox surface to the excited state Ox surface and the process is said to be *diabatic*. This is illustrated in the right hand panel of Figure 1.16. The act of electron transfer is usually considered as the tunnelling of an electron between electronic states of the electrode and the redox ion. The strength of the tunnelling depends on the square of the electronic coupling matrix element $\gamma(z)$:

$$\gamma(z)^2 = (\gamma^0)^2 \exp(-\beta z), \tag{1.54}$$

where z is the distance from the reactive species to the electrode, β is a parameter which reflects the sensitivity of the electronic coupling matrix element to distance, and γ^0 is the value of the electronic coupling matrix element when $z = 0$. For an electron tunnelling between two pieces of metal through a vacuum [40]

$$\beta \approx 4\pi(2mW)^{1/2}/h \approx 1.02\,\text{Å}^{-1}\text{eV}^{-1/2} \times W^{1/2}, \tag{1.55}$$

where m is the mass of the electron, and W is the work function of the metal. For Pt (the metal used in most of the simulations reported in this thesis), $W = 5.7\,\text{eV}$ and $\beta = 2.4\,\text{Å}^{-1}$. In the diabatic limit $\gamma \to 0$.

It is not the remit of this thesis to attempt the calculation of $\gamma(z)$, but this is surely an important area of further study. We can say, however, that the success of Marcus theory rests in the fact that for most electron transfer reactions the splitting is enough to ensure that the reaction is adiabatic, but not enough to significantly perturb the reactant energy surfaces. Accordingly, the transition state is identified as the crossing point of the *isolated* energy surfaces Ox and Red. This is the *modus operandi* used to formulate an expression for the activation energy $\Delta A^{\dagger}$ in Section 1.6.4.

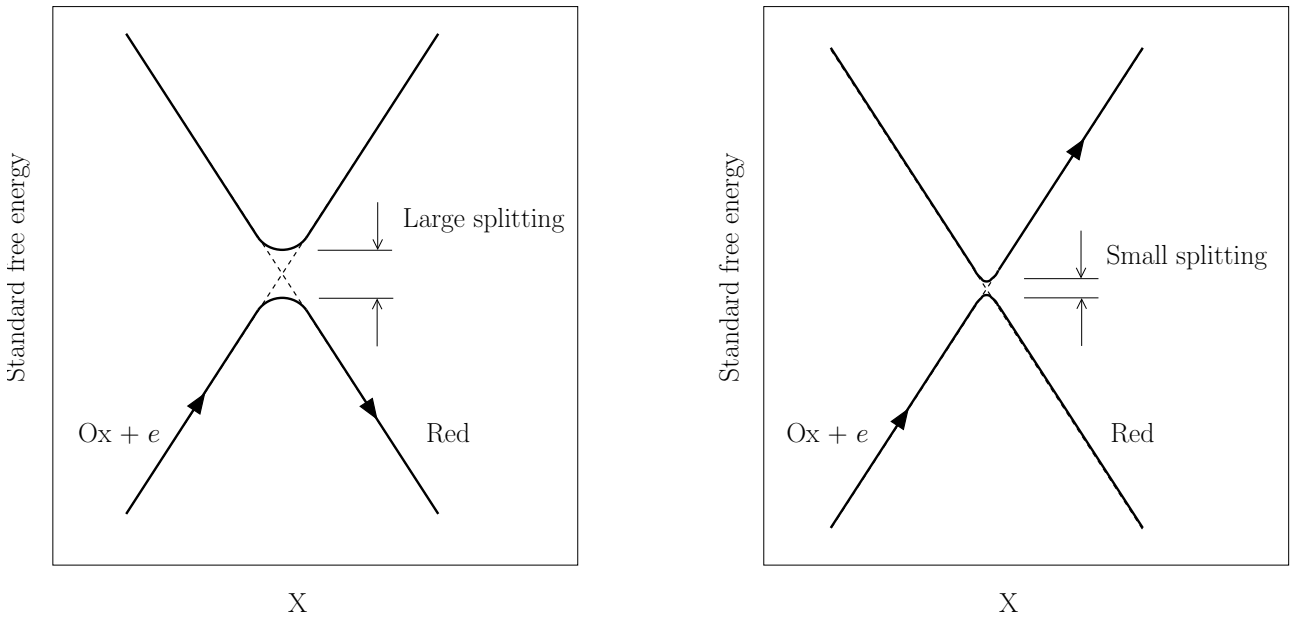

Figure 1.16: *Left:* The coupling between the reactant Ox and the electrode is strong, which leads to a large splitting ($> k_{\mathrm{B}}T$) in the energy curves in the intersection region. If the redox species Ox reaches the transition state, it is likely to proceed into the valley corresponding to the species Red. This is the adiabatic mechanism. *Right:* The coupling between the reactant Ox and the electrode is weak, which leads to a small splitting ($< k_{\mathrm{B}}T$) in the energy curves in the intersection region. If the redox species Ox reaches the transition state, it has a propensity for staying on the Ox + e curve. This is the diabatic mechanism.

In the Marcus formalism, the electrochemical rate constant is usually written as [4]

$$k(\Psi, z) = \frac{\rho_i(z, \Psi)}{\rho_i(\infty)} \gamma(z)^2 \upsilon_n \exp\left[\frac{-\Delta A^\dagger(\Psi, z)}{RT}\right], \tag{1.56}$$

where $\Delta A^\dagger$ is the activation energy, derived in the next section; $\frac{\rho_i(z,\Psi)}{\rho_i(\infty)}$ is the ratio of the concentration of redox species i in the reactive position at the electrode to the concentration in the bulk solution; υ_n is the nuclear frequency factor (s^{-1}) which represents the frequency of attempts on the energy barrier, and is associated with bond vibrations and solvent motion; and $\gamma(z)$ is the electronic coupling matrix element which represents the probability of electron tunnelling and was discussed in this section. This expression is appropriate to the fast diffusion limit, where the electron transfer event is the slow step of the overall electrochemical process. Note that the concentration of each redox species will depend (non-trivially) on the distance from the electrode, z, and the applied potential, Ψ. This point will be discussed further in Section 5.3.

1.6.4 Calculating the Helmholtz energy of activation

There is an assumption inherent in Marcus theory that the solvent responds linearly to the electric displacement field (which in this work is the electric field due to the wall charges). Marcus demonstrated that the free energy curves for the oxidized (Ox) and reduced (Red) species in this linear response régime are parabolas with the same curvature [41] :

$$A_{\mathrm{Ox}} = A_{\mathrm{Ox}}(x = x_{\mathrm{Ox}}) + \frac{1}{2}k(x - x_{\mathrm{Ox}})^2, \tag{1.57}$$

$$A_{\mathrm{Red}} = A_{\mathrm{Red}}(x = x_{\mathrm{Red}}) + \frac{1}{2}k(x - x_{\mathrm{Red}})^2, \tag{1.58}$$

where k is the "force constant" for a change in the solvent polarization. The transition state is the position where Ox and Red have the same configuration, denoted by the reaction coordinate

$x^\dagger$. The free energies at the transition state are given by

$$A^\dagger = A_{\mathrm{Ox}}(x = x_{\mathrm{Ox}}) + \frac{1}{2}k(x^\dagger - x_{\mathrm{Ox}})^2, \tag{1.59}$$

$$A^\dagger = A_{\mathrm{Red}}(x = x_{\mathrm{Red}}) + \frac{1}{2}k(x^\dagger - x_{\mathrm{Red}})^2. \tag{1.60}$$

Solving these expressions for $x^\dagger$ in terms of x_{Ox} and x_{Red} we obtain

$$x^\dagger = \frac{1}{2}(x_{\mathrm{Ox}} + x_{\mathrm{Red}}) - \frac{A_{\mathrm{Red}}(x = x_{\mathrm{Red}}) - A_{\mathrm{Ox}}(x = x_{\mathrm{Ox}})}{k(x_{\mathrm{Ox}} - x_{\mathrm{Red}})}. \tag{1.61}$$

We now substitute Equation 1.61 into both Equations 1.59 and 1.60 to obtain an expression for the Helmholtz energy of activation:

$$\begin{aligned}\Delta A^\dagger &= A^\dagger - A_{\mathrm{Ox}}(x = x_{\mathrm{Ox}}) \\ &= \frac{1}{8}k(x_{\mathrm{Ox}} - x_{\mathrm{Red}})^2 + \frac{1}{2}[A_{\mathrm{Red}}(x = x_{\mathrm{Red}}) - A_{\mathrm{Ox}}(x = x_{\mathrm{Ox}})] \\ &\quad + \frac{[A_{\mathrm{Red}}(x = x_{\mathrm{Red}}) - A_{\mathrm{Ox}}(x = x_{\mathrm{Ox}})]^2}{2k(x_{\mathrm{Ox}} - x_{\mathrm{Red}})^2}.\end{aligned} \tag{1.62}$$

Simplifying gives

$$\Delta A^\dagger = \frac{\lambda}{4}\left(1 + \frac{\Delta A}{\lambda}\right)^2, \tag{1.63}$$

where

$$\lambda = \frac{1}{2}k(x_{\mathrm{Ox}} - x_{\mathrm{Red}})^2, \tag{1.64}$$

and

$$\Delta A = A_{\mathrm{Red}}(x = x_{\mathrm{Red}}) - A_{\mathrm{Ox}}(x = x_{\mathrm{Ox}}). \tag{1.65}$$

For an electrode reaction Equation 1.63 is written as:

$$\Delta A^\dagger = \frac{\lambda}{4}\left(1 + \frac{F(E - E^0)}{\lambda}\right)^2. \tag{1.66}$$

We note that Equation 1.66 predicts that the activation Helmholtz energy will have a quadratic dependence on the applied potential E.

The reorganization energy λ is described in Marcus theory as having two components:

$$\lambda = \lambda_i + \lambda_o, \tag{1.67}$$

where λ_i is the contribution arising from the distortion of the inner coordination shell in the transition state geometry, and λ_o that from the rearrangement of the solvent dipoles between the reactants and the transition state. If the normal modes of the reactant are harmonic over the range of distortion required to reach the transition state, we could calculate λ_i through

$$\lambda_i = \sum_j \frac{1}{2} k_j \left(q_j^{\mathrm{Ox}} - q_j^{\mathrm{Red}}\right)^2, \tag{1.68}$$

where the sum is over the normal vibrational modes of the reactant, the k's are force constants, and the q's are displacements in the normal mode coordinates. To facilitate the calculation of λ_o, it is assumed that changes in solvation energy arise from the chance fluctuation of the solvent dipoles around the reactant species, and that the potential energy of the latter varies parabolically with displacement along the solvent coordinate. For a redox species at a distance d from the electrode surface, it can be shown that [42, 43]

$$\lambda_o = e^2 \left[\frac{1}{\epsilon_\infty} - \frac{1}{\epsilon_s}\right] \left[\frac{1}{2a} - \frac{1}{2d}\right]. \tag{1.69}$$

When d is large, Equation 1.69 gives the reorganization energy appropriate to an electron transfer in the bulk melt: it contains the contribution of the nonelectronic part of the dielectric response of the melt[1] to the change in the charge of a redox species of radius a. As such, it involves the difference between the static and infinite frequency longitudinal dielectric susceptibilities ($\epsilon_\infty^{-1} - \epsilon_s^{-1}$). Closer to the electrode surface, the d-dependent term begins to contribute, which reflects the polarization of the metal by the newly changed charge. We will describe the model for the electrode response in Section 2.3, and compare our simulation results with Equation 1.69 in Chapter 6.

[1] *i.e.*, that caused by reorganization of the nuclear positions.

1.7 Butler Volmer *vs.* Marcus kinetics

We can obtain the predicted value for the transfer coefficient α through Equation 1.66:

$$\alpha = \frac{1}{F}\frac{\partial A^{\dagger}}{\partial E} = \frac{1}{2}\left(1 + \frac{F(E - E^{0})}{\lambda}\right). \tag{1.70}$$

At potentials close to E^0 when $\lambda \gg \Delta A$, then $\alpha \approx 1/2$. If $\Delta A \gg 0$ and the reaction is thermodynamically uphill, since $\Delta A \approx \lambda$, under these conditions $\alpha \to 1$. Contrariwise, when $\Delta A \ll 0$, or a thermodynamically very favourable reaction, then $\Delta A \approx -\lambda$ and $\alpha \to 0$. The potential dependent term in Equation 1.70 is usually very small and the great majority of experiments find α to be a constant. This is because typically the free energy of activation has a magnitude of a few eV, whereas the change in activation energy observable in experiment is often $50 - 200\,\mathrm{meV}$. The kinetically operable potential range is narrow because the rate constant rises exponentially with potential, and the reaction becomes limited by mass transfer.

1.8 Orientation

Our primary aim in this work is to explore the factors governing the rate of charge transfer at a metallic electrode from a Marcus perspective. We introduced in this vein the Marcus expression for the heterogeneous electrochemical rate constant (Equation 1.56). The first term therein is the concentration factor $\rho_i(z, \Psi)/\rho_i(\infty)$, which expresses how the equilibrium (zero current) concentrations of the individual ionic species at the interface deviate from their bulk values. The concentration profiles will be presented in **Chapter 5**, with which we will calculate the mean electrical (Poisson) potential across the cell. Armed with the concentration profiles, Poisson potential profiles, and interfacial capacitance calculations, we will compare our microscopic representation of the interfacial structure with the mean-field Gouy-Chapman theory.

The other term in Equation 1.56 we will consider in this work is the Boltzmann factor $\exp[\Delta A^{\dagger}(\Psi, z)/RT]$. We present in **Chapter 6** the calculated Marcus free energy curves of the redox ions in our ionic melt, which we characterize by the reorganization energy and the

reaction Helmholtz free energy.

The realism of these simulated results will depend to a large extent on the quality of the interaction potentials. Already well established are the potentials governing the interaction between species in bulk liquid electrolytes. Less well researched heretofore are the potentials suitable at a metallic surface, and this is the focus of **Chapter 7**.

Before any results are reported there are three chapters setting out how the simulations are performed. **Chapter 2** considers fundamental aspects of molecular dynamics simulations including the integration of the classical equations of motion and the form of the model for the interaction potentials. The chapter also details a more specific technique employed in our calculations *viz.* a direct representation of the electrode as a polarizable metal held at a constant preset potential. This includes an explicit formulation of the algorithms governing the polarization of the anions by their mutual interaction and the interaction with the electrode charges, and the polarization of the electrode by the interaction of its constituent charges with the charges and dipoles of the melt ions.

It is desirable in this work to preset the *absolute* electrode potential, *i.e.* the potential with reference to a vacuum. This is achieved by periodically replicating the simulation cell in only two dimensions, such that the full system consists of two infinite parallel plate electrodes sandwiching a set of melt ions. This ensures that each electrode is isolated and does not interact spuriously with the periodic image of the other. **Chapter 3** details the method employed for efficiently computing the long-range electrostatic interactions in this two-dimensional periodicity. Explicit equations are given for the total energy, interatomic forces, and the electric field and potential at each ion's position.

The theory in **Chapter 4** illustrates the use of the vertical diabatic energy gap as a reaction coordinate for the study of redox reactions. A set of convenient expressions are derived for the computation of the diabatic Helmholtz free energy surfaces for the electroactive species. Perhaps the most salient characteristic of the vertical energy gap is its potential for the computation of the activation free energy, as required in the expression for the electrochemical rate constant.

2 Simulation techniques

2.1 Interaction potentials

Our system models an electrochemical cell as a pair of parallel plate electrodes maintained at a preset electrical potential difference and separated by the molten salt $K_3Eu^{3+}_{0.5}Eu^{2+}_{0.5}Cl_{5.5}$. The interionic interactions are represented by Born-Mayer pair potentials, together with a representation of dipole polarization *via* the interionic interactions. The melt ions are assigned their formal valence charges through point charge distributions and the electrode atoms carry variable Gaussian charge distributions which are determined at each MD step so as to maintain a constant electrical potential at the sites of all the constituent atoms of an electrode. Throughout the discussion we will be careful to distinguish between the melt–melt, melt–electrode, and electrode–electrode interactions. The Born-Mayer interaction model contains contributions from charge–charge, dispersion and overlap repulsion interactions; these are formulated in Section 2.1.2 and are collectively denoted the *rigid ion model* (RIM). Additionally, our simulation model allows for chloride ions which are spherically polarizable, with the induction of dipoles through their mutual interaction and the interaction with the electrode charges. Section 2.1.3 details the polarization terms which are added to the total interaction model which is then termed the *dipole polarizable ion model* (DIPPIM). But we summarize beforehand the results of two previous simulations of polarizable MCl_3 melts to indicate the verisimilitude of

the interaction potential model used.

2.1.1 Description of MCl_3 melts with the DIPPIM

A number of technologies involve solutions of trivalent metal halides in molten alkali halides, including the proposed electrolytic separation of nuclear waste (see Section 2.1.1.2) and the electrodeposition of refractory metals. Such processes often preclude detailed empirical characterization by virtue of their extreme temperatures or the presence of radioactive elements, and therefore greater is the need for computer simulations in predicting the properties of these systems. Furthermore, the trivalent cations of the lanthanide, transition metal, and main group elements are of fundamental interest in that they exhibit widely differing degrees of ionic character. $AlCl_3$ melts at low temperature with an enormous (80%) volume increase to produce a liquid which is thought to be composed of Al_2Cl_6 dimers, whereas $LaCl_3$ has a high melting temperature and a volume change ($\sim 16\%$) typical of ionic compounds.

The form of the MCl_3 interaction potentials suggested by *ab initio* electronic structure calculations on the condensed phase have been refined to better reproduce neutron and X-ray diffraction experiments on lanthanide, main group, and transition metal trivalent halides (see [44] and Section 2.1.1.1). Subsequent predictions of Raman spectroscopic and transport properties using the refined potentials have also married well with experiment [45]. The differences between the parameter sets used for different materials are all related to the cation crystallographic radius, and therefore potentials for other materials (*e.g.* actinides) are predictable. And because the materials of interest are essentially ionic with closed shells and formal charges, the potentials are transferable to ionic mixtures.

The empirical verification of the interaction potentials is exampled below by two diverse previous studies, the first spectroscopic and the second thermodynamic.

2.1.1.1 Neutron scattering [44]

In the top panel of Figure 2.1 the experimental and simulated total neutron weighted structure factors for the $ScCl_3$ melt are compared along with the simulated neutron weighted partial

structure factors. The calculation replicates well the experimental structure factor, including two unusual features: the prominent pre-peak at $\sim 0.7\,\text{Å}^{-1}$, and the replacement of the principal peak by a broad maximum extending over about $2\,\text{Å}^{-1}$.

An instantaneous configuration of the simulated $ScCl_3$ melt is shown in the lower panel of Figure 2.1. The structure is a remarkable cross-linked network of edge-sharing coordination polyhedra, supporting in between a number of voids. The range of separation of these voids suggests that the inter-void correlations are responsible for the low-k pre-peak.

The partial structure factors clarify why there is no principal peak. The principal peaks of the Sc-Sc and Cl-Cl partials both occur at $\sim 2\,\text{Å}^{-1}$, where they are cancelled by the negative peak in the Sc-Cl partial. The remaining broad feature is primarily due to the Sc-Cl partial in this k-range. That the Sc-Sc and Cl-Cl partials exhibit principal peaks at a similar wave vector implies that the nearest-neighbour cation–cation and anion–anion separations are much the same. This unexpected drawing together of the triply-charged cations in adjacent, edge-sharing polyhedra is stabalized by the polarization effects on the anions, as has been noticed elsewhere [46, 47, 48].

2.1.1.2 Calculation of the activities of ions in molten salts

Throughout the world today there is much interest in the design of future nuclear reactors. An important goal of this research is to minimize the environmental impact of nuclear waste reprocessing. Pyroprocessing is one way of dealing with this waste, and can present fewer proliferation and environmental risks than traditional solvent–solvent extraction methods. The technique involves the electrochemical reduction of the spent fuel rods in a molten salt electrolyte to selectively deposit the radioactive waste elements as metals or alloys at appropriately chosen cathodes. The separability of the fission products is determined *inter alia* by the differences between the interactions of the fission product cations with the other ions in the molten salt "solvent".

A theoretical method for predicting the effect of the solvent on the separability is desirable, not least due to the hazards of laboratory experiments involving radionucleides. Changing the

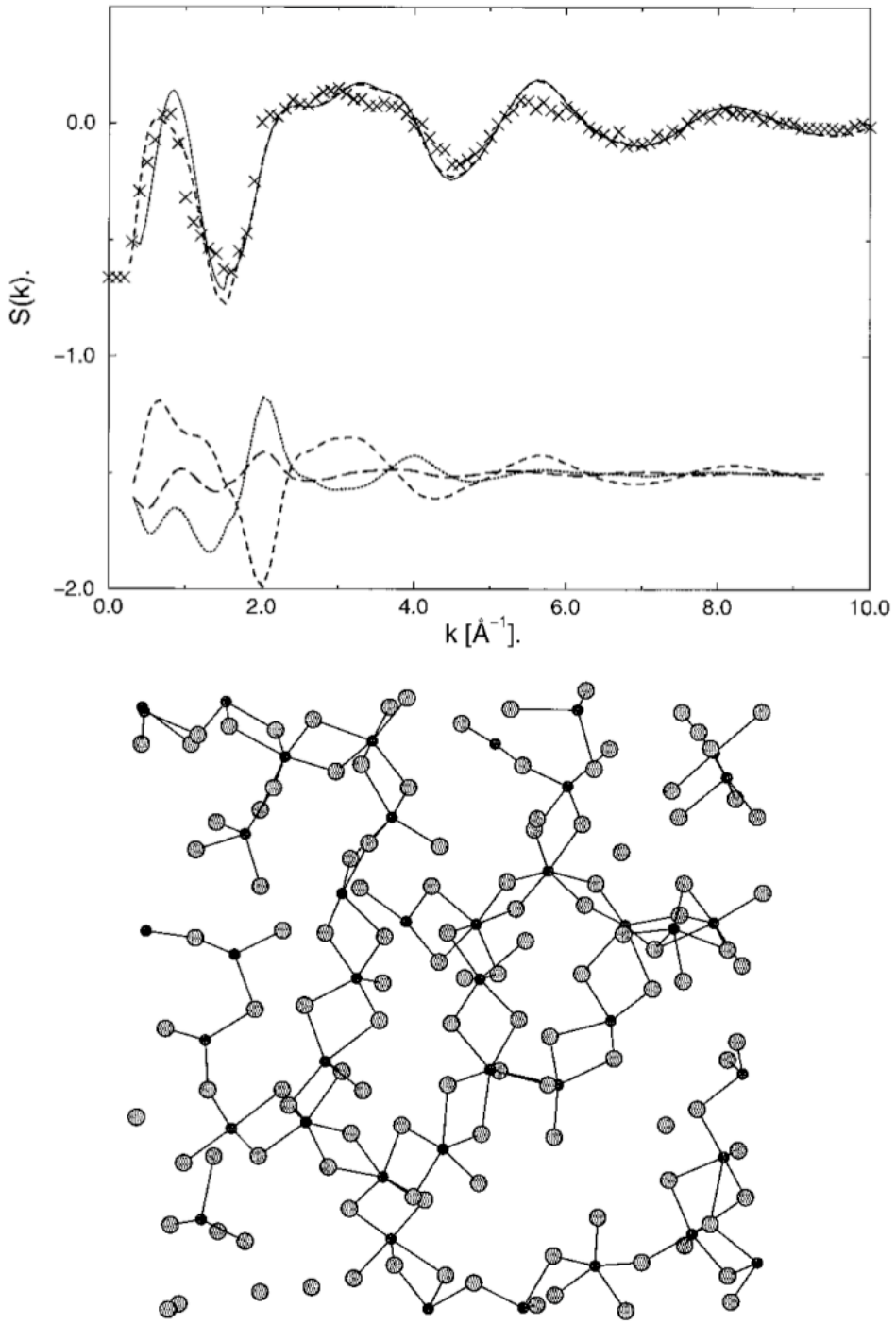

Figure 2.1: *Top:* Simulated total neutron weighted structure factor (solid line) for $ScCl_3$ compared with experimental total structure factor (×), with the neutron weighted partials shown below shifted by a constant of −1.5 (dotted line, S_{Cl-Cl}; dashed line, S_{Sc-Cl}; and long dashed line, S_{Sc-Sc}). The upper dashed line is the total structure factor from a simulation with a greater number of ions. *Bottom:* A molecular graphics snapshot of the liquid $ScCl_3$ showing the edge-linked chain structural motif. The large circles represent the Cl^- anions and the smaller circles the Sc^{3+} cations. Both figures are taken from reference [44].

redox couple	E^0/V	$(RT/3F)\cdot$ $\ln(\gamma_{M^{3+}}/\gamma_{La^{3+}})$/V	E'^0_{calc}/V	E'^0_{exp}/V
U	0.65	0.00 ± 0.03	0.65 ± 0.03	$0.63, 0.60, 0.65$
Sc	0.51	-0.14 ± 0.06	0.37 ± 0.06	0.30
Tb	0.23	-0.08 ± 0.03	0.15 ± 0.03	0.14
Y	0.20	-0.10 ± 0.03	0.10 ± 0.03	$0.02, 0.02$
La	0.00	0.00	0.00	0.00

Table 2.1: Formal standard potentials of various M(III)/M(0) redox couples. Taken from reference [49].

identity of the electrolyte ions will affect the activities of different ions to different degrees, and the separability of fission product cations can be related to the ratios of their activity coefficients. Salanne *et al.* [49] have obtained these activity coefficient ratios using thermodynamic integration methods to calculate differences between free energies of solvation of different cations. To provide contact with experiment, their results are expressed as formal standard potentials:

$$E'^0_{M^{3+}/M} = E^0_{M^{3+}/M} + \frac{RT}{3F}\ln[\gamma_{M^{3+}}]. \tag{2.1}$$

Table 2.1 compares with experiment the values of $E'^0_{M^{3+}/M}$ for various redox couples, taking the La(III)/La(0) couple as a fiducial reference. The agreement between the calculated and empirical activity coefficient ratios is in general good, despite the small overestimation of the formal potential of the Y(III)/Y(0) redox couple. This suggests that the potential model incorporates the essential features of the interactions between the metal ions and the electrolyte.

2.1.2 The rigid ion model

The rigid ion model can be formulated as the sum of three components: charge–charge, dispersion, and overlap repulsion, *viz.*,

$$U^{RIM} = U^{q-q} + U^{disp} + U^{rep}. \tag{2.2}$$

These components are all pairwise additives and offer a computationally inexpensive description of interactions between ions which are regarded as spherical and incompressible. This rigid ion model may be expected to be appropriate for ions whose electron density is less sensitive to changes in the local environment. For a system composed of n_p point charges and n_g Gaussian distributions, the charge–charge interaction energy is

$$U^{q-q} = \frac{1}{2}\sum_{i}^{n_p}\sum_{j}^{n_p}{}' q_i T_{ij} q_j + \sum_{i}^{n_p}\sum_{j}^{n_g} q_i T_{ij} q_j + \frac{1}{2}\sum_{i}^{n_g}\sum_{j}^{n_g} q_i T_{ij} q_j, \tag{2.3}$$

where q_i is the fixed formal charge on a melt ion or the variable charge of an electrode atom, as appropriate. T_{ij} is the charge–charge interaction tensor defined in Appendix B. The first double summation in Equation 2.3 represents the electrostatic interactions within the point charge subsystem; the prime indicates that the $i = j$ terms are omitted. Note that there is no prime on the double summation representing the electrostatic interactions within the Gaussian subsystem because a Gaussian will interact with itself; this "self interaction" is explicitly formulated in Chapter 3 (Equation 3.4j) and Appendix A (Equation A.30).

The dispersion component is split into dipole–dipole and dipole–quadrupole terms:

$$U^{\text{disp}} = -\frac{1}{2}\sum_{i}^{n_p}\sum_{j}^{n_p}{}' \left[\frac{f_{ij}^6(r_{ij})C_{ij}^6}{(r_{ij})^6} + \frac{f_{ij}^8(r_{ij})C_{ij}^8}{(r_{ij})^8}\right] - \sum_{i}^{n_p}\sum_{j}^{n_g}\left[\frac{f_{ij}^6(r_{ij})C_{ij}^6}{(r_{ij})^6} + \frac{f_{ij}^8(r_{ij})C_{ij}^8}{(r_{ij})^8}\right], \tag{2.4}$$

where C_{ij}^6 and C_{ij}^8 are respectively the dipole-dipole and dipole-quadrupole dispersion coefficients. The electrode atoms are of *fixed* position: consequently there are no short-range electrode–electrode interactions included in the potential model. The dispersion interactions decay as $\frac{1}{r^6}$ and $\frac{1}{r^8}$ and consequently would reach unphysical values at small r were they not damped. We in this regard employ the Tang-Toennies dispersion damping functions f_{ij}^n [50] which take the form

$$f_{ij}^n(r_{ij}) = 1 - e^{-b_{ij}r_{ij}}\sum_{k=0}^{n}\frac{(b_{ij}r_{ij})^k}{k!}, \tag{2.5}$$

and are plotted in Figure 2.2. This function tends to 1 at large r and to 0 when r is less than b^{-1} and thus effects a short-range correction only.

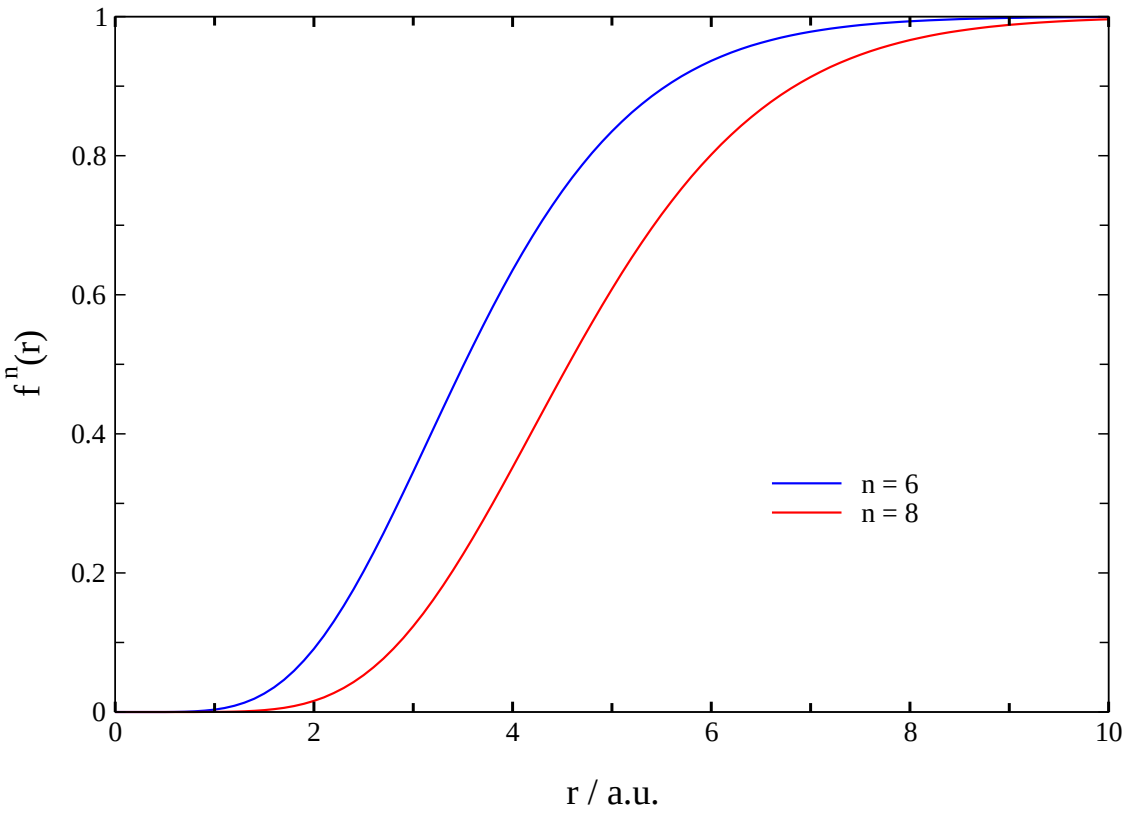

Figure 2.2: The Tang-Toennies damping function. The figure shows functions defined by Equation 2.5 with $b = 1.9$ a.u. and $n = 6, 8$.

The short-range repulsive interaction arising from the overlap of electron densities on neighbouring ions is written as a sum of Born-Mayer exponentials:

$$U^{\mathrm{rep}} = \frac{1}{2}\sum_{i}^{n_p}\sum_{j}^{n_p}{}' B_{ij}e^{-a_{ij}r_{ij}} + \sum_{i}^{n_p}\sum_{j}^{n_g} B_{ij}e^{-a_{ij}r_{ij}}, \tag{2.6}$$

where the parameter a_{ij} indicates the steepness of the repulsive wall between the ions i and j.

2.1.3 The dipole polarizable ion model

There are dipolar contributions to the total potential energy resulting from charge–dipole and dipole–dipole electrostatic interactions; these are respectively denoted $U^{q-\mu}$ and $U^{\mu-\mu}$. There is also a "polarization energy", U^{pol}, associated with deforming the electron density on an ion to form a dipole. The total energy within the DIPPIM is written as:

$$U^{\mathrm{DIPPIM}} = U^{\mathrm{RIM}} + U^{q-\mu} + U^{\mu-\mu} + U^{\mathrm{pol}}. \tag{2.7}$$

The charge–dipole interaction energy is given by

$$\begin{aligned} U^{q-\mu} = &-\frac{1}{2}\sum_{i}^{n_p}\sum_{j}^{n_p}{}' \left\{\left[\mu_{j\alpha}q_i g_{ij}(r_{ij}) - q_j\mu_{i\alpha}g_{ij}(r_{ij})\right] T_{ij}^{\alpha}\right\} \\ &+ \sum_{i}^{n_p}\sum_{j}^{n_g}\left\{\mu_{i\alpha}q_j + \left[g_{ij}(r_{ij}) - 1\right]\mu_{i\alpha}r_{ij}^3\right\} T_{ij}^{\alpha}, \end{aligned} \tag{2.8}$$

where α_i is the dipole polarizability of ion i[1], T_{ij}^{α} is the charge–dipole interaction tensor (given in Appendix B), and α is an index representing the Cartesian coordinate x, y, or z. The short-range corrections to the charge-dipole asymptotic terms are represented by functions based upon the Tang-Toennies dispersion damping of Equation 2.5. For the melt charge–melt dipole interactions we employ

$$g_{ij}(r_{ij}) = 1 - c_{ij}e^{-b_{ij}r_{ij}}\sum_{p=0}^{p_{\max}}\frac{(b_{ij}r_{ij})^p}{p!}, \tag{2.9}$$

[1]We assume that the polarizability of each species is independent of its environment. This seems justified in that small changes in the polarizability of an ion may be expected to produce smaller changes in the total ionic interaction energy of the system than those due to changes in the dipole moments themselves.

where b_{ij} determines the distance at which the overlap of the charge densities begins to affect the induced dipoles, and c_{ij} measures the strength of the ion response to this effect. The correction required for the damping of an anion by a neighbouring cation is a short-range component of the dipole which opposes the asymptotic dipole [51]; this effect is represented when $c_{ij} > 0$. The short-range dipole reinforces the asymptotic one when $c_{ij} < 0$ as appropriate for either the damping of a cation dipole by near neighbour anions or the damping of an anion by another anion [51]. This latter effect will be small unless the electron densities of like ions overlap significantly.

The short-range correction to the melt dipole–electrode charge interactions is different from that to the melt charge–melt dipole interactions in two ways. First, the short-range correction to the asymptotic melt dipole–electrode charge interaction is added on as a separate term with the electrode charge removed: this is to ensure that the variable electrode charges are determined solely by the long-range Coulombic interactions[1]. Second, the short-range correction to the asymptotic melt dipole–electrode charge interaction contains no r_{ij}^{-3} dependence. This is to prevent an ion from acquiring a rapidly-increasing dipole as it approaches the electrode surface: the attraction between such a dipole and the electrode charges was found to drag the associated ion into the electrode, causing instabilities in simulations.

The dipole–dipole interaction energy is given by

$$U^{\mu-\mu} = -\frac{1}{2}\sum_{i}^{n_p}\sum_{j}^{n_p}{}' \mu_{j\alpha}\mu_{i\beta}T_{ij}^{\alpha\beta}, \tag{2.10}$$

with the interaction tensor $T_{ij}^{\alpha\beta}$ given in Appendix B. The only remaining contribution to the energy within the DIPPIM is that associated with the distortion of the electron density on an ion to create a dipole (see Section 3.4.4):

$$U^{\mathrm{pol}} = \sum_{i}\frac{|\boldsymbol{\mu}_i|^2}{2\alpha_i}, \tag{2.11}$$

[1]The electrode charges are obtained at each MD step through a conjugate gradient procedure which maintains the electrode at a constant preset potential. See Sections 2.3 and 2.4 for a description of this method.

where α_i is the polarizability of ion i.

Consider a system containing one melt anion i ($q_i = -1$) and one melt cation j ($q_j = +1$) separated by the vector $\mathbf{r}_{ij}$. Only the anion is allowed to polarize so that $\boldsymbol{\mu}_j = \mathbf{0}$. We can use Equation 2.8 to calculate the electric field $\mathbf{E}_i$ at the site of anion i:

$$\begin{aligned} E_{i\alpha} &= -\frac{\partial U}{\partial \mu_{i\alpha}} \\ &= -g_{ij} T_{ij}^{\alpha}. \end{aligned} \tag{2.12}$$

The dipole $\boldsymbol{\mu}_i$ associated with ion i results from this nonzero electric field $\mathbf{E}_i$:

$$\begin{aligned} \mu_{i\alpha} &= \alpha_i E_{i\alpha} \\ &= -\alpha_i g_{ij} T_{ij}^{\alpha}. \end{aligned} \tag{2.13}$$

The calculation of the dipoles in a more complex system is a many-body problem because each electric field $\mathbf{E}_i$ will depend upon the dipoles of the surrounding ions. We outline in Section 2.4 the use of conjugated gradients as an efficient method for solving this N-dimensional system of linear equations.

The short range interactions U^{disp} and U^{rep} are truncated in real space using a simple cut-off procedure and are calculated with the application of the minimum image convention [52]. The charge–charge, charge–dipole, and dipole–dipole electrostatic interactions act over a much larger range of ionic separations and must be carefully handled. The most popular technique for treating these long-range interactions is the Ewald summation detailed in Chapter 3.

2.2 Verlet algorithm

In order to simulate the dynamics of a system of N classically interacting particles, we must solve numerically Newton's equations for the motion of the particles,

$$m_i \ddot{\mathbf{r}}_i = \mathbf{F}_i, \quad i = 1, \ldots, 3N, \tag{2.14}$$

where $\mathbf{r}_i$ is the ith coordinate of the system, m_i is its associated mass, and $\mathbf{F}_i = -\frac{\partial U}{\partial \mathbf{r}_i}$ is the force acting on $\mathbf{r}_i$. The method most commonly used to integrate these equations is the finite difference Verlet algorithm [52, 53] in which the time t is discretized in intervals of Δt. The variant we implement is the velocity Verlet algorithm [52] which casts the coordinates as the truncated Taylor expansion

$$\mathbf{r}_i(t + \Delta t) = \mathbf{r}_i(t) + \mathbf{v}_i(t)\Delta t + \frac{\mathbf{F}_i(t)}{2m_i}\Delta t^2, \tag{2.15}$$

and subsequently updates the velocities using

$$\mathbf{v}_i(t + \Delta t) = \mathbf{v}_i(t) + \frac{\mathbf{F}_i(t + \Delta t) + \mathbf{F}_i(t)}{2m_i}\Delta t. \tag{2.16}$$

These equations are the discretized form of Newton's equations $\dot{\mathbf{r}}_i = \mathbf{p}_i/m_i$ and $\dot{\mathbf{p}}_i = \mathbf{F}_i$ with $\mathbf{p}_i = m_i\mathbf{v}_i$. The estimate of the new position in Equation 2.15 contains an error that is of order Δt^4, and the expression for the velocity in Equation 2.16 is only accurate to order Δt^2. The algorithm requires a single evaluation of the forces per integration step, which is advantageous since this is computationally the most expensive part of the calculation. The total Hamiltonian whose value is conserved during the simulation is

$$H = \sum_{i=1}^{3N} \frac{|\mathbf{p}_i|^2}{2m_i} + U(\{q_i\}). \tag{2.17}$$

Here, the first term represents the kinetic energy of the particles and the second term represents the potential energy of the system. If the dynamics of the system are ergodic, the sampling of phase-space is equivalent to that of the micro-canonical (NVE) ensemble, where the number of particles N, the volume V, and the energy E of the system, are conserved quantities. In the long-time limit, time-averages correspond to averages of the micro-canonical ensemble.

Unless otherwise specified, the simulations described in this thesis are performed in the micro-canonical ensemble. It is sometimes desirable, however, to carry out simulations in which the temperature and/or pressure oscillate about pre-set values. The constant temperature

condition can be obtained by the thermostatting method proposed by Nosé [54] and Hoover [55] and extended by Martyna *et al* [56]. The instantaneous temperature is calculated from the total kinetic energy of the ions using the equipartition principle:

$$T = \frac{1}{3Nk_{\mathrm{B}}} \sum_{i}^{N} \frac{|\mathbf{p}_i|^2}{m_i}. \tag{2.18}$$

Energy is then exchanged between the system and a heat reservoir to ensure that the temperature of the system oscillates around the set value. The constant pressure condition can be obtained by a barostat [57] which allows the lengths of the cell to vary isotropically according to the instantaneous value of the pressure tensor, $\mathbf{P}$, which is defined through

$$P_{\alpha\beta} = \frac{1}{V} \sum_{i=1}^{N} \left[\frac{p_{i\alpha} p_{i\beta}}{m_i} + F_{i\alpha} r_{i\beta} \right], \tag{2.19}$$

where $\mathbf{r}_i$ and $\mathbf{p}_i$ are the position and momentum of particle i, m_i is the mass, $\mathbf{F}_i$ is the force, and V is the cell volume. The alpha index represents the Cartesian coordinate x, y, or z. The isothermal-isobaric (NPT) ensemble is used for an initial equilibration of the $K_3Eu^{3+}_{0.5}Eu^{2+}_{0.5}Cl_{5.5}$ melt at a density appropriate to the desired temperature. The system is then sandwiched between two electrodes and the simulations to obtain the redox data are performed in the micro-canonical ensemble.

2.3 Modelling the metallic electrodes

Electrochemistry is a field of very diverse application. Electrolysis, electrocatalysis, electrosynthesis and corrosion inhibition amongst others all involve redox reactions at a metal surface and understanding the microscopic behaviour of the interfacial region is crucial in understanding the electrode kinetics. A realistic computer simulation model should therefore characterize such factors as the competition for absorption sites on the electrode, the rate of diffusion in the interfacial region, and the profile of the mean electrical potential across the interface. The most realistic determination of the structure and dynamics of the electrochemical interface is

through *ab initio* studies [58, 59] which model explicitly the adiabatic electronic structures of the electrode and the electrolyte. The computational expense of this methodolgy however limits its use to simulations of size and length insufficient to offer contact with classical electrochemical phenomena. Classical studies of an electrolyte [60, 61] in the presence of an interface of fixed charge density have allowed for simulations of longer length and timescales, but the main shortcoming here is that the electrodes in real electrochemical cells operate at constant *potential*. Furthermore, the charges in the electrolyte will polarize the electron density in the metal. This effect can be incorporated in a classical model by image charges as illustrated in Figure 2.3. The surface of the metal is regarded as a mirror plane such that an ion at a distance r from the wall induces an image charge[1] of equal and opposite magnitude at a distance r inside the metal. Each ion thus experiences an attractive potential interaction with its own image charge, and each ion interacts explicitly with every image. This works well for a perfectly smooth geometric surface with external point charges. However an atomistic representation of the substrate along with short range non-electrostatic interactions with the external charges introduces a certain arbitrariness in the positioning of the mirror plane [62].

We outline in this section a methodology proposed by Siepmann and Sprik [62] for directly representing the electrode as a polarizable metal held at constant potential within a classical simulation. Recent *ab initio* simulations [58] graphically illustrate the strong screening of the interfacial potential drop by the outermost electrons of the metal's surface. Without further refinement herein lies perhaps the most unrealistic facet of this method.

Each electrode in our simulations consists of three layers of atoms arranged with crystalline order; at any position vector $\mathbf{r}$ in the metal the potential is equal to the externally applied value Ψ^0:

$$\Psi(\mathbf{r}) = \int \mathrm{d}\mathbf{r'} \frac{\rho(\mathbf{r'})}{|\mathbf{r'} - \mathbf{r}|} = \Psi^0 = \text{const}, \tag{2.20}$$

where $\rho(\mathbf{r})$ is the total charge density of the system $\rho(\mathbf{r}) = \rho_{\text{wall}}(\mathbf{r}) + \rho_{\text{melt}}(\mathbf{r})$. The charges induced in the metal by the ions of the melt are represented by Gaussians centred on the

[1] Of course the image charges have no physical reality and one should not imagine well defined ions moving within the metallic electrode. This is however a mathematically rigorous method to describe the effect of the complex electron density rearrangements that occur as ions approach the metal surface.

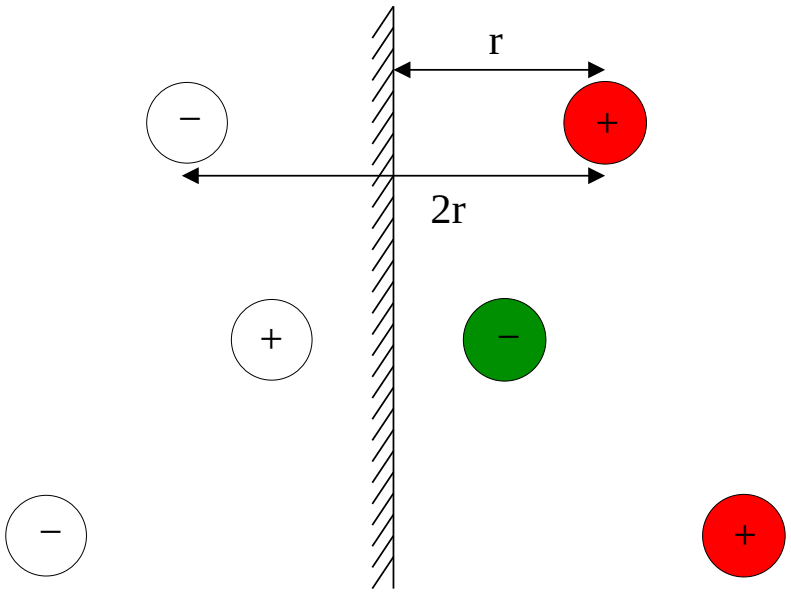

Figure 2.3: In the image charge method there is for each ion in the simulation a corresponding image charge of equal and opposite magnitude within the electrode. The ion and its image charge are equidistant from the interface. Each ion interacts with every image charge and each image charge interacts with every other image charge.

atoms:

$$\rho_j(\mathbf{r}) = \frac{q_j \kappa^3}{\pi^{3/2}} \exp\left(-\kappa^2(\mathbf{r} - \mathbf{r}_j)^2\right). \tag{2.21}$$

The Gaussians are of fixed width κ and have an integrated charge of q_j. Each ion in the melt has a point charge so that its charge distribution is

$$\rho_i(\mathbf{r}) = q_i \delta\left(\mathbf{r} - \mathbf{r}_i\right), \tag{2.22}$$

where $\delta\left(\mathbf{r} - \mathbf{r}_i\right)$ is the Kronecker delta function. If we substitute the expression for the total charge density in Equations 2.21 and 2.22 into equation 2.20 we obtain the potential at the discrete metal sites $\mathbf{r}_i$ as

$$\Psi_i + \frac{q_i(t)\sqrt{2}\kappa}{\sqrt{\pi}} = \Psi^0. \tag{2.23}$$

The first term Ψ_i is the potential at position i due to all the other melt and wall ions and the second term is a result of the interaction of a Gaussian charge distribution with itself. The value of the charge on each electrode atom at each time step in a molecular dynamics procedure is obtained by requiring the constant potential condition of Equation 2.20 which is achieved by

minimizing the potential energy,

$$U = \sum_i q_i \left[\frac{\Psi_i(\{q_i\})}{2} + \frac{q_i(t)\kappa}{\sqrt{2\pi}} - \Psi^0 \right], \tag{2.24}$$

where the sum runs over the variable electrode charges. The method of conjugated gradients explicated in Section 2.4 is the variational method employed.

The variable electrode charges will take the adiabatic values appropriate for a metal responding to the instantaneous ionic positions in the sense that they take account of the polarization of the electrode by the melt. This correspondence with the classical image charge response is elucidated in Figure 2.4 in which the atoms of the anode are colour coded according to the magnitude of the charge induced on them by a nearby anion. If the charge on the ion is changed, the charge difference is fully transferred to the electrodes to maintain charge neutrality with a constant electrode potential [63]. It is this feature which will enable us to calculate Marcus curves for electrochemical charge transfer in Chapter 6.

2.4 Conjugate gradient method

Conjugate Gradients (CG) is the most popular iterative method for finding the minimum of an n dimensional system of quadratic equations,

$$f(\mathbf{x}) = \frac{1}{2}\mathbf{x}^{\mathrm{T}}\mathbf{A}\mathbf{x} - \mathbf{b}^{\mathrm{T}}\mathbf{x} + c, \tag{2.25}$$

where $\mathbf{x}$ is a vector of unknowns, $\mathbf{b}$ is a vector of knowns, $\mathbf{A}$ is a symmetric positive-definite matrix[1], and c is a scalar. A superscript T signifies the transpose. The gradient of the function

[1] An $n \times n$ real symmetric matrix $\mathbf{A}$ is positive definite if $\mathbf{x}^{\mathrm{T}}\mathbf{A}\mathbf{x} > 0$ for all nonzero vectors $\mathbf{x}$.

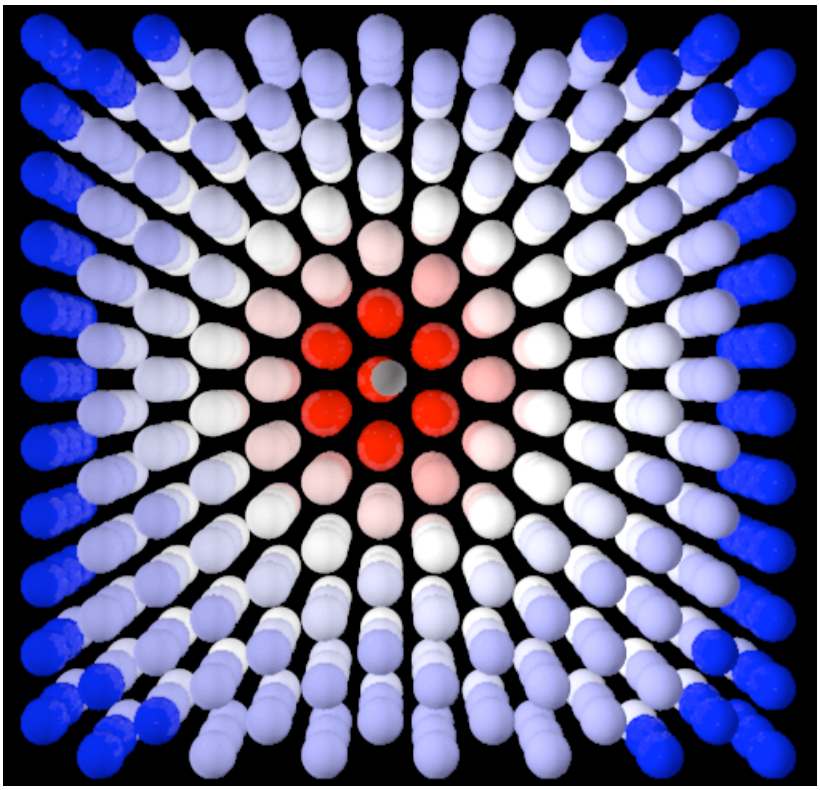

Figure 2.4: The image charge induced by an anion 10 Å above the anode at a potential of +0.005 a.u. The anion is grey and the wall ions are coloured according to their charge. Ions with an average charge are white, more positively charged ions are red, and more negatively charged ions are blue.

$f(\mathbf{x})$ is given by

$$f'(\mathbf{x}) = \begin{bmatrix} \frac{\partial}{\partial x_1} f(\mathbf{x}) \\ \frac{\partial}{\partial x_2} f(\mathbf{x}) \\ . \\ . \\ . \\ \frac{\partial}{\partial x_n} f(\mathbf{x}) \end{bmatrix}. \tag{2.26}$$

The minimum of $f(\mathbf{x})$ will occur when this gradient is zero. Applying equation 2.26 to equation 2.25 we find

$$f'(\mathbf{x}) = \frac{1}{2}\mathbf{A}^{\mathrm{T}}\mathbf{x} + \frac{1}{2}\mathbf{A}\mathbf{x} - \mathbf{b}. \tag{2.27}$$

If $\mathbf{A}$ is symmetric this gives

$$f'(\mathbf{x}) = \mathbf{A} \cdot \mathbf{x} - \mathbf{b}, \tag{2.28}$$

and hence if the gradient is zero we are left with the linear equations

$$\mathbf{A} \cdot \mathbf{x} = \mathbf{b}. \tag{2.29}$$

Providing that $\mathbf{A}$ is positive-definite then this stationary point will be a minimum.

2.4.1 Calculation of dipoles

The equation we need to solve for the melt dipoles $\boldsymbol{\mu}$ is:

$$\boldsymbol{\mu} = \boldsymbol{\alpha} \cdot (\mathbf{E}^q + \mathbf{T} \cdot \boldsymbol{\mu}), \tag{2.30}$$

where $\mathbf{E}^q$ is the electric field due to the charges on the melt and wall ions, $\mathbf{T}$ is the dipole–dipole interaction tensor as in Appendix B, and $\boldsymbol{\alpha}$ is a diagonal matrix of polarizabilities. Rearranging Equation 2.30 gives

$$(\mathbf{1} - \boldsymbol{\alpha} \cdot \mathbf{T}) \cdot \boldsymbol{\mu} = \boldsymbol{\alpha} \cdot \mathbf{E}^q, \tag{2.31}$$

which is a linear equation of the general form

$$\mathbf{A} \cdot \mathbf{x} = \mathbf{b}, \tag{2.29}$$

where

$$\mathbf{x} = \boldsymbol{\mu}, \tag{2.32}$$

$$\mathbf{b} = \boldsymbol{\alpha} \cdot \mathbf{E}^q, \tag{2.33}$$

$$\mathbf{A} = (\mathbf{1} - \boldsymbol{\alpha} \cdot \mathbf{T}). \tag{2.34}$$

Given a set of dipoles $\boldsymbol{\mu}$ our program calculates the electric field $\mathbf{E}[\boldsymbol{\mu}] = \mathbf{E}^q + \mathbf{T} \cdot \boldsymbol{\mu}$. We first set $\boldsymbol{\mu} = \mathbf{0}$ to obtain

$$\begin{aligned} \boldsymbol{\alpha} \cdot \mathbf{E}[\boldsymbol{\mu} = \mathbf{0}] &= \boldsymbol{\alpha} \cdot \mathbf{E}^q \\ &= \mathbf{b}. \end{aligned} \tag{2.35}$$

We now set $\boldsymbol{\mu} = \mathbf{x}_{(0)}$ where $\mathbf{x}_{(0)}$ are the dipoles appropriate to the preceeding configuration. This generates a new electric field $\mathbf{E}[\mathbf{x}_{(0)}] = \mathbf{E}^q + \mathbf{T} \cdot \mathbf{x}_{(0)}$. The first residual $\mathbf{r}_{(0)}$ is defined as

$$\begin{aligned} \mathbf{r}_{(0)} &= \mathbf{b} - \mathbf{A} \cdot \mathbf{x}_{(0)} \\ &= \mathbf{b} - (\mathbf{1} - \boldsymbol{\alpha} \cdot \mathbf{T}) \cdot \mathbf{x}_{(0)} \\ &= -\mathbf{x}_{(0)} + \boldsymbol{\alpha} \cdot \mathbf{E}[\mathbf{x}_{(0)}]. \end{aligned} \tag{2.36}$$

Iteration i = 0

We define an initial search direction $\mathbf{d}_{(0)}$ as

$$\mathbf{d}_{(0)} = \mathbf{r}_{(0)}. \tag{2.37}$$

We set $\boldsymbol{\mu} = \mathbf{d}_{(0)}$ and perform the Ewald summation to obtain the electric field $\mathbf{E}[\mathbf{d}] = \mathbf{E}^q + \mathbf{T} \cdot \mathbf{d}_{(0)}$.

We can now calculate the product $\mathbf{A} \cdot \mathbf{d}_{(0)}$ which is

$$\begin{aligned} \mathbf{A} \cdot \mathbf{d}_{(0)} &= (\mathbf{1} - \boldsymbol{\alpha} \cdot \mathbf{T}) \cdot \mathbf{d}_{(0)} \\ &= \mathbf{d}_{(0)} - \boldsymbol{\alpha} \cdot \mathbf{E}[\mathbf{d}] + \mathbf{b}. \end{aligned} \tag{2.38}$$

We are now in a position to find a new set of dipoles $\mathbf{x}_{(i+1)}$:

$$\mathbf{x}_{(i+1)} = \mathbf{x}_{(i)} + \boldsymbol{\zeta}_{(i)} \cdot \mathbf{d}_{(i)}, \tag{2.39}$$

where

$$\boldsymbol{\zeta}_{(i)} = \frac{\mathbf{r}_{(i)}^T \mathbf{r}_{(i)}}{\mathbf{d}_{(i)}^T \mathbf{A} \mathbf{d}_{(i)}}, \tag{2.40}$$

and a residual $\mathbf{r}_{(i+1)}$:

$$\mathbf{r}_{(i+1)} = \mathbf{r}_{(i)} - \boldsymbol{\zeta}_{(i)} \mathbf{A} \cdot \mathbf{d}_{(i)}. \tag{2.41}$$

Iterations i $\geq$ 1

Subsequent search directions are calculated using

$$\mathbf{d}_{(i+1)} = \mathbf{r}_{(i+1)} + \boldsymbol{\beta}_{(i+1)} \mathbf{d}_{(i)}, \tag{2.42}$$

where

$$\boldsymbol{\beta}_{(i)} = \frac{\mathbf{r}_{(i+1)}^T \mathbf{r}_{(i+1)}}{\mathbf{r}_{(i)}^T \mathbf{r}_{(i)}}, \tag{2.43}$$

and the vectors $\mathbf{x}_{(i+1)}$ and $\mathbf{r}_{(i+1)}$ are calculated using Equations 2.39 and 2.41.

2.4.2 Calculation of wall charges

The equation we need to solve for the variable wall charges $\boldsymbol{\delta}$ is:

$$\boldsymbol{\Psi}^q + \mathbf{T} \cdot \boldsymbol{\delta} + \boldsymbol{\delta} \cdot \boldsymbol{\xi}^{-1} - \boldsymbol{\Psi}^0 = 0, \tag{2.44}$$

where $\boldsymbol{\Psi}^q$ is the potential due to the charges on the melt ions, $\mathbf{T}$ is the charge–charge interaction tensor as in Appendix B, $\boldsymbol{\xi}$ is a diagonal matrix of elements $\frac{\sqrt{\pi}}{\sqrt{2}\kappa}$ corresponding to the Gaussian self interaction term of Equation 2.23, and $\boldsymbol{\Psi}^0$ is the constant externally-applied potential. Rearranging Equation 2.44 gives

$$(\mathbf{1} - \boldsymbol{\xi} \cdot \mathbf{T}) \cdot \boldsymbol{\delta} = -\boldsymbol{\xi} \cdot \left(\boldsymbol{\Psi}^q - \boldsymbol{\Psi}^0\right), \tag{2.45}$$

which is a linear equation of the general form

$$\mathbf{A} \cdot \mathbf{x} = \mathbf{b}, \tag{2.29}$$

where

$$\mathbf{x} = \boldsymbol{\delta}, \tag{2.46}$$

$$\mathbf{b} = -\boldsymbol{\xi} \cdot \left(\boldsymbol{\Psi}^q - \boldsymbol{\Psi}^0\right), \tag{2.47}$$

$$\mathbf{A} = (\mathbf{1} + \boldsymbol{\xi} \cdot \mathbf{T}). \tag{2.48}$$

Given a set of wall charges $\boldsymbol{\delta}$ our program calculates the potential $\boldsymbol{\Psi}[\boldsymbol{\delta}] = (\mathbf{T} \cdot \boldsymbol{\delta} + \boldsymbol{\Psi}^q)$. We first set $\boldsymbol{\delta} = 0$ to obtain

$$\boldsymbol{\Psi}[\boldsymbol{\delta} = \mathbf{0}] = \boldsymbol{\Psi}^q, \tag{2.49}$$

from which we can calculate $\mathbf{b}$ using Equation 2.47. We now set $\boldsymbol{\delta} = \mathbf{x}_{(0)}$ where $\mathbf{x}_{(0)}$ are the wall charges appropriate to the preceeding configuration. This generates a new potential $\boldsymbol{\Psi}[\mathbf{x}_{(0)}] = \left(\mathbf{T} \cdot \mathbf{x}_{(0)} + \boldsymbol{\Psi}^q\right)$. The first residual $\mathbf{r}_{(0)}$ is defined as

$$\begin{aligned} \mathbf{r}_{(0)} &= \mathbf{b} - \mathbf{A} \cdot \mathbf{x}_{(0)} \\ &= -\boldsymbol{\xi} \cdot \left(\boldsymbol{\Psi}^q - \boldsymbol{\Psi}^0\right) - (\mathbf{1} + \boldsymbol{\xi} \cdot \mathbf{T}) \cdot \mathbf{x}_{(0)} \\ &= -\mathbf{x}_{(0)} - \boldsymbol{\xi} \cdot \left(\boldsymbol{\Psi}[\mathbf{x}_{(0)}] - \boldsymbol{\Psi}^0\right). \end{aligned} \tag{2.50}$$

Iteration i = 0

We define an initial search direction $\mathbf{d}_{(0)}$ as

$$\mathbf{d}_{(0)} = \mathbf{r}_{(0)}. \qquad [2.37]$$

We set $\boldsymbol{\delta} = \mathbf{d}_{(0)}$ and perform the Ewald summation to generate the potential $\boldsymbol{\Psi}[\mathbf{d}] = \boldsymbol{\Psi}^q + \mathbf{T}\cdot\mathbf{d}_{(0)}$. We can now calculate the product $\mathbf{A}\cdot\mathbf{d}_{(0)}$ which is

$$\begin{aligned} \mathbf{A}\cdot\mathbf{d}_{(0)} &= (\mathbf{1} + \boldsymbol{\xi}\cdot\mathbf{T})\cdot\mathbf{d}_{(0)} \\ &= \mathbf{d}_{(0)} + \boldsymbol{\xi}\cdot\mathbf{T}\cdot\mathbf{d}_{(0)} \\ &= \mathbf{d}_{(0)} + \boldsymbol{\xi}\cdot\boldsymbol{\Psi}[\mathbf{d}_{(0)}] + \mathbf{b} - \boldsymbol{\xi}\cdot\boldsymbol{\Psi}^0. \end{aligned} \qquad (2.51)$$

We are now in a position to find a new set of wall charges $\mathbf{x}_{(i+1)}$:

$$\mathbf{x}_{(i+1)} = \mathbf{x}_{(i)} + \boldsymbol{\zeta}_{(i)}\cdot\mathbf{d}_{(i)}, \qquad [2.39]$$

where

$$\boldsymbol{\zeta}_{(i)} = \frac{\mathbf{r}_{(i)}^T\mathbf{r}_{(i)}}{\mathbf{d}_{(i)}^T\mathbf{A}\mathbf{d}_{(i)}}, \qquad [2.40]$$

and a residual $\mathbf{r}_{(i+1)}$:

$$\mathbf{r}_{(i+1)} = \mathbf{r}_{(i)} - \boldsymbol{\zeta}_{(i)}\mathbf{A}\cdot\mathbf{d}_{(i)}. \qquad [2.41]$$

Iterations i ≥ 1

Subsequent search directions are calculated using

$$\mathbf{d}_{(i+1)} = \mathbf{r}_{(i+1)} + \boldsymbol{\beta}_{(i+1)}\mathbf{d}_{(i)}, \qquad [2.42]$$

where

$$\boldsymbol{\beta}_{(i)} = \frac{\mathbf{r}_{(i+1)}^T\mathbf{r}_{(i+1)}}{\mathbf{r}_{(i)}^T\mathbf{r}_{(i)}}, \qquad [2.43]$$

and the vectors $\mathbf{x}_{(i+1)}$ and $\mathbf{r}_{(i+1)}$ are calculated using Equations 2.51, 2.39– 2.41.

3

A 3D simulation cell with 2D periodicity

3.1 Introduction

The most widely used method for computing the electrostatic energy in a three-dimensional periodic lattice of point charges is the Ewald summation [64]. Our system differs in three ways. Most fundamentally, our simulation is periodic in two dimensions but bounded by two parallel electrodes in the third dimension. Second, the charge distibution on each electrode atom is modelled as a Gaussian. Third, we wish to incorporate induction (polarization) interactions by allowing the anions to deform with dipolar symmetry.

All three of the above features have been addressed separately in previous work, but our purpose here is to derive Ewald expressions which incorporate all within the same code. Specifically, Reed *et al.* [26] performed 2D simulations of an ionic liquid sandwiched between two parallel electrodes, in which the ions were modelled as point charges and the electrode atoms carried Gaussian charge distributions. And separately, Aguado *et al.* [65] derived expressions including multipolar interactions for systems with three-dimensional periodicity.

The full derivation of the Ewald summation appropriate to a system periodically replicated in two dimenions which incorporates both point charges and Gaussian distributions is given in Appendix A. We start the chapter with a discussion of those derived expressions, and go on

from there to incorporate the dipolar interactions. We present expressions for the total energy, interatomic forces, and the electric field and potential at each ion's position. The respective motivations for each of these are as follows: diabatic energy gaps of redox processes are used in the calculation of the Marcus curves, the interatomic forces are an essential component of the Newtonian mechanics, the electric fields enable the calculation of the anion dipoles, and the potential at each electrode atom site is required for the calculation of the variable wall charges. The chapter ends with some verifications of the coded expressions.

3.2 The two-dimensional Ewald summation

One obvious approach to modelling 2D systems was developed by Yeh and Berkowitz [66], in which vacuum boundary conditions (VBC) are created in the direction of the restricted lattice whilst conducting boundary conditions are retained in the two perpendicular directions. The long range interactions are dealt with by a 3D Ewald summation: spurious interactions between periodic replicas in the z direction are obviated if the vacuum region is sufficiently large.

This method cannot be employed in our work beause we require isolated electrodes. If VBC were employed, the anode in the central cell would interact with the neighbouring periodic images of the cathode. The conjugate gradient minimization of the wall charges would then result in a value for the anode potential which was relative to the neighbouring cell, rather than an absolute potential value. An experimental analogy would be to measure a half-cell potential with a reference electrode of unknown potential. The direction of this area of research is towards calculating rate constants for electron transfer at an electrode. In Chapter 1 we wrote the rate constant as a function of electrode potential Ψ. It is not as meaningful to express the rate constant as a function of potential *difference* $\Delta\Psi$, because there are an infinite number of anode potentials which correspond to any particular potential difference across a cell.

The most straightforward solution is to use the same approach as for the three-dimensional Ewald summation, but restrict the reciprocal-space sum to vectors in the infinite x, y directions. An accurate formulation of the two-dimensional Ewald summation was first introduced by Parry [67], and the same formulae were independently rederived by Heyes *et al.* [68], and de

Leeuw and Perram [69]. The computational burden of this formulation for each $\mathbf{k}$ wavevector is N^2, such that its direct use in MD simulations has been limited. This method was accurately reformulated by Kawata and Mikami [70] to significantly reduce the computational time. The derivation in Appendix A extends the application of that latter work to systems containing both point charges and Gaussian charge distributions.

The Coulomb energy of a system of charges which is periodic in two dimensions is

$$U_c = \frac{1}{2}\sum_{i,j}\sum_{k,l}{}' \int\int \frac{\rho_i(\mathbf{r}')\rho_j(\mathbf{r}'')\ \mathrm{d}\mathbf{r}'\mathrm{d}\mathbf{r}''}{|\mathbf{r}_{ij}+\mathbf{r}'-\mathbf{r}''+k\mathbf{a}+l\mathbf{b}|}, \tag{3.1}$$

where ρ_i is the charge distribution associated with particle i, $\mathbf{r}_{ij} = \mathbf{r}_i - \mathbf{r}_j$, and $\mathbf{a}$ and $\mathbf{b}$ are elementary lattice vectors in the periodic dimensions. The prime on the sum over periodic replicas indicates that for the cell (0,0,0) the terms $i = j$ should be omitted.

Each ion in the melt has a point charge so that its charge distribution is

$$\rho_i(\mathbf{r}) = q_i\delta(\mathbf{r}-\mathbf{r}_i), \tag{3.2}$$

where $\delta(\mathbf{r}-\mathbf{r}_i)$ is the Kronecker delta function. The Gaussian charge density centred on each metal atom j has an integrated charge of q_j and is of fixed width κ:

$$\rho_j(\mathbf{r}) = q_j\kappa^3\pi^{3/2}\exp\left(-|\mathbf{r}-\mathbf{r}_j|^2\kappa^2\right). \tag{3.3}$$

The final result for the total Coulomb energy of a system comprised of n_p point charges and

n_g Gaussian charges is

$$U_c = \frac{1}{2}\sum_{i,j}^{n_p} q_i q_j \frac{1}{r_{ij}} \operatorname{erfc}(\alpha r_{ij}) \tag{3.4a}$$

$$+ \sum_{i}^{n_p}\sum_{j}^{n_g} q_i q_j \frac{1}{r_{ij}} \operatorname{erfc}(\gamma r_{ij}) \tag{3.4b}$$

$$+ \frac{1}{2}\sum_{i,j}^{n_g} q_i q_j \frac{1}{r_{ij}} \operatorname{erfc}(\beta r_{ij}) \tag{3.4c}$$

$$+ \frac{1}{ab}\sum_{k=-\infty}^{\infty}\sum_{l=-\infty}^{\infty}{}' \int_{-\infty}^{\infty} \frac{1}{4\pi^2|\mathbf{k}|^2 + h^2} \times \exp\left(-\frac{4\pi^2|\mathbf{k}|^2 + h^2}{4\alpha^2}\right) |S(\mathbf{k},h)|^2 \,\mathrm{d}h \tag{3.4d}$$

$$- \frac{1}{ab}\sum_{i,j}^{n_p} q_i q_j \left\{\frac{\sqrt{\pi}}{\alpha}\exp\left(-z_{ij}^2\alpha^2\right) + z_{ij}\,\pi\mathrm{erf}\left(z_{ij}\alpha\right)\right\} \tag{3.4e}$$

$$- \frac{2}{ab}\sum_{i}^{n_p}\sum_{j}^{n_g} q_i q_j \left\{\frac{\sqrt{\pi}}{\gamma}\exp\left(-z_{ij}^2\gamma^2\right) + z_{ij}\,\pi\mathrm{erf}\left(z_{ij}\gamma\right)\right\} \tag{3.4f}$$

$$- \frac{1}{ab}\sum_{i,j}^{n_g} q_i q_j \left\{\frac{\sqrt{\pi}}{\beta}\exp\left(-z_{ij}^2\beta^2\right) + z_{ij}\,\pi\mathrm{erf}\left(z_{ij}\beta\right)\right\} \tag{3.4g}$$

$$- \sum_{i}^{n_p} \frac{\alpha q_i^2}{\sqrt{\pi}} \tag{3.4h}$$

$$- \sum_{i}^{n_g} \frac{\beta q_i^2}{\sqrt{\pi}} \tag{3.4i}$$

$$+ \sum_{i}^{n_g} \frac{\kappa q_i^2}{\sqrt{2\pi}}, \tag{3.4j}$$

where

$$\begin{aligned} S(\mathbf{k},h) = &\sum_{i=1}^{n_p} q_i \exp\left[i\left(2\pi\mathbf{k}.\mathbf{r}_i' + hz_i\right)\right] \\ &+ \exp\left(-\frac{4\pi^2k^2 + h^2}{4\kappa^2}\right)\sum_{j=1}^{n_g} q_j \exp\left[i\left(2\pi\mathbf{k}.\mathbf{r}_j' + hz_j\right)\right], \end{aligned} \tag{3.5}$$

with $\mathbf{r}'_i = (x_i, y_i)$, $\mathbf{k} = (k/a, l/b)$, $\beta = \kappa\alpha(\kappa^2 + 2\alpha^2)^{-1/2}$ and $\gamma = \kappa\alpha(\kappa^2 + \alpha^2)^{-1/2}$.

First, a discussion of the real space contribution, Equations 3.4a–3.4c. There is a duplication of terms due to the different charge distributions on melt ions and electrode atoms. Equation 3.4a is the familiar real-space charge–charge interaction energy, with the screening parameter α chosen such that the summation over ions is restricted to $\mathbf{k} = 0$. Hence in the real-space terms we now drop the k- and l-sums over periodic replicas which were present in Equation 3.1. Equation 3.4b is the real-space contribution of the interactions between the point charges and the Gaussian charge distributions. The initial factor of $\frac{1}{2}$ is not present in this term because the particles have either a point charge or a Gaussian charge distribution, and there is consequently no double counting. The final real-space term, Equation 3.4c, is that appropriate to the Gaussian charge subsystem.

The prime in the reciprocal-space contribution to the energy (Equation 3.4d) indicates that the $k = l = 0$ term is excluded from the summation. This subtraction is necessary in the derivation to avoid a divergent integral (see Appendix A), and the term is added on separately (Equations 3.4e–3.4g). A sufficient number of reciprocal vectors $\mathbf{k}$ are chosen to ensure convergence of the reciprocal space sum. Note that Equation 3.4d has the same overall structure as the reciprocal-space sum in the 3D Ewald summation,

$$U^{\mathrm{3D}}_{\mathrm{recip}} = \frac{2\pi}{V} \sum_{\mathbf{k}' \neq 0} \frac{1}{|\mathbf{k}'|^2} \exp\left(-\frac{|\mathbf{k}'|^2}{4\alpha^2}\right) |S(\mathbf{k}')|^2, \tag{3.6}$$

where $\mathbf{k}'$ is the 3D reciprocal vector, V is the volume of the simulation box, and the structure factor $S(\mathbf{k}')$ is defined as

$$S(\mathbf{k}') = \sum_{j=1}^{N} q_j \, e^{i\mathbf{k}'\cdot\mathbf{r}_j}. \tag{3.7}$$

Equation 3.4d erroneously includes part of the interaction of a particle with itself, and this is subtracted in Equations 3.4h and 3.4i. Unlike in the case of point charges, there will be an interaction of a Gaussian with itself, and the full self-term which needs to be added is Equation 3.4j.

A variable h is used in Equation 3.5 instead of the z component of the 3D reciprocal space

vector $\mathbf{k}'$ used in Equation 3.7, and the summation with respect to the z component of the 3D reciprocal-space vector in Equation 3.6 is replaced with an integration with respect to h in Equation 3.4d. This integral is in theory over all space but rapidly dies away outside the simulation cell such that it can be truncated and replaced with a summation:

$$\int_{-\infty}^{+\infty} f(h)\mathrm{d}h \approx \int_{-h_c}^{+h_c} f(h)\mathrm{d}h \approx \sum_{n=-N_c}^{+N_c} f(n\Delta h), \tag{3.8}$$

where

$$N_c = \frac{h_c}{\Delta h}. \tag{3.9}$$

This method requires two parameters, Δh and h_c, which are chosen such that convergence is achieved. For our system we found that setting $\Delta h = 1.1$ and $h_c = k_{\max}c/a$ was sufficient, where $k_{\max}$ is the number of terms in the reciprocal space sums in the x and y directions, and c/a is the ratio of the length of the tetragonal simulation cell in the finite (z) direction to the length in either of the two perpendicular (x and y) directions. Note that the computational burden of Equation 3.4d is essentially the same as the 3D sum of Equation 3.6.

3.3 Incorporating dipolar interactions

The incorporation of dipolar interactions into the Ewald summation expressions follows the methodology outlined by Aguado and Madden [65], although we here extend its application to 2D periodic systems. For a system of molecules (represented by italic indices $i, j, \ldots$), each composed of several partial charges (represented by ia, ib etc.), we can recast the real and reciprocal contributions of Equation 3.4 as

$$U_{\text{real}} = \frac{1}{2}\sum_{i}^{N}\sum_{a} q_{ia} \sum_{j}^{N}\sum_{b} q_{jb} \frac{\operatorname{erfc}(A_{ij}r_{iajb})}{r_{iajb}}, \tag{3.10}$$

$$U_{\text{recip}} = \frac{1}{ab}\sum_{k=-\infty}^{\infty}\sum_{l=-\infty}^{\infty}\int_{-\infty}^{\infty}\frac{1}{4\pi^2|\mathbf{k}|^2+h^2}\times\exp\left(-\frac{4\pi^2|\mathbf{k}|^2+h^2}{4\alpha^2}\right)|S(\mathbf{k},h)|^2\,\mathrm{d}h \quad (3.11)$$

$$-\frac{1}{ab}\sum_i\sum_a\sum_{j>i}\sum_b q_{ia}q_{jb}\left\{\frac{\sqrt{\pi}}{A_{ij}}\exp\left(-z_{iajb}^2A_{ij}^2\right)+z_{iajb}\,\pi\mathrm{erf}\left(z_{iajb}A_{ij}\right)\right\},$$

where the structure factor now is

$$S(\mathbf{k},h)=\sum_{i=1}^{n_p}\sum_a q_{ia}\exp\left[i\left(2\pi\mathbf{k}.\mathbf{r}'_{ia}+hz_{ia}\right)\right]+\exp\left(-\frac{4\pi^2k^2+h^2}{4\kappa^2}\right)\sum_{j=1}^{n_g}q_j\exp\left[i\left(2\pi\mathbf{k}.\mathbf{r}'_j+hz_j\right)\right], \quad (3.12)$$

and where

$$A_{ij}=\begin{cases}\alpha & \text{for point-charge–point-charge terms,}\\ \beta=\kappa\alpha(\kappa^2+2\alpha^2)^{-1/2} & \text{for wall-wall terms,}\\ \gamma=\kappa\alpha(\kappa^2+\alpha^2)^{-1/2} & \text{for point-charge–wall terms.}\end{cases} \quad (3.13)$$

In these expressions, q_{ia} is the charge on site a of molecule i, whose position is given by the vector $\mathbf{r}_{ia}$, and $r_{iajb}=|\mathbf{r}_{ia}-\mathbf{r}_{jb}|$. The sums over i and j run over all $N=n_p+n_g$ molecules. We consider Equations 3.10 and 3.11 as applied to the specific case of molecules with two partial charges. Each partial charge of a given molecule i is described by the position vector $\mathbf{r}_{ib}=\mathbf{r}_i+(-1)^b\boldsymbol{\xi}_i$, with $\mathbf{r}_i$ the position vector of the midpoint of the molecule (this point is not associated with any charge) and $b=1,2$. With this notation, the total length of the molecule i is equal to $2\xi_i$. The distance between two molecules i and j will be denoted by $r_{ij}=|\mathbf{r}_i-\mathbf{r}_j|$; similarly, $r_i=|\mathbf{r}_i|$. We consider expressions 3.10 and 3.11 for the total energy as functions of the set of variables $\{\boldsymbol{\xi}_i\}$ and expand these functions about $\boldsymbol{\xi}_i=\mathbf{0}(i=1,2,\ldots,N)$. In this process, we are able to identify the total charge $q_i=q_{i1}+q_{i2}$ and dipole $\boldsymbol{\mu}_i=(q_{i2}-q_{i1})\boldsymbol{\xi}_i$ of molecule i, where a and b refer to Cartesian components. Terms of quadrupolar, octupolar, and hexadeculpolar symmetry are neglected, but could easily be introduced if required.

3.4 Ewald expressions

This section contains the Ewald expressions for the total energy, interatomic forces, electric field and electrical potential. The additions to the Ewald subroutine were parallelised using MPI and the final code was ported to the Edinburgh Parallel Computing Centre (EPCC) BlueGene/L system[1].

3.4.1 Real space

If we consider the real space energy contribution, Equation 3.10, as a function $f(\xi_i, \xi_j)$, we may perform the following series expansion:

$$f(\boldsymbol{\xi}_i, \boldsymbol{\xi}_j) = f(\mathbf{0}, \mathbf{0}) + [\boldsymbol{\xi}_i \cdot \boldsymbol{\nabla}_i f(\mathbf{0}, \mathbf{0}) + \boldsymbol{\xi}_j \cdot \boldsymbol{\nabla}_i f(\mathbf{0}, \mathbf{0})] + \cdots . \tag{3.14}$$

After reintroducing each term in this expansion back into Equation 3.10 and performing the a and b summations, we can separately identify the charge–charge, charge–dipole, and dipole–dipole interactions. The expressions for the interaction tensors between molecules i and j, T_{ij}, and Ewald screening functions, $f_n(r_{ij})$, are given explicitly in Appendices B and C respectively.

3.4.1.1 Energy

Charge–charge

The charge-charge energy comes from the first term in expansion 3.14 and has the well-known form

$$U_{\text{real}}^{q-q} = \sum_i \sum_{j>i} f_0(r_{ij}) q_i T_{ij} q_{ij}. \tag{3.15}$$

[1]The EPCC BlueGene has a large number of relatively slow processors: 1024 chips in a single cabinet, with each chip having two 700 MHz PowerPC 440 processors and 512 MB of memory. The simulations reported in this thesis were typically run on 128 chips.

Charge–dipole Similarly, the charge-dipole interaction is recovered from the first-order terms in expansion 3.14:

$$U_{\text{real}}^{q-\mu} = -\sum_i \sum_{j>i} f_1(r_{ij})(q_i T_{ij}^{\alpha} \mu_{j\alpha} - q_j T_{ij}^{\alpha} \mu_{i\alpha}). \tag{3.16}$$

In this expression and throughout, the Einstein summation convention of greek indices ($A^{\alpha}a_{\alpha} \equiv \sum_{\alpha} A^{\alpha}a_{\alpha}$) will be employed.

Dipole–dipole The second-order terms in Equation 3.14 lead to the dipole-dipole interaction

$$U_{\text{real}}^{\mu-\mu} = -\sum_i \sum_{j>i} [f_1(r_{ij})\mu_{i\alpha} T_{ij}^{\alpha\beta} \mu_{j\beta} + f_2(r_{ij})\mu_{i\alpha} D_{ij}^{\alpha\beta} \mu_{j\beta}]. \tag{3.17}$$

We now switch to a more compact notation, in terms of modified multipolar tensors. For a finite system (that is, in the absence of any periodic boundary conditions), the electrostatic energy of a set of charges and dipoles can be shown to be [71]

$$U = \sum_i \sum_{j>i} \left(q_i T_{ij} q_j - q_i T_{ij}^{\alpha} \mu_{j\alpha} + q_j T_{ij}^{\alpha} \mu_{i\alpha} - \mu_{i\alpha} T_{ij}^{\alpha\beta} \mu_{j\beta} \right). \tag{3.18}$$

The corresponding Ewald summation expressions given in Equations 3.15 to 3.17 can be recovered directly from Equation 3.18 by replacing $1/r_{ij}^{2n+1} (n = 0, 1, 2, 3, \ldots)$ in the multipole interaction tensors, by their screened counterparts $\widehat{1}/r_{ij}^{2n+1}$, where

$$\frac{\widehat{1}}{r_{ij}} = \frac{\text{erfc}(A_{ij} r_{ij})}{r_{ij}}, \tag{3.19}$$

and

$$\frac{\widehat{1}}{r_{ij}^{2n+1}} = \frac{1}{r_{ij}^2} \left(\frac{\widehat{1}}{r_{ij}^{2n-1}} + \frac{(2A_{ij}^2)^n}{\sqrt{\pi} A_{ij} (2n-1)!!} e^{-A_{ij}^2 r_{ij}^2} \right). \tag{3.20}$$

This provides for a more compact notation, which is very convenient in order to show the results for the forces, electric fields, and potentials.

3.4.1.2 Force

The α component of the force acting on particle i is easily evaluated by taking the partial derivative of the energy with respect to $r_{i\alpha}$:

$$F_{i\alpha} = -\frac{\partial U}{\partial r_{i\alpha}}. \tag{3.21}$$

We employ a simple partial derivative because we are assuming for the moment that the multipoles are rigid (see Section 3.4.4 for an extension of this formalism). The net result of applying this to the real space energy is

$$F_{i\alpha}^{\text{real}} = \sum_{j\neq i} \left(-q_i \widehat{T}_{ij}^{\alpha} q_j + q_i \widehat{T}_{ij}^{\alpha\beta} \mu_{j\beta} - q_j \widehat{T}_{ij}^{\alpha\beta} \mu_{i\beta} + \mu_{i\beta} \widehat{T}_{ij}^{\alpha\beta\gamma} \mu_{j\gamma} \right). \tag{3.22}$$

3.4.1.3 Electric field

The α component of the electric field at position i induced by a charge or dipole at position j can be obtained from

$$E_{i\alpha}^{\text{real}} = -\frac{\partial U}{\partial \mu_{i\alpha}}. \tag{3.23}$$

Applying this expression to the real space contribution to the charge-dipole and dipole-dipole energies we obtain

$$E_{i\alpha}^{\text{real}} = \sum_{j\neq i} (-q_j \hat{T}_{ij}^{\alpha} + \mu_{j\beta} \hat{T}_{ij}^{\alpha\beta}). \tag{3.24}$$

3.4.1.4 Potential

The electrical potential on particle i is defined as

$$V_i = \frac{\partial U}{\partial q_i}. \tag{3.25}$$

Applying this expression to the real space contribution to the charge-charge and charge-dipole energies we obtain

$$V_i = \sum_{j \neq i} \left(\widehat{T}_{ij} q_j - \widehat{T}^{\alpha}_{ij} \mu_{j\alpha} \right). \tag{3.26}$$

3.4.2 Reciprocal space

To calculate the different contributions to the reciprocal space energy, we expand the trigonometric functions of Equation 3.11 about $\boldsymbol{\xi}_i = \mathbf{0}$:

$$\begin{aligned} \cos\left[(2\pi\mathbf{k}.\mathbf{r}'_i + hz_i) + (-1)^a (2\pi\mathbf{k} + \hat{\mathbf{z}}h) \cdot \boldsymbol{\xi}_i\right] = \cos\left(2\pi\mathbf{k}.\mathbf{r}'_i + hz_i\right) \\ - (-1)^a \sin\left(2\pi\mathbf{k}.\mathbf{r}'_i + hz_i\right) \left[(2\pi\mathbf{k} + \hat{\mathbf{z}}h) \cdot \boldsymbol{\xi}_i\right] \\ - \frac{1}{2}\cos\left(2\pi\mathbf{k}.\mathbf{r}'_i + hz_i\right) \left[(2\pi\mathbf{k} + \hat{\mathbf{z}}h) \cdot \boldsymbol{\xi}_i\right]^2 + \cdots, \end{aligned} \tag{3.27}$$

$$\begin{aligned} \sin\left[(2\pi\mathbf{k}.\mathbf{r}'_i + hz_i) + (-1)^a (2\pi\mathbf{k} + \hat{\mathbf{z}}h) \cdot \boldsymbol{\xi}_i\right] = \sin\left(2\pi\mathbf{k}.\mathbf{r}'_i + hz_i\right) \\ + (-1)^a \cos\left(2\pi\mathbf{k}.\mathbf{r}'_i + hz_i\right) \left[(2\pi\mathbf{k} + \hat{\mathbf{z}}h) \cdot \boldsymbol{\xi}_i\right] \\ - \frac{1}{2}\sin\left(2\pi\mathbf{k}.\mathbf{r}'_i + hz_i\right) \left[(2\pi\mathbf{k} + \hat{\mathbf{z}}h) \cdot \boldsymbol{\xi}_i\right]^2 + \cdots. \end{aligned} \tag{3.28}$$

If we now perform the summation over the a index, we obtain

$$\sum_a q_{ia} \cos\left(2\pi\mathbf{k}.\mathbf{r}'_{ia} + hz_{ia}\right) = q_i \cos\left(2\pi\mathbf{k}.\mathbf{r}'_i + hz_i\right) - \left[\boldsymbol{\mu}_i \cdot (2\pi\mathbf{k} + h\hat{\mathbf{z}})\right] \sin\left(2\pi\mathbf{k}.\mathbf{r}'_i + hz_i\right) + \cdots, \tag{3.29}$$

$$\sum_a q_{ia} \sin\left(2\pi\mathbf{k}.\mathbf{r}'_{ia} + hz_{ia}\right) = q_i \sin\left(2\pi\mathbf{k}.\mathbf{r}'_i + hz_i\right) + \left[\boldsymbol{\mu}_i \cdot (2\pi\mathbf{k} + h\hat{\mathbf{z}})\right] \cos\left(2\pi\mathbf{k}.\mathbf{r}'_i + hz_i\right) + \cdots. \tag{3.30}$$

We now square the i summations:

$$\begin{aligned}\left[\sum_i\sum_a q_{ia}\cos\left(2\pi\mathbf{k}.\mathbf{r}'_{ia}+hz_{ia}\right)\right]^2 &= \left[\sum_i q_i\cos\left(2\pi\mathbf{k}.\mathbf{r}'_i+hz_i\right)\right]^2 \\ &\quad -\left\{2\sum_i q_i\cos\left(2\pi\mathbf{k}.\mathbf{r}'_i+hz_i\right)\right. \\ &\quad \left.\times\sum_j\left[\boldsymbol{\mu}_j\cdot(2\pi\mathbf{k}+h\hat{\mathbf{z}})\right]\sin\left(2\pi\mathbf{k}.\mathbf{r}'_j+hz_j\right)\right\} \\ &\quad +\left\{\sum_i\left[\boldsymbol{\mu}_i\cdot(2\pi\mathbf{k}+h\hat{\mathbf{z}})\right]\sin\left(2\pi\mathbf{k}.\mathbf{r}'_i+hz_i\right)\right\}^2,\end{aligned} \tag{3.31}$$

$$\begin{aligned}\left[\sum_i\sum_a q_{ia}\sin\left(2\pi\mathbf{k}.\mathbf{r}'_{ia}+hz_{ia}\right)\right]^2 &= \left[\sum_i q_i\sin\left(2\pi\mathbf{k}.\mathbf{r}'_i+hz_i\right)\right]^2 \\ &\quad +\left\{2\sum_i q_i\sin\left(2\pi\mathbf{k}.\mathbf{r}'_i+hz_i\right)\right. \\ &\quad \left.\times\sum_j\left[\boldsymbol{\mu}_j\cdot(2\pi\mathbf{k}+h\hat{\mathbf{z}})\right]\cos\left(2\pi\mathbf{k}.\mathbf{r}'_j+hz_j\right)\right\} \\ &\quad +\left\{\sum_i\left[\boldsymbol{\mu}_i\cdot(2\pi\mathbf{k}+h\hat{\mathbf{z}})\right]\cos\left(2\pi\mathbf{k}.\mathbf{r}'_i+hz_i\right)\right\}^2.\end{aligned} \tag{3.32}$$

In these two expressions it is easy to recognize the charge-charge, charge-dipole, and dipole-dipole contributions. Now we write down the different contributions.

3.4.2.1 Energy

Charge–charge ($\mathbf{k} \neq \mathbf{0}$)

$$U_{\text{recip}}^{q-q}=\frac{1}{ab}\sum_{k=-\infty}^{\infty}\sum_{l=-\infty}^{\infty}\int_{-\infty}^{\infty}\frac{1}{4\pi|\mathbf{k}|^2+h^2}\exp\left(\frac{-4\pi|\mathbf{k}|^2+h^2}{4\alpha^2}\right)|S(\mathbf{k},h)|^2\,\mathrm{d}h, \tag{3.33}$$

$$S(\mathbf{k},h)=\sum_{i=1}^{N}q_i\exp\left(\frac{-4\pi|\mathbf{k}|^2+h^2}{4\kappa_i^2}\right)\exp\left[i\left(2\pi\mathbf{k}\cdot\mathbf{r}_i+hz_i\right)\right], \tag{3.34}$$

where

$$\kappa_i = \begin{cases} \infty & \text{if } i \text{ is a point-charge,} \\ \text{finite} & \text{otherwise.} \end{cases} \tag{3.35}$$

Charge–dipole ($\mathbf{k} \neq 0$)

$$\begin{aligned} U^{q-\mu}_{\text{recip}} = \frac{2}{ab} \sum_{k=-\infty}^{\infty} \sum_{l=-\infty}^{\infty} \int_{-\infty}^{\infty} \frac{1}{4\pi|\mathbf{k}|^2 + h^2} \exp\left(\frac{-4\pi|\mathbf{k}|^2 + h^2}{4\alpha^2}\right) \\ \times \left\{ \left[\sum_i^N q_i \exp\left(\frac{-4\pi|\mathbf{k}|^2 + h^2}{4\kappa_i^2}\right) \sin\left(2\pi\mathbf{k}\cdot\mathbf{r}_i + hz_i\right) \right. \right. \\ \left. \times \sum_j^N \boldsymbol{\mu}_j \cdot (2\pi\mathbf{k} + h\hat{\mathbf{z}}) \exp\left(\frac{-4\pi|\mathbf{k}|^2 + h^2}{4\kappa_j^2}\right) \cos\left(2\pi\mathbf{k}\cdot\mathbf{r}_j + hz_j\right) \right] \\ - \left[\sum_i^N q_i \exp\left(\frac{-4\pi|\mathbf{k}|^2 + h^2}{4\kappa_i^2}\right) \cos\left(2\pi\mathbf{k}\cdot\mathbf{r}_i + hz_i\right) \right. \\ \left. \left. \times \sum_j^N \boldsymbol{\mu}_j \cdot (2\pi\mathbf{k} + h\hat{\mathbf{z}}) \exp\left(\frac{-4\pi|\mathbf{k}|^2 + h^2}{4\kappa_j^2}\right) \sin\left(2\pi\mathbf{k}\cdot\mathbf{r}_j + hz_j\right) \right] \right\} \mathrm{d}h \end{aligned} \tag{3.36}$$

Dipole–dipole ($\mathbf{k} \neq 0$)

$$\begin{aligned} U^{\mu-\mu}_{\text{recip}} = \frac{1}{ab} \sum_{k=-\infty}^{\infty} \sum_{l=-\infty}^{\infty} \int_{-\infty}^{\infty} \frac{1}{4\pi|\mathbf{k}|^2 + h^2} \exp\left(\frac{-4\pi|\mathbf{k}|^2 + h^2}{4\alpha^2}\right) \\ \times \left\{ \left[\sum_i^N \boldsymbol{\mu}_i \cdot (2\pi\mathbf{k} + h\hat{\mathbf{z}}) \cos\left(2\pi\mathbf{k}\cdot\mathbf{r}_i + hz_i\right) \exp\left(\frac{-4\pi|\mathbf{k}|^2 + h^2}{4\kappa_i^2}\right) \right]^2 \right. \\ \left. + \left[\sum_i^N \boldsymbol{\mu}_i \cdot (2\pi\mathbf{k} + h\hat{\mathbf{z}}) \sin\left(2\pi\mathbf{k}\cdot\mathbf{r}_i + hz_i\right) \exp\left(\frac{-4\pi|\mathbf{k}|^2 + h^2}{4\kappa_i^2}\right) \right]^2 \right\} \mathrm{d}h \end{aligned} \tag{3.37}$$

Charge–charge ($\mathbf{k} = 0$)

$$U^{q-q}_{\text{recip}}(k=0) = -\frac{1}{ab} \sum_i^N \sum_j^N q_i q_j \left\{ \frac{\sqrt{\pi}}{A_{ij}} \exp\left(-z_{ij}^2 A_{ij}^2\right) + z_{ij}\pi \operatorname{erf}(z_{ij}A_{ij}) \right\}, \tag{3.38}$$

where A_{ij} is defined by Equation 3.13.

Charge–dipole (k = 0)

$$U^{q-\mu}_{\text{recip}}(k=0) = -\frac{1}{ab}\sum_{i}^{N}\sum_{j}^{N}\pi\,\text{erf}\left(z_{ij}A_{ij}\right)\left[q_j\mu_i^z - q_i\mu_j^z\right] \tag{3.39}$$

Dipole-dipole (k = 0)

$$U^{\mu-\mu}_{\text{recip}}(k=0) = +\frac{2}{ab}\sum_{i}^{N}\sum_{j}^{N}\mu_i^z\mu_j^z A_{ij}\sqrt{\pi}\,\exp\left(-z_{ij}^2A_{ij}^2\right) \tag{3.40}$$

3.4.2.2 Force

Charge–charge (k ≠ 0)

$$\begin{aligned}\mathbf{F}^{q-q}_{i,\text{recip}} = \frac{2q_i}{ab}\sum_{k=-\infty}^{\infty}\sum_{l=-\infty}^{\infty}\int_{-\infty}^{\infty}\frac{2\pi k\hat{\mathbf{x}}/a + 2\pi l\hat{\mathbf{y}}/b + h\hat{\mathbf{z}}}{4\pi|\mathbf{k}|^2+h^2}\exp\left(\frac{-4\pi|\mathbf{k}|^2+h^2}{4\alpha^2}\right)\\ \times\left\{\sin\left(2\pi\mathbf{k}\cdot\mathbf{r}_i + hz_i\right)\sum_j^N q_j\cos\left(2\pi\mathbf{k}\cdot\mathbf{r}_j+hz_j\right)\,\exp\left(\frac{-4\pi|\mathbf{k}|^2+h^2}{4\kappa_j^2}\right)\right.\\ \left.-\,\cos\left(2\pi\mathbf{k}\cdot\mathbf{r}_i + hz_i\right)\sum_j^N q_j\,\sin\left(2\pi\mathbf{k}\cdot\mathbf{r}_j+hz_j\right)\left(\frac{-4\pi|\mathbf{k}|^2+h^2}{4\kappa_j^2}\right)\right\}\,\mathrm{d}h\end{aligned} \tag{3.41}$$

Charge–dipole (k ≠ 0)

$$\begin{aligned}\mathbf{F}^{q-\mu}_{i,\text{recip}} = \frac{2}{ab}\sum_{k=-\infty}^{\infty}\sum_{l=-\infty}^{\infty}\int_{-\infty}^{\infty}\frac{2\pi k\hat{\mathbf{x}}/a + 2\pi l\hat{\mathbf{y}}/b + h\hat{\mathbf{z}}}{4\pi|\mathbf{k}|^2+h^2}\exp\left(\frac{-4\pi|\mathbf{k}|^2+h^2}{4\alpha^2}\right)\\ \times\left\{\boldsymbol{\mu}_i\cdot\left(2\pi\mathbf{k}+h\hat{\mathbf{z}}\right)\,\sin\left(2\pi\mathbf{k}\cdot\mathbf{r}_i+hz_i\right)\sum_j^N q_j\exp\left(\frac{-4\pi|\mathbf{k}|^2+h^2}{4\kappa_j^2}\right)\,\sin\left(2\pi\mathbf{k}\cdot\mathbf{r}_j+hz_j\right)\right.\\ +\boldsymbol{\mu}_i\cdot\left(2\pi\mathbf{k}+h\hat{\mathbf{z}}\right)\,\cos\left(2\pi\mathbf{k}\cdot\mathbf{r}_i+hz_i\right)\sum_j^N q_j\exp\left(\frac{-4\pi|\mathbf{k}|^2+h^2}{4\kappa_j^2}\right)\,\cos\left(2\pi\mathbf{k}\cdot\mathbf{r}_j+hz_j\right)\\ -q_i\cos\left(2\pi\mathbf{k}\cdot\mathbf{r}_i+hz_i\right)\sum_j^N\boldsymbol{\mu}_j\cdot\left(2\pi\mathbf{k}+h\hat{\mathbf{z}}\right)\,\exp\left(\frac{-4\pi|\mathbf{k}|^2+h^2}{4\kappa_j^2}\right)\,\cos\left(2\pi\mathbf{k}\cdot\mathbf{r}_j+hz_j\right)\\ \left.-q_i\sin\left(2\pi\mathbf{k}\cdot\mathbf{r}_i+hz_i\right)\sum_j^N\boldsymbol{\mu}_j\cdot\left(2\pi\mathbf{k}+h\hat{\mathbf{z}}\right)\,\exp\left(\frac{-4\pi|\mathbf{k}|^2+h^2}{4\kappa_j^2}\right)\,\sin\left(2\pi\mathbf{k}\cdot\mathbf{r}_j+hz_j\right)\right\}\,\mathrm{d}h\end{aligned} \tag{3.42}$$

Dipole–dipole (k $\neq$ 0)

$$\mathbf{F}^{\mu-\mu}_{i,\text{recip}} = \frac{2}{ab}\sum_{k=-\infty}^{\infty}\sum_{l=-\infty}^{\infty}\int_{-\infty}^{\infty}\frac{2\pi k\hat{\mathbf{x}}/a + 2\pi l\hat{\mathbf{y}}/b + h\hat{\mathbf{z}}}{4\pi|\mathbf{k}|^2+h^2}\exp\left(\frac{-4\pi|\mathbf{k}|^2+h^2}{4\alpha^2}\right)\boldsymbol{\mu}_i\cdot(2\pi\mathbf{k}+h\hat{\mathbf{z}})$$
$$\times\left\{\sin\left(2\pi\mathbf{k}\cdot\mathbf{r}_i+hz_i\right)\sum_j^N\boldsymbol{\mu}_j\cdot(2\pi\mathbf{k}+h\hat{\mathbf{z}})\,\exp\left(\frac{-4\pi|\mathbf{k}|^2+h^2}{4\kappa_j^2}\right)\cos\left(2\pi\mathbf{k}\cdot\mathbf{r}_j+hz_j\right)\right.$$
$$\left.-\cos\left(2\pi\mathbf{k}\cdot\mathbf{r}_i+hz_i\right)\sum_j^N\boldsymbol{\mu}_j\cdot(2\pi\mathbf{k}+h\hat{\mathbf{z}})\,\exp\left(\frac{-4\pi|\mathbf{k}|^2+h^2}{4\kappa_j^2}\right)\sin\left(2\pi\mathbf{k}\cdot\mathbf{r}_j+hz_j\right)\right\}\,\mathrm{d}h \tag{3.43}$$

Charge–charge (k = 0)

$$\mathbf{F}_{i,\text{recip}} = \frac{2q_i}{ab}\sum_j^N q_j\pi\,\text{erf}\left(z_{ij}A_{ij}\right)\hat{\mathbf{z}} \tag{3.44}$$

Charge–dipole (k = 0)

$$\mathbf{F}^{q-\mu}_{i,\text{recip}}(\mathbf{k}=0) = \frac{4}{ab}\sum_j^N\exp\left(-z_{ij}^2A_{ij}^2\right)\sqrt{\pi}A_{ij}[q_j\mu_i^z - q_i\mu_j^z]\hat{\mathbf{z}} \tag{3.45}$$

Dipole–dipole (k = 0)

$$\mathbf{F}^{\mu-\mu}_{i,\text{recip}} = \frac{8}{ab}\sum_j^N z_{ij}A_{ij}^3\sqrt{\pi}\mu_i^z\mu_j^z\exp\left(-z_{ij}^2A_{ij}^2\right)\hat{\mathbf{z}} \tag{3.46}$$

3.4.2.3 Electric field

Charge contribution (k $\neq$ 0)

$$\mathbf{E}^{q}_{\text{i,recip}} = \frac{2}{ab}\sum_{k=-\infty}^{\infty}\sum_{l=-\infty}^{\infty}\int_{-\infty}^{\infty}\frac{1}{4\pi|\mathbf{k}|^2+h^2}\exp\left(\frac{-4\pi|\mathbf{k}|^2+h^2}{4\alpha^2}\right)$$
$$\times\left\{-\cos(2\pi\mathbf{k}\cdot\mathbf{r}_i+hz_i)\sum_j^N q_j\sin(2\pi\mathbf{k}\cdot\mathbf{r}_j+hz_j)\exp\left(\frac{-4\pi|\mathbf{k}|^2+h^2}{4\kappa_j^2}\right)\right. \tag{3.47}$$
$$\left.+\sin(2\pi\mathbf{k}\cdot\mathbf{r}_i+hz_i)\sum_j^N q_j\cos(2\pi\mathbf{k}\cdot\mathbf{r}_j+hz_j)\exp\left(\frac{-4\pi|\mathbf{k}|^2+h^2}{4\kappa_j^2}\right)\right\}\,\mathrm{d}h$$

Dipole contribution ($\mathbf{k} \neq 0$)

$$\begin{aligned}\mathbf{E}^{\mu}_{\mathrm{i,recip}} = -\frac{2}{ab}\sum_{k=-\infty}^{\infty}\sum_{l=-\infty}^{\infty}\int_{-\infty}^{\infty}\frac{1}{4\pi|\mathbf{k}|^2+h^2}\exp\left(\frac{-4\pi|\mathbf{k}|^2+h^2}{4\alpha^2}\right)\\ \times\left\{\cos\left(2\pi\mathbf{k}\cdot\mathbf{r}_i+hz_i\right)\sum_j^N\boldsymbol{\mu}_j\cdot\left(2\pi\mathbf{k}+h\hat{\mathbf{z}}\right)\cos\left(2\pi\mathbf{k}\cdot\mathbf{r}_j+hz_j\right)\exp\left(\frac{-4\pi|\mathbf{k}|^2+h^2}{4\kappa_j^2}\right)\right.\\ \left.\times\ \sin\left(2\pi\mathbf{k}\cdot\mathbf{r}_i+hz_i\right)\sum_j^N\boldsymbol{\mu}_j\cdot\left(2\pi\mathbf{k}+h\hat{\mathbf{z}}\right)\sin\left(2\pi\mathbf{k}\cdot\mathbf{r}_j+hz_j\right)\exp\left(\frac{-4\pi|\mathbf{k}|^2+h^2}{4\kappa_j^2}\right)\right\}\mathrm{d}h\end{aligned} \tag{3.48}$$

Charge contribution ($\mathbf{k} = 0$)

$$\mathbf{E}^{q}_{i,\mathrm{recip}}(\mathbf{k}=0) = \frac{2}{ab}\sum_j^N \pi\,\mathrm{erf}\left(z_{ij}A_{ij}\right)q_j \tag{3.49}$$

Dipole contribution ($\mathbf{k} = 0$)

$$\mathbf{E}^{\mu}_{i,\mathrm{recip}}(\mathbf{k}=0) = -\frac{4}{ab}\sum_j^N \mu_j^z A_{ij}\sqrt{\pi}\exp\left(-z_{ij}^2A_{ij}^2\right)\hat{\mathbf{z}} \tag{3.50}$$

3.4.2.4 Potential

Charge–charge ($\mathbf{k} \neq 0$)

$$\begin{aligned}V^{q-q}_{i,\mathrm{recip}} = \frac{2}{ab}\sum_{k=-\infty}^{\infty}\sum_{l=-\infty}^{\infty}\int_{-\infty}^{\infty}\frac{1}{4\pi|\mathbf{k}|^2+h^2}\exp\left(\frac{-4\pi|\mathbf{k}|^2+h^2}{4\alpha^2}\right)\\ \left\{\cos\left(2\pi\mathbf{k}\cdot\mathbf{r}_i+hz_i\right)\sum_j^N q_j\cos\left(2\pi\mathbf{k}\cdot\mathbf{r}_j+hz_j\right)\exp\left(\frac{-4\pi|\mathbf{k}|^2+h^2}{4\kappa_j^2}\right)\right.\\ \left.+\ \sin\left(2\pi\mathbf{k}\cdot\mathbf{r}_i+hz_i\right)\sum_j^N q_j\sin\left(2\pi\mathbf{k}\cdot\mathbf{r}_j+hz_j\right)\exp\left(\frac{-4\pi|\mathbf{k}|^2+h^2}{4\kappa_j^2}\right)\right\}\mathrm{d}h\end{aligned} \tag{3.51}$$

Charge–dipole ($\mathbf{k} \neq 0$)

$$V_{i,\mathrm{recip}}^{q-\mu} = \frac{2}{ab} \sum_{k=-\infty}^{\infty} \sum_{l=-\infty}^{\infty} \int_{-\infty}^{\infty} \frac{1}{4\pi|\mathbf{k}|^2 + h^2} \exp\left(\frac{-4\pi|\mathbf{k}|^2 + h^2}{4\alpha^2}\right) \times \left\{ \sin\left(2\pi\mathbf{k}\cdot\mathbf{r}_i + hz_i\right) \sum_j^N \boldsymbol{\mu}_j \cdot (2\pi\mathbf{k} + h\hat{\mathbf{z}}) \exp\left(\frac{-4\pi|\mathbf{k}|^2 + h^2}{4\kappa_j^2}\right) \cos\left(2\pi\mathbf{k}\cdot\mathbf{r}_j + hz_j\right) - \cos\left(2\pi\mathbf{k}\cdot\mathbf{r}_i + hz_i\right) \sum_j^N \boldsymbol{\mu}_j \cdot (2\pi\mathbf{k} + h\hat{\mathbf{z}}) \exp\left(\frac{-4\pi|\mathbf{k}|^2 + h^2}{4\kappa_j^2}\right) \sin\left(2\pi\mathbf{k}\cdot\mathbf{r}_j + hz_j\right) \right\} \mathrm{d}h \tag{3.52}$$

Charge–charge ($\mathbf{k} = 0$)

$$V_{i,\mathrm{recip}}^{q-q}(\mathbf{k}=0) = -\frac{2}{ab} \sum_j^N q_j \left\{ \frac{\sqrt{\pi}}{A_{ij}} \exp\left(-z_{ij}^2 A_{ij}^2\right) + z_{ij}\pi \operatorname{erf}\left(z_{ij}A_{ij}\right) \right\} \tag{3.53}$$

3.4.2.4.1 Charge–dipole ($\mathbf{k} = 0$)

$$V_{i,\mathrm{recip}}^{q-\mu}(\mathbf{k}=0) = \frac{2}{ab} \sum_j^N \pi \operatorname{erf}\left(z_{ij}A_{ij}\right) \mu_j^z \tag{3.54}$$

3.4.3 Self-energy corrections

3.4.3.1 Energy

Charge–charge

The reciprocal space expressions erroneously include part of the electrostatic interaction of each particle with itself. This contribution, which must be subtracted, may be determined by considering $U_{\mathrm{total}}^{q-q} - U_{\mathrm{real}}^{q-q}$ for a single particle:

$$\begin{aligned} U_{\mathrm{recip}}^{q-q} &= \lim_{r_{ij}\to 0} \left\{ \frac{q_i q_j}{2r_{ij}} - \frac{q_i q_j \operatorname{erfc}(A_{ij}r_{ij})}{2r_{ij}} \right\} \\ &= \lim_{r_{ij}\to 0} \left\{ q_i q_j \frac{\operatorname{erf}(A_{ij}r_{ij})}{2r_{ij}} \right\}. \end{aligned} \tag{3.55}$$

Employing the error function series expansion

$$A_{ij}\frac{\mathrm{erf}(A_{ij}r_{ij})}{A_{ij}r_{ij}} = \frac{2A_{ij}}{\sqrt{\pi}}\left(1 - \frac{(A_{ij}r_{ij})^2}{3} + \frac{(A_{ij}r_{ij})^4}{5} - \cdots\right) \tag{3.56}$$

we obtain the charge–charge self-energy for each melt ion:

$$U_{\mathrm{self}}^{q-q} = -\frac{\alpha q_i^2}{\sqrt{\pi}}, \tag{3.57}$$

and the charge–charge self-energy for each electrode atom:

$$U_{\mathrm{self}}^{q-q} = -\frac{\beta q_i^2}{\sqrt{\pi}}. \tag{3.58}$$

Dipole–dipole

We proceed in an analogous manner by considering the reciprocal space contribution as the difference $U_{\mathrm{total}}^{\mu-\mu} - U_{\mathrm{real}}^{\mu-\mu}$. Thus the term to be subtracted for each melt particle is found by taking the following limit:

$$\begin{aligned} U_{\mathrm{recip}}^{\mu-\mu} = \frac{1}{2}\lim_{r_{ij}\to 0}\Bigg\{ & -(\mu_{i\alpha}S_{ij}^{\alpha\beta}\mu_{j\beta}) \\ & \times \frac{1}{r_{ij}^2}\left[\alpha\frac{\mathrm{erf}(\alpha r_{ij})}{\alpha r_{ij}} - \frac{2\alpha}{\sqrt{\pi}}e^{-\alpha^2 r_{ij}^2}\right] \\ & + \frac{4\alpha^3}{\sqrt{\pi}}e^{-\alpha^2 r_{ij}^2}\frac{(\mathbf{r}_{ij}\cdot\boldsymbol{\mu}_i)(\mathbf{r}_{ij}\cdot\boldsymbol{\mu}_j)}{r_{ij}^2}\Bigg\}, \end{aligned} \tag{3.59}$$

where $S_{ij}^{\alpha\beta} = r_{ij}^3 T_{ij}^{\alpha\beta}$ is a tensor which has a well-defined limit when r_{ij} tends to zero. Expanding the exponentials ($e^{-\alpha^2 r^2} = 1 - \alpha^2 r^2 + \cdots$), and employing also the error function series expansion, we easily arrive at the dipole–dipole self-energy:

$$U_{\mathrm{self}}^{\mu-\mu} = \frac{2\alpha^3}{3\sqrt{\pi}}|\boldsymbol{\mu}_i|^2. \tag{3.60}$$

3.4.3.2 Electric field

If we express Equation 3.60 as

$$U_{\text{self}}^{\mu-\mu} = \frac{1}{2}\sum_i \left(-\mu_{i\alpha} E_{i\alpha}^{\text{self}}\right), \tag{3.61}$$

we obtain a self-correction for the electric field on particle i:

$$E_{i\alpha}^{\text{self}} = -\frac{4\alpha^3 \mu_{i\alpha}}{3\sqrt{\pi}}. \tag{3.62}$$

3.4.4 Polarization energy

The expressions obtained above are directly applicable to a set of rigid dipoles. However, by regarding the components of the dipoles as additional degrees of freedom to specify the instantaneous degree of polarization of a molecule, they may also be applied in the representation of the induction, or polarization, interactions in a polarizable system. In this case, we consider the total potential energy:

$$U = U_{\text{real}} + U_{\text{recip}} - U_{\text{self}} + U_{\text{pol}}, \tag{3.63}$$

where the first three terms have been defined previously and the last one is the polarization energy: [72]

$$U_{\text{pol}} = \sum_i \frac{|\boldsymbol{\mu}_i|^2}{2\alpha_i}, \tag{2.11}$$

which accounts for the energy cost of deforming the electron densities of the ions to create the induced dipoles, in a generalized Drude form. In this expression α_i is the polarizability of ion i, which we have assumed to be isotropic.

3.5 Empirical verification of equations

We indicated in the introduction to this chapter that the VBC model was inappropriate for the simulation of a 2D system containing isolated electrodes. We can however use it to validate

the coding of the melt–melt Ewald terms. This is because the 2D Ewald and VBC Ewald summations should generate the same results for a configuration containing only melt particles (*i.e.* in which the electrodes have been removed). We follow the VBC implementation of Yeh and Berkowitz [66], which has already been used in our group [73, 74, 75] to study liquid-vapour interfaces.

The melt system is made periodic in the z-direction and a slab of vacuum is added between the periodic images (see Figure 3.1). Spohr [76] has demonstrated that even with a vacuum length (d) which is four times that of the z-dimension of the cell (c), the system does not exhibit limiting behaviour. This is because a periodically replicated slab behaves like a slab of parallel plate capacitors. If the slab has a net dipole moment, there will be spurious electric fields between the periodic images of the slab. More significantly, the depolarizing field that prevails in a (periodic) slab geometry is not accounted for by the usual assumption that the system is embedded in a conducting sphere. Yeh and Berkowitz [66] have added a correction term to obtain the correct limiting behaviour in the limit of an infinitely thin slab. The following terms are added to the energy and forces resulting from the usual 3D Ewald sum:

$$U = \frac{2\pi}{V} M_z^2, \tag{3.64}$$

$$F_i^z = -\frac{4\pi q_i}{V} M_z, \tag{3.65}$$

where V is the volume of the simulation cell, and M_z is the z component of the total dipole moment of the simulation cell.

We first equilibrated a KCl melt at a density appropriate to 1300 K using the 2D periodic boundary code. The configuration at the end of the equilibration run was then used as the basis of a single step MD run using both the 2D and VBC codes. Table 3.1 lists for both methods the total coulombic energy, and the force and electric field at the site of a randomly-selected ion. The close agreement between the results from the two different Ewald summations validates our implementation of the melt–melt terms derived in this chapter.

To test the melt–wall expressions we placed a single polarizable test atom with no coulombic charge equidistant from two parallel metal surfaces. With an applied potential difference of zero

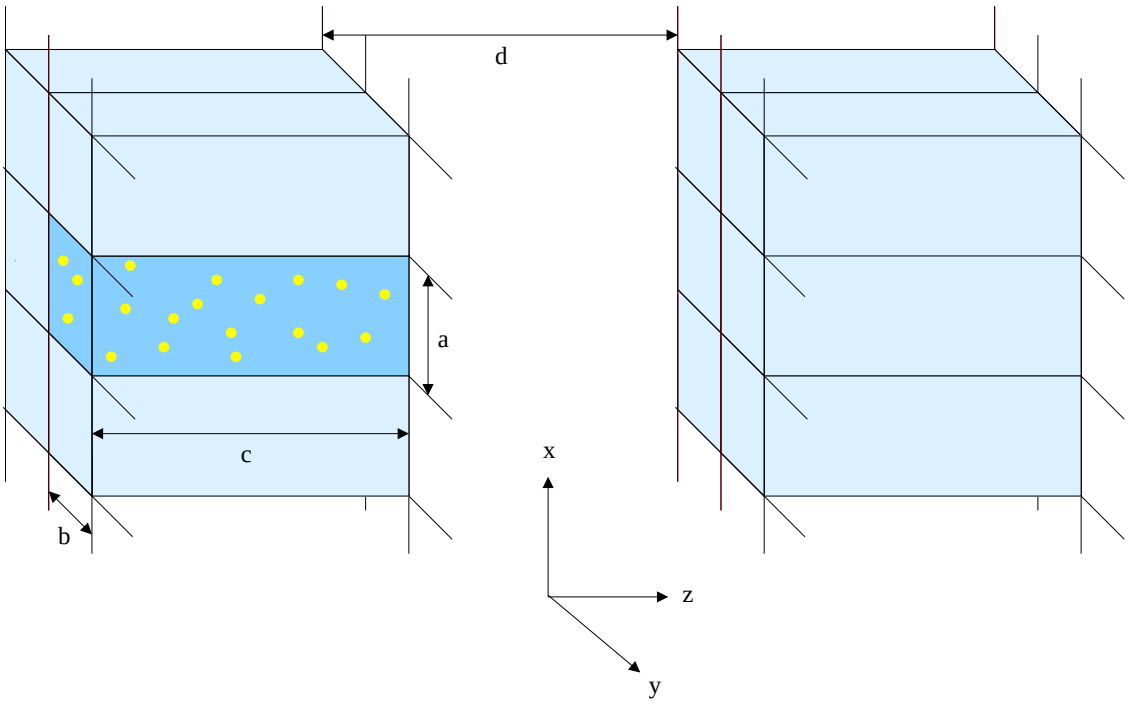

Figure 3.1: A vacuum region of length d is created on either side of the central simulation box in the z direction, and then the supercell is built by periodically replicating in all three directions.

	2D Ewald	3D Ewald
$\mathbf{F}_x$	-5.671148×10^{-3}	-5.671140×10^{-3}
$\mathbf{F}_y$	$+1.013566 \times 10^{-2}$	$+1.013560 \times 10^{-2}$
$\mathbf{F}_z$	$+7.022830 \times 10^{-2}$	$+7.022829 \times 10^{-2}$
$\mathbf{E}_x$	$+4.643222 \times 10^{-3}$	$+4.643215 \times 10^{-3}$
$\mathbf{E}_y$	-1.035659×10^{-2}	-1.035653×10^{-2}
$\mathbf{E}_z$	-7.119575×10^{-2}	-7.114496×10^{-2}
U_c	-7.0935229×10^{1}	-7.0935238×10^{1}

Table 3.1: A quantitative comparison of terms in: (i) a 2D Ewald summation and (ii) a 3D Ewald summation with conducting boundary conditions in the two lateral directions but vacuum boundary conditions in the perpendicular one. The forces and electric fields are associated with a randomly selected ion from an equilibrium MD configuration, and U_c is the total coulombic energy for the system. All quantities are in atomic units.

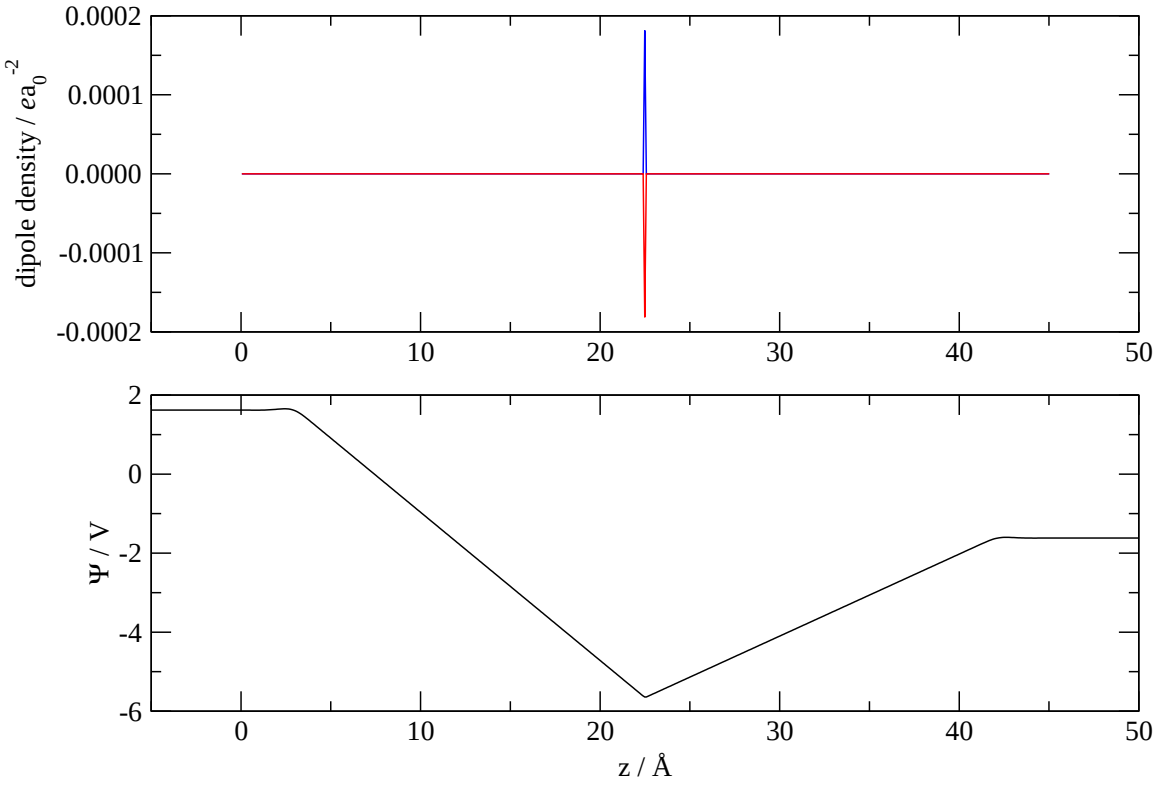

Figure 3.2: The top panel illustrates the dipole induced on a single polarizable atom (with no coulombic charge) placed equidistantly from two parallel metal surfaces held at an anode potential of $\Psi^+ = 1.63\,\mathrm{V}$ (blue) and $\Psi^+ = -1.63\,\mathrm{V}$ (red). The bottom panel shows the Poisson potential corresponding to the $\Psi^+ = 1.63\mathrm{V}$ case.

the ion does not acquire a dipole moment. The (left-hand) anode and (right-hand) cathode are then set respective potential values of $\Psi^+ = 1.63\,\mathrm{V}$ and $\Psi^- = -1.63\,\mathrm{V}$ and the resultant positive dipole moment on the test atom is evidenced by the blue line in the top panel in Figure 3.2. The anode and cathode were then switched around and the dipole moment remained of the same magnitude but with reversed direction (red line).

The bottom panel of Figure 3.2 displays the mean electrical (Poisson) potential for the single charge system. We first met the Poisson potential in Chapter 1 (see Equation 1.8), but we now have an additional contribution to the potential arising from the induced dipoles. The

potential difference across the simulation cell $\Delta\Psi(z)$ is now given by [77]:

$$\begin{aligned}\Delta\Psi(z) &= \Delta\Psi_{\mathrm{q}}(z) + \Delta\Psi_{\boldsymbol{\mu}}(z) \\ &= -\int_{z_0}^{z} \mathbf{E}(z')\mathrm{d}z' + \frac{1}{\epsilon_0}\int_{z_0}^{z} \rho_{\boldsymbol{\mu}}(z')\mathrm{d}z',\end{aligned} \tag{3.66}$$

where the electrostatic field $\mathbf{E}$ is computed using Gauss's theorem,

$$\mathbf{E}(z) = \frac{1}{\epsilon_0}\int_{-\infty}^{z} \rho_{\mathrm{q}}(z')\mathrm{d}z'. \tag{3.67}$$

We can predict a value for the induced dipole through the expression $\mu^z = \alpha \cdot (\Delta\Psi/d)$, where d is the inter-electrode spacing, α the polarizability, and $\Delta\Psi$ the potential difference across the cell (obtained from the Poisson plot in Figure 3.2). This predicts a dipole $\mu^z = 0.014755\,\mathrm{a.u.}$ The dipole obtained from the Ewald electric field compares well: $\mu^z = \alpha \cdot E^z = 0.014746\,\mathrm{a.u.}$

Although such agreement indicates that the long-range melt–wall interactions are correct, there are no short-range effects here. The nature of the metal–salt interface was first examined by sandwiching a perfect KCl crystal between the two parallel metal plates with an applied potential of $\Psi^+ = 1.63\,\mathrm{V}$. With *no coulombic charges on the melt ion sites* and allowing only the anions to polarize, the resulting dipole density in the top panel of Figure 3.3 betrays a distance-independent electric field strength. The lower panel of Figure 3.3 breaks down the Poisson profile into its charge and dipole contributions. As the melt charges have been set to zero, the only charges in the system are on the electrode atoms, and consequently the second integral over the charge density is a line of constant gradient. The dipole contribution is a step function because the KCl is in a crystalline phase.

We now reset the melt ion coulombic charges to their usual values ($q_{\mathrm{K}^+} = +e$; $q_{\mathrm{Cl}^-} = -e$), and recalculate the anion dipoles. As demonstrated in Figure 3.4, the anions in the two layers adjacent to the electrodes exhibit dipoles differentiated from those of the bulk. This is due to the arrangement of the ions close to the interface. There is a slight displacement of the Cl^- ions in the outermost layers towards their respective adjacent electrodes, perhaps because an excess of polarizable particles at an interface lowers the surface energy [75]. This local violation of the

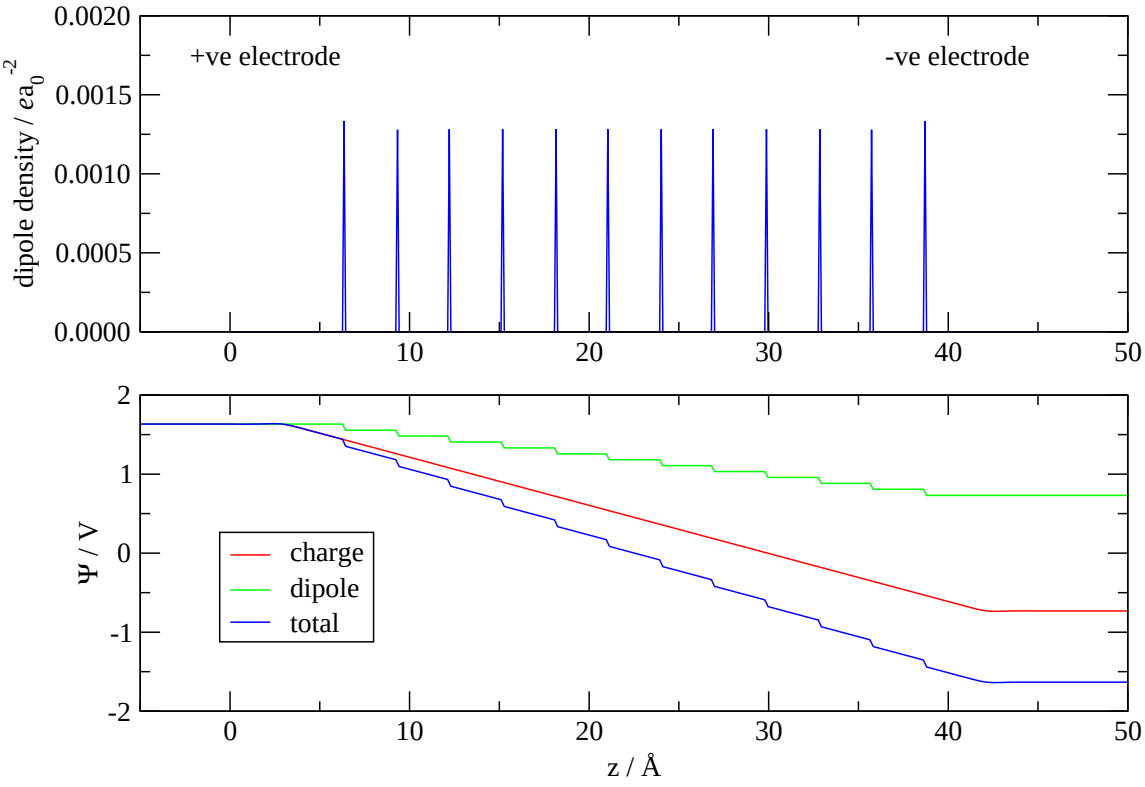

Figure 3.3: In the top panel is the dipole density of a perfect KCl crystal (with the coulombic charges switched off) sandwiched between two metal walls held at an anode potential of $\Psi^+ = 1.63\,\mathrm{V}$. Only the anion sites are polarizable. The bottom panel shows the Poisson potential for the system.

electroneutrality condition leads to the induced dipoles on the anions in these outermost layers having their negative ends pointing towards the bulk. The same phenomenon was observed by Salanne *et al.* [78] in their studies of molten $LiBeF_3$.

The ultimate empirical verification of the self-consistency of the force and energy expressions in the Ewald equations is the conservation of the total energy of the system during an MD run. Figure 3.5 demonstrates that (i) fluctuations in the energy typically have a magnitude of less than $1 \times 10^{-2}\,E_\mathrm{h}$; and (ii) there is no drift in the mean energy over runs of more than 100 ps in length.

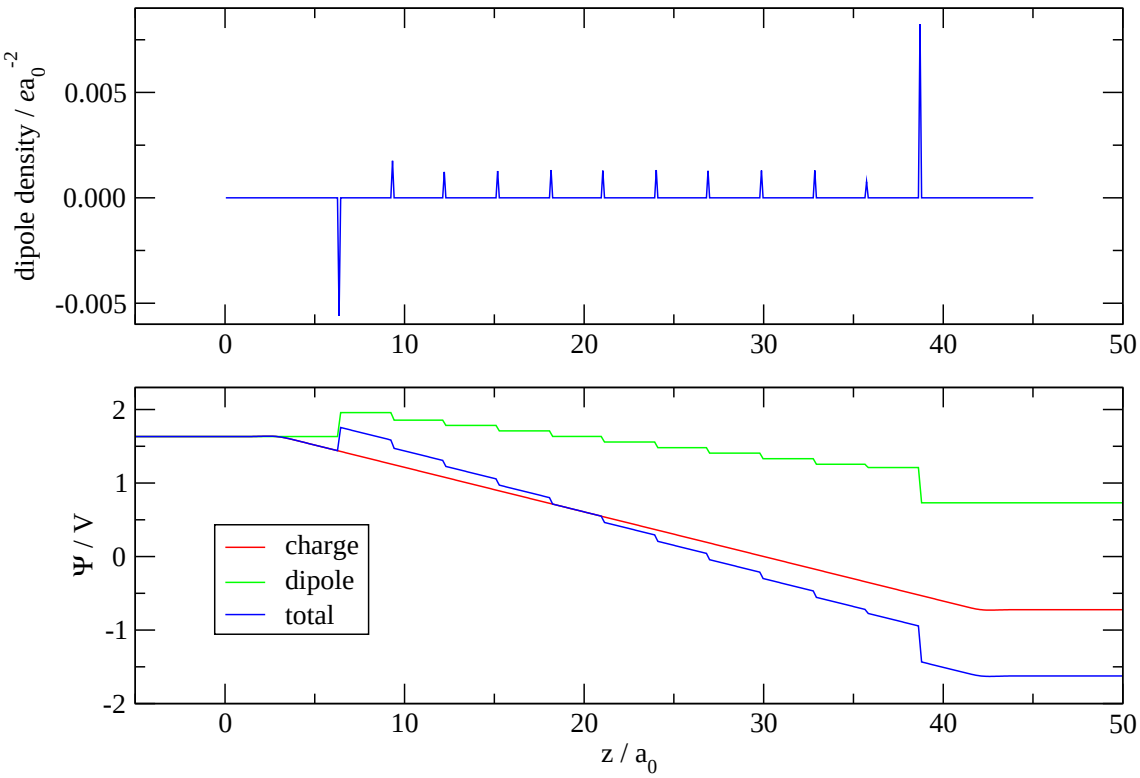

Figure 3.4: The dipole density (top) and Poisson potential (bottom) for a perfect KCl crystal sandwiched between two metal walls held at an anode potential of $\Psi^+ = 1.63\,\mathrm{V}$. This is the same system as represented in Figure 3.3 but with the coulombic charges associated with each site in the KCl lattice turned back on.

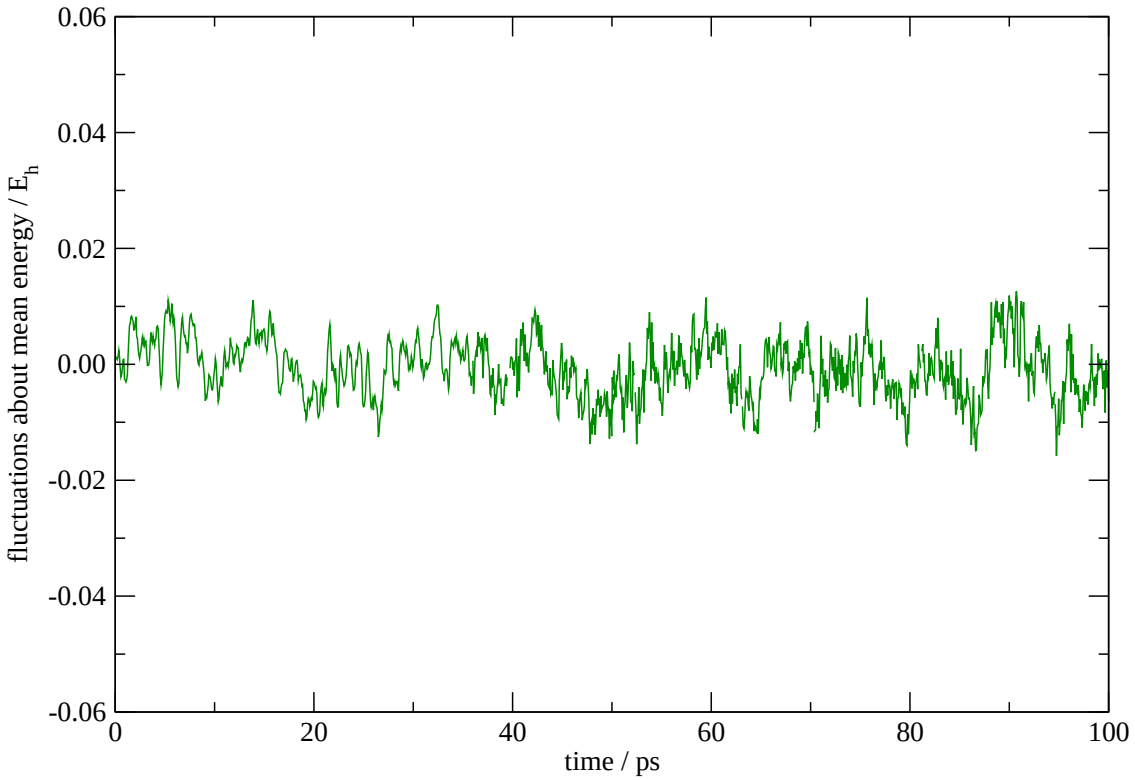

Figure 3.5: Fluctuations in the energy typically have a magnitude of less than $1 \times 10^{-2}\, E_\mathrm{h}$, and there is no drift in the mean energy over runs of more than 100 ps in length.

4

Redox potentials and energy gaps

4.1 Introduction

A major concern of the work presented in this thesis is the calculation of the Marcus diabatic surfaces for our molten salt system to enable the characterization of the factors affecting the rate of electron transfer reactions at the electrochemical interface. A central tenet of the original Marcus construction is that the reaction coordinate reflects the arrangement of the coordinating species around the electroactive ion. Although it is presumably possible to determine a ground state observable to incorporate all relevant aspects of the solvent response, for diabatic electron transfer the vertical energy gap between the two reactant surfaces is an ideal reaction coordinate. This was first exploited in computer simulation by Warshel [79] and more recently by Blumberger et al. [80], which latter review we here follow closely.

4.2 The diabatic energy gap

Consider a two state electronic system defined by the Hamiltonian $\hat{\mathrm{H}} = \hat{\mathrm{H}}_0 + \hat{\mathrm{H}}'$ where $\hat{\mathrm{H}}_0$ is the unperturbed Hamiltonian:

$$\hat{\mathrm{H}}_0 = \begin{pmatrix} E_{\mathrm{A}}(\mathbf{R}^N) & 0 \\ 0 & E_{\mathrm{B}}(\mathbf{R}^N) \end{pmatrix}, \tag{4.1}$$

and $\hat{\mathrm{H}}'$ is the perturbation Hamiltonian:

$$\hat{\mathrm{H}}' = \begin{pmatrix} 0 & \gamma(\mathbf{R}^N) \\ \gamma(\mathbf{R}^N) & 0 \end{pmatrix}. \tag{4.2}$$

The two diagonal elements of $\hat{\mathrm{H}}_0$ represent the diabatic potential energy surface (PES) of reactant A and product B where $\mathbf{R}^N$ are the atomic positions of all N atoms in the system. The diabatic states are coupled by the off-diagonal matrix element γ which depends on the overlap between the electron wavefunctions in reactant and product states and will decrease exponentially with the distance between donor and acceptor. This is a measure of the propensity in our system for the electron to tunnel between the redox ion and the electrode. The vertical energy gap between the two electronic states is the difference between the diagonal matrix elements of Equation 4.1:

$$\Delta E(\mathbf{R}^N) = E_{\mathrm{B}}(\mathbf{R}^N) - E_{\mathrm{A}}(\mathbf{R}^N). \tag{4.3}$$

The solutions to Schrödinger's equation for $\hat{\mathrm{H}}_0$ are known to be

$$\hat{\mathrm{H}}_0'\psi_{\mathrm{A}} = E_{\mathrm{A}}\psi_{\mathrm{A}}, \tag{4.4}$$

$$\hat{\mathrm{H}}_0'\psi_{\mathrm{B}} = E_{\mathrm{B}}\psi_{\mathrm{B}}, \tag{4.5}$$

where $E_{\mathrm{A}} \neq E_{\mathrm{B}}$. The exact solutions $|\phi\rangle$ of

$$\left(\hat{\mathrm{H}}_0 + \hat{\mathrm{H}}'\right)|\phi\rangle = E\,|\phi\rangle\,, \tag{4.6}$$

can be expanded to give

$$|\phi\rangle = c_{\mathrm{A}}\,|\psi_{\mathrm{A}}\rangle + c_{\mathrm{B}}\,|\psi_{\mathrm{B}}\rangle\,, \tag{4.7}$$

Substituting Equation 4.7 into Equation 4.6 gives

$$c_{\mathrm{A}}\left(E_{\mathrm{A}} + \hat{\mathrm{H}}'\right)|\psi_{\mathrm{A}}\rangle + c_{\mathrm{B}}\left(E_{\mathrm{B}} + \hat{\mathrm{H}}'\right)|\psi_{\mathrm{B}}\rangle = E\left(c_{\mathrm{A}}\,|\psi_{\mathrm{A}}\rangle + c_{\mathrm{B}}\,|\psi_{\mathrm{B}}\rangle\right). \tag{4.8}$$

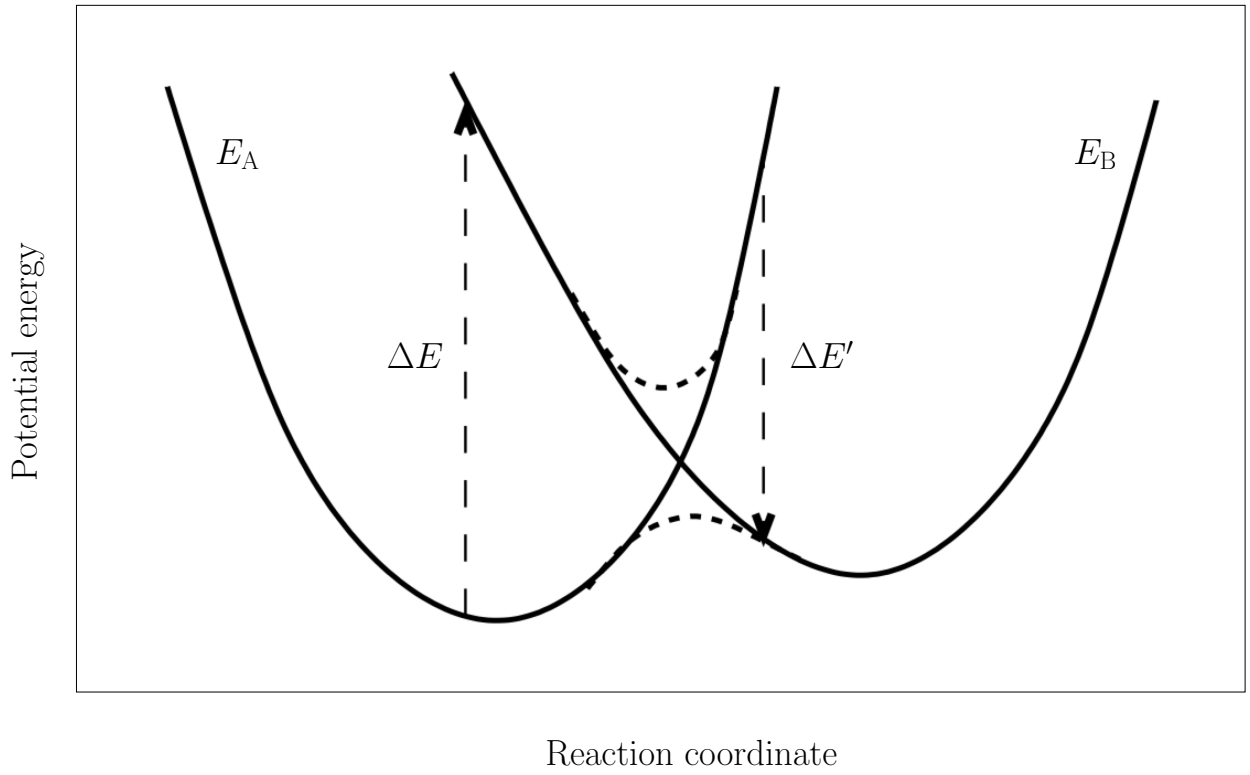

Figure 4.1: The diabatic (solid lines) and adiabatic (dashed lines) potential energy surfaces of two electronic states A and B. The arrow represents the vertical diabatic energy gap defined in Equation 4.3.

Taking the inner product with $\langle\psi_{\mathrm{A}}|$ and $\langle\psi_{\mathrm{B}}|$ in turn gives

$$c_{\mathrm{A}}\left(E_{\mathrm{A}}-E\right)+c_{\mathrm{B}}\gamma=0, \tag{4.9}$$

$$c_{\mathrm{B}}\left(E_{\mathrm{B}}-E\right)+c_{\mathrm{A}}\gamma=0. \tag{4.10}$$

We now eliminate c_{A} and c_{B}:

$$\left(E_{\mathrm{A}}-E\right)\left(E_{\mathrm{B}}-E\right)=\gamma^2, \tag{4.11}$$

which is quadratic in E

$$E^2-E\left(E_{\mathrm{A}}+E_{\mathrm{B}}\right)-\gamma^2+E_{\mathrm{A}}E_{\mathrm{B}}=0, \tag{4.12}$$

with the exact solutions

$$E=\frac{E_{\mathrm{A}}+E_{\mathrm{B}}\pm\sqrt{\left(E_{\mathrm{A}}-E_{\mathrm{B}}\right)^2+4\gamma^2}}{2}. \tag{4.13}$$

We thus arrive at the adiabatic energy gap

$$\Delta E=\sqrt{\left(E_{\mathrm{A}}-E_{\mathrm{B}}\right)^2+4\gamma^2}. \tag{4.14}$$

If the off-diagonal matrix element $\hat{\mathrm{H}}'_{\mathrm{AB}}=\hat{\mathrm{H}}'_{\mathrm{BA}}=\gamma$ is small, the diabatic energy gap of Equation 4.3 can be equated with the adiabatic energy gap of Equation 4.14.

4.3 Reaction free energy

The diabatic formalism illustrated in Figure 4.1 consists of two independent potential energy surfaces and leads to two separate free energy profiles. The total free energy is defined as

$$A_{\mathrm{M}}=-k_{\mathrm{B}}T\ln\Lambda^{-3N}\int\mathrm{d}\mathbf{R}^N\exp\left[-\beta E_{\mathrm{M}}(\mathbf{R}^N)\right], \tag{4.15}$$

where $\mathrm{M}=\mathrm{A},\mathrm{B}$. E_{A} and E_{B} are the respective diabatic potential energy surfaces of state A and state B, and Λ is the average thermal wavelength $\Lambda^{-3N}=\Pi_j\lambda_j^{-3N_j}/N_j!$ with $\lambda_j=h/\sqrt{2\pi m_j k_{\mathrm{B}}T}$

the thermal wavelength of the nuclear species j. The free energy change is linked to a ratio of partition functions:

$$\Delta A = A_{\mathrm{B}} - A_{\mathrm{A}} = -k_{\mathrm{B}}T \ln \frac{\int \mathrm{d}\mathbf{R}^N \exp\left[-\beta E_{\mathrm{B}}(\mathbf{R}^N)\right]}{\int \mathrm{d}\mathbf{R}^N \exp\left[-\beta E_{\mathrm{A}}(\mathbf{R}^N)\right]}, \tag{4.16}$$

where as in Equation 4.15 the integration is over the full configuration space.

The computation of the free energy profiles $A_{\mathrm{M}}(x), \mathrm{M} = \mathrm{A}, \mathrm{B}$ necessitates the specification of an order parameter $X(\mathbf{R}^N)$ and the integration in Equation 4.15 must now be restricted to configurations with $X(\mathbf{R}^N) = x$:

$$A_{\mathrm{M}}(x) = -k_{\mathrm{B}}T \ln \Lambda^{-3N} \int \mathrm{d}\mathbf{R}^N \exp\left[-\beta E_{\mathrm{M}}(\mathbf{R}^N)\right] \delta\left(X(\mathbf{R}^N) - x\right), \tag{4.17}$$

where the Dirac delta function $\delta\left(X(\mathbf{R}^N) - x\right)$ effects the restriction of the integration over configuration space. The probability distribution $p_{\mathrm{M}}(x)$ can be defined by a similar integral normalized by the unrestricted partition function:

$$p_{\mathrm{M}}(x) = \frac{\int \mathrm{d}\mathbf{R}^N \exp\left[-\beta E_{\mathrm{M}}(\mathbf{R}^N)\right] \delta\left(X(\mathbf{R}^N) - x\right)}{\int \mathrm{d}\mathbf{R}^N \exp\left[-\beta E_{\mathrm{M}}(\mathbf{R}^N)\right]} = \langle \delta(X - x) \rangle_{\mathrm{M}}. \tag{4.18}$$

Equations 4.17 and 4.18 enable us to recast the definition of the diabatic free energy in Equation 4.15 into a form suitable for computation:

$$A_{\mathrm{M}}(x) = -k_{\mathrm{B}}T \ln p_{\mathrm{M}}(x) + A_{\mathrm{M}}. \tag{4.19}$$

The free energy profiles are shown in Figure 1.14 (with A = Ox and B = Red). If the location of the minima are denoted respectively as x_{A} and x_{B} then the reorganization free energies λ can be written as

$$\lambda_{\mathrm{A}} = A_{\mathrm{A}}(x_{\mathrm{B}}) - A_{\mathrm{A}}(x_{\mathrm{A}}), \tag{4.20}$$

$$\lambda_{\mathrm{B}} = A_{\mathrm{B}}(x_{\mathrm{A}}) - A_{\mathrm{B}}(x_{\mathrm{B}}), \tag{4.21}$$

and $\lambda_{\mathrm{A}} = \lambda_{\mathrm{B}}$ in Marcus theory (see Section 4.4). The difference between the stable minima of the $A_{\mathrm{M}}(x)$ surfaces determines the reaction free energy change:

$$\Delta A_x = A_{\mathrm{B}}(x_{\mathrm{B}}) - A_{\mathrm{A}}(x_{\mathrm{A}}), \tag{4.22}$$

and the activation free energy for the forward (M = A) and backward (M = B) reaction is

$$\Delta A^{\dagger}_{\mathrm{M}} = A_{\mathrm{M}}\left(x^{\dagger}\right) - A_{\mathrm{M}}\left(x_{\mathrm{M}}\right), \tag{4.23}$$

where $x^{\dagger}$ is the value of the reaction coordinate at the intersection of the diabatic curves.

4.4 Free energy perturbation method

We can substitute a rearranged Equation 4.3 into the Boltzmann factor of Equation 4.16 to generate the free energy perturbation expression

$$\Delta A = -\frac{1}{\beta} \ln \frac{\int \mathrm{d}\mathbf{R}^N \exp\left(-\beta \Delta E\right) \exp\left(-\beta E_{\mathrm{A}}\right)}{\int \mathrm{d}\mathbf{R}^N \exp\left(-\beta E_{\mathrm{A}}\right)}, \tag{4.24}$$

$$= -\frac{1}{\beta} \ln \left\langle e^{-\beta \Delta E} \right\rangle_{\mathrm{A}}, \tag{4.25}$$

$$= \frac{1}{\beta} \ln \left\langle e^{\beta \Delta E} \right\rangle_{\mathrm{B}}, \tag{4.26}$$

where $\langle \cdots \rangle_{\mathrm{M}}$ represents the canonical average over the PES of state M = A, B. A perfunctory look at Figure 4.1 highlights the uselessness of this profound expression in MD simulation. The configurations visited by a trajectory in state A will generate large positive values of ΔE and a concomitant vanishing exponential weight in Equation 4.25. The ΔE values for equilibrium configurations of state B are contrariwise large and negative resulting in a huge exponent. In other words the unequal canonical averages in Equations 4.25 and 4.26 are a manifestation of the ubiquitous problem in free energy calculations, namely that there is no overlap between regions in configuration space accessible by thermal fluctuations of the equilibrium reactant and product.

The diabatic formalism provides a solution to this problem. We follow a similar derivation to that of Equations 4.25 and 4.26 to relate the order parameter probability distribution of one diabatic state to the other:

$$\begin{aligned}
\frac{p_{\mathrm{B}}(x)}{p_{\mathrm{A}}(x)} &= \frac{\int \mathrm{d}\mathbf{R}^N \exp\left[-\beta E_{\mathrm{B}}(\mathbf{R}^N)\right] \delta\left(X(\mathbf{R}^N) - x\right)}{\int \mathrm{d}\mathbf{R}^N \exp\left[-\beta E_{\mathrm{B}}(\mathbf{R}^N)\right]} \cdot \frac{\int \mathrm{d}\mathbf{R}^N \exp\left[-\beta E_{\mathrm{A}}(\mathbf{R}^N)\right]}{\int \mathrm{d}\mathbf{R}^N \exp\left[-\beta E_{\mathrm{A}}(\mathbf{R}^N)\right] \delta\left(X(\mathbf{R}^N) - x\right)} \\
&= \frac{\int \mathrm{d}\mathbf{R}^N \exp\left[-\beta E_{\mathrm{A}}(\mathbf{R}^N)\right]}{\int \mathrm{d}\mathbf{R}^N \exp\left[-\beta E_{\mathrm{A}}(\mathbf{R}^N)\right]} \cdot \frac{\int \mathrm{d}\mathbf{R}^N \exp\left[-\beta E_{\mathrm{B}}(\mathbf{R}^N)\right] \delta\left(X(\mathbf{R}^N) - x\right)}{\int \mathrm{d}\mathbf{R}^N \exp\left[-\beta E_{\mathrm{B}}(\mathbf{R}^N)\right]} \cdot \frac{1}{\langle \delta(X-x) \rangle_{\mathrm{A}}} \\
&= e^{\beta \Delta A} \cdot \frac{\left\langle e^{-\beta \Delta E} \delta\left(X(\mathbf{R}^N) - x\right) \right\rangle_{\mathrm{A}}}{\langle \delta(X-x) \rangle_{\mathrm{A}}}. \qquad (4.27)
\end{aligned}$$

Equations 4.27 and 4.19 enable us to write

$$A_{\mathrm{B}}(x) - A_{\mathrm{A}}(x) = -k_{\mathrm{B}} T \ln \left[\frac{\left\langle e^{-\beta \Delta E} \delta(X-x) \right\rangle_{\mathrm{A}}}{\langle \delta(X-x) \rangle_{\mathrm{A}}} \right]. \qquad (4.28)$$

If we identify the reaction coordinate with the energy gap (by setting $\Delta E = X$) we can take the exponent outside the configurational integral to give the Zwanzig relation

$$A_{\mathrm{B}}(\epsilon) - A_{\mathrm{A}}(\epsilon) = \epsilon, \qquad (4.29)$$

where ϵ denotes a given value of the gap ΔE. Thus by the addition of ϵ to the free energy curve of the reactant we obtain the free energy curve of the product. Equation 4.29 yields a computationally useful expression of the reorganization energies if we substitute in Equations 4.20 and 4.21:

$$\lambda_{\mathrm{A}} = +\Delta A_{\epsilon} - \epsilon_{\mathrm{B}}, \qquad (4.30)$$

$$\lambda_{\mathrm{B}} = -\Delta A_{\epsilon} + \epsilon_{\mathrm{A}}, \qquad (4.31)$$

where ΔA_{ϵ} is the reaction free energy determined by the minima of the $A_{\mathrm{M}}(\epsilon)$ curves at ϵ_{A} and ϵ_{B}. Equations 4.30 and 4.31 provide a route to the reorganization energy from the equilibrium values of the diabatic gap which can be practically equated with the average gap in the reactant

and product state. Equations 4.30 and 4.31 also intimate that

$$\epsilon_{\mathrm{B}} < \Delta A_{\epsilon} < \epsilon_{\mathrm{A}}, \tag{4.32}$$

because reorganization energies are by definition positive. Thus the equilibrium energy gaps set a lower and upper bound to the reaction free energy change. In the diabatic approximation the electron transfer takes place at $\epsilon^{\dagger} = 0$ such that we can use Equation 4.23 to write

$$\Delta A^{\dagger}_{\mathrm{M}} = A_{\mathrm{M}}(\epsilon = 0) - A_{\mathrm{M}}(\epsilon_{\mathrm{M}}). \tag{4.33}$$

There is an assumption within Marcus theory that the medium surrounding the redox ion responds linearly to the change in charge and interaction potentials upon excitation. This is consistent with taking the probability distribution for the energy gap defined by Equation 4.18 as a Gaussian

$$p_{\mathrm{M}}(\epsilon) = \frac{1}{\sqrt{2\pi}\sigma_{\mathrm{M}}} \exp\left[-(\epsilon - \epsilon_{\mathrm{M}})^2 / \left(2\sigma^2_{\mathrm{M}}\right)\right], \tag{4.34}$$

which we can substitute into Equation 4.19 to generate the parabolic Marcus curves

$$A_{\mathrm{M}}(\epsilon) = A^{\epsilon}_{\mathrm{M}} + \frac{k_{\mathrm{B}}T}{2\sigma^2_{\mathrm{M}}}\left(\epsilon - \epsilon_{\mathrm{M}}\right)^2, \tag{4.35}$$

where the minimum free energy $A^{\epsilon}_{\mathrm{M}}$ is given by

$$A^{\epsilon}_{\mathrm{M}} = A_{\mathrm{M}} + \frac{k_{\mathrm{B}}T}{2} \ln\left[2\pi\sigma^2_{\mathrm{M}}\right]. \tag{4.36}$$

The Gaussians of Equation 4.34 are characterized by maxima at

$$\epsilon_{\mathrm{M}} = \langle \Delta E \rangle_{\mathrm{M}}, \tag{4.37}$$

and are of variance

$$\sigma^2_{\mathrm{M}} = \left\langle \left(\Delta E - \langle \Delta E \rangle_{\mathrm{M}}\right)^2 \right\rangle_{\mathrm{M}}. \tag{4.38}$$

Equation 4.29 dictates that the free energy functions for vertical gaps can differ only by a linear term. Thus the quadratic terms in the free energy functions must cancel:

$$\sigma_{\mathrm{A}}^2 = \sigma_{\mathrm{B}}^2 = 2k_{\mathrm{B}}T\lambda'. \tag{4.39}$$

The second identity defines the linear response reorganization free energy λ' and is a consequence of the Gaussian approximation. The constraints imposed by Equation 4.29 on the linear coefficients in Equation 4.35 require that

$$\lambda' = \frac{1}{2}\left(\epsilon_{\mathrm{A}} - \epsilon_{\mathrm{B}}\right). \tag{4.40}$$

Substituting Equations 4.40 and 4.35 into Equation 4.30 results in

$$\lambda_{\mathrm{A}} = \frac{1}{4\lambda'}\left(\epsilon_{\mathrm{A}} - \epsilon_{\mathrm{B}}\right)^2 = \lambda' = \lambda. \tag{4.41}$$

The same result is found for the λ_{B} of Equation 4.31. Such simplifications afforded by the Gaussian approximation extend to an equation of the reaction free energies ΔA and ΔA_ϵ defined respectively in Equations 4.16 and 4.22. Rearrangement of Equations 4.30 and 4.31 then yields

$$\Delta A = \frac{1}{2}\left(\epsilon_{\mathrm{A}} + \epsilon_{\mathrm{B}}\right), \tag{4.42}$$

$$\lambda = \frac{1}{2}\left(\epsilon_{\mathrm{A}} - \epsilon_{\mathrm{B}}\right). \tag{4.43}$$

4.5 Computational details

Figure 4.2 illustrates how the vertical energy gap for oxidation ($\delta E_{\mathrm{Eu}^{2+}\rightarrow\mathrm{Eu}^{3+}+\delta q(\Psi)}$) can be calculated in a simulation. A Eu^{2+} ion is selected from a configuration $\mathbf{R}^N$ of an MD trajectory maintained at an electrical potential difference $\Delta\Psi$ and its ionic charge and interaction potentials are converted to those appropriate to a Eu^{3+} ion. The constant potential condition is then

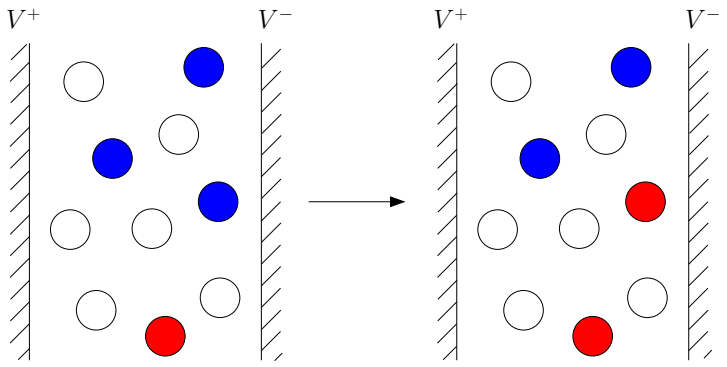

Figure 4.2: Illustration of the diabatic electron transfer step in a simulation of an $K_3\,Eu^{3+}_{0.5}\,Eu^{2+}_{0.5}\,Cl_{5.5}$ system confined between positive and negative electrodes. The Eu^{2+} ions are coloured blue, the Eu^{3+} red, and the unshaded circles are K^+ and Cl^- ions. The left hand panel illustrates a configuration from a normal MD run in which an Eu^{2+} ion is selected and converted into Eu^{3+} (right hand panel) without moving any of the ions but allowing re-equilibration of the anion dipoles and electrode charges which re-establishes the constant potential condition in an overall uncharged simulation cell. The difference between the interaction energies in the two configurations is the δE value for that particular configuration.

restored by minimizing the energy with respect to the melt dipoles and electrode charges whilst keeping the configuration $\mathbf{R}^N$ fixed. The vertical energy gap corresponds to the energy difference between the two arrangements. This energy minimization was discussed in Section 2.3, where we noted that the electrodes become polarised in the presence of a charge in the melt region in a way which corresponds to the classical image charge response.

Equation 4.19 above shows that the Marcus diabatic free energy curves can be obtained from the probability distribution of the vertical energy gaps, which in turn is obtained by sampling excitations over many configurations $\mathbf{R}^N$. After each potential switching operation, the simulation is returned to its initial pre-switching state, and the MD trajectory run on before repeating the switching procedure to build up a histogram of δE values. The free energy surface $\Delta A_{Eu^{2+}}(\Delta E)$ for the initial state in the oxidation step is obtained from the probability distribution $P_{Eu^{2+}}(\Delta E = \delta E_{Eu^{2+}\rightarrow Eu^{3+}+\delta q(\Psi)} + I + \delta q\, W)$ through

$$A_{Eu^{2+}}(\Delta E) = -k_B T \ln P_{Eu^{2+}}(\Delta E = \delta E_{Eu^{2+}\rightarrow Eu^{3+}+\delta q(\Psi)} + I + \delta q\, W) + A_{Eu^{2+}}, \qquad (4.44)$$

where $A_{Eu^{2+}}$ corresponds to the total free energy defined by Equation 4.15. I and W are respectively the ionization energy of Eu^{2+} and the work function of the metal from which the

electrode is made. In Chapter 6 we will obtain a value for $I + \delta q\, W$ by matching the computed reaction free energy with experimental values for the redox potential relevant to our system. By sampling the energy gaps for Eu^{2+} ions at a given distance from the electrode we can probe the d-dependent Marcus curves.

The reaction coordinate is defined as the energy gap for oxidation and so the reaction coordinate for reduction is given by minus the energy difference between the final and initial states:

$$A_{\mathrm{Eu}^{3+}+\delta q(\Psi)}(\Delta E) = -k_{\mathrm{B}}T \ln P_{\mathrm{Eu}^{3+}+\delta q(\Psi)}(\Delta E = -\delta E_{\mathrm{Eu}^{3+}+\delta q(\Psi)\rightarrow \mathrm{Eu}^{2+}} + I + \delta q\, W) + A_{\mathrm{Eu}^{3+}+\delta q(\Psi)}. \tag{4.45}$$

We then use Equation 4.29 to characterize the free energy surfaces away from the stable configurations by calculating the energy gap in the free-running simulation, and Equations 4.42 and 4.43 as a convenient route to the free energy ΔA and the reorganization energy λ.

5

The structure of $K_3Eu^{2+}_{0.5}Eu^{3+}_{0.5}Cl_{5.5}$

5.1 Introduction

If a species is to participate in reduction or oxidation at an electrode it must migrate to the interface (where the tunneling matrix element γ is sufficiently large) and adjust its coordination sphere as it receives or discards electrons. In Chapter 1 we introduced the Marcus expression for the heterogeneous rate constant appropriate to the fast diffusion limit:

$$k(\Psi, z) = \frac{\rho_i(z, \Psi)}{\rho_i(\infty)} \gamma(z)^2 \upsilon_n \exp\left[\frac{-\Delta A^{\dagger}(\Psi, z)}{RT}\right]. \qquad [1.56]$$

The exponential term in Equation 1.56 represents the contribution to the total rate constant from the reorganization of the coordination sphere, and this is the subject of Chapter 6. The present chapter concerns itself with the calculation of the concentration factor $\frac{\rho_i(z,\Psi)}{\rho_i(\infty)}$ in Equation 1.56, which in essence reflects the probability of finding an ion at a position z. And by expressing it as a free energy we can study (Section 5.7) how the rate of diffusion between the interfacial region and the bulk is affected by the ordering of the ions imposed by the electrode surface. We also seek to characterise the interfacial region by computing its differential capacitance (Section 5.5) and explore the effect of its structure on the electrical potential across the cell (Section 5.4).

5.2 Simulation details

The simulation cell consists of 352 Cl^- ions, 32 Eu^{2+} ions, 32 Eu^{3+} ions, and 192 K^+ ions at a density appropriate to a temperature of 1300 K. The two model electrodes are arranged as parallel plates separated by a distance of 49.0 Å. Each electrode contains three layers of atoms carrying variable charges arranged in the face centred cubic lattice with the (100) face exposed. The lattice parameter is 3.9 Å and each wall contains 216 atoms such that the simulation cell has dimensions of $a = 23.7$ Å, $b = 23.7$ Å, $c = 56.9$ Å. An equilibrated configuration is illustrated in Figure 5.3.

The parameters governing the interaction potential are given in Tables 5.1 and 5.2. The melt–melt parameters are taken from previous work[1] [49], to which we needed to add interactions between the melt ions and the wall. Guymon *et al.* [82] have performed *ab initio* calculations of copper clusters interacting with NaCl. They also developed a classical simulation method not dissimilar to the one presented in Chapter 2 which incorporates both the image charge effect and uses pairwise additive potentials. They then fitted a modified Morse potential,

$$U(r) = -\epsilon \left(1 - \{1 - \exp[-A(r - r^*)]\}^2\right), \tag{5.1}$$

to the difference between the *ab initio* and the coulombic part of the classical interactions. We subsequently fitted a Born Mayer potential to their Morse potential using the nonlinear curve fitting functionality in the Grace program [83]. Shown in Figure 5.1 are the Morse potential (circles) and the Born Mayer potential (solid lines) for both anion–wall (green) and cation–wall (red) interactions. The fitted Born Mayer parameters are included in Table 5.1.

The energy of the system is found to depend only weakly on the induced electrode charge width κ (recall Equation 2.21 which describes the electron density centred on the electrode atoms as Gaussians). Figure 5.2 illustrates the variation with κ of the reduced coulombic energy ($U_c^* = U_c 2/Q\Delta\Psi$) for an empty capacitor carrying a charge $\pm Q$ on each plate. Although the

[1] The parameters governing the europium interactions were set equal to the equivalent terbium parameters in reference [49]. As we reported in Section 2.1.1, the differences between the parameter sets used for different materials are related to the crystallographic radius of the cation. Octahedrally coordinated Tb^{3+} and Eu^{3+} have very similar radii [81] (respectively 106.3 pm and 108.7 pm).

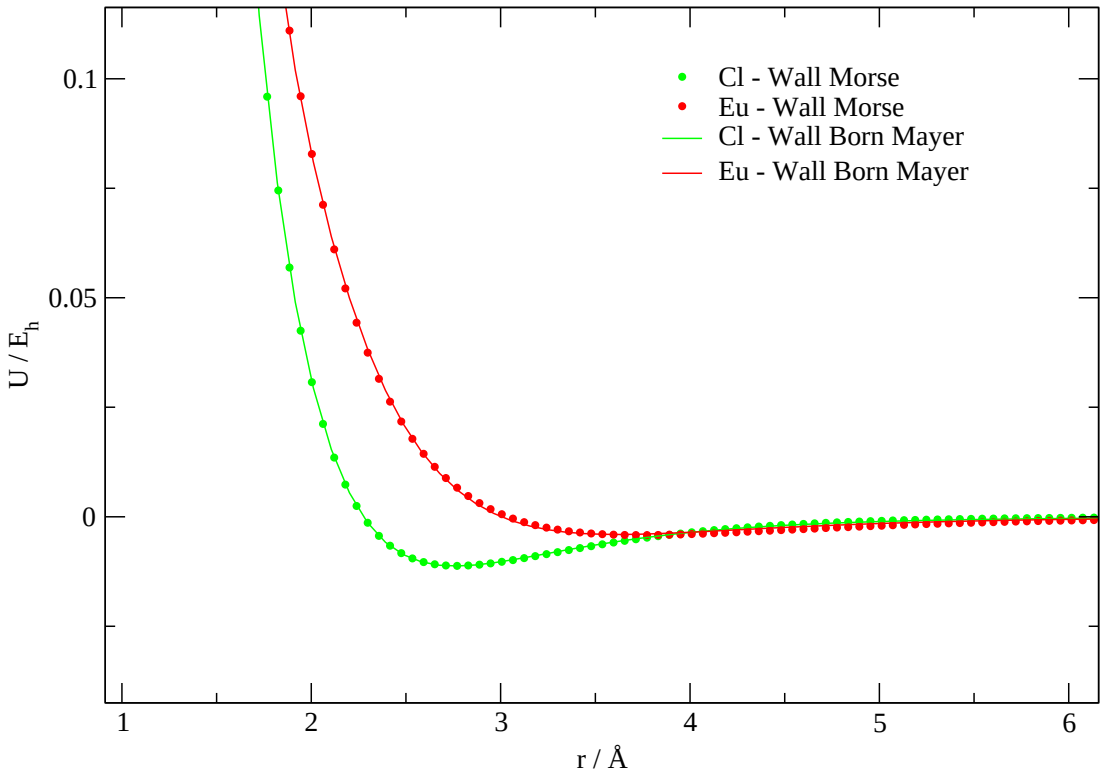

Figure 5.1: The fit of a Born Mayer potential (straight lines) to the modified Morse potential (circles) in reference [82]. The energy describes the interaction between a Cu metal electrode with its (111) plane exposed and respectively Cl (green) and Li (red) ions.

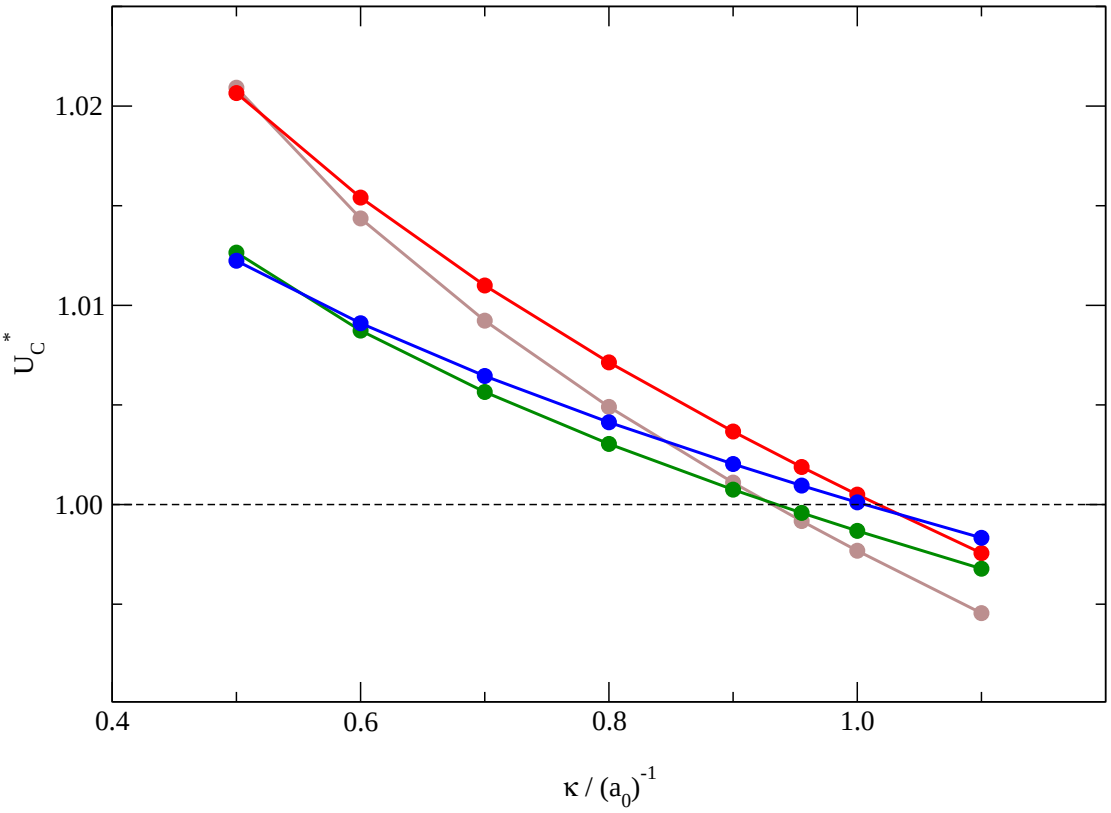

Figure 5.2: Variation of the reduced Coulomb energy, U_c^*, with the Gaussian width, κ, for different systems. Brown: (001) surface comprising 800 atoms. Red: (111) surface comprising 900 atoms. Green: (100) surface comprising 98 atoms. Blue: (111) surface comprising 100 atoms. The lines are simply a guide to the eye. Taken from reference [26].

optimum value of κ is independent of system size, it does depend on the surface structure. Specifically, it is found that the optimum value of κ is inversely proportional to the square root of the area per surface atom. We set $\kappa = 0.5052\,\text{Å}^{-1}$ as appropriate to our (100) surface. The Ewald screening parameter α is $0.265\,\text{Å}^{-1}$. The trajectory is integrated with a timestep of 0.36 fs in a NVE ensemble.

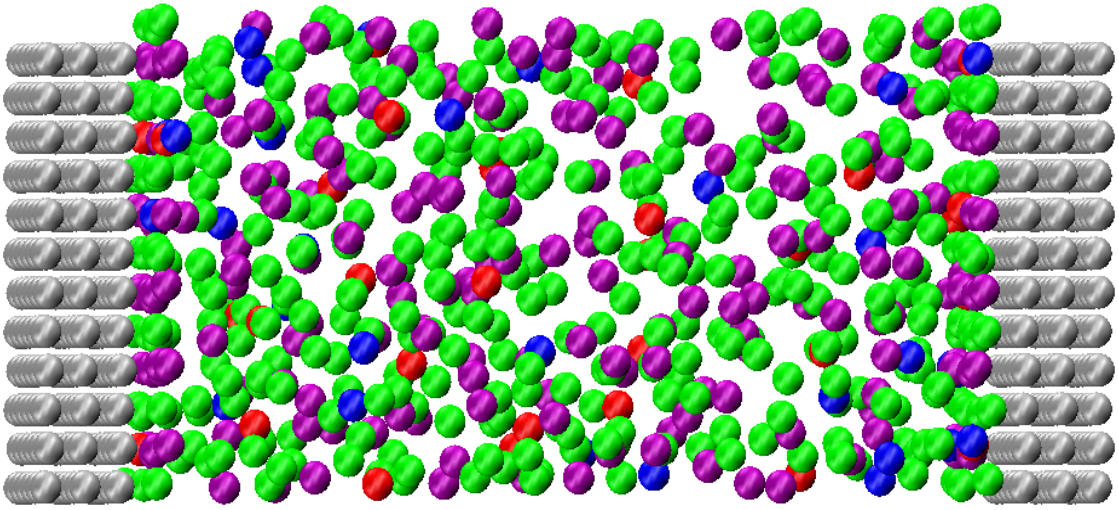

Figure 5.3: A snapshot of the simulation cell. The Cl^- ions are represented by green spheres, the Eu^{2+} by blue, the Eu^{3+} by red, and the K^+ by violet. The metal wall atoms are coloured grey and arranged in two parallel plates of three layers each. The lattice parameter used is 3.9 Å, which is that of platinum.

Interaction	a_{ij}	B_{ij}	C^6_{ij}	C^8_{ij}	f^6_{ij}	f^8_{ij}
Cl–Cl	1.53	100.0	222.26	7455.5	1.70	1.70
Cl–Eu	1.80	283.8	53.90	800.0	1.52	1.02
Cl–K	1.55	57.7	20.14	272.3	10.00	10.00
Cl–Wall	1.58	92.4	841.20	−3658.4	1.70	1.70
Eu–Eu	3.00	15.0	16.87	50.0	1.55	1.03
Eu–K	1.57	10.5	1.39	3.2	1.0×10^6	1.0×10^6
Eu–Wall	1.26	43.8	1405.14	−7816.4	1.52	1.02
K–K	1.56	54.5	25.38	89.5	10.00	10.00
K–Wall	1.26	43.8	1405.14	−7816.4	10.00	10.00
Wall–Wall	1.53	100.00	222.26	7455.5	1.70	1.70

Table 5.1: The parameters for the Born Mayer pair potential. All values are in atomic units. The parameters were defined in Section 2.1.2.

Interaction	b_{ij}	$p_{\max}$	c_{ij}
Cl–Eu	1.317	4	1.00
Cl–K	1.258	4	1.00
Cl–Wall	1.300	4	−2.00

Table 5.2: The polarization parameters. All values are in atomic units. The Cl^- polarizability was set to 20.0 au. The parameters were defined in Section 2.1.3.

5.3 Ion density profiles

In Figure 5.4 we show the mean ion number densities, $\rho_i(z)$, across the simulation cell under constant potential conditions. The density profiles are computed by dividing the simulation cell into 500 bins, each of width 0.11 Å, and averaging over the 36 ps of the production run. The profiles are all symmetrical which is consistent with the applied potential in this case being zero. The density profiles exhibit oscillations which extend approximately 15 Å from the interface into the bulk. Beyond the outermost layer there is a tendency for the cation and anion densities to oscillate out of phase. Such structure has been found in previous work on molten salts at charged walls [24, 84, 85], and is not consistent with the traditional double layer conception outlined in Chapter 1. The oscillatory structure is much more complex, and relates to the packing requirements of the ions which will be discussed in Section 5.6. The density of the outer layers will be determined by the strength of the melt–electrode interaction potential, discussed in Chapter 7, and by whether the MD run is of sufficient time length to allow the inter-layer energy barriers to be crossed, a point taken up in Section 5.7.

5.4 The mean electrical potential

The Poisson potential across the simulation cell $\Delta\Psi(z)$ is calculated through Equation 3.66. The first term contains the charge density $\rho_{\mathrm{q}}(z)$ which is calculated at a particular z position through $\rho_{\mathrm{q}} = \sum_i \rho_i q_i$, where ρ_i is the ion number density of species i, q its formal charge, and the sum runs over the number of different species (including the electrode charges). This is the

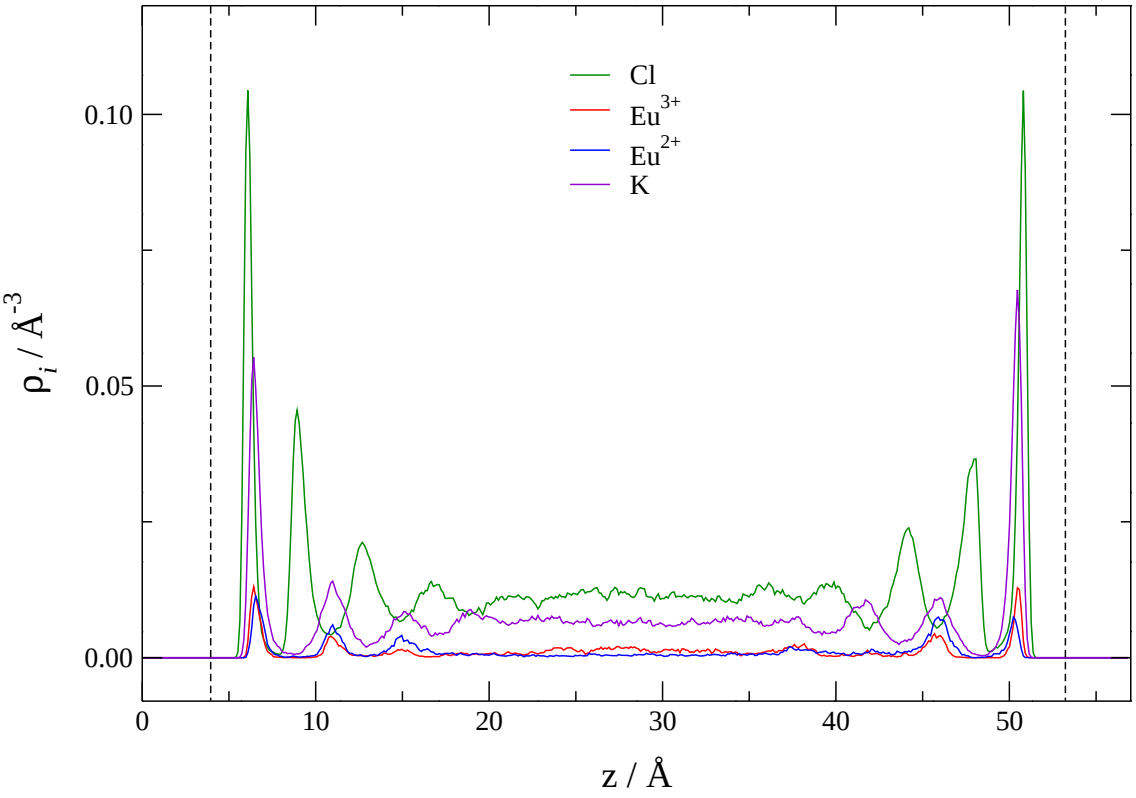

Figure 5.4: Mean ion number density profiles for $K_3Eu^{3+}_{0.5}Eu^{2+}_{0.5}Cl_{5.5}$ with an applied potential of $\Psi^+ = 0.00\,\mathrm{V}$.

red line in Figure 5.5, in which the reference coordinate z_0 is taken to be inside the left hand electrode, where $\Psi_{\rm q}(z_0 < 0) = \Psi^+$ and $\Psi_{\boldsymbol{\mu}}(z_0 < 0) = 0.0$ V. The second contribution to the electrostatic potential $\Delta\Psi(z)$ is of the induced dipoles (green line) which opposes that due to the charge distribution. This is the first time that induction (polarization) effects have been included in a calculation of the Poisson potential; note in particular that this contribution to the total potential is large. That the total potential (blue line) is a constant in the centre of the cell indicates that the melt ions completely screen the potential due to the polarized electrodes. The strong oscillations near the interface result primarily from the out-of-phase oscillations of the cation and anion densities. Note that the potential is constant within the electrodes as befits a metal, and that the potential drop across the cell calculated from the induced charge density marries with the externally-applied potential $\Psi^+ = 0.00\,\mathrm{V}$.

Figure 5.6 illustrates the Poisson potential across the cell for four different externally-applied potential differences. The value of the bulk potential $\Psi^{\rm bulk}$ is the same in each case and is non-zero even for an applied potential of $\Psi^+ = 0.00\,\mathrm{V}$. It follows that when $\mid \Psi^+ - \Psi^- \mid$ is non-zero the potential drop across each of the two interfaces will be different. This point is emphasized in the schematic Figure 5.7, where $\mid \Psi^+ - \Psi^- \mid = 1.0\,\mathrm{V}$. If we take $\Psi^{\rm bulk}$ to be $2.0\,\mathrm{V}$, then at the left hand anode the potential drop is $\Delta\Psi_1 = \Psi^+ - \Psi^{\rm bulk} = -1.5\,\mathrm{V}$, whilst at the right hand cathode $\Delta\Psi_2 = \Psi^- - \Psi^{\rm bulk} = -2.5\,\mathrm{V}$. This difference in the interfacial potential drops is a reflection of the different ionic distributions adjacent to the two electrodes, as illustrated in Figure 5.8. There is a shift in the cation density towards the negatively charged cathode relative to the symmetrical density distribution of a zero applied potential. An interesting observation is the closer approach of the smaller and more highly-charged Eu^{3+} ion to both electrodes than its Eu^{2+} counterpart. The opposite trend was observed by Reed *et al.* [26] in their simulation of an equimolar LiCl:KCl molten salt mixture where the K^+ ion approached both the anode and cathode more closely than the much smaller Li^+ ion. There are two opposing contributory factors here. For an ion to approach the wall closely it must lose some of its coordinating anions to in effect replace them with wall ions. The wall ions carry much smaller charges than the melt anions and there is a lesser propensity for the cation with the higher charge density

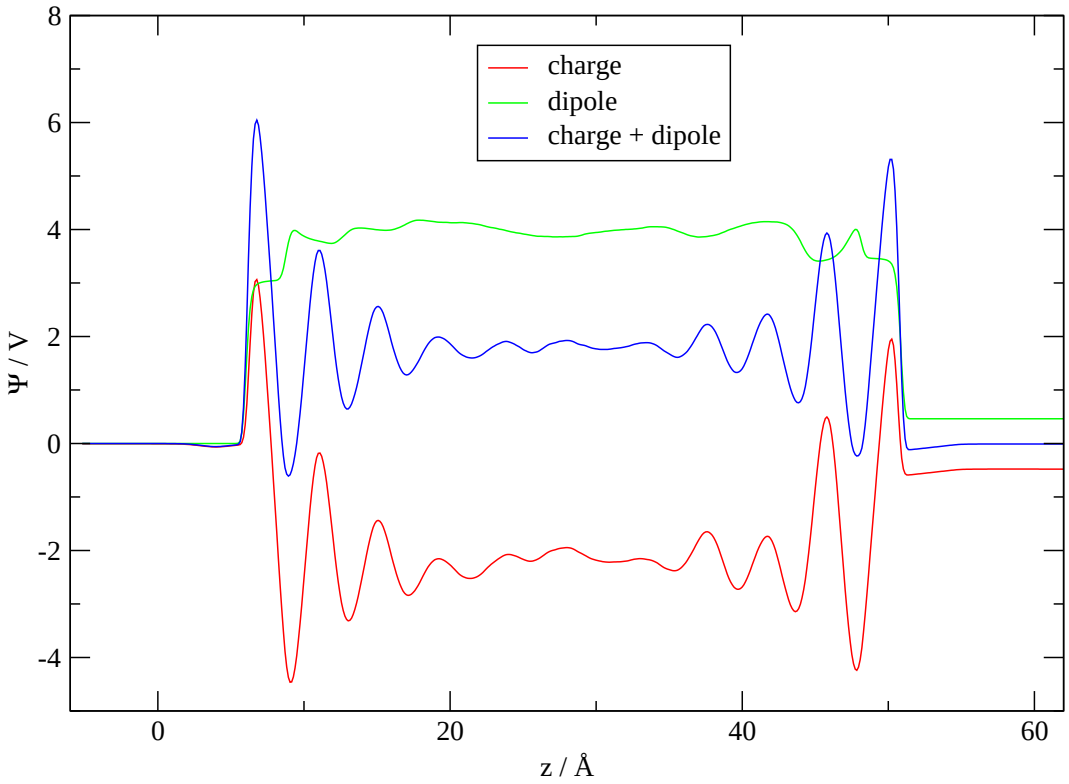

Figure 5.5: Variation of the Poisson potential across the cell for $\Psi^+ = 0.00\,\mathrm{V}$. The contributions to the total potential from the point charges and the induced dipoles on the anions are also shown separately. The profile extends beyond the usual bounds of the simulation cell because the Gaussian charge distributions have a finite width and the outermost electrode atoms mark the limits of the cell. To obtain the Poisson profile it is necessary to integrate over the whole charge density.

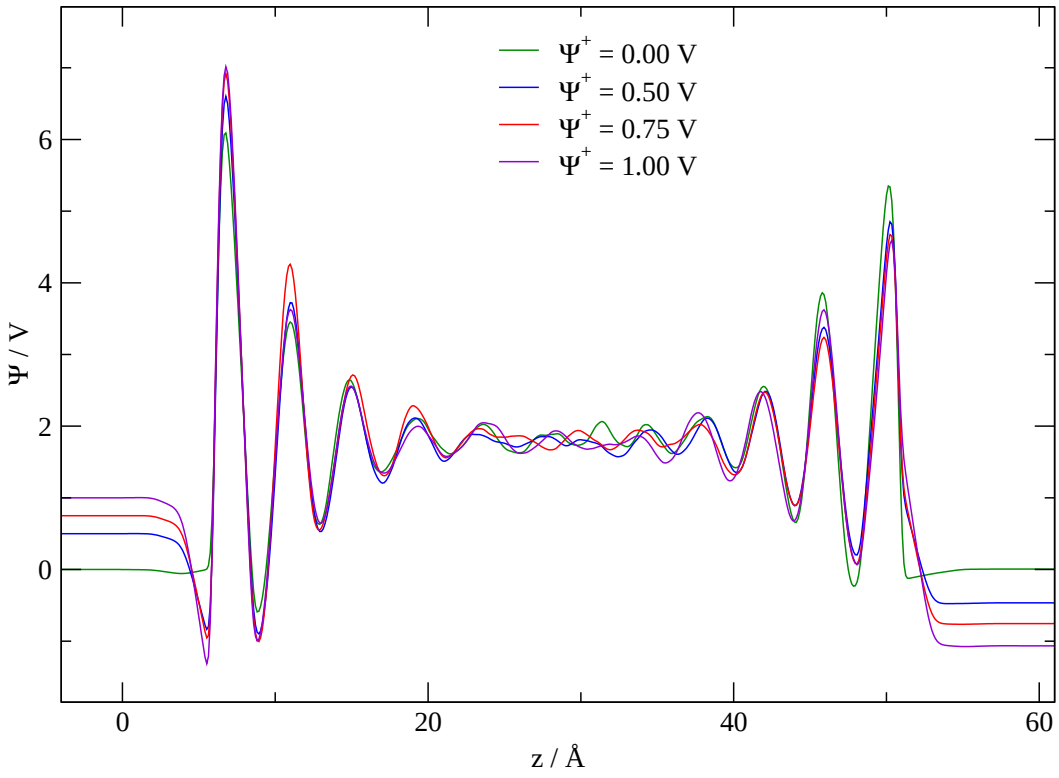

Figure 5.6: Variation of the Poisson potential across the cell for anode potentials $\Psi^+ = 0.00\,\mathrm{V}, 0.50\,\mathrm{V}, 0.75\,\mathrm{V}, 1.00\,\mathrm{V}$.

(smaller radius or higher coulombic charge) to leave the bulk. However, the cation with the higher charge density can also approach more closely its larger image charge at both walls, which in our system appears to be the dominating effect.

The Poisson potential is that experienced by an infinitesimal test charge added to the system and is the potential classically invoked in discussions of electrodic phenomena [86, 35]. Another measure of potential is that on an ion due only to the charges of the other ions and the electrodes. This is known as the Madelung potential and is given by

$$V_i = \frac{\partial U}{\partial q_i}, \qquad [3.25]$$

where U is the coulombic potential and q_i is the charge of ion i. The Madelung potential therefore differs from the Poisson potential by being dependent on the identity of the species

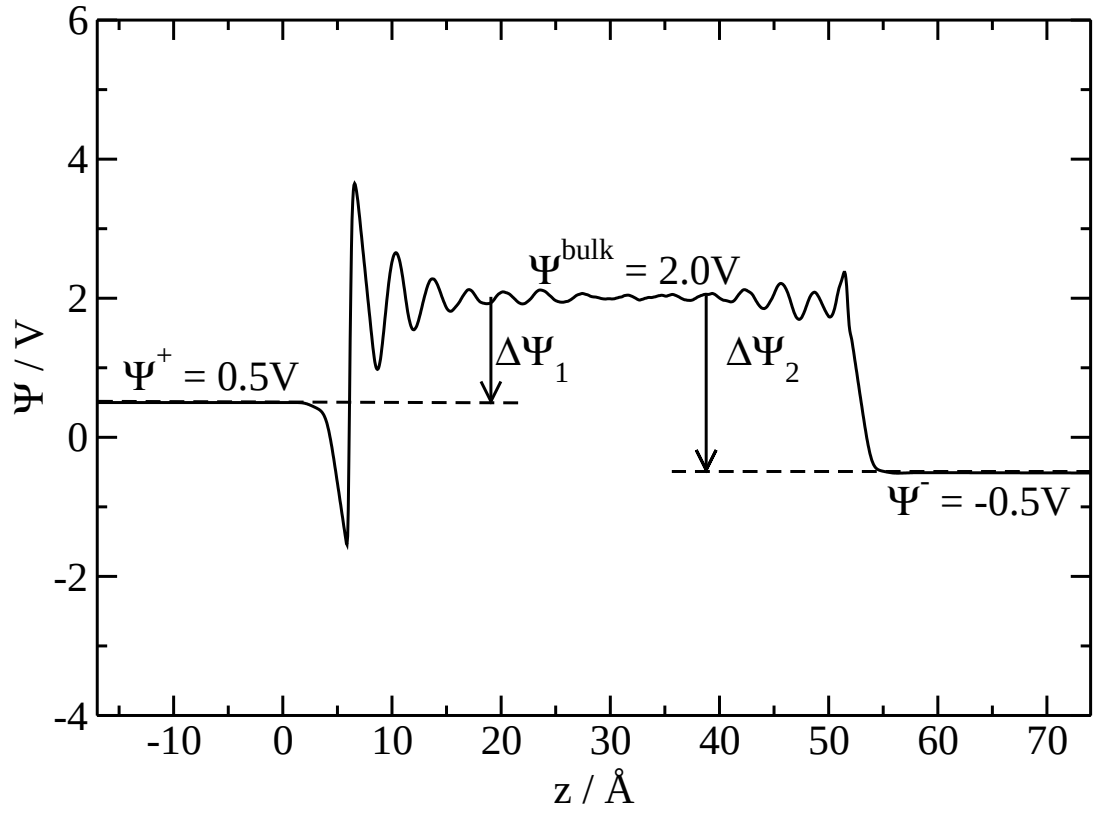

Figure 5.7: Graphical explanation of the notation introduced in the text for an applied potential $\mid \Psi^+ - \Psi^- \mid$ of 1.0 V. The potential reaches a value of $\Psi^{\mathrm{bulk}} = 2.0$ V in the bulk liquid. Two metal/molten salt interfaces are then defined: at the left-hand electrode the potential difference $\Delta\Psi_1 = \Psi^+ - \Psi^{\mathrm{bulk}}$ is -1.5 V, while on the right-hand side $\Delta\Psi_2 = \Psi^- - \Psi^{\mathrm{bulk}}$ equals -2.5 V.

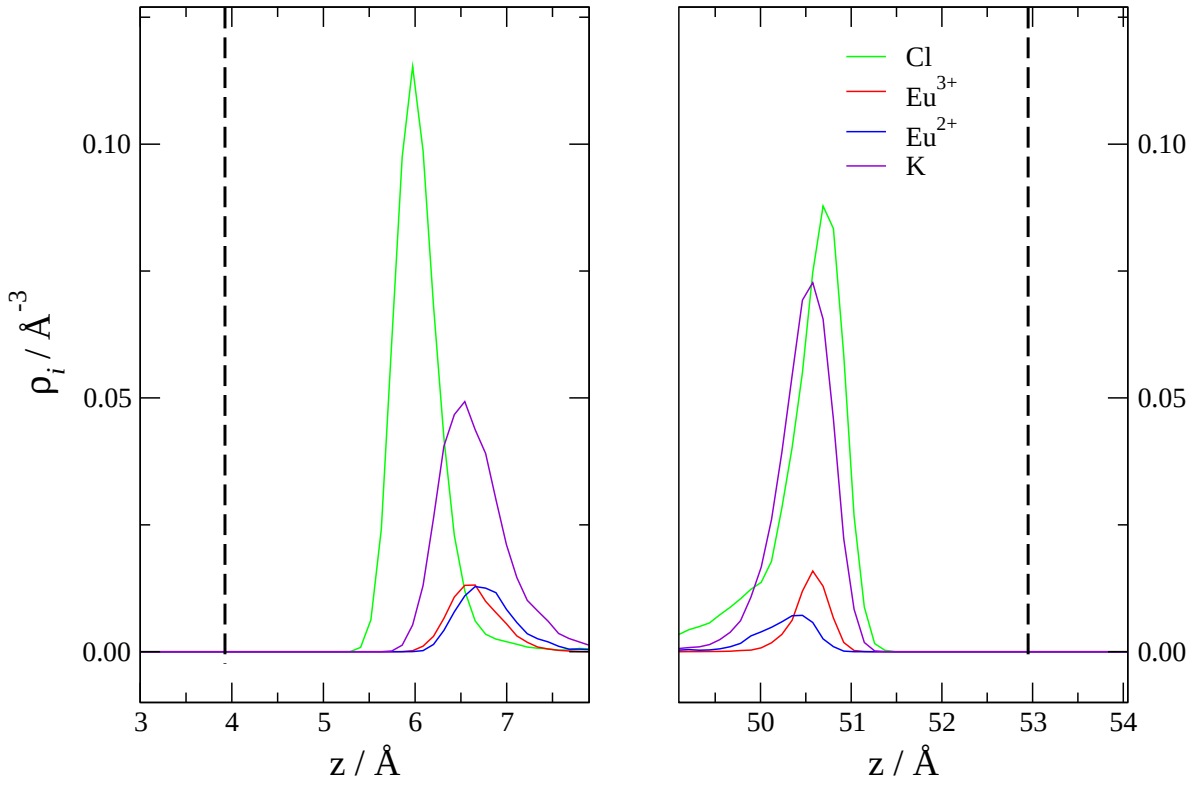

Figure 5.8: Mean ion number density profiles $\rho_i(z)$ adjacent to the electrodes for an applied potential of $\Psi^+ = 1.00\,\mathrm{V}$. The left-hand panel represents the ions adjacent to the anode and the right-hand panel those adjacent to the cathode. The centres of the inner layers of atoms in the electrodes are indicated by the vertical dashed lines.

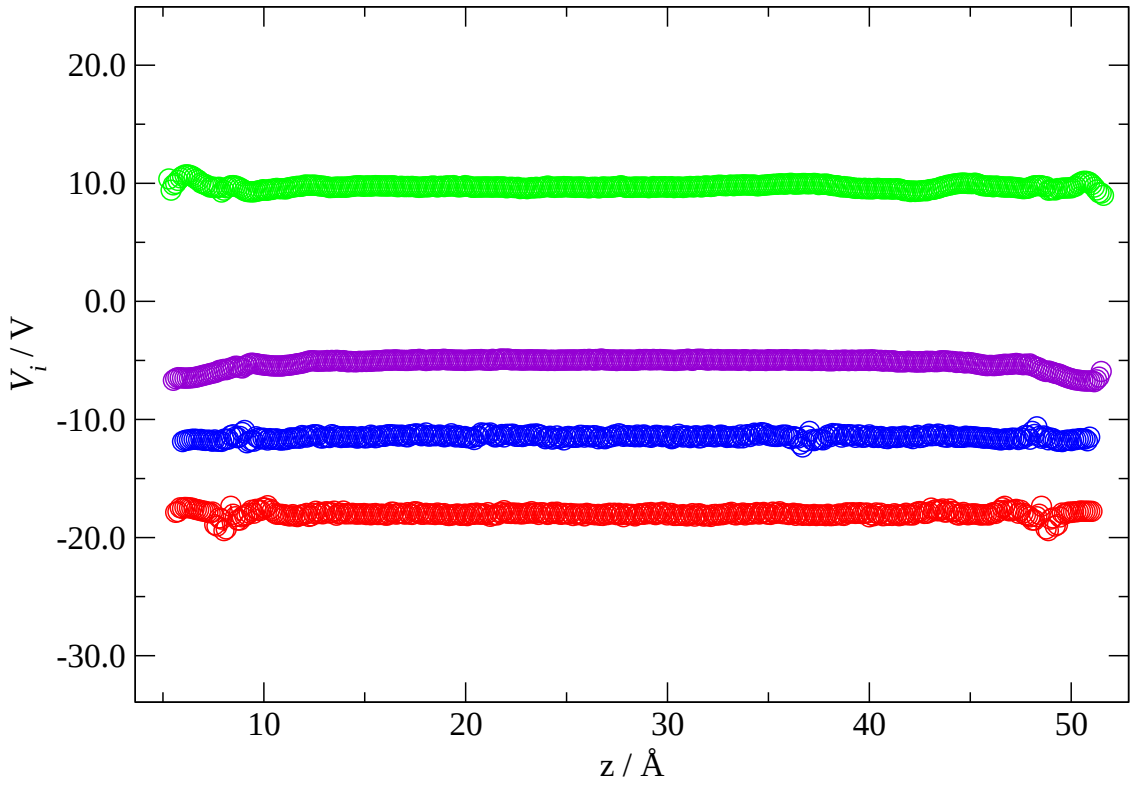

Figure 5.9: The Madelung potential profiles across the cell for the individual species with an applied potential $\Psi^+ = 0.00\,\mathrm{V}$. Green: Cl^-, violet: K^+, blue: Eu^{2+}, red: Eu^{3+}.

on which the potential is evaluated. It also markedly differs in its behaviour across the cell, as is apparent in Figure 5.9. In contrast to the Poisson profile, the Madelung potential shows perfect screening of the electrode even very close to the electrodes with no oscillatory character. The question therefore arises as to which potential is the more apposite for discussing interfacial electron transfer. We will provide an answer in Section 6.2.

5.5 The electrode capacitance

A classical method of characterizing the interfacial structure is the measurement of the differential capacitance[1] $C = (\partial\sigma^{\mathrm{M}}/\partial\Delta\Psi)$, where σ^{M} is the charge density on the electrode and $\Delta\Psi$ is the drop in the Poisson potential[2] across the interface (*i.e.* $\Delta\Psi_1$ at the anode and $\Delta\Psi_2$ at the cathode). We can thus obtain approximate values for the capacitances of the individual positive and negative electrodes by combining the values of the Poisson potential drops in Figure 5.6 with the values of the average charge density induced on the electrodes under the constant potential condition. This capacitance reflects that of a parallel plate capacitor in which one plate is the electrode and the other plate in effect carries the net charge of the screening layer induced in the electrolyte. Since we see perfect screening of the electrode charge in the bulk of the melt, it is clear that the screening charge is equal in magnitude and opposite in sign to the charge on the electrode. The oscillatory nature of the Poisson potential suggests that this is a crude construct and would be improved by modelling the capacitance of the screening density as a set of capacitors connected in series. The charge density σ^{M} on the anode (blue) and the cathode (red) are plotted as a function of the potential drop across the interface $\Delta\Psi$ in the top panel of Figure 5.10. This results in a differential capacitance (lower panel) of $\approx 11\,\mu\mathrm{F.cm}^2$ across the range of potential drops sampled.

The interfacial capacitances calculated in any theoretical work will be extremely sensitive to the parameters governing the short range interactions between the melt and the wall, and in our calculations this was the crudest part of the potential model. Esnouf *et al.* [85] measured the interfacial capacitance of KCl confined between two charged plates. Although obviously their system is different from that of the present work we recall from Figure 5.8 that the K^+ ions approach the electrodes more closely than the Eu^{2+} and Eu^{3+} ions. They calculate the interfacial capacitance to be $12.5\,\mu\mathrm{Fcm}^2$. At first glance this appears to be in good agreement with the value of our linear capacitance, however they take the potential difference $\Delta\Psi$ as the

[1] Technically a capacitance *density* as we use the wall charge density rather than the charge. This common electrochemical practice removes the dependence on the size of the electrode.

[2] The Poisson potential is used in the calculation of all capacitances in this thesis as this is the potential measured experimentally.

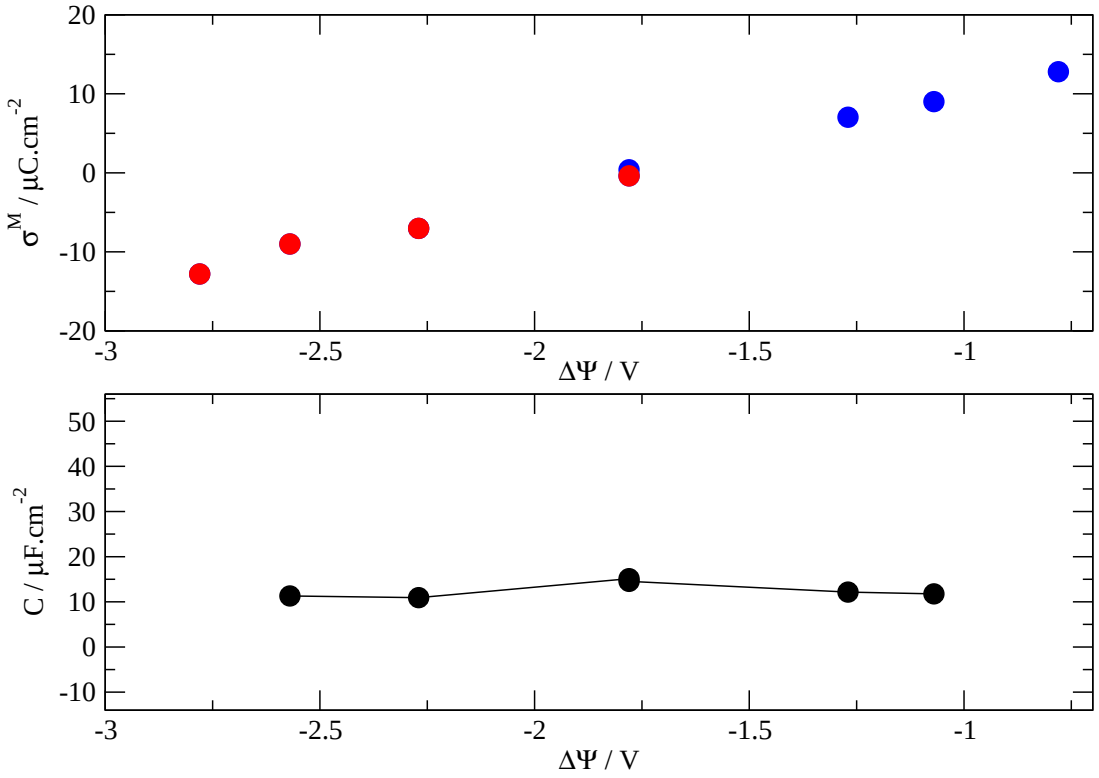

Figure 5.10: The top panel shows the variation of the charge density σ^{M} on the anode (blue circles) and cathode (red circles) with the difference in potential $\Delta\Psi$ between the bulk melt and the electrode. The bottom panel plots the variation in the differential capacitance C against the same interfacial potential drop $\Delta\Psi$. Both data sets take the bulk melt value as the reference point.

potential drop across the whole cell as distinct from across one interface. Therefore *if* the potential drop at each interface were identical (which is manifestly not the case in Figure 5.6) the capacitance would be artificially doubled. Moreover, Esnouf *et al.* use a planar wall with the charge located at the surface which will reduce the distance between the wall charge and the centres of the ions adjacent to the wall in comparison to our calculation, with a concomitant increase in the capacitance.

Booth and Haymet [87] made a comparison of the singlet-integral equation theory of molten salts with Monte Carlo simulations, and obtained decaying oscillations in the ionic concentration profiles near the electrode, and a capacitance of $10.3\,\mu\mathrm{Fcm}^{-2}$ at *both* electrodes. Furthermore, their capacitance profile varies by less than $1\,\mu\mathrm{Fcm}^{-2}$ in the $\pm 1\,\mathrm{V}$ potential range. Kornyshev has tentatively suggested that such near-linear capacitance profiles may correspond to the crossover between the bell-shape and camel-shape curves (see the $\Gamma = 1/3$ data set in Figure 1.11 near the PZC).

A constant capacitance is the behaviour expected for a dielectric and it is tempting to suggest that we see this behaviour because of the electronic polarization of the Cl^- ions close to the electrode surface (which is not accounted for in the mean-field treatments, nor in any previous simulation study). It is certainly manifest in Figure 5.5 that the induced dipoles make a substantial contribution to the interfacial potential drop.

As mentioned in Chapter 1, the experimental capacitance profiles of molten salts are mostly parabolic about a minimum at the PZC. However there is often an area around the capacitance minimum which is much flatter than Gouy Chapman theory predicts. Kisza [88] notes that the literature contains a wide range of values spanning two orders of magnitude for the experimental double layer capacitance, and so further work would help to eliminate these ambiguities.

5.6 The interfacial structure

The average coordination number of Eu^{2+} and Eu^{3+} ions in the melt is illustrated in Figure 5.11. At positions sufficiently far from the electrode ($z > 10\,\text{Å}$) it can be seen that these cations are predominantly octahedrally coordinated. A typical bulk europium ion surrounded by six

chloride ions is shown in two perpendicular orthographic projections in Figure 5.12. However the coordination shell is affected by the oscillations in the ion number densities in the region close to the electrodes: witness the range of coordination numbers of Eu^{2+} and Eu^{3+} ions at positions $z < 10\,\text{Å}$ in Figure 5.11. At the interface there forms a strongly adsorbed, regular array of chloride ions sitting over a proportion of the holes in the (100) face of the electrode, as illustrated in Figure 5.13. The cations in this outermost layer are on average coordinated to four chloride ions in an approximately square planar arrangement, and one or two additional chloride ions from the region corresponding to the neighbouring oscillation of the chlorine density in Figure 5.4. The chloride ions in this second layer are not as strongly adsorbed onto the electrode and exhibit faster diffusion such that the interfacial europium ions have coordinating shells ranging in shape from square pyramidal (Figure 5.14) to triangular prismatic (Figure 5.15).

For a cation to approach the wall closely it must replace some of the chloride ions in its coordination shell with atoms from the wall. (Note in Figure 5.11 that europium ions at positions $z < 6.5\,\text{Å}$ are on average coordinated to fewer than six chloride ions.) But the wall atoms carry only small charges in comparison with the anions in the melt: even at an applied potential of $\Psi^+ = 1.00\,\text{V}$, corresponding to the highest charge density in Figure 5.10, the average induced charge on the atoms in the innermost layer of the cathode is $-0.060\,e$. Were a cation therefore to lose one coordination sphere counter ion it would require an unphysical 17 wall atoms to balance the charge loss.

Finally, we note that the coordination shell is also dependent on the oxidation state of the europium: as expected, the higher charge density of the Eu^{3+} ion effects a more tightly packed coordination shell than that which surrounds the Eu^{2+} ion. The average Eu–Cl bond length for each oxidation state corresponds to the position of the first peak of the radial distribution functions shown in Figure 5.16.

5.7 The potential of mean force

The ion density profiles in Figure 5.4 are of constant value away from the electrodes which is one manifestation of an equilibrium configuration, although interestingly not a prerequisite for

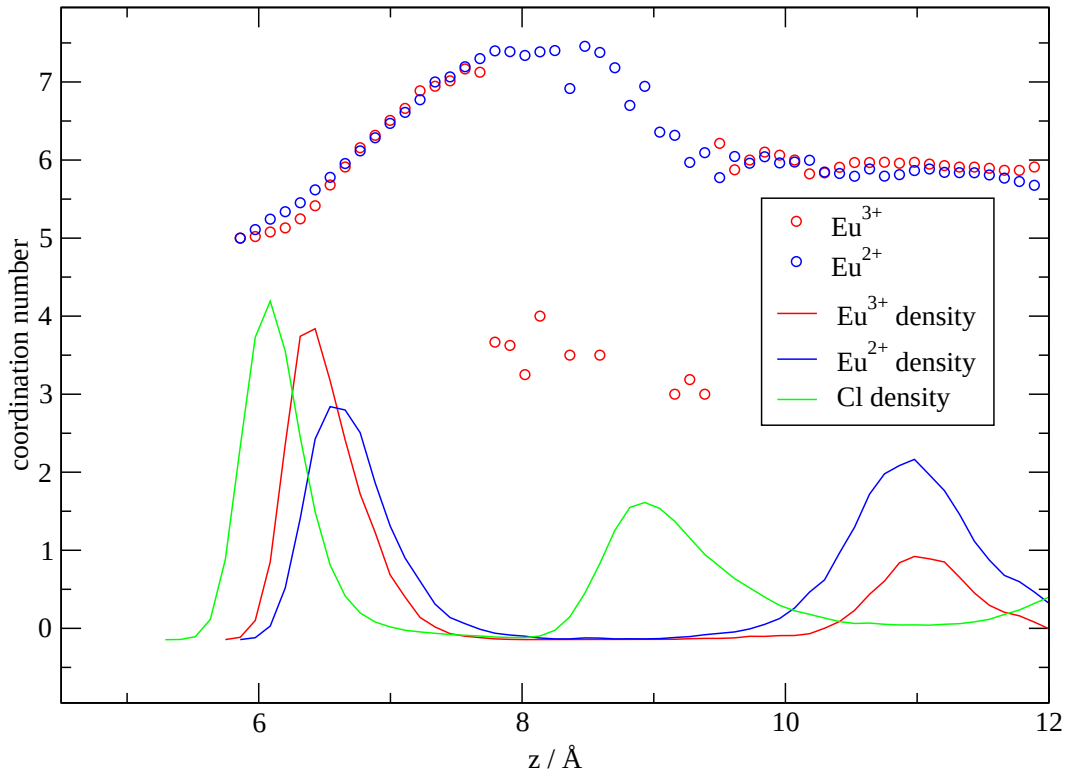

Figure 5.11: The variation in the number of chloride ions coordinated to each Eu^{2+} (blue circles) and Eu^{3+} ion (red circles) with distance from the electrode. Also shown is the ion number density (arb. units) of the Cl^- (green line), Eu^{2+} (blue line), and Eu^{3+} (red line) ions.

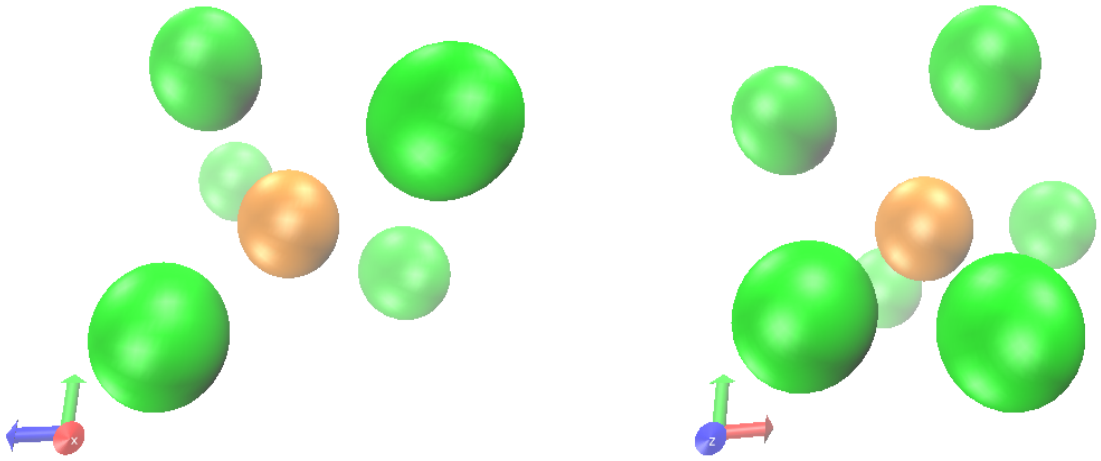

Figure 5.12: The coordination environment of a Eu^{3+} ion in the bulk of the melt, viewed in orthographic projection perpendicular to the metal surface (left) and parallel to it (right). The Eu^{3+} ion is shown in orange and the Cl^- ions in green.

perfect screening of the electrode charge [89]. The rate of relaxation of concentration depends on the appropriateness of the starting configuration and the diffusion rate, which latter factor in turn depends on the diffusion coefficient divided by the square of the distance between the electrodes. A second relaxation process relates to the exchange of ions between the strongly adsorbed outer layer and the bulk, which might be imagined to be a slow process if the ions are to carry their coordinating molecules between the two regions. This is of obvious importance for the rate of electron transfer because, at those positions where the tunneling matrix element γ is sufficiently large to allow the redox process, there is a non-trivial dependence of the ion density on z. In order to quantify this effect we can write the concentration factor in Equation 1.56 as a free energy. To this end we obtain a potential of mean force (PMF), $\phi_i(z, \Psi)$, for the approach of Eu^{2+} and Eu^{3+} to the electrode in a cell at potential Ψ from

$$\phi_i(z, \Psi) = -k_\mathrm{B}T \ln \left[\frac{\rho_i(z, \Psi)}{\rho_i(\infty)} \right]. \tag{5.2}$$

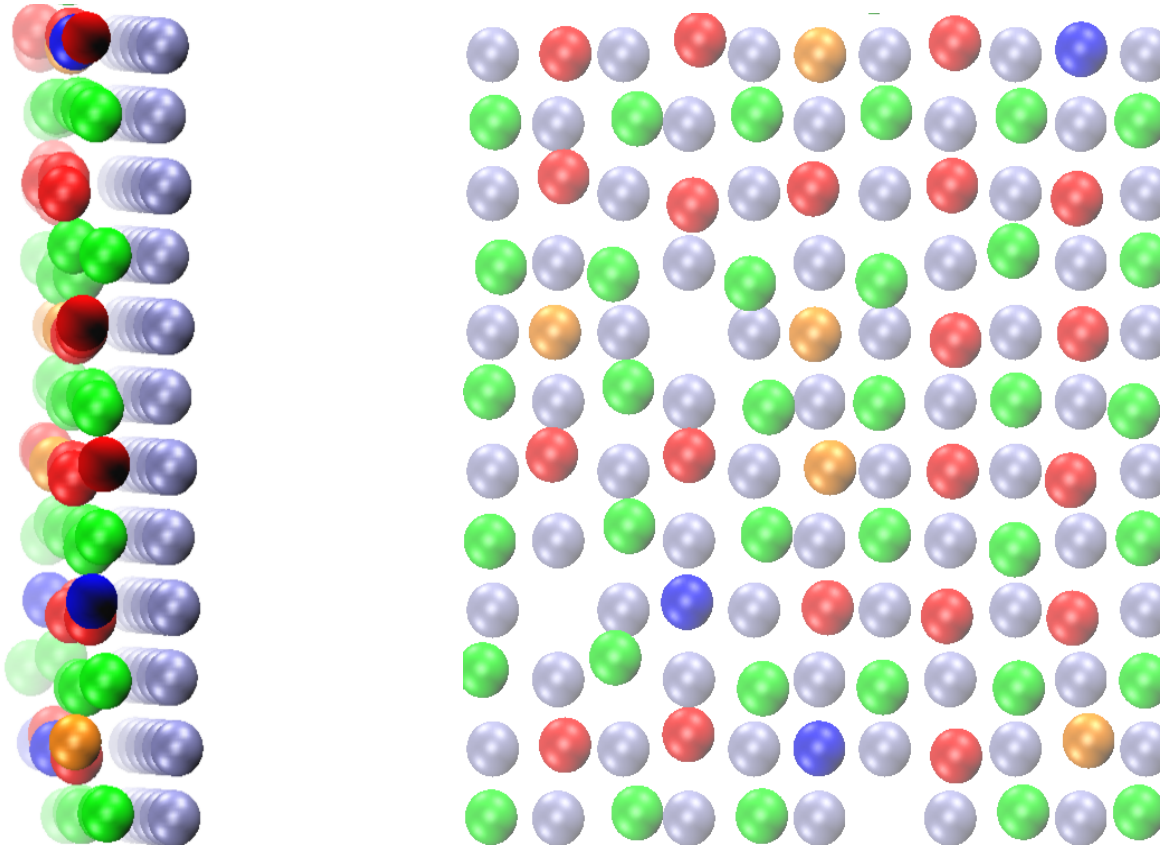

Figure 5.13: The layer of ions adjacent to the anode viewed perpendicular to the metal surface (left) and parallel to it (right). The Eu^{3+} ions are shown in orange, the Eu^{2+} ions in blue, the Cl^- ions in green, the K^+ ions in red, and the wall atoms in grey.

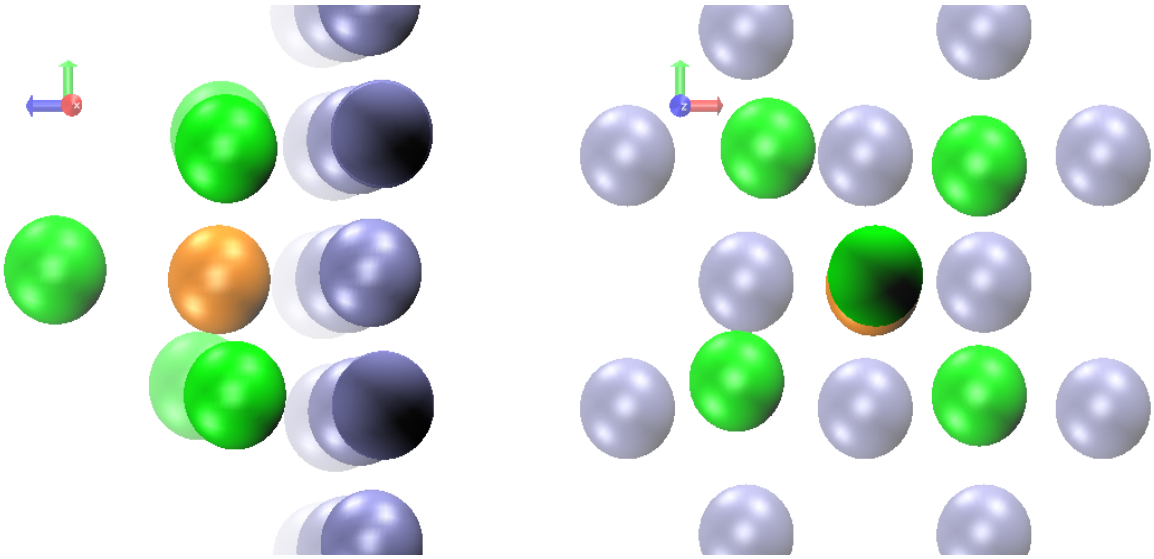

Figure 5.14: A five-fold coordination environment of a Eu^{3+} ion next to the anode, viewed perpendicular to the metal surface (left) and parallel to it (right). The Eu^{3+} ion is shown in orange, the Cl^- ions in green, and the wall atoms in grey.

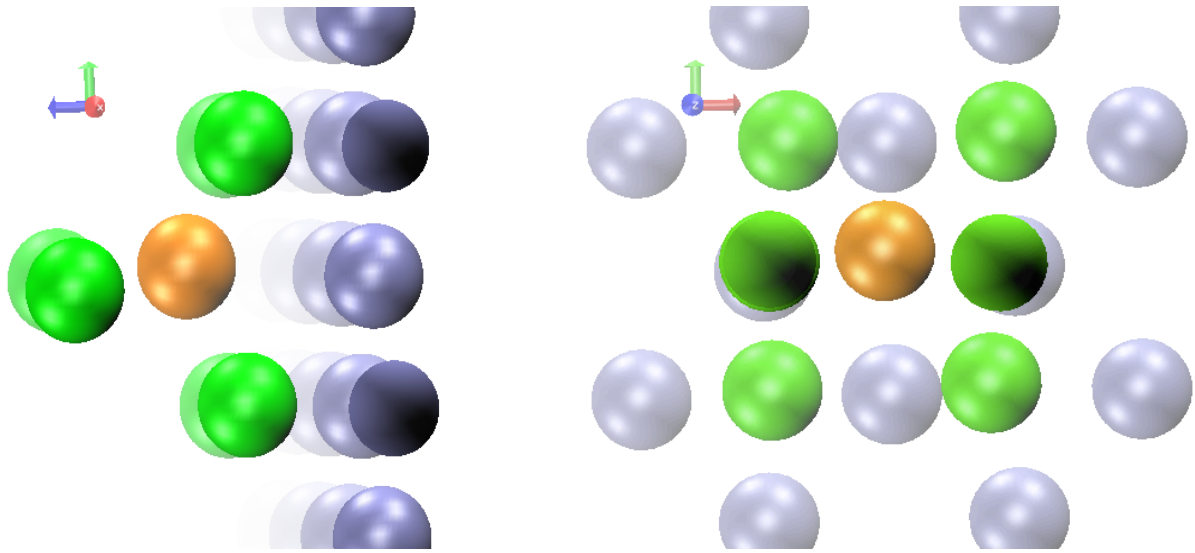

Figure 5.15: A six-fold coordination environment of a Eu^{3+} ion next to the anode, viewed perpendicular to the metal surface (left) and parallel to it (right). The Eu^{3+} ion is shown in orange, the Cl^- ions in green, and the wall atoms in grey.

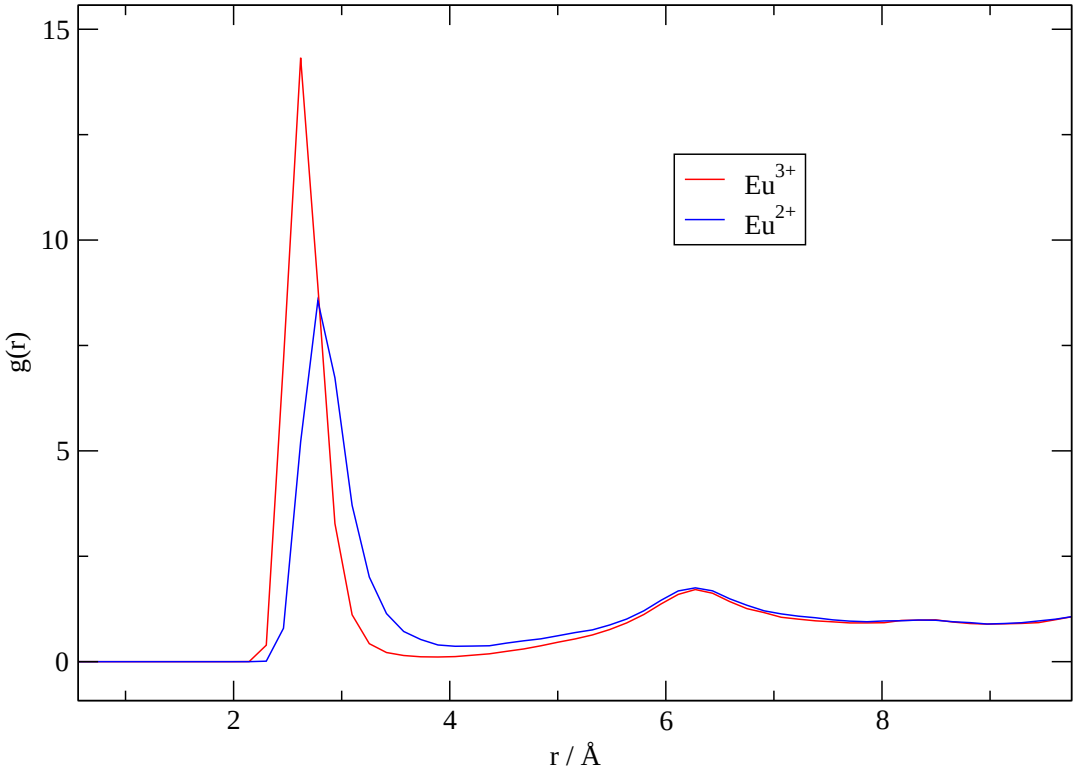

Figure 5.16: Radial distribution functions for the Eu^{3+}– Cl (red) and Eu^{2+}– Cl (blue) pairs.

This would provide a method for calculating the barrier for exchange between the adsorbed layer and the bulk were it not for the poor statistics in the barrier region. A way around this problem is the use of umbrella sampling techniques: we compute the mean force $F(z)$ in the z direction perpendicular to the electrode on an atom i in the simulation by constraining the atom i at some position z_0 in an harmonic potential $U_{z_0}(z) = +\frac{k}{2}(z - z_0)^2$, where k is the force constant of the harmonic well, taken to be $41.76\,k_\mathrm{B}T\,\text{Å}^{-2}$. The mean force on atom i at position z_0 can be estimated as $F(\overline{z}) = -k(\overline{z} - z_0)$ where $\overline{z}$ is the average value of z for species i constrained to U_{z_0} during a simulation. The potential of mean force $\phi_i(z, \Psi)$ obtained by integrating over $F(\overline{z})$ can exhibit hysteresis [90] if there is an energy barrier in the chosen coordinate (z) frustrating equilibration on short timescales. We therefore chose two sets of initial conditions. The first corresponds to electrode desorption and was initiated by selecting a europium ion at the interface, setting z_0 at the position corresponding to the density peak of the outermost layer, and then equilibrating with $U_{z_0}(z)$ for 1 picosecond. The mean force was computed by averaging z over an 11.78 picoseconds trajectory. The next member of this set of initial conditions was generated by changing $z_0 \rightarrow z_0 + 0.265\,\text{Å}$ and again equilibrating with $U_{z_0}(z)$ for 1 picosecond. This procedure was continued with incremental changes in z_0 of 0.265 Å for approximately 6 Å. The second set of initial conditions corresponds to electrode adsorption and was generated analogously by choosing an ion in the bulk and moving z_0 towards the electrode in 0.265 Å steps.

Figure 5.17 contains the potential of mean force $\phi_i(z)$ for a Eu^{3+} ion in a cell of applied potential $\Psi^+ = 0.00\,\text{V}$. The blue circles represent the desorption process and the red circles represent adsorption. These two data sets are in close agreement over the z-range sampled, *i.e.* the system exhibits little hysteresis. The barrier to desorption from the first adlayer suggested by these data is of the order of $12.6\,k_\mathrm{B}T$, which is sufficient to lead to extremely slow exchange of the adsorbed ions and the bulk. The interfacial structure will consequently not equilibrate in a realistic simulation timeframe, so the number of adsorbed ions will depend on the initial conditions under which the system was set up. We can illustrate how far the system is from equilibrium in this respect by using the density profiles from Figure 5.4 as a second route to the

PMF through Equation 5.2. The solid black line in Figure 5.17 represents the PMF obtained in this way: the values in the range $z < 8\,\text{Å}$ have been displaced along the y-axis to bring the minimum value into agreement with that obtained from the umbrella sampling; the dashed line represents the unshifted values. Note that the density profiles in the z-range $\sim 8 - 10\,\text{Å}$ were excluded from this calculation because of their very poor statistics in this region. The PMF profiles obtained *via* these two different methods are in very close agreement.

The PMFs appropriate to the Eu^{2+} (blue circles) and Eu^{3+} (red circles) ions are compared in Figure 5.18. The umbrella sampling data have in each case been averaged over the desorption and adsorption data sets, and the black lines again represent the PMF obtained on inputting the density profiles to Equation 5.2. It is apparent that the barrier height for desorption of Eu^{2+} ($\sim 8.9\,k_\text{B}T$) is lower than that of Eu^{3+} ($\sim 12.6\,k_\text{B}T$). We can relate this difference to the variation in the coordination number of the two oxidation states of europium across the cell in Figure 5.11. The coordination number of the smaller Eu^{3+} ion (red circles) drops to around 3-4 at z positions in between the two Eu^{3+} density peaks (solid red line). Conversely, the coordination number of the Eu^{2+} ions rises to over 7 in the same region, and consequently europium ions in the lower oxidation state will have a greater thermodynamic propensity for desorption and adsorption.

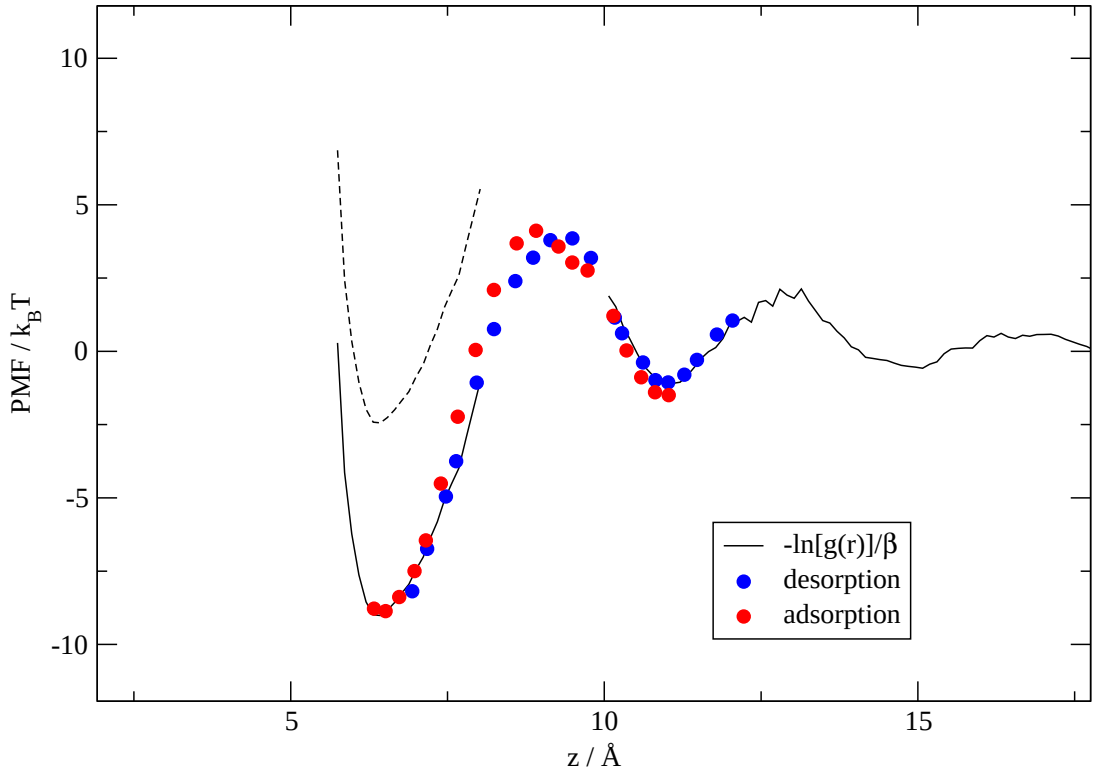

Figure 5.17: The potential of mean force (PMF) obtained *via* an umbrella sampling methodology for a Eu^{3+} ion with initial conditions appropriate to electrode desorption (blue circles) and electrode adsorption (red circles). These results show almost no hysteresis. The black line represents the PMF calculated through Equation 5.2. The density profiles in the z-range $\sim 8-10$ Å are excluded from the calculation of this latter PMF due to poor statistics; and the curve in the range $z < 8$ Å has been vertically shifted to bring its minimum into agreement with the corresponding umbrella sampling data. The dashed line indicates the unshifted position: this vertical shift of $6\,k_BT$ is a measure of how far the system is from its fully equilibrated interfacial structure.

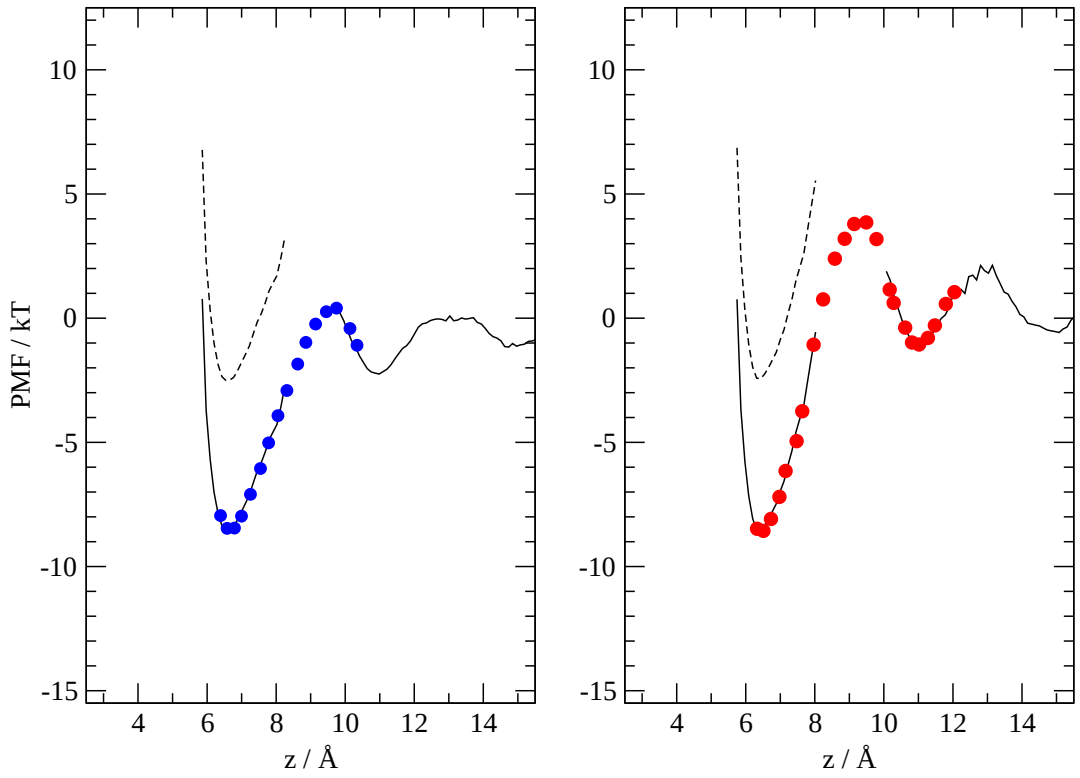

Figure 5.18: The potential of mean force (PMF) obtained *via* an umbrella sampling methodology for a Eu^{2+} (blue circles) and Eu^{3+} (red circles) averaged over the initial conditions appropriate to electrode desoprtion and adsorption. It is apparent that the barrier height for desorption of Eu^{2+} ($\sim$ $8.9\,k_{\mathrm{B}}T$) is lower than that of Eu^{3+} ($\sim$ $12.6\,k_{\mathrm{B}}T$). The black lines represent the correspoding PMFs calculated through Equation 5.2. The density profiles in the z-range $8 - 10\,\text{Å}$ are excluded from the calculation of these latter PMFs due to poor statistics; and the curves in the range $z < 8\,\text{Å}$ have been vertically shifted to bring their minima into agreement with the corresponding umbrella sampling data. The dashed line indicates the unshifted positions: the vertical shift of the black curve in both panels is $\sim 6\,k_{\mathrm{B}}T$.

6

Marcus free energy curves

6.1 Introduction

The remit of the work reported in this chapter is to calculate the free energy surfaces of the redox ions in our ionic melt, and to investigate their dependencies on the coordinates of the ion and the potential applied at the electrode. We will thereby establish whether the Marcus linear response description is appropriate to our system, and facilitate a computation of the exponential term in the rate constant expression (see Equation 1.56). The method we employ is that detailed in Chapter 4, which takes the vertical energy gap as the reaction coordinate. We end the chapter by tracking the coordination sphere of the redox ion as it changes with the reaction coordinate.

6.2 Zero applied potential

In Figure 6.1 we plot the normalized probability distributions for the oxidation and reduction steps in a cell with an applied potential difference of zero. The energy gaps are obtained from the difference between the total interaction energies calculated before and after the $Eu^{2+} \rightarrow Eu^{3+}$ and $Eu^{3+} \rightarrow Eu^{2+}$ events. These are combined with an energy constant to represent the ionization energy of the ion and the work function of the metal $I + \delta qW$; a value of $0.5951\,\mathrm{H}$ ($\simeq 16\,\mathrm{eV}$) is added to the oxidation energies and subtracted from the reduction

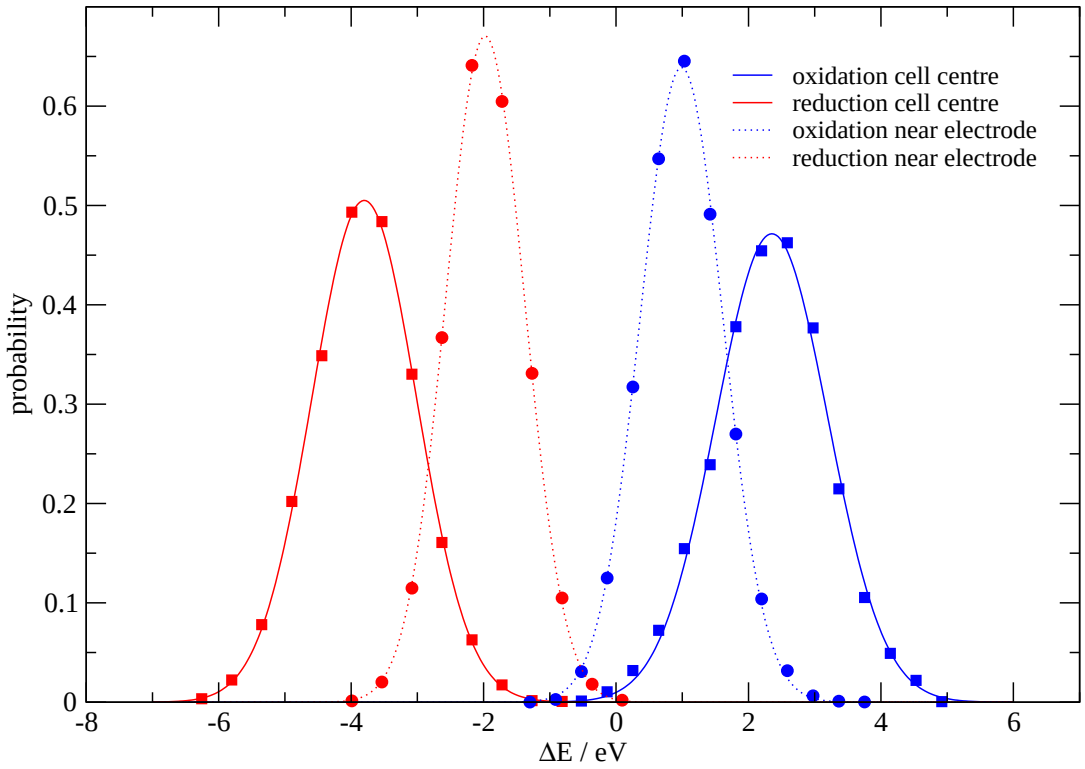

Figure 6.1: Probability distributions for ΔE with the applied potential equal to zero for both the oxidation ($\Delta E = \delta E_{\mathrm{Eu}^{2+}\rightarrow\mathrm{Eu}^{3+}+\delta q(\Psi)} + I + \delta qW$) and reduction ($\Delta E = -\delta E_{\mathrm{Eu}^{2+}\rightarrow\mathrm{Eu}^{3+}+\delta q(\Psi)} + I + \delta qW$) steps calculated for ions within layers in the centre of the cell (squares) and near the anode surface (circles). The lines are Gaussians chosen to pass through the data points.

energies. The constant offset is chosen to bring the relative mean free energies of the oxidized and reduced forms into agreement with experimental results for this system [3]. The abscissa in the figure is the energy gap ΔE, which we again stress is defined as the energy gap for the oxidation process; and the ordinate is the probability of obtaining a given energy gap $P_{\mathrm{Eu}^{2+}}(\Delta E = \delta E_{\mathrm{Eu}^{2+}\rightarrow\mathrm{Eu}^{3+}+\delta q(\Psi)} + I + \delta qW)$ or $P_{\mathrm{Eu}^{3+}+\delta q(V)}(\Delta E = -\delta E_{\mathrm{Eu}^{3+}+\delta q(\Psi)\rightarrow\mathrm{Eu}^{2+}} + I + \delta qW)$. The data represent ions in planar slabs 2.65 Å thick at distances d of 2.66 Å and 18.53 Å from the left-hand electrode, *i.e.* close to the electrode surface and in the centre of the simulation cell. The figure demonstrates that the probability distributions are Gaussian in shape which

accords with the predictions of Marcus linear response theory. There is also a marked dependence of the energy gap on the distance from the electrode, since the positions of the maxima in the probability distributions close to and far from the electrode are very different. Furthermore, the widths of the distributions are seen to be dependent on the distance from the electrode.

We can relate the dependence of the mean energy gap on the position of the redox ion in the cell to the image charge effect introduced in Section 2.3. The effect of the image charges on the vertical energy gap can be envisaged by considering the charge transfer process from the perspective of a redox ion immersed in the fluid at a certain distance d from the electrode. If this were a Eu^{2+} ion being oxidised to Eu^{3+} a unit positive charge would be created at the position d. When we variationally obtain the wall charges we transfer a unit negative charge to the electrodes and allow the electrode to polarize in response to the newly-created unit positive charge at position d. We recall that in the *diabatic* description of the charge transfer process the positions of the melt ions do not relax after the excitation event, and consequently the interaction between the newly-created image charge and the change in charge of the redox ion is not screened. This interaction depends on the inverse distance from the electrode d and on the square of the charge created, and so effects a decrease in the value of the excitation energies δE_i for both oxidation and reduction processes. To understand why both probability distributions in Figure 6.1 move to the origin of ΔE as redox processes nearer to the electrode are sampled, we must further recall that $\Delta E = +\delta E_{\mathrm{Eu}^{2+}\rightarrow\mathrm{Eu}^{3+}+\delta q(\Psi)} + I + \delta qW$ and $\Delta E = -\delta E_{\mathrm{Eu}^{3+}+\delta q(\Psi)\rightarrow\mathrm{Eu}^{2+}} + I + \delta qW$.

The assertion that the image effect is responsible for the shift in energy gap with position in the cell is apodeictic. The contribution of the image interactions to the vertical energy gap will depend on the position of the redox ion in the same manner as the energy associated with the creation of a unit charge at the same position in an otherwise empty cell, *i.e.* with electrodes but in the absence of all the melt ions. Figure 6.2 is a scatter plot of the vertical gap energies collected at different positions z across the cell, superposed on which is a line representing the energy associated with the creation of a unit charge at the point z in an empty cell of the same dimensions. It is apparent that the position-dependence of the latter is the same as that of

the mean gap energies and hence that the image interactions are directly responsible for the observed position-dependence of the gap energies.

Armed with the probability distributions for ΔE we construct in Figure 6.3 the Marcus free energy curves through Equations 4.29, 4.44, and 4.45. Given that the probability distributions were seen in Figure 6.1 to be Gaussians, it is apparent from the form of Equations 4.44 and 4.45 that the corresponding Marcus curves will be harmonic about the mean values of the reaction coordinate for the oxidation and reduction processes, respectively $\langle \Delta E_1 \rangle$ and $\langle \Delta E_2 \rangle$. We related in Chapter 4 how this scenario is consistent with the fundamental assumption within Marcus theory that the medium surrounding the redox ion responds linearly to the change in charge and interaction potentials upon excitation. We show as solid lines in Figure 6.3 the parabolae predicted from this linear response assumption, which are characterized by Equations 4.35–4.38.

There is seen to be a close marriage between the data points and the quadratic curves, even well away from the equilibrium positions. Note that the ability to sample the curves away from their minima (through Equation 4.29) means that we can obtain the Helmholtz free energy at the crossing point, which determines the kinetics of the electron transfer event[1]. We again stress that the parabolae are not fits, but rather predictions determined solely from the positions of the peaks of the probability distributions, $\langle \Delta E_1 \rangle$ and $\langle \Delta E_2 \rangle$. Consequently Figure 6.3 demonstrates that the linear response limit is applicable to our data: both that collected from redox ions close to the wall and in the middle of the cell. And this despite the observation that $\langle \Delta E_1 \rangle$ and $\langle \Delta E_2 \rangle$ depend strongly upon the distance from the electrode due to the image interactions. Further, the position-dependence of the widths of the probability distributions in Figure 6.1 is seen to be contained within the linear response description and is a direct consequence of the effect of the image interaction on the energy gaps.

That our system exhibits linear response behaviour is consistent with observations on aqueous systems. The potentials describing the interaction of the Eu^{2+} and Eu^{3+} ions with the Cl^- ions were chosen such that the cations had similar coordination shells. Studies of aqueous systems have shown that this condition is conducive to a linear response [80, 91].

[1]To be strictly accurate, it can be understood from Figure 6.3 that Equation 4.29 is only necessary to calculate the Helmholtz free energy at the crossing point appropriate to ions in the centre of the cell.

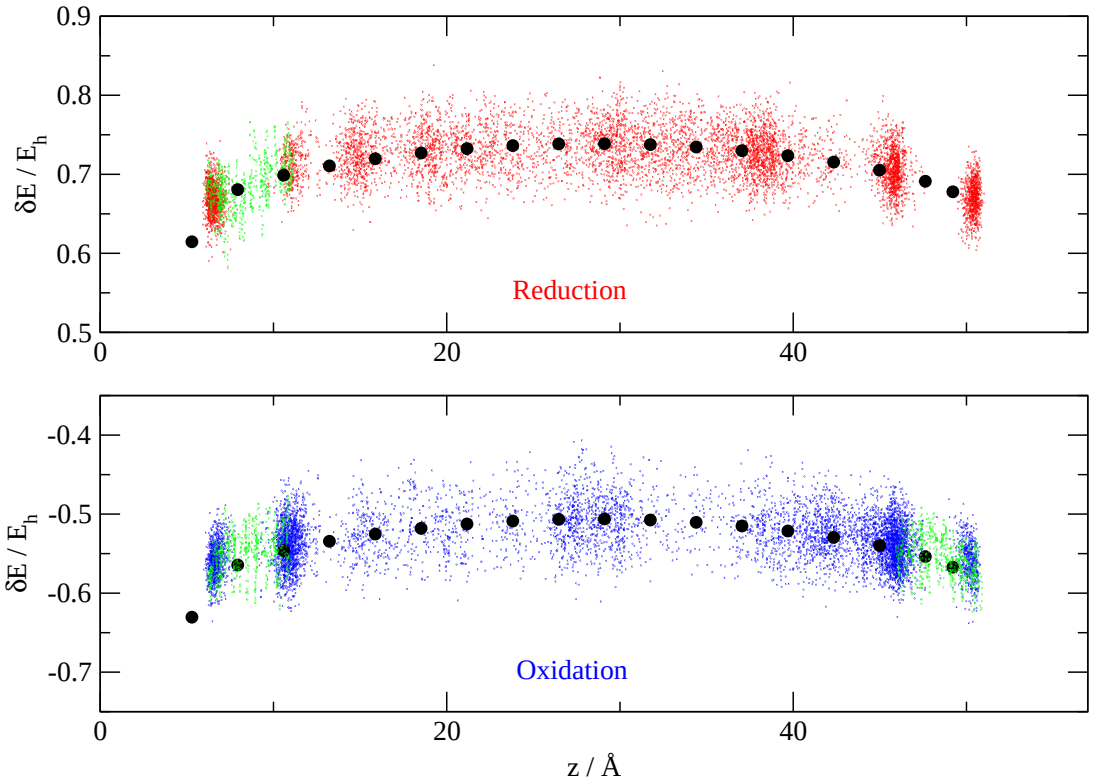

Figure 6.2: Scatter graph showing the vertical energy gaps obtained for individual $Eu^{3+} + \delta q(\Psi = 0.00\,V) \rightarrow Eu^{2+}$ events, upper set of points, $Eu^{2+} \rightarrow Eu^{3+} + \delta q(\Psi = 0.00\,V)$, lower points, for ions at different positions z across the cell with a zero applied potential. The green points are the vertical energy gaps obtained *via* the umbrella sampling method detailed in Chapter 5. The black circles show the total Coulomb energy (offset by an arbitrary constant) for moving an isolated point charge across an empty cell. The shape of this is seen to describe well the dependence of the mean gap energy on z.

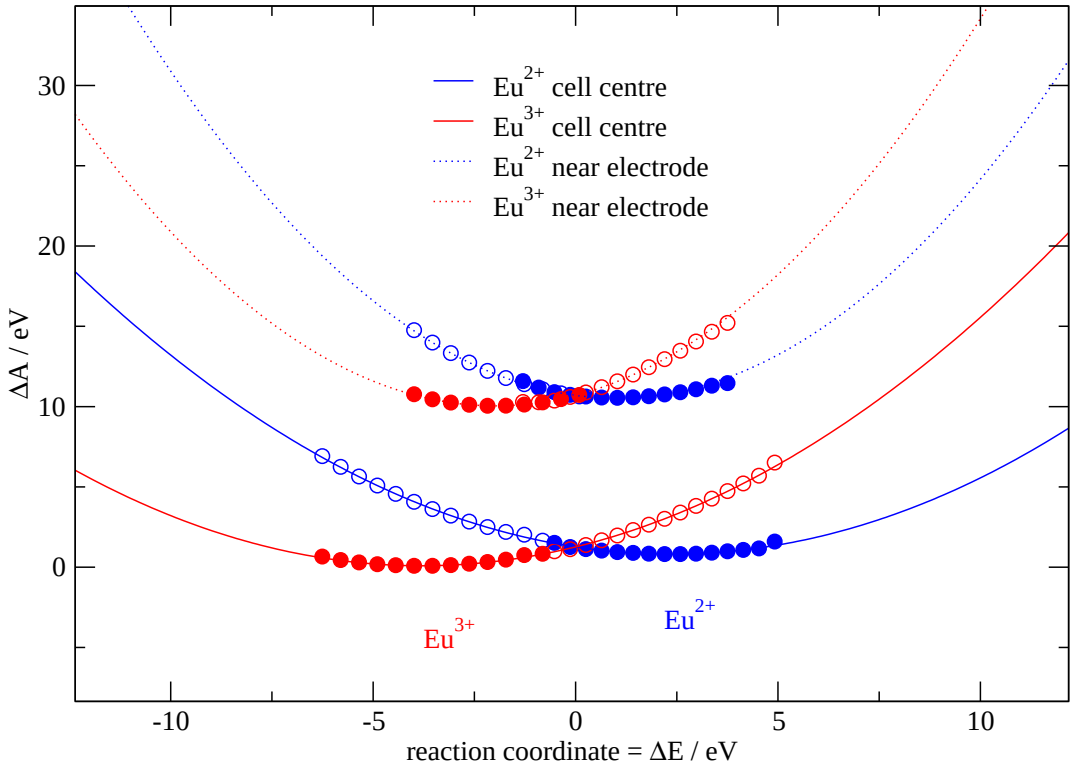

Figure 6.3: Marcus free energy curves $A_{\mathrm{Eu}^{3+}}(\Delta E)$, red, and $A_{\mathrm{Eu}^{2+}}(\Delta E)$, blue, obtained from the probability distributions shown in Figure 6.1. The filled symbols indicate the values close to the minima obtained using Equations 4.44 and 4.45, whilst open symbols, far away from the equilibrium configurations, are obtained by the application of Equation 4.29. The continuous lines are quadratic curves obtained from Equation 4.35; note that their extensions pass through the open symbol points indicating that these Marcus curves are harmonic, even well away from the equilibrium positions. In plotting this data we have set $I + \delta qW$ to 0.5951 eV. The curves for ions near the anode have been displaced upwards by 10 eV for clarity.

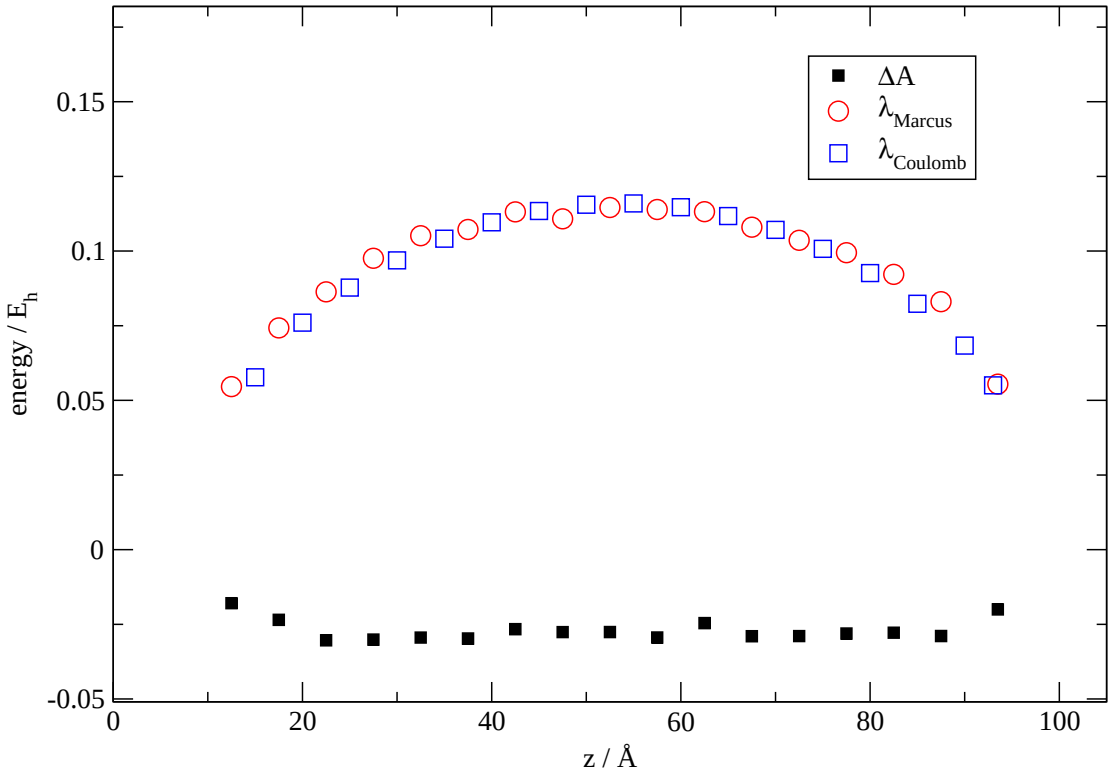

Figure 6.4: Variation of the reaction free energy ΔA (black squares) and the reorganization energy λ (red circles) across the cell. The blue squares show the variation of the total Coulomb energy, offset by a constant, as a single test charge is moved across an empty cell, which corresponds to the energy associated with the image charge effects.

It is usual to describe the Marcus curves in terms of the Helmholtz reaction free energy ΔA and the reorganization energy λ, see Figure 1.14. We plot in Figure 6.4 these quantities as a function of the position of the redox ion using Equations 4.42 and 4.43 from Chapter 4; note that ΔA here corresponds to the reaction at the anode. Because the image effect contributes to $\langle \Delta E_1 \rangle$ and $\langle \Delta E_2 \rangle$ with equal magnitude and opposite sign, we can see from Equations 4.42 and 4.43 that it should affect the reorganization energy λ but not the free energy ΔA.

The Marcus expression for the reorganization energy of a charge in a dielectric medium at

a distance d from a metallic surface was given in Chapter 1:

$$\lambda_o = e^2 \left[\frac{1}{\epsilon_\infty} - \frac{1}{\epsilon_s}\right] \left[\frac{1}{2a} - \frac{1}{2d}\right]. \qquad [1.69]$$

This casts the position-dependence of the image effect contribution as that expected for a charge in a vacuum, *i.e.* $(2d)^{-1}$, multiplied by the nonelectronic part of the dielectric response $(\epsilon_\infty^{-1} - \epsilon_s^{-1})$. We cannot make a direct comparison with this expression because our sample geometry is periodic in the transverse direction and has *two* metallic surfaces. We can however directly compare with the effective image interaction in our periodic system, *viz.* the position-dependent energy of a charge introduced into a vacuum. This is represented by the blue squares in Figure 6.4, which reveal that the equivalent of the dielectric response factor in our reorganization energy is unity.

In Section 1.7 we used Marcus theory to obtain an expression for the transfer coefficient, α, of Butler Volmer theory as a function of the applied potential (see Equation 1.70). We noted that although it is clear that the geometry of the intersection of the free energy profiles changes with potential, the Butler Volmer model cannot be used to predict the form of such a dependence, and indeed the classical formalism considers α to be a potential-independent factor. We have now established how the reorganization energy, λ, varies with the position of the redox ion in the cell, so we can use Equation 1.70 to predict the position dependence of α[1].

A dielectric response factor $(\epsilon_\infty^{-1} - \epsilon_s^{-1})$ of unity was also found by Lynden-Bell on examining homogeneous electron transfer in ionic liquids [92], and by Reed *et al.* on investigating heterogeneous electron transfer in an ionic melt [63]. This can be rationalized by regarding the effective static dielectric constant of the conducting medium as infinite, and ϵ_∞ as equal to unity. This latter assumption is appropriate to the work described in references [92] and [63] because the ions therein are not polarizable; however with our polarizable anion model, we would expect the value for ϵ_∞ to be greater than 1, and a consequent reduction in the curvature of $\lambda(z)$. That this is not the case is evidenced by Figure 6.4.

Blumberger and Lamoureux [93] are the only other people to our knowledge to have ex-

[1]We recall from Figure 6.4 that the Helmholtz reaction free energy is position dependent in the immediate vicinity of the electrodes, and so this factor will also contribute to the change in α with position of the redox ion.

amined the effect of a polarizable ion model on the reorganization free energy for electron transfer reactions. Their simulated system consists of two hexa-hydrates, $Ru(II)(H_2O)_6$ and $Ru(III)(H_2O)_6$, constrained at a fixed separation and solvated with $\sim$ 500 water molecules. They compute the reorganization free energy for the self-exchange reaction between Ru ions,

$$Ru^{2+} + Ru^{3+} \rightarrow Ru^{3+} + Ru^{2+}, \tag{6.1}$$

for three different polarizable water models, and compare with the reorganization free energy obtained with unpolarizable water molecules. The two Ru ions and their primary solvation spheres (defined as the "solute") are treated as unpolarizable throughout. They calculate the reorganization energy through Equation 4.43:

$$\lambda = \frac{1}{2}\left(\epsilon_{\mathrm{A}} - \epsilon_{\mathrm{B}}\right) = \epsilon_{\mathrm{A}} = \left\langle \Delta E \right\rangle_{\mathrm{A}}, \tag{6.2}$$

where $\epsilon_{\mathrm{A}} = -\epsilon_{\mathrm{B}}$ as appropriate to a self-exchange reaction, and the last equality recalls Equation 4.37. Marcus theory predicts the outer-sphere ("solvent") contribution to the reorganization energy of homogeneous electron transfer through an analogy of Equation 1.69:

$$\lambda_o = e^2 \left[\frac{1}{\epsilon_\infty} - \frac{1}{\epsilon_s}\right] \left[\frac{1}{2a_1} + \frac{1}{2a_2} - \frac{1}{d}\right], \tag{6.3}$$

where a_1 and a_2 are the radii of the spherical solute cavities, and d is the ion–ion separation. Taking $\epsilon_\infty = 1.6$ and $\epsilon_{\mathrm{s}} = 80$ for their polarizable water models, and $\epsilon_{\mathrm{s}} = 92$ for unpolarizable water, Equation 6.3 predicts that the reorganization energy obtained with a polarizable solvent will decrease by a factor of $(1/1.6 - 1/80)/(1 - 1/92) = 0.62$ (38%) relative to that obtained with an unpolarizable solvent. Two of the polarizable water models effect reductions in λ which are markedly less than that predicted by Equation 6.3 (11% and 22%), whilst the third model results in a 5% *increase*. This confirms that continuum theory predicts a stronger dependence of solvent reorganization on the infinite frequency dielectric constant than what is obtained from atomistic simulation. Further, the degree of reduction in the reorganization energy obtained

from simulation depends markedly on the polarizable model used.

We next separated out the contribution that the polarizability of the anions makes to the position dependence of the mean energy gaps. The results are shown in Figure 6.5 for the reduction process. The red circles represent the mean energy gaps across the cell after implementing a conjugate gradient minimization of the wall charges but without allowing the ions to polarize in response to the charge transfer event (*i.e.* the RIM result), whilst the blue circles show the same quantity after carrying out a subsequent conjugate gradient minimization of the anion dipoles (*i.e.* the DIPPIM result[1]). The green circles show the total Coulomb energy associated with moving an isolated point charge across the cell (the same data set which appeared in both Figures 6.2 and 6.4). It can be seen that the effect of the polarization of the anions is to reduce the magnitude of the mean energy gaps by a value which is independent of the position of the redox ion. In other words, the introduction of polarization effects has offset the mean energy gaps curve in Figure 6.5 (an additive effect), but it has not scaled its curvature (a multiplicative effect) in the manner predicted by Equation 1.69[2].

This is undoubtedly an area for further study, which should *inter alia* seek to clarify the significance of the spurious lateral interactions necessarily included in a periodic calculation of the vertical energy gap. The energy which Equation 1.69 describes is related to the interactions which appear in Figure 6.6 labelled U_{1a} and U_{1b}; these energies are functions of both ϵ_∞ and d. However, it is apparent that any calculated vertical energy gap will contain two types of spurious lateral interaction. First, any newly-created unit charge in the melt will interact (unscreened) with its periodic images in the infinite x and y directions. There will be an infinite number of periodic images; one such interaction is shown in Figure 6.6 and labelled U_2. The total contribution to the vertical energy gap of these lateral interactions will be ϵ_∞-dependent, but d-independent. Second, an image charge in the electrode will interact with its periodic images

[1]The blue circles represent in fact a mean of *approximations* of the individual vertical energy gaps in Figure 6.2, in which latter data set the wall charge and subsequent anion dipole conjugate gradient minimizations were performed over seven iterations to achieve convergence.

[2]Strictly speaking, we are not making a direct comparison here: Equation 1.69 describes the reorganization energy, whereas in Figure 6.5 we are plotting the mean energy gap for the reduction process. We could have additionally performed the calculation reported in Figure 6.5 for the oxidation process, and then calculated the reorganization energy through Equation 4.43 for both the RIM and DIPPIM: this would have facilitated a more direct comparison with Equation 1.69.

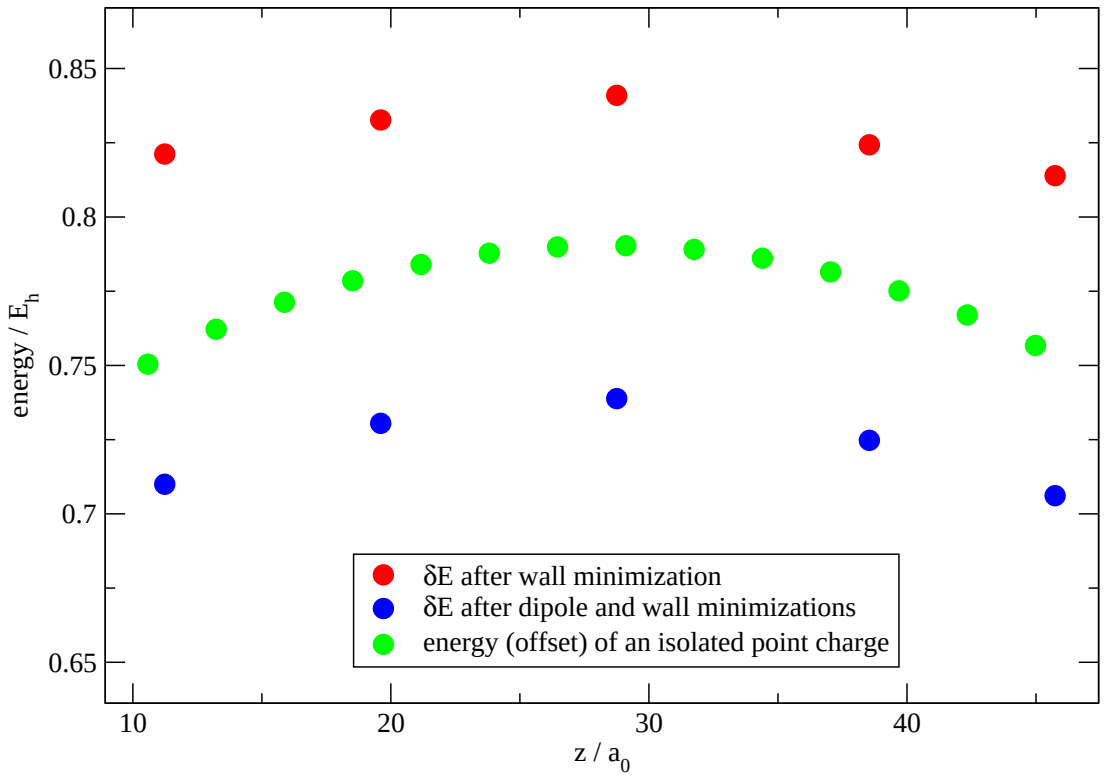

Figure 6.5: Mean energy gaps for the $Eu^{3+} + \delta q(\Psi^+ = 0.00\,V) \rightarrow Eu^{2+}$ reduction at different positions z across the cell with a zero applied potential: (i) after the wall minimization only (red circles) (ii) after both the wall and dipole minimizations (blue circles). The green circles show the total coulomb energy (offset by an arbitrary constant) for moving an isolated point charge across an empty cell.

in the infinite x and y directions. There will also be an infinite number of these interactions; one is shown in each electrode in Figure 6.6, where they are labelled respectively U_{3a} and U_{3b}. The total contribution to the vertical energy gap of this type of lateral interaction will be ϵ_∞-independent, but d-dependent (in a way which reflects the change in the magnitude of the image charge itself with d). The effect of introducing polarization on the interaction U_1 could be masked if the lateral interactions U_3 are significant contributions to the total calculated vertical energy gap. Clearly, any lateral contribution will increase in significance as the size of the simulation cell in the x and y directions decreases, and as the ion approaches the centre of the cell.

It can be seen in Figure 6.4 that ΔA is a constant across the simulation cell except in the immediate vicinity of the electrodes. That the oscillations in the Poisson potential are not reflected in ΔA suggests that this is not the potential which describes the changes in the energy levels of an ion induced by charges on other ions and a nearby electrode. Indeed, the mean electrical (Poisson) potential is the potential experienced by an infinitesimal test charge added to the system, whereas it is the Madelung potential which is the potential at an ion's center due only to the other charges. Notwithstanding these considerations, the Poisson potential is invoked in all classical discussions of electrodic phenomena and the double layer description of the electrochemical surface [4, 35]. The difference between the Poisson and Madelung potentials is marked: compare Figures 5.5 and 5.9 in Chapter 5, and it can be seen that the shape of the latter accords much better with the position-independence of ΔA away from the immediate vicinity of the electrodes.

6.3 Applied potential difference

The results in the previous section were obtained from a system with an applied potential of zero. When a non-zero potential difference is applied there will be an additional contribution to the energy gap. Figure 6.7 presents (filled circles) the mean energy gaps for the oxidation $\langle \Delta E(\Psi, z) \rangle = \left\langle \delta E_{\mathrm{Eu}^{2+} \rightarrow \mathrm{Eu}^{3+}+\delta q(\Psi)} + I + \delta q W \right\rangle$ and reduction $\langle \Delta E(\Psi, z) \rangle = \left\langle -\delta E_{\mathrm{Eu}^{3+}+\delta q(\Psi) \rightarrow \mathrm{Eu}^{2+}} + I + \delta q W \right\rangle$ processes at different positions across the cell for a system

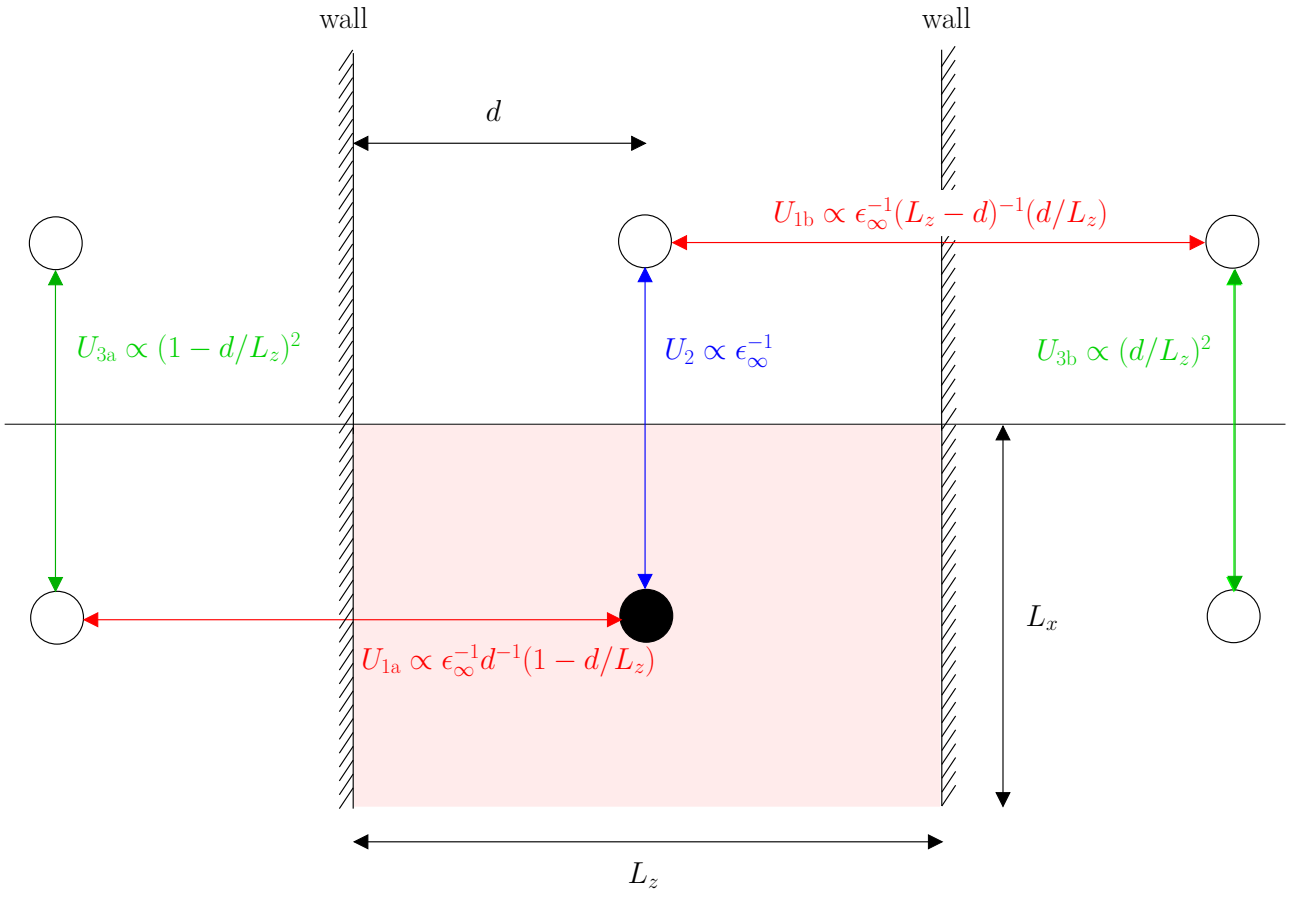

Figure 6.6: During the calculation of the vertical energy gap of a redox ion, a unit charge (filled black circle) is created in the central simulation box (shaded pink). This unit charge will interact with its image charges within both electrodes, without any screening from the melt ions. It is anticipated that these interactions (labelled U_{1a} and U_{1b}) will have the same dependence on ϵ_∞ and d as the energy described by Equation 1.69. However, the simulation is periodic in two dimensions (x and y), and consequently there will be spurious contributions to the calculated vertical energy gap arising from two types of lateral interaction. First, there are interactions between the unit charge and its *periodic* images (for example U_2): these are d-independent, but are anticipated to be ϵ_∞-dependent. Second, there are interactions between a wall image charge and its *periodic* images (for example U_{3a} and U_{3b}): these are ϵ_∞-independent, but d-dependent.

with a fixed anode potential of $\Psi^+ = 1.00\,\mathrm{V}$. The curvature of these plots is again a manifestation of the interaction of the newly-created unit charge with its image, which is an effect independent of Ψ. If we subtract this contribution to the energy gap (*i.e.* that associated with the creation of a unit charge at position z in an empty cell at zero potential, as illustrated in Figure 6.2) we obtain the sloping straight lines indicated by open circles.

On applying a non-zero potential difference across the cell we are modifying the electrical work of transferring the charge from the ion to the electrode by an amount equal to $\delta q \Psi^+(d)$. We recall from Figure 5.6 that the potential in the bulk of the material is perfectly screened from the electrode charges, so we might expect the vertical energy gaps in Figure 6.7 to be z-independent. The discrepancy arises because we model the electrode response adiabatically: when an ionic charge is changed ($Eu^{2+} \rightarrow Eu^{3+}$) the charge δq is transferred to *both* electrodes in a proportion which depends on the position of the ion in the cell. The constraint of constant potential difference is then instantaneously achieved through minimization of the electrode charges, which process mimics a flow of current through a battery. In the conventional description of electrochemical charge transfer, however, a whole electron is transferred to a single electrode, and the subsequent redistribution of charge *via* the external circuit to maintain constant potential is the electrical signal measured in experiment. This latter diabatic electrode response can be calculated from a knowledge of the change in charge on the anode ($\delta q_+(z)$) and cathode ($\delta q_-(z)$) for each electron transfer event. These quantities exhibit in Figure 6.8 a linear dependence on the position of the redox ion in the cell; $\delta q_+(z) + \delta q_-(z) = \delta q = +e^-$ or $-e^-$ for oxidation and reduction respectively. Application of potential Ψ^+ at the anode and Ψ^- at the cathode will therefore contribute the quantity $\delta q_+(z)\Psi^+ + \delta q_-(z)\Psi^-$ to the vertical energy gaps. Because Ψ^+ and Ψ^- are constants, and because $\delta q_\pm(z)$ vary linearly with z, this term accounts for the linear z-dependence observed in Figure 6.7. The correction for a diabatic electrode response to the transfer of a whole charge δq to the anode at potential Ψ^+ is

$$\delta E^{\mathrm{anode}} = \delta E - (\delta q^+ \Psi^+ + \delta q^- \Psi^-) + \delta q \Psi^+. \tag{6.4}$$

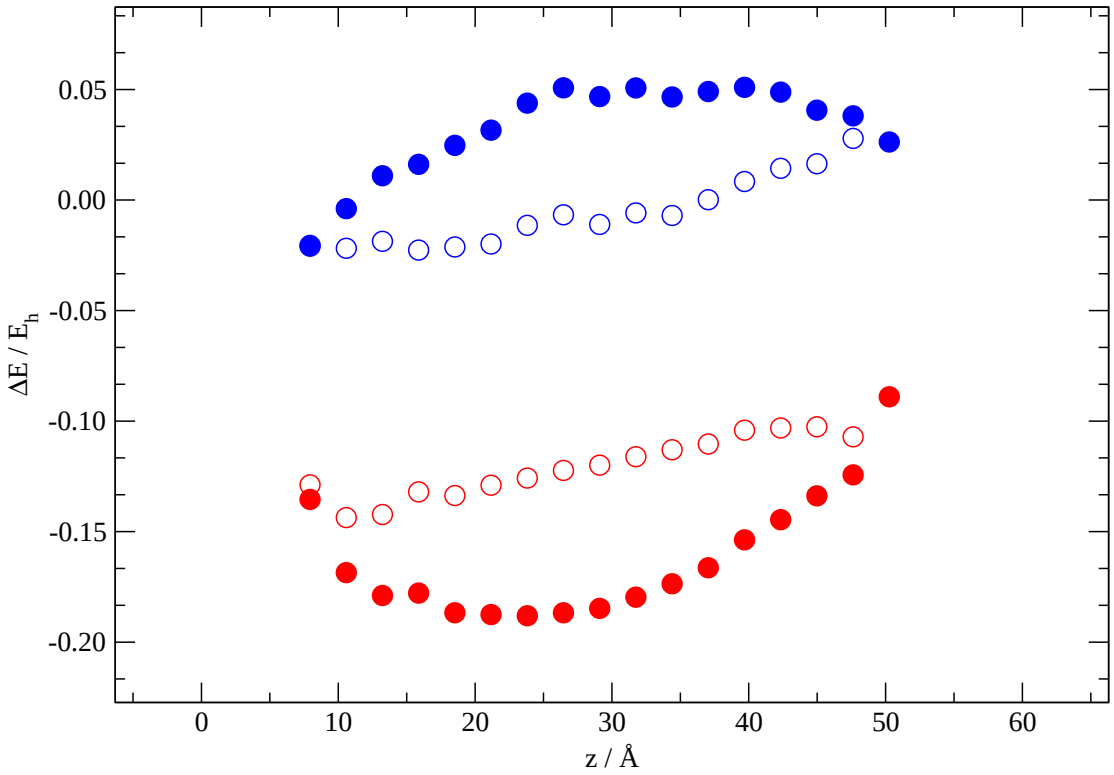

Figure 6.7: Variation of the mean energy gap with the position of the redox ion in the cell, z, for the $Eu^{2+} \rightarrow Eu^{3+} + \delta q$ (filled blue circles) and $Eu^{3+} + \delta q \rightarrow Eu^{2+}$ (filled red circles) processes with an applied potential at the anode of $\Psi^{+} = 1.0\,\mathrm{V}$. The open symbols show the mean energy gap but with the image contribution removed.

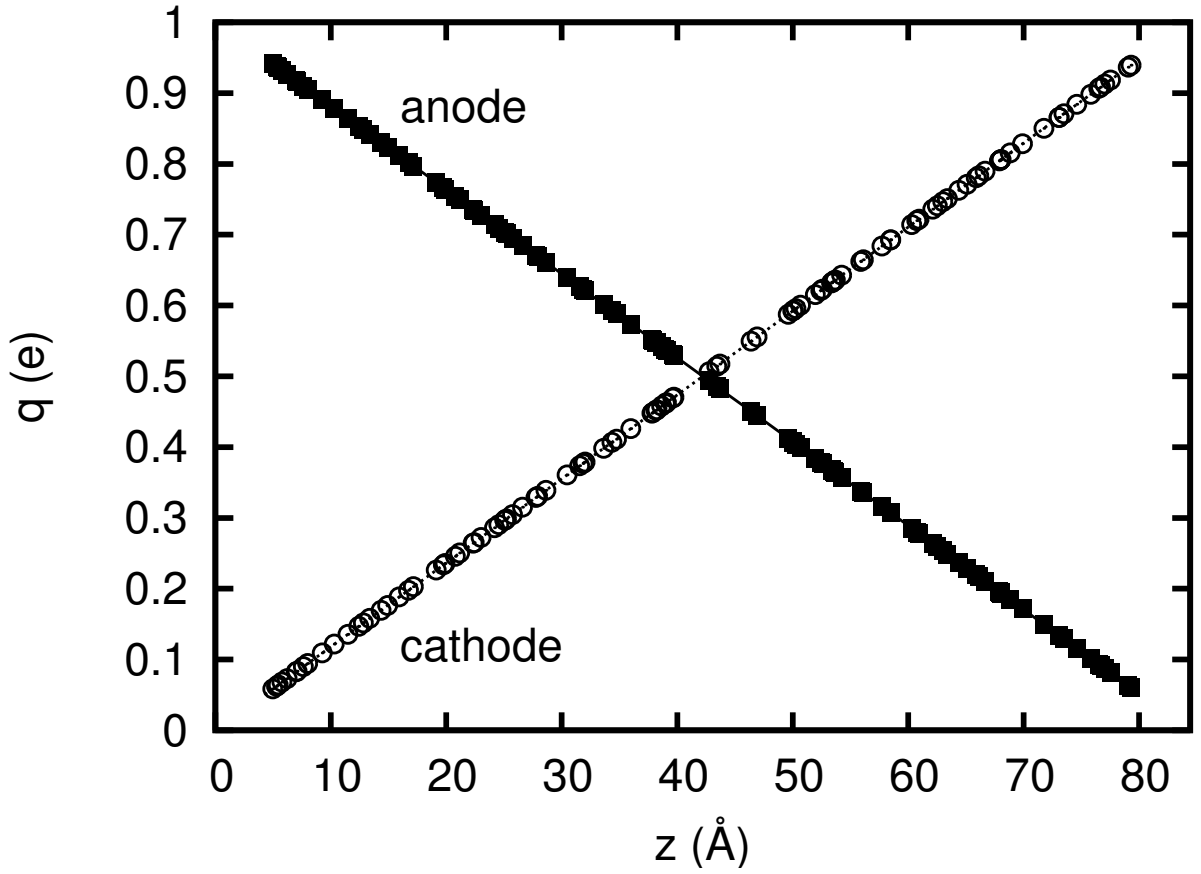

Figure 6.8: Fractional charges induced on the electrodes by the $Eu^{3+} + \delta q \rightarrow Eu^{2+}$ reaction on the anode (squares) and on the cathode (circles) in electron transfer events occurring at different positions z across the cell. The lines show the charges induced by placing a single test charge at z in an empty cell. Taken from reference [63].

The corrected energy gaps δE^{anode} for the oxidation and reduction events may be used to construct Marcus free energy curves in the same manner as for $\Psi^+ = 0.00\,\text{V}$ described above. Figure 6.9 presents the Marcus curves obtained with applied potentials of $\Psi^+ = 0.00\,\text{V}$ and $\Psi^+ = 1.00\,\text{V}$ when the redox ions are close to and far from the electrode. The quadratic curves appropriate to the linear response régime remain an accurate description of the energy surfaces. When the anode potential is changed from $\Psi^+ = 0.0\,\text{V}$ to $\Psi^+ = 1.0\,\text{V}$, the height of the minimum in the $\text{Eu}^{3+} + e^-$ curve shifts by 1 eV relative to the Eu^{2+} minimum. This indicates that the redox ion is perfectly screened from the electrode charges, because the change in reaction free energy on applying a non-zero electrode potential is seen to be equal to the change in energy of the electron resident on the electrode. This accords with the assumption inherent in Butler Volmer theory, which we highlighted in the discussion of Figure 1.12 in Section 1.5.

In Figure 6.10 we plot the dependence of the reorganization energy λ and reaction free energy ΔA on the cell position at anode potentials $\Psi^+ = 0.0\,\text{V}$ and $\Psi^+ = 1.0\,\text{V}$. (The $\Psi^+ = 0.0\,\text{V}$ data are reproduced from Figure 6.4 for comparison.) At non-zero applied potential, it is apparent that the curvature of $\lambda(z)$ remains described by the variation of the energy of a test charge as it is moved across an otherwise empty cell; in other words, the reorganization energy has no observable potential-dependence. And ΔA at $\Psi^+ = 1.0\,\text{V}$ is shifted by 1 eV with respect to ΔA at $\Psi^+ = 0.0\,\text{V}$, which confirms the linear dependence of ΔA on the anode potential which we noted in the discussion of Figure 6.9.

6.4 The transition state

Now that the Marcus free energy surfaces have been determined, it is possible to examine how the coordination structure of a europium ion changes as it undergoes a redox process. At frequent intervals along the MD trajectory the vertical energy gap (as reaction coordinate) is calculated for each europium ion in the configuration $\mathbf{R}^{\text{N}}$, as was detailed in Chapter 4. An ion can be identified as being in the transition state if it has a value of the reaction coordinate corresponding to the crossover of the free energy surfaces (labelled $x^\dagger$ in Figure 1.14). Similarly,

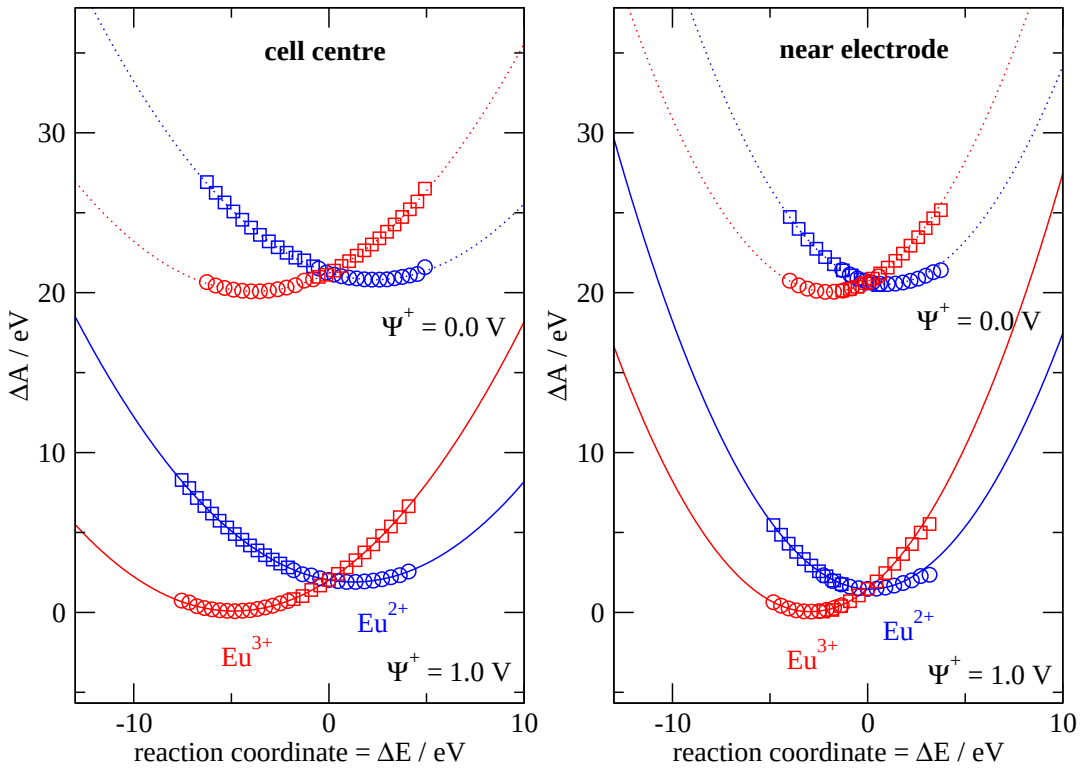

Figure 6.9: Marcus curves for layers 2.65 Å thick in the centre of the cell (left-hand panel) and near the electrode (right-hand panel) for anode potentials $\Psi^+ = 0.0\,\mathrm{V}$ and $\Psi^+ = 1.0\,\mathrm{V}$. The circles indicate the values close to the minima obtained using Equations 4.44 and 4.45, and the squares, far away from the equilibrium configurations, are obtained by the application of Equation 4.29. The continuous lines are quadratic curves obtained from Equation 4.35; note that their extensions pass through the square points indicating that these Marcus curves are harmonic, even well away from the equilibrium positions. In plotting this data we have set $I + \delta qW$ to 0.5951 eV. The curves corresponding to an anode potential of $\Psi^+ = 0.0\,\mathrm{V}$ have been displaced upwards by 20 eV for clarity.

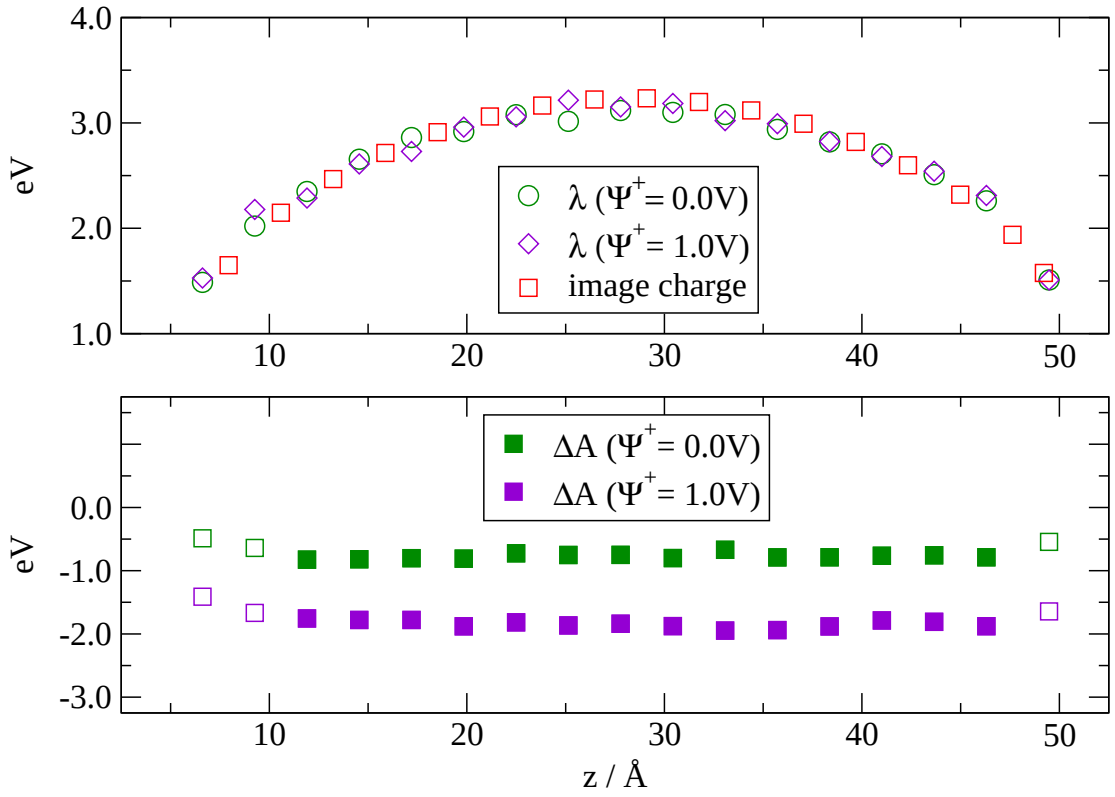

Figure 6.10: Dependence of the reorganization energy λ (top panel) and reaction free energy ΔA (bottom panel) on cell position at anode potentials $\Psi^+ = 0.0\,\mathrm{V}$ and $\Psi^+ = 1.0\,\mathrm{V}$. Also shown in the top panel is the variation of the energy (shifted by an additive constant) of a test charge as it is moved across an otherwise empty cell, which reflects the energy associated with the image charge effects in our simulations. The open squares in the bottom panel correspond to positions in the immediate vicinity of the electrode where ΔA becomes sensitive to z.

it is possible to identify a europium ion as being in the Eu^{2+} or Eu^{3+} ground state if it has a vertical energy gap corresponding to one of the respective free energy minima (labelled x_{Red} and x_{Ox} in Figure 1.14). In order to observe how the Eu-Cl bond length in the coordination complex changes during a redox process, we have calculated the Eu-Cl radial distribution functions (RDFs) associated with each of the reaction coordinates x_{Red}, $x^{\dagger}$, and x_{Ox}. The first peaks of the functions are shown in Figure 6.11. The ground state Eu^{3+}– Cl bond length of $\sim 2.60\,\text{Å}$ is seen to be shorter than the ground state Eu^{2+}– Cl bond length of $\sim 2.76\,\text{Å}$. This is the expected ordering as in the former case the metal ion is smaller and more highly charged, and the primary coordination sphere is consequently more compact. Ions can be identified as being in the transition state by having a vertical energy gap $\delta E_{\mathrm{Eu}^{2+}\rightarrow\mathrm{Eu}^{3+}+\delta q(\Psi)} = x^{\dagger}$ or alternatively $\delta E_{\mathrm{Eu}^{3+}+\delta q(\Psi)\rightarrow\mathrm{Eu}^{2+}} = x^{\dagger}$; consequently there are *two* RDFs computed for the transition state complex, but they give the same value for the Eu-Cl bond length of $\sim 2.68\,\text{Å}$. As is physically reasonable, this transition complex bond length is exactly equidistant from the two ground state bond lengths $Eu^{2+} - Cl$ and $Eu^{3+} - Cl$.

It is possible to qualitatively predict whether an electron transfer will be slow or fast by considering whether the difference in the reaction coordinates of Ox and Red is large or small. With all other factors remaining equal, it will be appreciated that the greater the difference in ground state reaction coordinates then the greater is the magnitude of the activation energy. Since the difference between the ground state reaction coordinates of Ox and Red is related to the change in bond length during the redox process, we can use the data obtained from Figure 6.11 to qualitatively predict how fast the electron transfer will be for our system. Listed in Table 6.1 are heterogeneous rate constants ($k/\mathrm{cm.s^{-1}}$) for a variety of electron transfer reactions.

The anthracene/anthracene radical anion couple

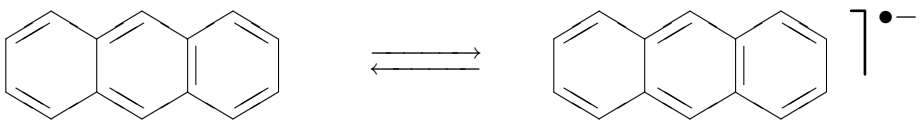

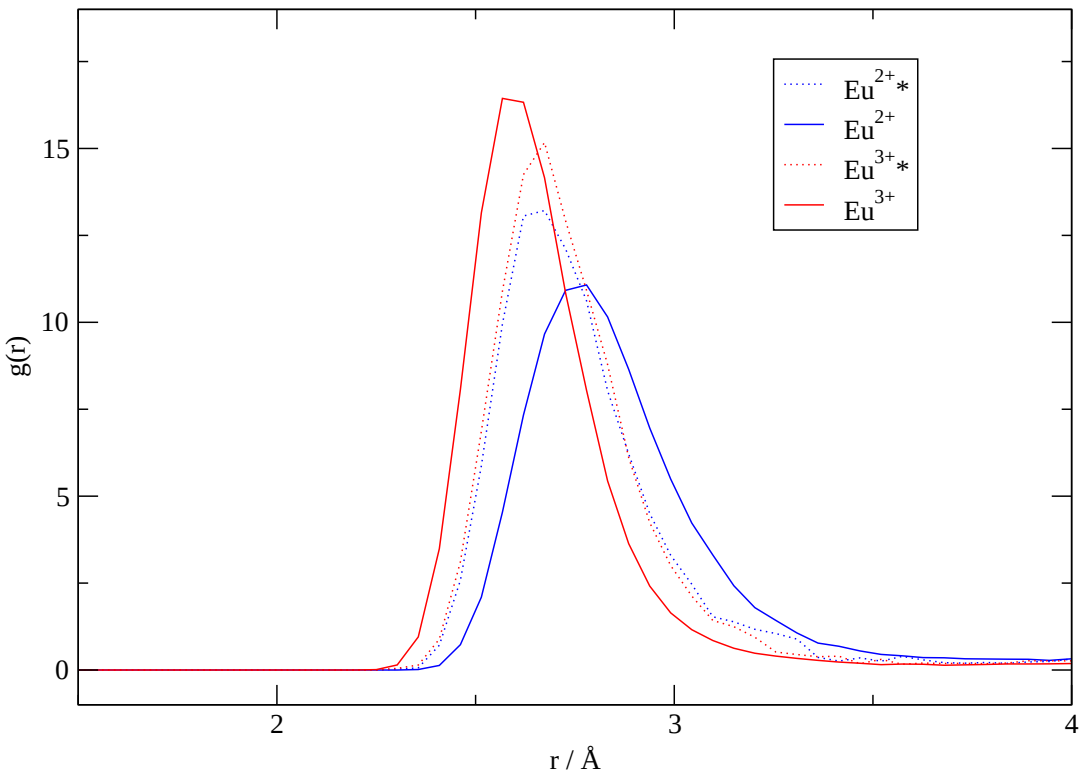

Figure 6.11: The Eu–Cl radial distribution functions for: (i) europium in its 2+ oxidation state at a reaction coordinate corresponding to the crossover of the Eu^{3+} and Eu^{2+} free energy curves (dotted blue); (ii) europium in its 2+ oxidation state at a reaction coordinate corresponding to the minimum of the Eu^{2+} free energy curve (solid blue); (iii) europium in its 3+ oxidation state at a reaction coordinate corresponding to the crossover of the Eu^{3+} and Eu^{2+} free energy curves (dotted red); (iv) europium in its 3+ oxidation state at a reaction coordinate corresponding to the minimum of the Eu^{3+} free energy curve (solid red).

Reaction	$k/\mathrm{cm.s^{-1}}$
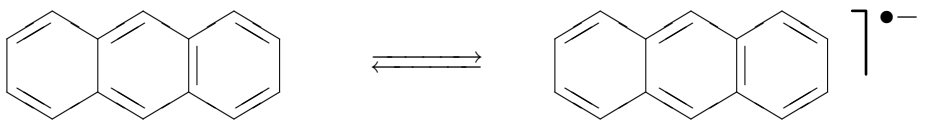	4[a]
$MnO_4^- + e^- \rightleftharpoons MnO_4^{2-}$	0.2
$Fe(CN)_6^{3-} + e^- \rightleftharpoons Fe(CN)_6^{4-}$	0.1
$Fe(H_2O)_6^{3+} + e^- \rightleftharpoons Fe(H_2O)_6^{2+}$	7×10^{-3}
$V^{3+} + e^- \rightleftharpoons V^{2+}$	4×10^{-3}
$Eu^{3+} + e^- \rightleftharpoons Eu^{2+}$	3×10^{-4}
$Co(NH_3)_6^{3+} + e^- \rightleftharpoons Co(NH_3)_6^{2+}$	5×10^{-8}

[a]In dimethylformamide

Table 6.1: The heterogeneous rate constant ($k/\mathrm{cm.s^{-1}}$) for various electrochemical reactions in aqueous solution at 25°C, unless otherwise stated. Taken from reference [94].

in dimethylformamide solution exhibits the fastest electrochemical rate constant, which reflects the closeness of the molecular geometry of the reactants and products. The electron in the anthracene radical anion is delocalized, and hence the bond angles are unchanged during the redox process, and the change in bond lengths is negligible. The activation barrier, such as it is, may derive from a change in solvation between anthracene and its radical anion.

The couple

$$MnO_4^- + e^- \rightleftharpoons MnO_4^{2-}$$

displays fast electrode kinetics because the reactants and products have the same tetrahedral geometry, and the Mn–O bond lengths are very similar: 1.63 Å in MnO_4^- and 1.66 Å in MnO_4^{2-}.

The ferrous/ferric couple $Fe(H_2O)_6^{3+} + e^- \rightleftharpoons Fe(H_2O)_6^{2+}$ shows somewhat more sluggish electrode kinetics. The geometry of both species is octahedral, but the Fe–O bond length changes from 2.21 Å in the Fe(II) species to 2.05 Å in the Fe(III) species. This is indeed the same difference in bond length as was computed for our system above. The rate constant of

the europium redox reaction in KCl melt was measured experimentally by Kuznetsov *et al.* [95] to be $3.10 \times 10^{-2}\,\mathrm{cm.s^{-1}}$ at 1073 K.

The couple $Co(NH_3)_6^{3+} + e^- \rightleftharpoons Co(NH_3)_6^{2+}$ displays pathologically slow electron transfer kinetics. The sluggishness of the electron transfer probably reflects not only the size of the activation barrier, but also the fact that the Co(II) complex has a high spin d^7 electron configuration, whereas the Co(III) complex has a low spin d^6 configuration. The redox process therefore entails a flip of electron spin, which is an improbable event.

7

The melt–electrode interaction potential

7.1 Introduction

The quality of intermolecular potentials is of paramount importance for accurate molecular simulations. Reliable interaction potentials between species in bulk liquid electrolytes are well established, however the potentials suitable at a metallic interface are less well researched. In this chapter we focus on generating accurate potentials between the melt species and the metal which subsume the many-body effects discussed in Chapter 2.

The first consideration in the ionic field of many-body effects was the shell model of Dick and Overhauser [96] which sought to account for the effects of dipole polarization. This was over five decades ago when the only source of information for the potential parameters was experimental. Subsequently *ab initio* methods were developed which enlarged the data set with which to determine functional forms and parameters, and provided information on systems for which experimental observables were not easily available.

The method outlined below is based upon the work of Laio *et al.* [97]. They constructed representative condensed phase configurations in periodic boundary conditions using MD simulations at some thermodynamic statepoint with an approximate potential, and also calculated the electronic structure *ab initio*. The potential was then refined by fitting its parameters to

minimize the difference between the classical and *ab initio* forces on the ions in these configurations.

Aguado *et al.* [98] used results from a wide range of electronic structure calculations to construct models for interionic forces and the multipoles on the ions due to their interactions. These developments ensure that the component parts of the interaction model faithfully reflect the component parts of the true interactions and also that the potential model will be reliable over a wider range of thermodynamic states and mixtures.

The possibility of applying this fitting methodology to the melt-electrode interactions in our electrochemical system is entirely dependent on our being able to model the polarization response of the electrode to the melt charges because this effect will be manifest in the *ab initio* results. Consequently it is imperative to allow the wall charges to vary during the fitting procedure in the manner described in Chapter 2.

We begin by outlining the overall strategy for fitting the melt–wall parameters in the DIPPIM. Next we describe the procedure for extracting the *ab initio* dipoles, which involves the construction of maximally localized Wannier functions (MLWFs) [99] from the Kohn-Sham orbitals. We then describe the incorporation of short-range dipole damping in our ionic picture of the melt–wall interactions, before illustrating the quality of the fit to the *ab initio* dipoles. Finally in Section 7.4 we present the quality of the fit of the remainder of the interaction model to the *ab initio* forces.

7.2 General strategy

The computational expense of *ab initio* electronic structure calculations requires that a smaller system is used for fitting the DIPPIM potential than the one investigated in Chapters 5 and 6. We use for this purpose a simulation cell consisting of 64 Cl^- ions and 64 Li^+ ions sandwiched between two parallel plates of Al in the face-centred cubic (FCC) lattice with the (100) face exposed to the melt. The potential fitting procedure, schematized in Figure 7.1, starts by equilibrating the system at 1200 K using the MD code with the potential parameters listed in reference [26]. This generates a configuration with which to initiate a short equilibration run

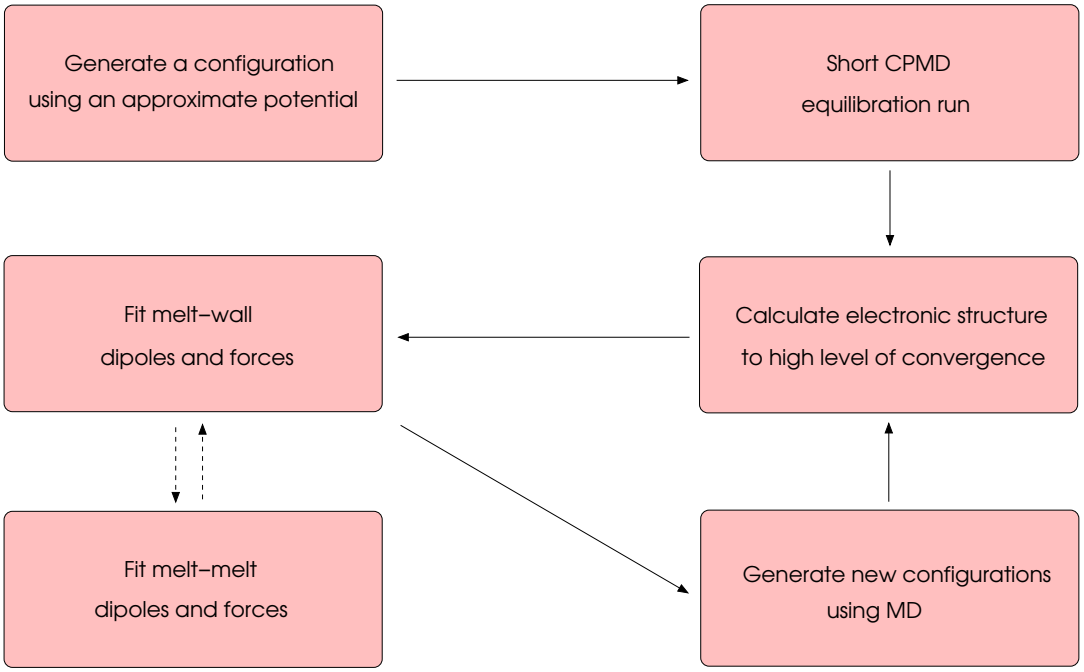

Figure 7.1: A schematic rendering of the potential fitting process.

using the *ab initio* CPMD code [100]. We can then refine our model for the melt–wall potential by simultaneously associating the *ab initio* forces and dipoles with those calculated using our ionic picture of the interactions.

The melt–wall potential can be further refined by generating additional configurations with the newly-determined potential, and using these in a subsequent round of force and dipole matching. This enlargement of the training set of configurations should improve the reliability of the potential model over a wide range of configuration space. As indicated in Figure 7.1, there is also the option of including in the fitting process the parameters governing the melt–melt interactions. The melt–melt and melt–wall parts of the interaction model are interdependent and should therefore be fitted iteratively.

We first fit the polarization parts of the melt–wall interactions by minimizing the objective function

$$A_{\mathrm{P}}\left(\{\chi_{\mathrm{P}}\}\right) = \sum_{i=1}^{N_{\mathrm{anion}}} \sum_{A=1}^{N_{\mathrm{config}}} \frac{\left|\boldsymbol{\mu}_i^{A,\mathrm{ai}} - \boldsymbol{\mu}_i^{A}\left(\{\chi_{\mathrm{P}}\}\right)\right|^2}{N_{\mathrm{anion}} N_{\mathrm{config}} \left|\boldsymbol{\mu}_i^{A}\left(\{\chi_{\mathrm{P}}\}\right)\right|^2} \,, \tag{7.1}$$

by varying the set $\{\chi_{\mathrm{P}}\}$ of parameters in the polarization parts of the DIPPIM appropriate to the melt–wall interactions. The index i runs over all the polarizable anions and the index A

labels the configuration. Therefore $\boldsymbol{\mu}_i^A\{\chi_\mathrm{P}\}$ is the dipole calculated from the DIPPIM for ion i in configuration A with the parameter set $\{\chi_\mathrm{P}\}$, and $\boldsymbol{\mu}_i^{A,\mathrm{ai}}$ is the corresponding *ab initio* value. A total of eight configurations were used, and the sum over i, α, and A thus involves 1536 terms. A simplex algorithm [101] is used to minimize the objective function, each iteration of which involves an evaluation of the wall charges and dipoles using the conjugate gradient algorithm discussed in Section 2.4. The choice of the set of parameters to be varied within the fit is discussed in Section 7.3.2.

The parameters which control the polarization effects are not allowed further variation during the subsequent force fitting process for which the objective function is

$$A_\mathrm{F}\left(\{\chi_\mathrm{F}\}\right) = \sum_{i=1}^{N_\mathrm{melt}} \sum_{A=1}^{N_\mathrm{config}} \frac{\left|\mathbf{F}_i^{A,\mathrm{ai}} - \mathbf{F}_i^A\left(\{\chi_\mathrm{F}\}\right)\right|^2}{N_\mathrm{melt} N_\mathrm{config} \left|\mathbf{F}_i^A\left(\{\chi_\mathrm{F}\}\right)\right|^2} \ , \tag{7.2}$$

which is a function of the set $\{\chi_\mathrm{F}\}$ of short-range melt–wall potential parameters. $\mathbf{F}_i^{A,\mathrm{ai}}$ denotes the force on ion i in the *ab initio* calculation on configuration A, and $\mathbf{F}_i^A(\{\chi_\mathrm{F}\})$ to that predicted from the DIPPIM with parameters $\{\chi_\mathrm{F}\}$ for the same configuration. The sum over i and A involves 3072 terms. We will discuss which melt-wall parameters are allowed to vary in the fits in Section 7.4.

The CPMD calculations were performed by Mathieu Salanne[1] using Troullier-Martins pseudopotentials [102] together with a kinetic energy cutoff of 952.37 eV on a 128 × 128 × 384 grid. The $3s^2$ and $3p^5$ electrons are included for each Cl^- ion whilst those in the first and second shells are pseudized; both 1s electrons appropriate to each Li^+ are included; and the $3s^2$ and $3p^1$ electrons are included for each Al atom with those in the first two shells pseudized. The planewave cutoff is considerably larger than would normally be used in order to ensure a high degree of convergence of the forces with respect to basis set size.

The *ab initio* code works in three-dimensional periodicity in contradistinction to the two-dimensional periodicity of the MD calculations. This necessitates a change in the positioning of the wall atoms on moving between the two periodicities. Each electrode in the MD system

[1]Mathieu Salanne, Université Pierre et Marie Curie-Paris6, CNRS, ESPCI, UMR 7612, laboratoire LI2C, case courrier 51, 4 Place Jussieu, 75252 Paris Cedex 05, France.

contains three layers of atoms arranged in the FCC lattice with the (100) plane exposed to the melt. A unit cell from each electrode is shown in red in the top panel of Figure 7.2, and we note that the relative positioning of the two electrodes is such that they are mirror images of each other. The starting configurations for the MD trajectory to be used in the training set are readied for CPMD by shifting one electrode relative to the other along the x-axis by a value equal to half of the FCC lattice constant ($a/2$). The *ab initio* system is periodically replicated in three dimensions, with an origin chosen such that there are in the unit cell six layers of atoms forming a single slab. These shifted positions are shown in blue in the lower panel of Figure 7.2. Whether or not the difference in periodicity between the two codes will prevent a satisfactory fit of the potential model will depend on the extent to which the metal screens the interaction between melt species on opposite sides of the electrode.

7.3 Calculation of and fitting to the *ab initio* dipoles

7.3.1 Calculation of the *ab initio* dipoles

The electronic wavefunctions output from the CPMD code are the delocalized and periodic Kohn-Sham orbitals. The calculation of dipole moments necessitates however a localized representation which associates orbitals with each ion. Aguado *et al.* [98] effected this *via* a Wannier transformation of the Kohn-Sham eigenvectors

$$w_n(\mathbf{r}) = \sum_{m=1}^{J} U_{mn} \left|\phi_m\right\rangle , \tag{7.3}$$

where the sum runs over all the Kohn-Sham states ϕ_i, and the unitary matrix $\boldsymbol{U}$ was determined by iterative minimization of the Wannier function spread

$$\Omega = \sum_{n=1}^{J} \left(\left\langle r^2 \right\rangle_n - \left\langle \mathbf{r} \right\rangle_n^2 \right) . \tag{7.4}$$

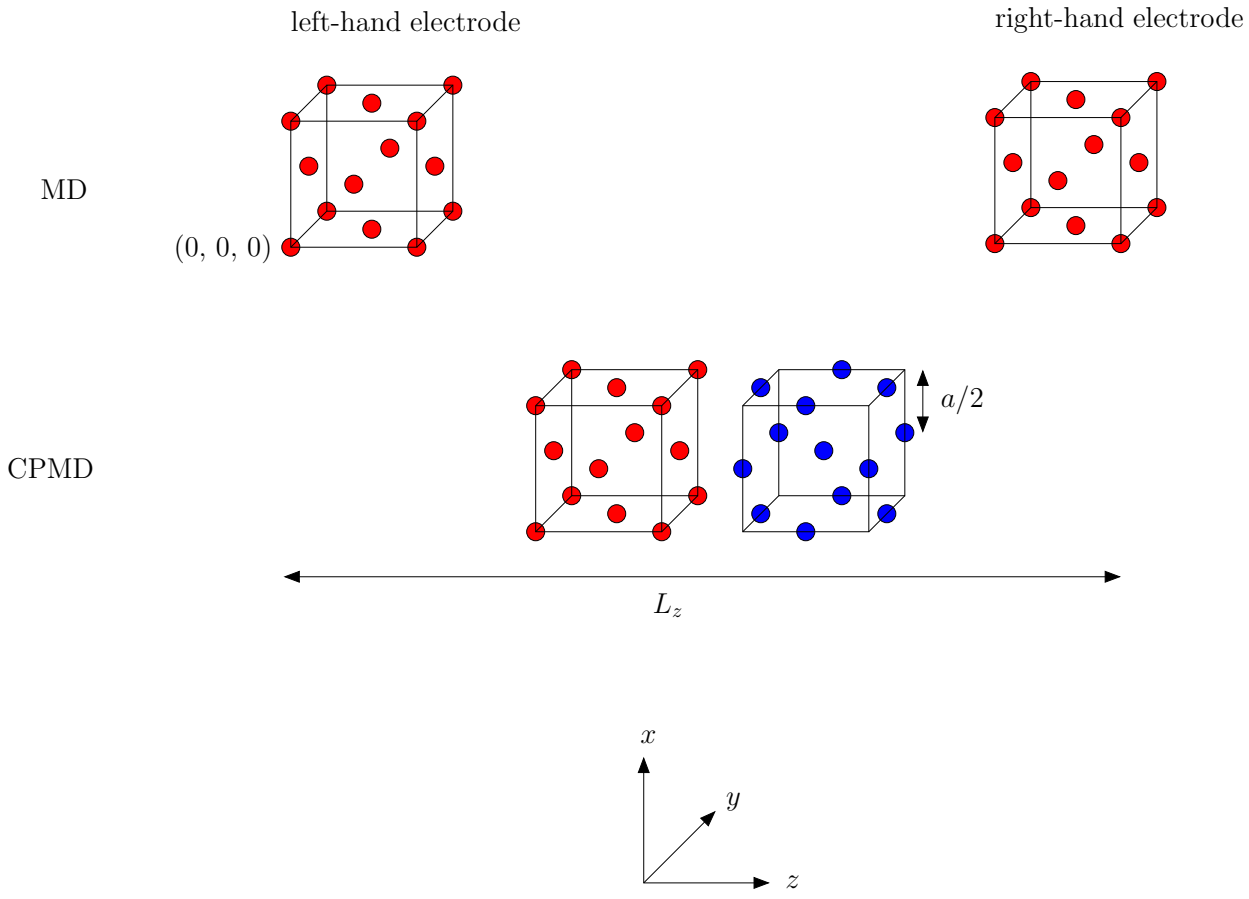

Figure 7.2: The CPMD system is periodically replicated in three dimensions whereas the classical MD system is finite in the z-direction. Consequently, the relative positioning of the two electrodes must be changed on moving between the different periodicities. This is so as to maintain the FCC lattice and is achieved by shifting one electrode along the x-axis relative to the other by half the FCC unit cell length $(a/2)$. The top panel shows in red one unit cell from each electrode in a configuration taken from an MD run. The corresponding CPMD configuration is shown in the lower panel. The blue atoms have been shifted along the x-axis, and the origin of the cell shifted such that there is a single six-layer slab centred at z-coordinate $(L_z/2)$.

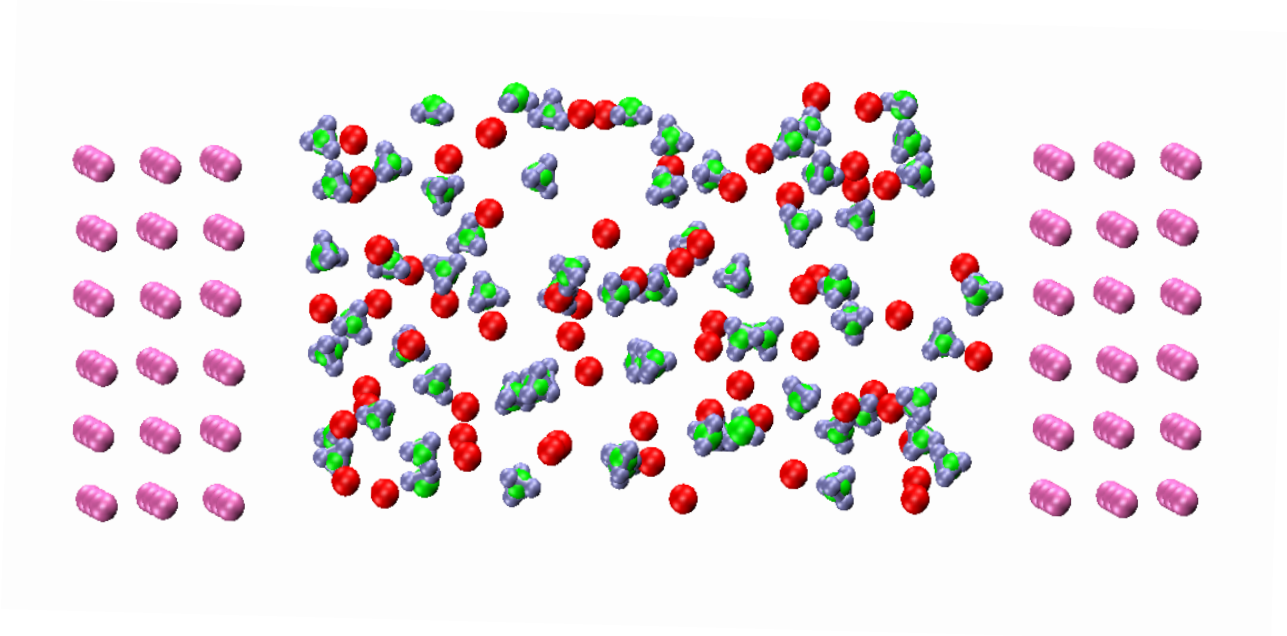

Figure 7.3: A rendering of the approximately tetrahedral distribution of MLWFs around each Cl^- ion. Green: Cl^- ions, blue: MLWFs, red: Li^+ ions, mauve: wall atoms.

The Wannier function centre positions were computed through [103, 104]

$$\mathbf{r}_n^\alpha = -\sum_{m=1}^{3} \frac{M_{nm}}{b_m} \Im \ln \left[U^\dagger K^{(m)} U\right]_{nm} , \qquad \alpha = x, y, z, \tag{7.5}$$

where $M_{nm} = (\mathbf{b}_n \cdot \mathbf{u}_m)\, b_n^{-1}$ is the normalized projection of the nth reciprocal lattice vector on the mth Cartesian vector, and

$$K_{ij}^{(m)} = \langle \phi_i | \, \mathrm{e}^{-i\mathbf{b}_m \cdot \mathbf{r}} \, | \phi_j \rangle \, . \tag{7.6}$$

It is then straightforward to calculate a dipole moment associated with each ion I using

$$\mu_\alpha^I = -2 \sum_{n \in I} r_{n,\alpha} + Z_I R_{I,\alpha} \, , \tag{7.7}$$

where the sum runs over those MLWFs which are in the vicinity of ion I, and Z_I is the charge of the pseudopotential core at the position $\mathbf{R}_I$. Figure 7.3 illustrates for one configuration of this system the MLWFs after transformation of the occupied orbitals. It can be seen that the distribution of MLWFs around each Cl^- ion is roughly tetrahedral.

7.3.2 Fitting to the *ab initio* dipoles

We initially allowed the polarization parameters b, c, and $p_{\max}$ in the Tang-Toennies function of Equation 2.9 to vary within the fit, whilst holding the polarizability α constant. Although a good fit was obtained with an objective function value of ~ 0.05, any subsequent MD trajectories using this fitted potential were highly unstable. The minimization procedure was consistently only using the tail of the Tang-Toennies function in the fit to the *ab initio* data. Therefore if an anion were to approach an electrode more closely than any in the training set of configurations, it would obtain a rapidly-increasing dipole. The attraction between such a dipole and the metallic surface apparently dragged the associated ion into the electrode.

We therefore sought an alternative function to model the short-range corrections to these melt–wall terms. We now rewrite Equation 2.8 as:

$$\begin{aligned} U^{q-\mu} = \frac{1}{2}\sum_{i}^{n_p}\sum_{j}^{n_p}{}' \left\{\left[\mu_{j\alpha}q_i g_{ij}(r_{ij}) - q_j\mu_{i\alpha}g_{ij}(r_{ij})\right]T_{ij}^{\alpha}\right\} \\ + \sum_{i}^{n_p}\sum_{j}^{n_g}\mu_{i\alpha}q_j T_{ij}^{\alpha} + \sum_{i}^{n_p}\sum_{j}^{n_g}\mathbf{F}_{ij}^{\mathrm{sr}}\cdot\boldsymbol{\mu}_i, \end{aligned} \tag{7.8}$$

where

$$\mathbf{F}^{\mathrm{sr}}(\mathbf{r}_{ij}) = \hat{\mathbf{r}}_{ij}A\exp\left[-b\left(r_{ij}-c\right)^2\right], \tag{7.9}$$

and $\hat{\mathbf{r}}_{ij}$ is a unit vector. There are, as before, three parameters in the set $\{\chi_{\mathrm{P}}\}$, which now relate to the height (A), width (b), and centre (c) of the Gaussian. It may at first seem odd to choose a Gaussian to represent the dipole damping, as any ion at a position $r_{ij} < c$ would be assigned a smaller short-range correction to its dipole than an ion at a greater distance from the wall at $r_{ij} = c$. We will find in Section 7.4 below, however, that the fitted parameters governing the repulsive part of the Born-Mayer potential are such that an ion has an essentially zero probability of exploring positions $r_{ij} < c$. This may not be simply fortuitous because limits are placed on the values the parameters $\{\chi_{\mathrm{P}}\}$ and $\{\chi_{\mathrm{F}}\}$ can take such that the minimization is tailored to avoid such unphysicalities.

Uniformly good fits were obtained across the range of configurations sampled, and this is

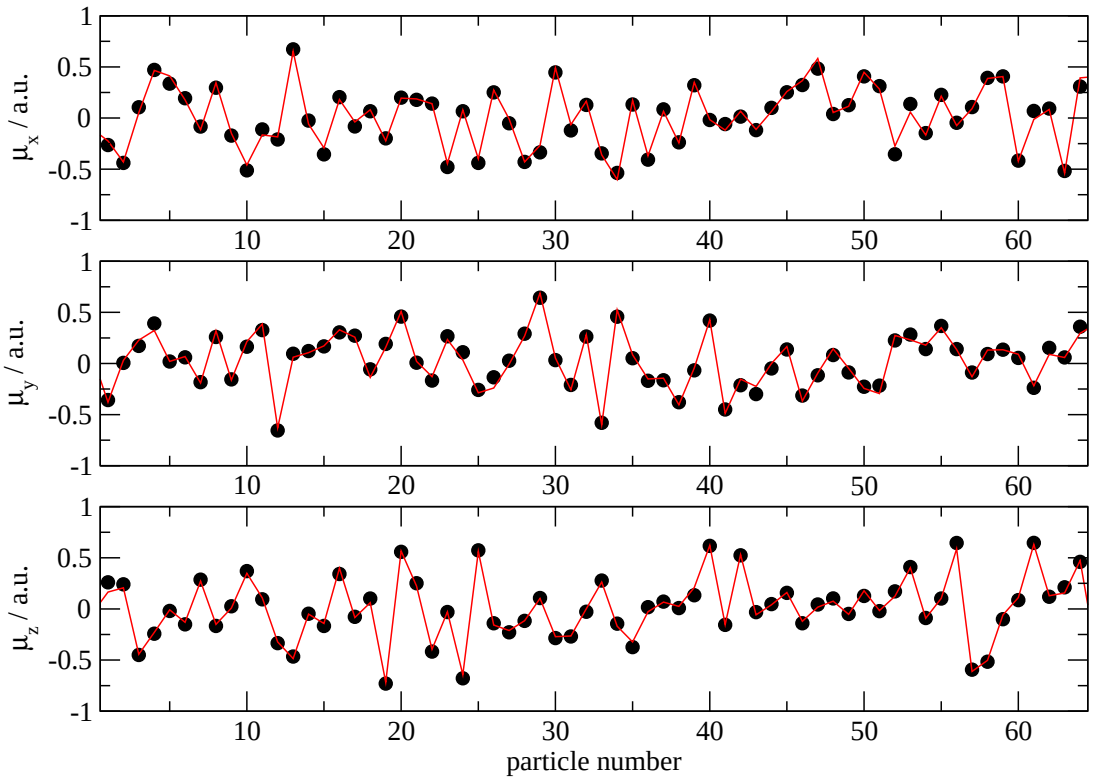

Figure 7.4: The quality of the fits of the x, y, and z components of the dipoles on the chlorine atoms to those obtained from the *ab initio* calculations is indicated for one of the eight configurations used as a training set. The solid lines show the predictions of the DIPPIM, and the circles the results from the *ab initio* calculations.

reflected in a value for the objective function A_{P} of 0.0507. The quality of the fit is illustrated in Figure 7.4 where only one of the configurations is shown for clarity. The solid line connects the predictions of the DIPPIM and the points indicate the corresponding *ab initio* results. The fitted parameters which characterize the Gaussian are given in Table 7.1. The width of the Gaussian is such that only the ions in the interfacial region will experience a non-negligible correction to their dipoles due to the wall charges. We can get a sense of the proportion of the system which is thus affected by examining Figure 7.5 in which is plotted the difference between the *ab initio* results and the prediction of the DIPPIM both with (red line) and without (blue line) the fitted short-range correction. It can be seen here that the fitted parameters are

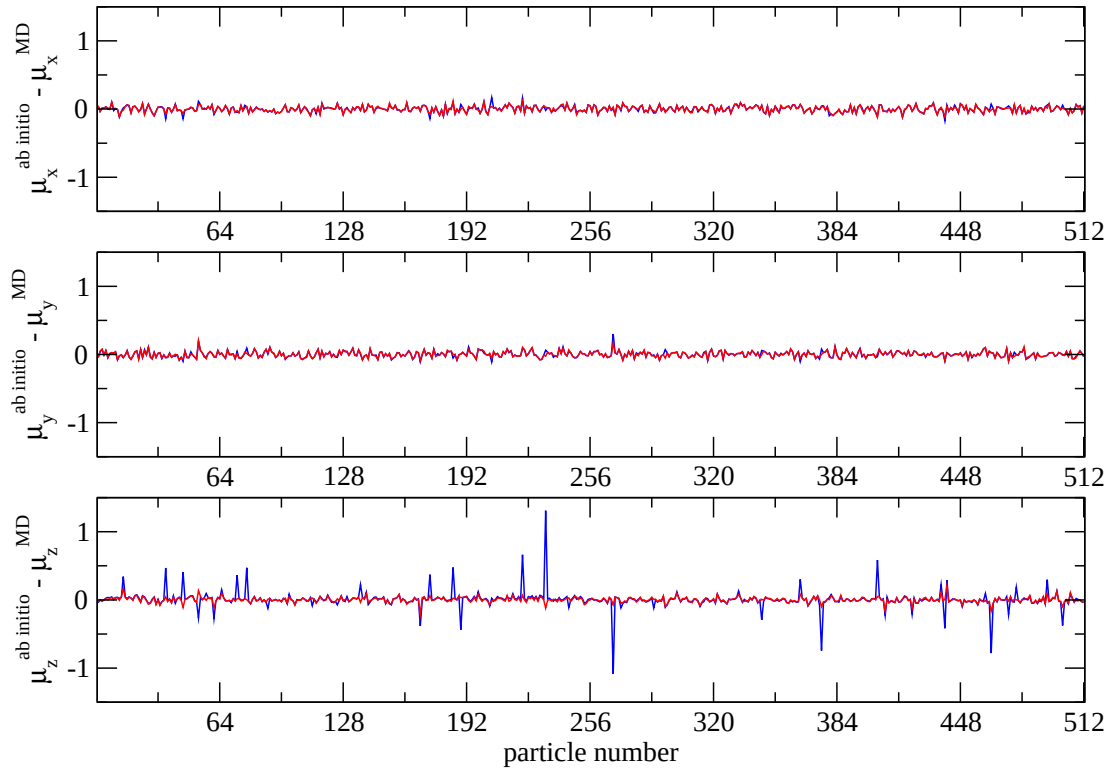

Figure 7.5: The difference between the *ab initio* dipoles and the predictions of the DIPPIM both with (red line) and without (blue line) the fitted short-range correction term in Equation 7.8. The differences from all eight configurations and all three x, y, and z coordinates are plotted. The fit only affects the z component of the dipole on the chlorine atoms situated at the interface.

of no consequence to the x and y components of the induced dipole, nor the z components of the chloride ions in the bulk. However there are a handful of anions in each configuration which are adjacent to an electrode and for which the short-range correction term is significant in magnitude. We can also glean from this figure a trend in the direction of electron displacement. It is found that those ions for which the quantity $\mu_\alpha^{\mathrm{ai}} - \mu_\alpha^{\mathrm{MD}}$ is positive before the fit and near-zero afterwards are adjacent to the left-hand electrode, and those ions for which the quantity $\mu_\alpha^{\mathrm{ai}} - \mu_\alpha^{\mathrm{MD}}$ is negative before the fit and near-zero afterwards are adjacent to the right-hand electrode. Therefore the effect of the short-range correction to the asymptotic dipole is in both cases to displace electron density away from the electrode.

Interaction	A	b	c
Cl–Wall	1.22134×10^{-2}	3.33853×10^{-1}	3.68818

Table 7.1: The fitted melt–wall dipole damping parameters. All values are in atomic units. The Cl^- polarizability was set to 20.0 au.

7.4 Fitting to the *ab initio* forces

The decision as to which parameters are to be included in the training set $\{\chi_F\}$ of Equation 7.2 is less straightforward than in the dipole fitting case. The parameters governing the short-range repulsion are included, but it is not *a priori* certain whether the dispersion interactions are accurately represented by the *ab initio* code [105]. Previous results [106] have intimated that some account is taken of the correlation effects responsible for these interactions, and we have decided to include the corresponding parameters in the parameter set $\{\chi_F\}$.

The fit gave a value for the objective function A_F of 0.141, and the quality of the fit is illustrated for the three Cartesian components of the force in Figure 7.6. The predictions of the DIPPIM are again represented by a solid line, and the points indicate the *ab initio* results for a representative configuration out of the training set of eight. The fitted parameter values are collected together in Table 7.2. We are again able to pick out the ions which are most affected by the variation of the parameter set $\{\chi_F\}$ through an analogy of Figure 7.5. Thus in Figure 7.7 we plot the difference between the *ab initio* forces and the predictions of the DIPPIM both with the fitted short-range parameters (red line) and without (blue line). The asterisked ions are those in closest proximity to an electrode, and for which the fit effects the greatest improvement.

Finally we return to the concern that the Gaussian is not a monotonically-increasing function with decreasing r_{ij}. That any potentially unphysical manifestations of this representation are obviated is demonstrated by Figure 7.8, in which the fitted Gaussian (lower panel) is plotted against the fitted Born-Mayer potentials (upper panel) in units of $k_B T$. The dotted black lines illustrate the distance of closest approach to the electrode for anions in the range of

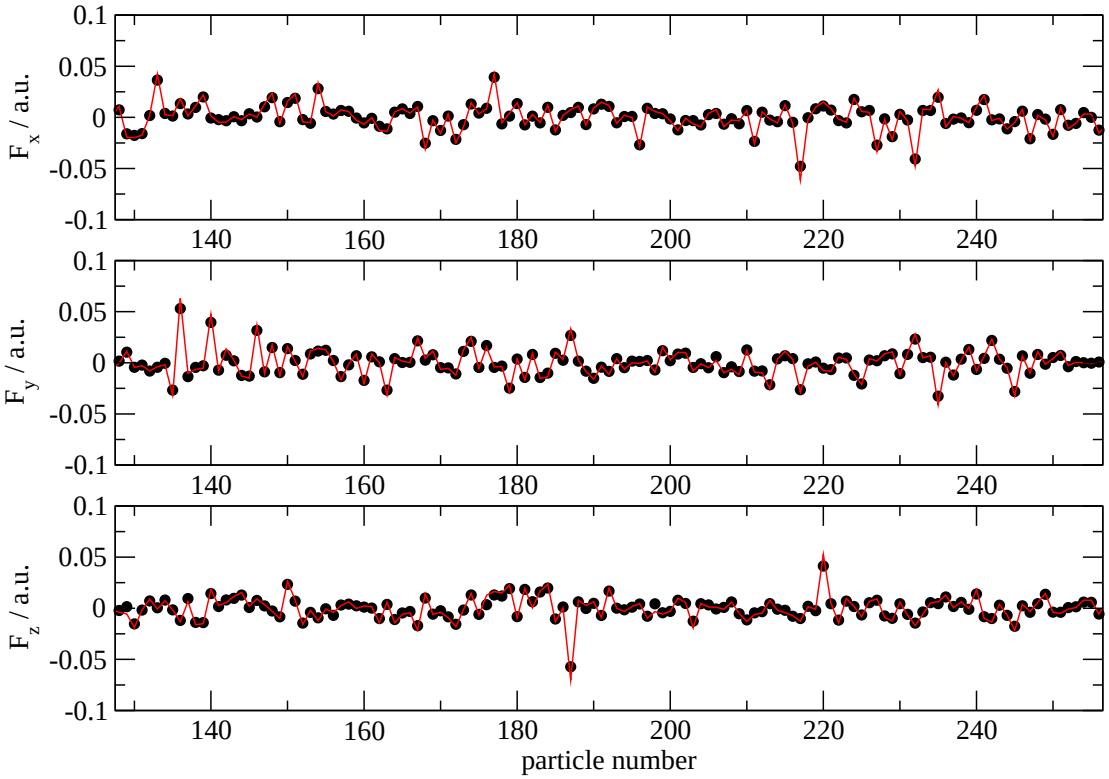

Figure 7.6: The quality of the fits of the x, y, and z components of the forces on the melt atoms to those obtained from the *ab initio* calculations is indicated for one of the eight configurations used as a training set. The solid lines show the predictions of the DIPPIM, and the circles the results from the *ab initio* calculations.

Interaction	a_{ij}	B_{ij}	C^6_{ij}	C^8_{ij}	f^6_{ij}	f^8_{ij}
Cl–Cl	1.59	1.151×10^2	1.449×10^2	1.000×10^2	1.68	1.65
Cl–Li	1.92	5.477×10^1	9.853×10^{-4}	8.363×10^{-4}	1.49	9.25
Cl–Wall	2.78	2.954×10^4	2.261×10^2	7.796×10^2	2.48	2.50
Li–Li	5.85	4.746×10^1	1.010×10^{-3}	1.007×10^{-3}	6.44	1.71
Li–Wall	3.32	7.287×10^4	4.201×10^{-1}	3.407×10^0	9.69	7.12

Table 7.2: The fitted parameters for the Born-Mayer pair potential. All values are in atomic units. The parameters were defined in Section 2.1.2.

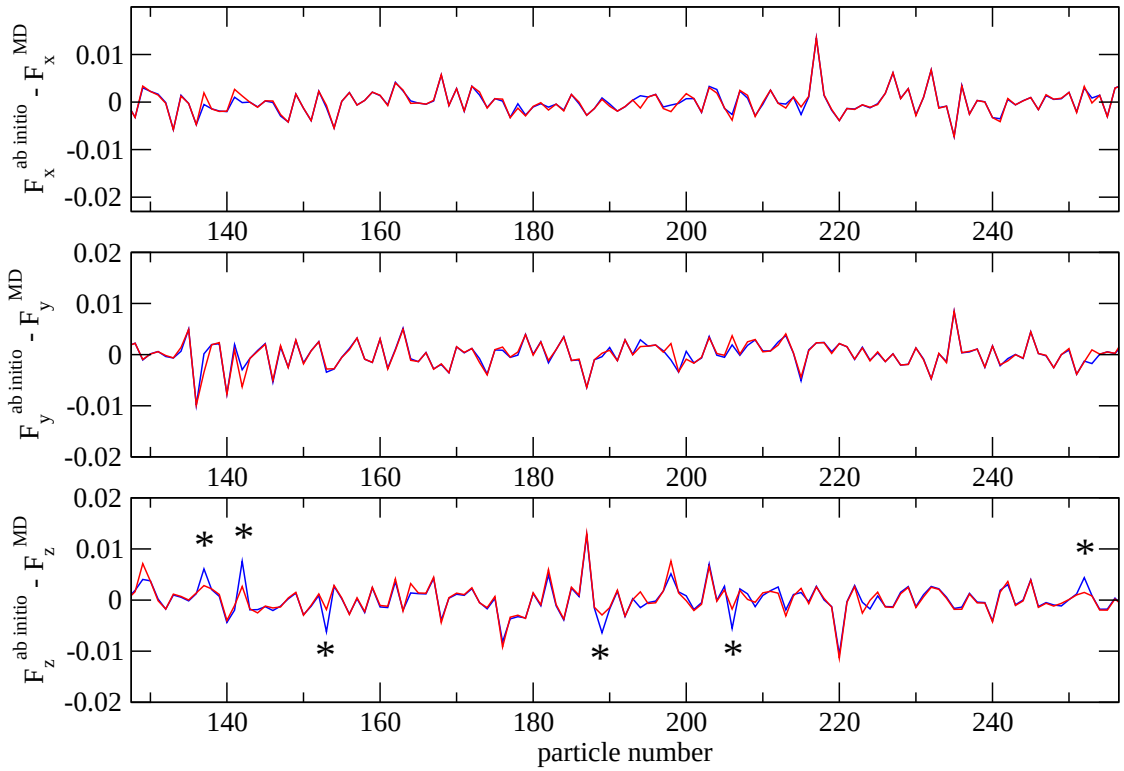

Figure 7.7: The difference between the *ab initio* forces and the predictions of the DIPPIM both with (red line) and without (blue line) the fitted short-range correction term in Equation 7.8. The differences from all three x, y, and z coordinates from a representative configuration are plotted. The fit only affects the z component of the force on the chlorine atoms situated at the interface (asterisked).

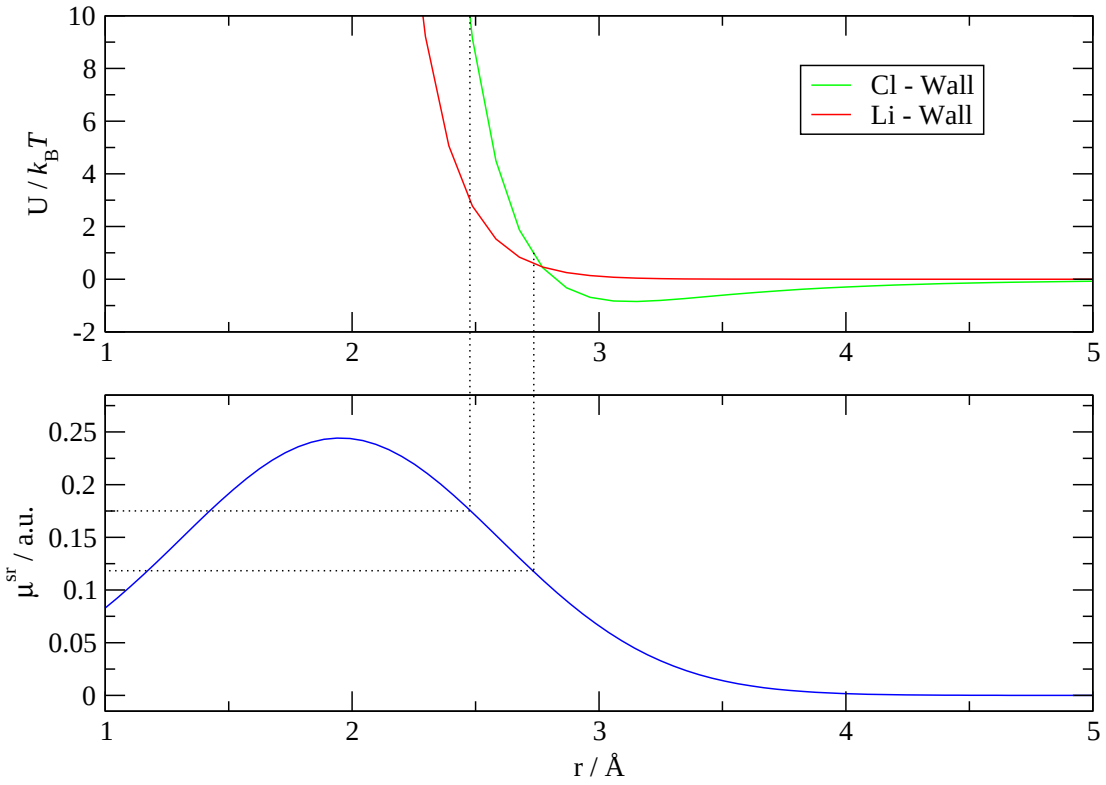

Figure 7.8: The fitted Gaussian function (lower panel) which describes the short-range dipole damping appropriate to the melt–wall interactions. The top panel illustrates for comparison the fitted Born Mayer potential which describes the Cl–Wall (green) and Li–Wall (red) energy of interaction in units of $k_B T$.

energies $1 - 10\,k_B T$. Table 7.1 reports that the abscissa of the mean value of the Gaussian is at $r_{ij} = 1.9517\,\text{Å}$, to be at which position an anion would require an energy of $> 200\,k_B T$!

7.5 Interfacial structure in the Al/LiCl system

7.5.1 Molecular dynamics simulations

Several classical simulations of the Al electrode-LiCl melt have been run for differing values of the applied electrode potential difference in order to examine the potential dependence of the melt structure at the interface. The simulations were carried out on considerably larger

systems than those prepared for input to the *ab initio* calculations. The melt consisted of 500 Li^+ and 500 Cl^- ions at a density appropriate to 1200 K, and the electrodes included 432 fixed Al atoms arranged, as before, in an FCC structure with the (100) surface exposed to the melt. The dimensions of the cell were 24.297 Å in the x and y directions, and 49.8345 Å between the innermost layers of electrode atoms along z. The x and y distances are appropriate to 6 FCC Al unit cells and the simulations were initiated by taking a melt configuration from a bulk liquid LiCl simulation in which the cell dimensions had been matched to these values. The simulation was then run for 100 ps to allow for equilibration and this was followed by 75 ps of production runs. The simulations with different applied potentials were initiated in sequence and an equilibration period of 60 ps was allowed before collecting statistics. The applied potential differences $|\Psi^+ - \Psi^-|$ investigated were of magnitude 0.0 V, 0.1 V, 0.2 V, 0.5 V, 1.0 V, 1.5 V, 2.0 V, 3.0 V, 4.0 V, and 5.0 V.

7.5.2 Ion density profiles

Figure 7.9 shows the profiles of the density of Li^+ and Cl^- ions across the simulation cell for various values of the applied potential. As viewed, a positive potential (Ψ^+) is applied to the left-hand electrode (the anode) and a negative potential of the same magnitude (Ψ^-) to the right-hand electrode (the cathode), so that the total potential drop across the cell is twice Ψ^+. For $\Psi^+ = 0$, a layer of weakly bound ions forms at the electrode surfaces and both species are seen, from the depth of the minimum separating this layer from the remaining fluid, to be in reasonably fast exchange with ions in the bulk. In common with Figure 5.4 in Chapter 5, there is a weak tendency for the anion and cation densities beyond the interfacial layer to oscillate out of phase. And again the ionic densities do not exhibit an electrical double layer in the conventional sense.

As the applied potential is increased, different behaviours are observed for the interfacial structure at the two electrodes. At the anode, the Cl^- ions are very strongly adsorbed and they drag the Li^+ ions with them; the depth of the minimum in the density profile increases, suggesting that exchange with the bulk is slowed markedly. The application of the potential

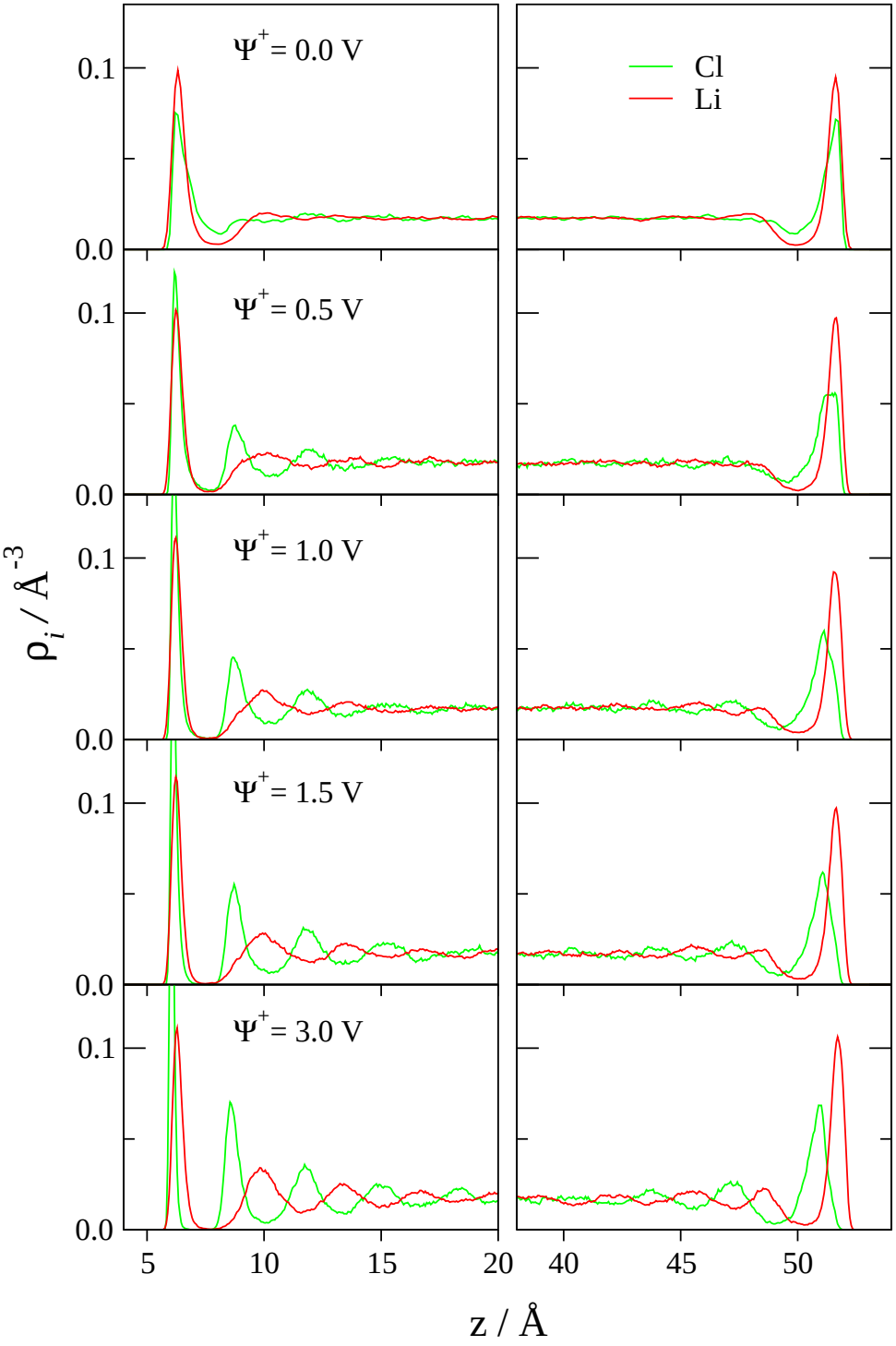

Figure 7.9: Ionic density profiles across the simulation cell for different values of the applied potential difference.

increases the amplitude of the out-of-phase oscillations in the densities of the two species. At the cathode, the behaviour is different: the Li^+ ions remain in a relatively loosely-held surface layer but the Cl^- ions are pushed out towards the bulk, creating a strongly polarized but apparently more fluid adsorbed film. In previous work on KCl [24], where the two ions were of very similar size and were not polarizable, the polarization of the two interfaces was much more symmetrical. In their study of a room temperature ionic liquid (RTIL) confined between two electrified walls, Pinilla *et al.* also observed differences between positively and negatively charged walls [25]. Their system consisted of dimethylimidazolium cations, which are molecular species and therefore have some orientational degrees of freedom, and chloride anions, for which polarization effects were neglected. At the negatively charged electrode, both species were adsorbed in the same layer, while at the positively charged electrode, the increase of the surface charge led to a closer approach of Cl^- ions only, inducing some kind of segregation. This is the opposite to what we report here; in LiCl the anion is the larger ion and also is the one which is polarizable and interacts most strongly with the electrode surface. The distinct behaviour observed between the two electrodes therefore reflects the important differences in size and polarizabilities of the two ionic species in the melt.

It is apparent on comparing the $\Psi^+ = 0.0\,\mathrm{V}$ density profiles in Figure 7.9 with those in Figure 5.4 that the melt–wall interactions in the latter case are substantially stronger and the interfacial structure more quasi-crystalline. This difference will also be apparent on comparing the Poisson potential profiles and the differential capacitance plots of the respective systems (see below).

7.5.3 Electrostatic potential profile

The electrostatic potential profile across the cell is calculated, as in Chapter 5, using Poisson's equation (3.66). The profiles obtained for ten different anode potentials in the range $0.0\,\mathrm{V}$ to $2.5\,\mathrm{V}$ are displayed in Figure 7.10. In the centre of the cell the potential is constant, due to the screening of the charges of the electrodes by the (ionically conducting) melt. Very strong oscillations are obtained near the interfaces; those are mainly due to the out-of-phase

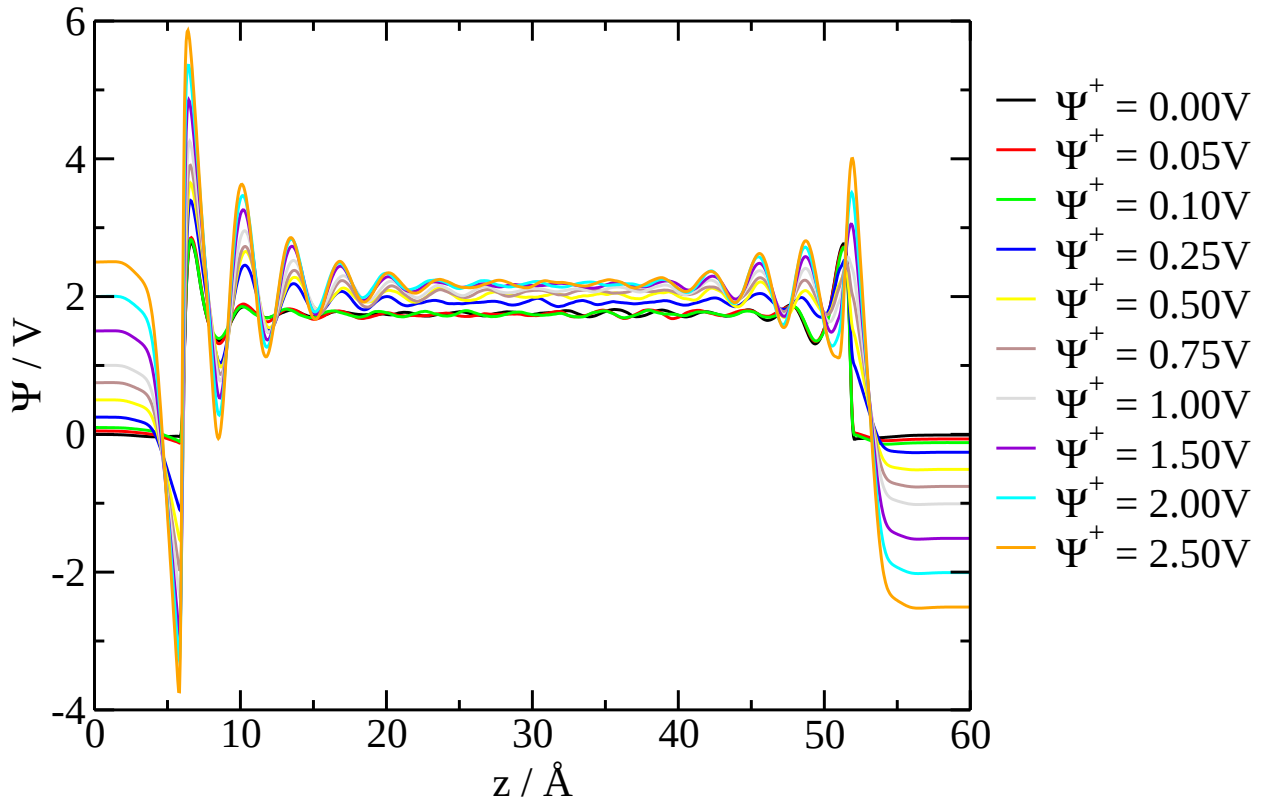

Figure 7.10: Electrostatic potential profile across the simulation cell.

oscillations of the densities of oppositely charged ions. A layer of 5 to 13 Å is necessary to completely screen the electrode potential and reach an in-bulk Ψ^{bulk} value of the potential. Three régimes are observed for Ψ^{bulk}. For some null or very weak applied potentials, the same value of $\Psi^{\text{bulk}} \sim 1.75$ V is obtained. Then, for $\Psi^{+} - \Psi^{-} > 0.5$ V, a progressive shift appears until a new almost constant value of $\Psi^{\text{bulk}} \sim 2.16$ V is obtained for $\Psi^{+} - \Psi^{-} > 3.0$ V. Each metal/melt interface can be viewed as a parallel plate capacitor, with a potential drop between the two plates given by $\Delta\Psi = \Psi^{\pm} - \Psi^{\text{bulk}}$ and an accumulated charge on a given plate equal to the sum of all the charges carried by the metallic electrode atoms. The variation of the surface charge σ^{M} with $\Delta\Psi$ is given in Figure 7.11, with two points for each simulation because of the existence of two distinct interfaces; the value of $\Delta\Psi$ has some imprecision due to the

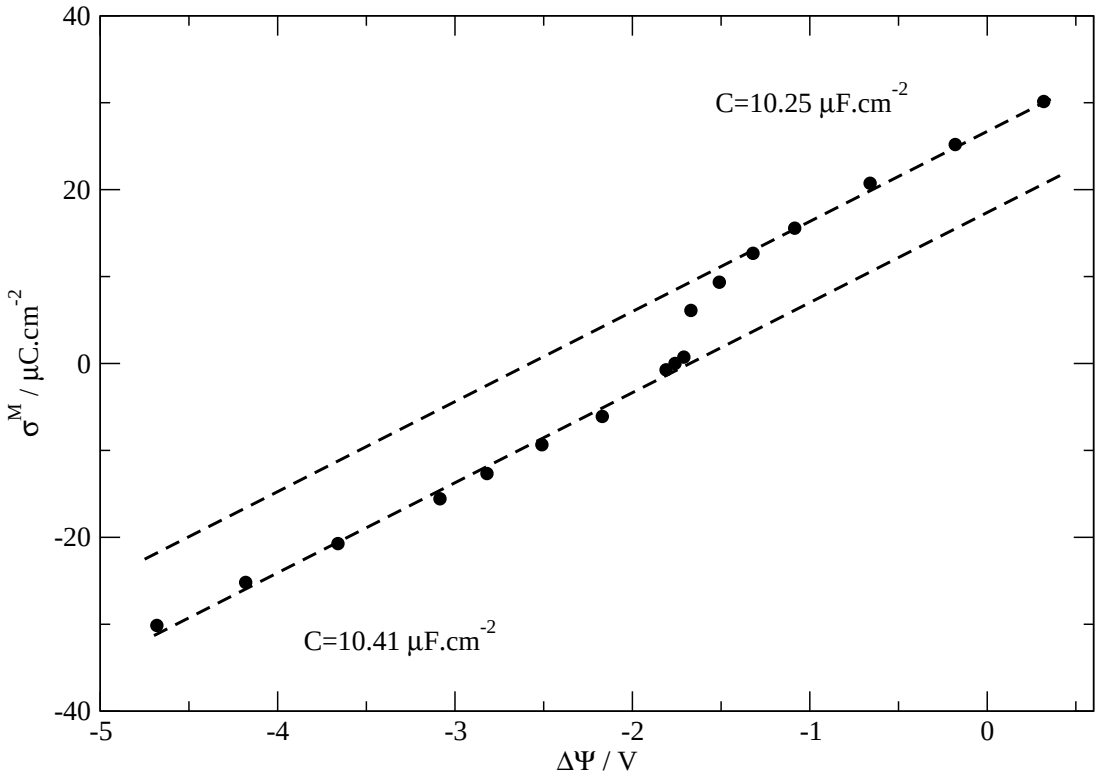

Figure 7.11: Variation of the surface charge σ^{M} with the potential drop across the interface $\Delta\Psi = \Psi^{\pm} - \Psi^{\mathrm{bulk}}$.

oscillations in Ψ^{bulk} in Figure 7.10.

The first quantity that can be evaluated from this plot is the PZC, $\Delta\Psi^{\mathrm{PZC}} = -1.76$ V. This seems like a large value compared to experimentally measured quantities; however the experimental value is always measured with respect to a reference electrode, whereas we are dealing with absolute potentials. In our calculations the potential drops very rapidly across the region between the surface layer of electrode atoms, where the electrode charges are located, and the first layer of melt ions. In a real metallic surface, the valence electron density of the metal would extend out into this region and contribute to a partial screening of the electrode charges, giving a different character to the potential across this gap [107]. If we were to use a reference electrode (with similar characteristics to the electrodes of our simulation model), this

limitation of our representation of the metallic surface would not be evident in the PZC value.

Secondly, we may obtain values for the differential capacitance $C = (\partial\sigma^{\mathrm{M}}/\partial\Delta\Psi)$ which can be extracted by differentiation of the surface charge with respect to the potential difference across the interface, as shown in Figure 7.11. Away from the PZC, almost constant differential capacitances of 10.41 and 10.25 μF.cm^{-2} are obtained. These regions of linear capacitance are similar to that observed for the europium melt in Figure 5.10, and we again stress the need for further research here: recall that the mean-field treatment of the double layer capacitance in Section 1.4.2 suggests that it should vary with the square-root of the potential drop across the interface [35]. The most negative of the potential differences occur at the right-hand electrode, where the corresponding ion density profiles are shown in the right-hand side of Figure 7.9. Between the two regions of constant slope in the σ^{M} *vs.* $\Delta\Psi$ figure, at potential differences slightly less negative than the PZC, a sudden increase of the surface charge with $\Delta\Psi$ is observed. This corresponds to a maximum in the differential capacitance.

7.5.4 Structure of the adsorbed layer

The steep rise in the surface charge density (and the corresponding peak in the differential capacitance) is caused by a change in the structure of the adsorbed layer of ions at the anode (left-hand electrode) as the potential applied to the electrode is increased. Referring to the ion density profiles in Figure 7.9, this rearrangement occurs for applied potentials between $\Psi^{+} = 0.25\,\mathrm{V}$ and $\Psi^{+} = 1.5\,\mathrm{V}$ in the panels on the left-hand side of the figure. Some typical snapshots of the adsorbed layer for different potential drops are given in Figure 7.12. The first two correspond to respective potential drops more negative than and equal to the PZC. In both cases, the arrangement of the ions is disordered. In the final snapshot, which corresponds to a potential drop less negative than the PZC, a significant ordering of both cations and anions is observed with the ions bound to the hollow sites of the aluminium surface.

In order to assign a potential to the transition between the disordered and ordered states of the adsorbed layer we have computed the in-plane partial structure factors for different applied potentials. The Cl^{-}-Cl^{-} partial structure factors for atoms in the adsorbed layer and in the

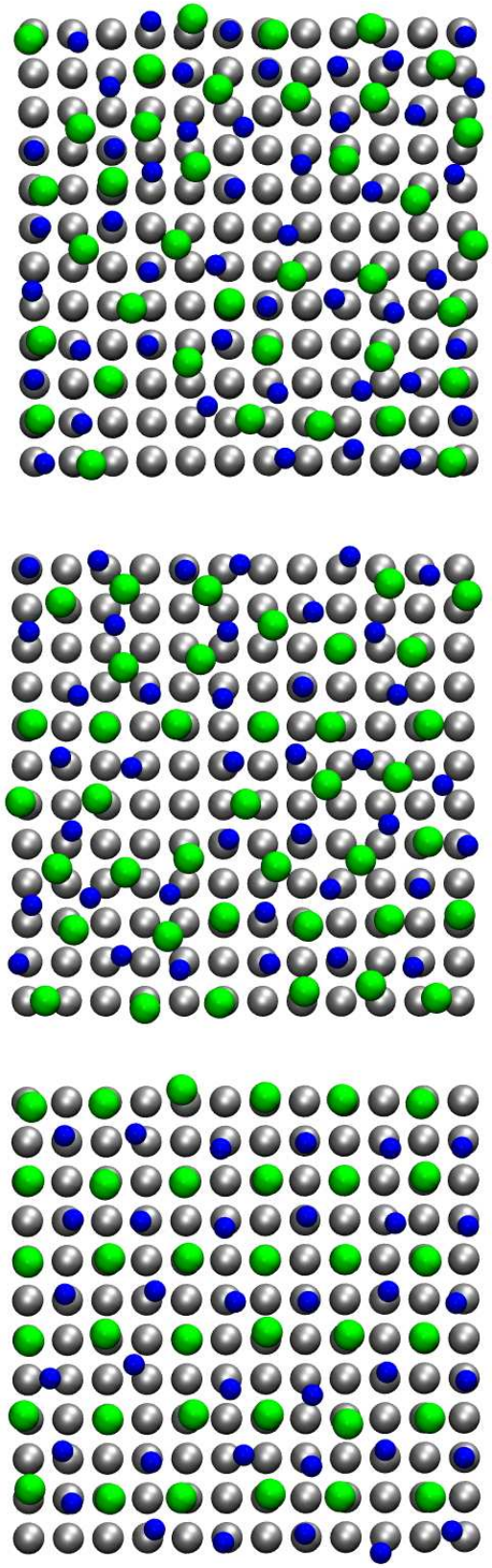

Figure 7.12: Snapshots of the adsorbed layer on the metal surface. From top to bottom, $\Psi^- = -2.5\,\mathrm{V}$, $\Psi^+ = 0.0\,\mathrm{V}$ and $\Psi^+ = 2.5\,\mathrm{V}$. Green: Cl^- ions, blue: Li^+ ions, grey: Al atoms.

adjacent layer of liquid for wavevectors in the plane of the surface are shown in Figure 7.13. A structural transition in the adsorbed layer is clearly observed: for $\Delta\Psi$ values more negative than $-1.66\,\mathrm{V}$, only weak features are seen in the structure factor; whereas for more positive $\Delta\Psi$ values, two sharp and very intense Bragg peaks are observed, which correspond to the $\mathbf{k} = \frac{2\pi}{a}(1,0)$ and $\frac{2\pi}{a}(1,1)$ scattering vectors, where a is the lattice parameter of the aluminium metal ($a = 4.0495\,\text{Å}$). This abrupt change in the interfacial structure is therefore responsible for the sharp increase in the surface charge density and the maximum in the differential capacitance close to the PZC. A similar potential-induced structural transition in the adsorbed layer of an ionic liquid was observed by Freyland *et al.* using *in situ* STM [108, 109]. The structure factors for the layers of liquid adjacent to the adsorbed layer are more liquid-like, although they do exhibit small peaks at the positions of the Bragg peaks, showing that the lateral ordering effect imposed by the atomic structure in the Al surface does propagate out into the liquid. (Recall, however, that the surface atoms are fixed in our simulations, so that the effect may be more exaggerated than in a physical system.)

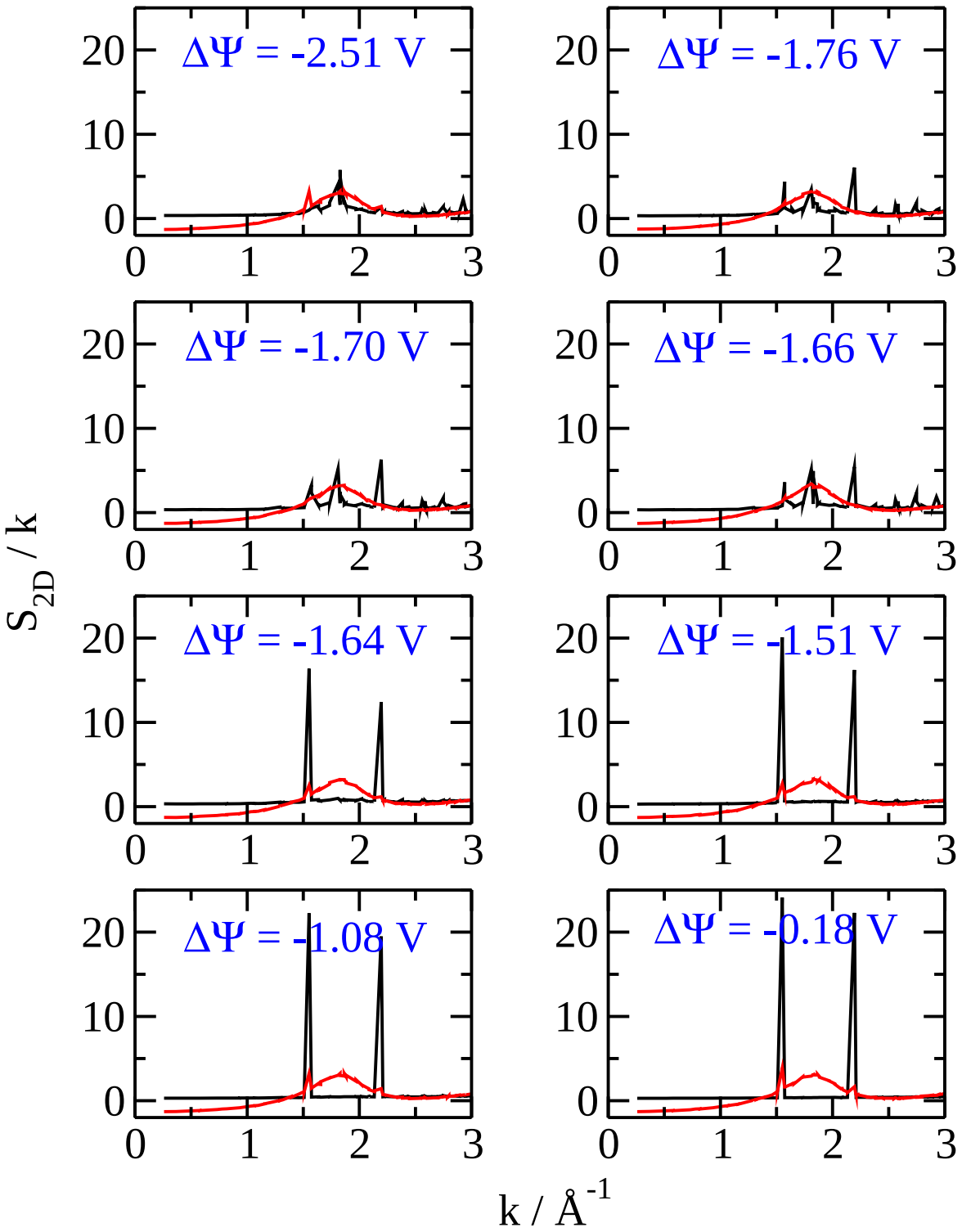

Figure 7.13: In-plane Cl^--Cl^- structure factor for various potential drops across the metal/molten salt interface. Black: adsorbed layer, red: liquid slice between the adsorbed layer on each electrode.

8

Summary and further work

8.1 Summary

The remit of Part I of this thesis was to investigate through MD simulation the factors which affect the rate of heterogeneous electron transfer at a metallic electrode in the context of Marcus theory. The simulations consisted of the ionic melt $K_3Eu^{3+}_{0.5}Eu^{2+}_{0.5}Cl_{5.5}$ sandwiched between two parallel plate platinum electrodes held at a constant preset potential difference. It was computationally advantageous to choose an ionic melt over an aqueous solution because the concentration of redox species near the electrodes is higher, allowing better statistics to be gathered. The electrode charges were variationally obtained through the method of Siepmann and Sprik ([62], Chapter 2), which incorporates the polarization of the electrode by the charges and dipoles on the melt ions, and maintains the constant potential condition. The long range interactions were computed using a two-dimensional Ewald summation ([70], Chapter 3) to ensure that the electrode potential was known with reference to a vacuum. The summation was extended to include dipoles on the chloride ions induced by their mutual interaction and the interaction with the electrode charges.

The diabatic Helmholtz free energy surfaces of the reduced and oxidised electroactive species were calculated through a method developed by Blumberger and Sprik ([80], Chapter 4) which takes the vertical energy gap as reaction coordinate. These data confirmed that the system

exhibits linear response behaviour. The Marcus surfaces were characterized by the Helmholtz reaction free energy ΔA and the reorganization energy λ, and their dependence on the position of the redox ion in the cell and the value of the applied electrode potential was investigated (Chapter 6). The change in the Eu–Cl radial distribution function during the redox process revealed that the bond length in the transition complex is exactly in between those of the ground state reactant and product complexes.

The reorganization energy displays the same position-dependence as a unit charge introduced into an otherwise empty cell. This suggests that the reorganization energy exhibits a much smaller dependence on the infinite frequency dielectric constant than predicted by continuum Marcus theory (see Equation 1.69), which is not inconsistent with other simulations of electron transfer using a polarizable electrolyte [93]. A knowledge of the position-dependent reorganization energy enables the calculation of the position-dependent transfer coefficient, α, appearing in Butler Volmer theory (see Equation 1.70).

ΔA is found to be independent of the position of the redox ion except in the immediate vicinity of the electrodes. This behaviour of ΔA does not reflect the medium-range oscillations in the mean electrical (Poisson) potential which extend out from the electrode surface, but rather the position-independence of the Madelung potential. And yet it is the Poisson potential which is always invoked in classical discussions of electrodic phenomena.

The pronounced oscillations in the Poisson potential near the interface are seen primarily to be a result of the out-of-phase oscillations of the cation and anion densities (Chapter 5). The oscillatory behaviour of both the Poisson potential and the concentration profiles is qualitatively inconsistent with a mean-field Gouy-Chapman description of the double layer. Furthermore, it undermines the assumption inherent in the Butler Volmer formalism that at equilibrium (when the net current is zero) the bulk concentrations of the reactant species are also found at the interface. We expressed the position-dependent concentration profile of each redox species as a potential of mean force, and found these to be in good agreement with those obtained through an umbrella sampling technique.

Finally, we demonstrated the feasibility of parameterizing potentials to describe the inter-

actions of melt ions with a metallic wall directly from planewave DFT electronic structure calculations (Chapter 7). The interaction potential included the polarization of the ions by their mutual interaction and the interfacial potential, and the polarization of the metal by the interactions with the charges and induced dipoles of the ions in the interfacial region. Such effects have not been incorporated in previous simulation studies of ionic liquids at interfaces. We generated interaction potentials for a system consisting of a LiCl melt and a solid aluminium electrode, and subsequently conducted simulations at various values of the applied electrical potential. The interfacial structure was strongly affected by the applied potential and we observed a potential-induced phase transition in the first layer of ions adsorbed on the surface. This was associated with a peak in the interfacial capacitance of a type very similar (though sharper) to that seen in experimental studies of RTILs [34]. At potentials away from the phase transition the capacitance was found to be independent of the applied potential.

8.2 Further work

1. **An adiabatic treatment of the electron transfer event.** The representation of the electron transfer event described in this thesis is appropriate to the diabatic limit, where the coupling between the electronic states of the metal and those of the redox ion is weak. Because there are many metallic states which may couple to the redox ion, the electronic coupling matrix element γ may be too large for weak coupling to apply [61, 110, 111]. A significant direction of further research should be the construction of an adiabatic representation of the electron transfer in the strong coupling limit, as has been incorporated in simulations of aqueous systems [59, 91].

   The tunnelling probability is thought to fall off exponentially with distance from the electrode, *i.e.* the electron transfer occurs over a region near the electrode rather than at a single position. This can normally be observed experimentally only under restricted circumstances (*i.e.* $D < 10^{-10}\,\mathrm{cm^2\,s^{-1}}$ [4]); however it is possible to hold a redox species at a fixed distance from the electrode by an adsorbed monolayer such as an oxide film.

The adsorbed layer may itself contain electroactive groups, such as an alkane thiol with a terminal ferrocene group [112]. The rate constant is measured as a function of the length of the alkyl chain, and the slope of the plot of $\ln(k)$ against position allows determination of β (see Equation 1.54).

2. **Investigation into the competition between diffusion and electrode kinetics.** The remit of the work in this thesis was to investigate the factors which affect the rate of electron transfer at the fast diffusion limit. We recall from Section 1.2 that when electrolytic reactions are induced to occur rapidly, mass transport effects become important for the interpretation of experimental voltammograms. Our adiabatic treatment of the electrode response to an electron transfer event maintains the constant potential condition across the cell and thus mimics the delivery of a current by a battery connected between the two electrodes. It is this ability to sustain an electrical current which will enable the use of our model to investigate the competition between diffusion and electrode kinetics which occurs at real working electrodes.

   To incorporate the effects of diffusion, we need to know the probability that an electron on a particular redox ion will tunnel into the electrode: this is governed by the electronic coupling matrix element discussed above. But we also require a scheme for determining whether an electron with a given probability of tunnelling actually does tunnel into the electrode or not.

   We propose a simple Monte Carlo scheme. Figure 8.1 illustrates the transmission coefficient, $\gamma(z)^2$, of Equation 1.54 (here with $(\gamma^0)^2 = 1$). To determine whether an electron transfer with a probability of $\exp(-\beta z)$ actually takes place, we first generate a random number ξ uniformly on (0,1). The random number is compared with $\exp(-\beta z)$. If it is less than $\exp(-\beta z)$ the electron transfers between the redox ion and the electrode. This would be the case if ξ_1 were the random number generated. If ξ_2 is chosen, however, the electron does not transfer.

3. **Investigation into the position-dependence of the reaction free energy ΔA**

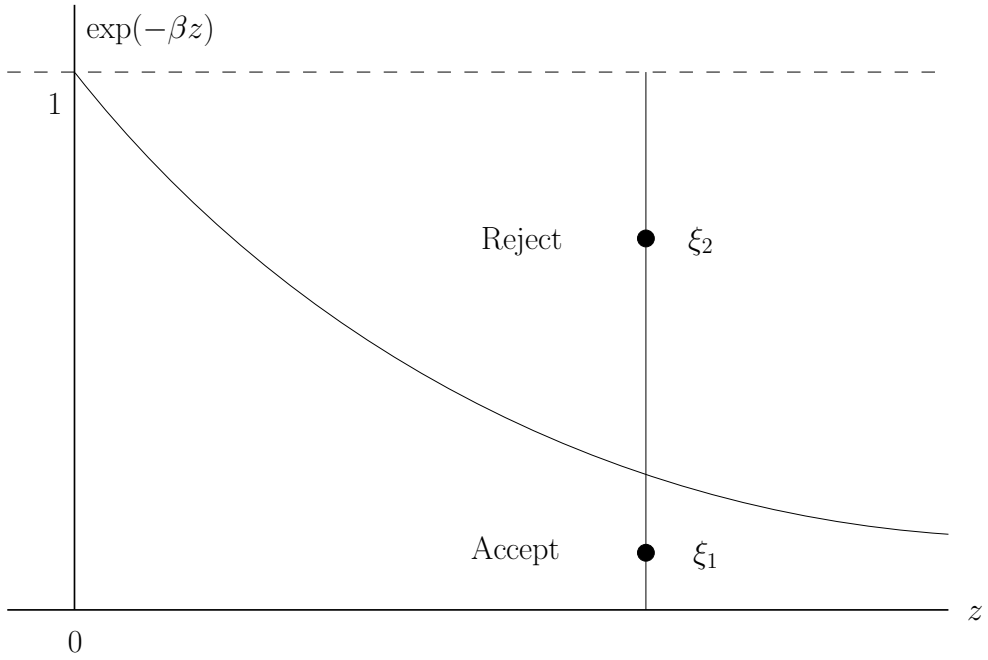

Figure 8.1: A Monte Carlo scheme for accepting or rejecting electron transfer events during the simulation.

in the immediate vicinity of the electrode. We recall from Figure 6.4 that the Helmholtz free energy of the oxidation reaction $Eu^{2+} \rightarrow Eu^{3+}$ is independent of position except in the immediate vicinity of the electrodes. It would be useful to obtain more data on this deviation of the reaction free energy away from its bulk value (ΔA^{bulk}), and this involves calculating the relevant vertical energy gaps *via* umbrella sampling. Another route to obtaining $\Delta A(z)$ near the electrode is to measure the difference between the Eu^{2+} PMF ($\phi_{\text{Eu(II)}}$) and Eu^{3+} PMF ($\phi_{\text{Eu(III)}}$) in Figure 5.18. The reaction free energy profile (for oxidation) across the cell is then given by

$$\Delta A(z) = \phi_{\text{Eu(III)}}(z) - \phi_{\text{Eu(II)}}(z) + \Delta A^{\text{bulk}}. \tag{8.1}$$

The variation of ΔA with position in the interfacial region is small and so a large data set of individual excitation energies is required to obtain reliable averages over narrow bin widths. The umbrella sampling technique involves attaching only *one* redox ion to each electrode with a spring, so long MD runs are necessary for precise values of ΔA corresponding to positions where the equilibrium redox ion density is low.

4. **Allow the wall atoms to move.** The positions of the wall atoms were fixed in this work, but allowing them to move would increase the verisimilitude of the simulation. When a solid is cleaved, the surface atoms no longer experience the same bonding forces and sometimes will change their configuration to minimize the surface energy. Such reconstruction of an electrode can depend on the extent of specific adsorption and the value of the applied potential. So the surface sometimes reconstructs during a potential scan [113]. For example, when a Au (100) electrode is heated under a flame, the surface layer reconstructs to form a slightly-buckled (110) arrangement. This surface structure is maintained when the electrode is immersed in a solution of $0.01\,M$ $HClO_4$. As the potential of the electrode is made more positive, the reconstructed surface is maintained to a potential of about $0.6\,V$ *vs.* a saturated calomel electrode [114], beyond which the surface reverts to the original (100) structure. This lifting of the reconstruction is accompanied by a large change in the capacitance curve and a shift in the PZC. Similar effects have been observed with other surfaces and indicate that substantial surface reconstructions can occur during potential sweeps.

5. **Nonplanar electrodes.** The model of the electrode as a polarizable metal held at constant potential, as distinct from a constant charge plus image charge model, facilitates its application to nonplanar electrodes. Real metal surfaces are never perfectly planar. They contain steps, kinks, edge vacancies, holes. And during electrodeposition there is a proliferation of macroscopic protuberances of many shapes and sizes due to screw dislocations, growth spirals, faceting, *etc.* Boulders, whiskers, dendrites, and pyramids *inter alia* may all be formed. It is known [86] that the electric field around a macroscopic protuberance becomes concentrated leading to faster growth than at the flat surface. It should be possible to investigate the electric field strength for different nonplanar geometries, and how they vary with the applied overpotential. It is known, for instance, that the slope of a growing pyramid changes if the overpotential is changed during the growth process [86].

Part II

Are dipolar liquids ferroelectric?

9

Are dipolar liquids ferroelectric?

9.1 Introduction

Recently, Shelton has reported the results of novel experiments in which the hyper-Rayleigh spectrum (HRS) of dipolar liquids has been measured [115, 116, 117, 118, 119]. In these experiments a pair of incident photons is scattered by thermal fluctuations in the *hyper*polarizability density ($\boldsymbol{\beta}$) of the fluid to give an outgoing photon with a frequency close to twice the frequency of the incident photons but slightly shifted due to the relaxation of the fluctuations in the *hyper*polarizability. Linear response arguments lead to the expectation that the scattered spectrum should be given by the time transform of a correlation function of the spatial fourier components of the hyperpolarizability density [115]:

$$\langle E_\epsilon^{2\omega}(t) E_\epsilon^{2\omega}(t+\tau)\rangle \propto E_\alpha^\omega E_\beta^\omega E_\gamma^\omega E_\delta^\omega \left\langle \sum_{a,b} \beta_{\epsilon\alpha\beta}(\mathbf{\Omega}_a, t)\ \beta_{\epsilon\gamma\delta}(\mathbf{\Omega}_b, t+\tau) \cos(\Delta\mathbf{k}\cdot[\mathbf{r}_a(t) - \mathbf{r}_b(t+\tau)]) \right\rangle, \tag{9.1}$$

where $\langle .....\rangle$ is the ensemble average, $\mathbf{\Omega}_a(\mathbf{\Omega}_b)$ and $\mathbf{r}_a$ $(\mathbf{r}_b)$ are the orientation and positions of molecule $a(b)$ at time $t(t+\tau)$, and a and b are summed over all N molecules in the sample. E_α^ω are Cartesian components of the linearly polarized incident light field, $E_\epsilon^{2\omega}$ is the ϵ polarized component of the scattered field, and repeated greek indices are summed. Several experiments

are possible, depending upon the relative polarization of the incident and scattered electric fields. $\beta_{\epsilon\alpha\beta}$ are the laboratory-frame Cartesian components of the molecular hyperpolarizability $\boldsymbol{\beta}$. $\Delta\mathbf{k} = 2\mathbf{k}_i - \mathbf{k}_s$, where $\mathbf{k}_i$ and $\mathbf{k}_s$ are the wavevectors of the incident and scattered radiation. Note that for visible incident radiation $\Delta\mathbf{k}$ is of the order of 5×10^{-2} Å^{-1}.

If we neglect interaction-induced contributions to the hyperpolarizability (as above), HRS is thus seen to be mediated by the dynamics associated with the molecular hyperpolarizability tensor $\boldsymbol{\beta}$. For an axially symmetric molecule like acetonitrile (CH_3CN), one of the liquids examined by Shelton, the molecular hyperpolarizability can be regarded as a combination of first- and third-rank spherical tensors, and the spectrum might be described from the perspective used to discuss a normal depolarized Rayleigh spectrum (where the spatial fourier components of a second-rank spherical tensor are observed). *If* the orientational correlations between molecules were sufficiently short-ranged that we could always replace $\cos(\Delta\mathbf{k} \cdot [\mathbf{r}_a(t) - \mathbf{r}_b(t+\tau)])$ by unity, the spectrum would reflect the molecular reorientational dynamics of first- and third-rank spherical tensors and, for a mobile liquid like acetonitrile, would be expected to be composed of almost Lorentzian features, centred about 2ω, with widths of a few cm^{-1}.

For some of the polarizations examined by Shelton, these expectations are borne out. However, for the case where the incident radiation is vertically polarized and the scattered horizontally polarized (VH-geometry), there is an additional extremely narrow feature, with an intensity comparable to the Lorentzian bands, centred on 2ω. This indicates the existence of a *very* slowly-relaxing contribution to the decay of the hyperpolarizability fluctuations, which is not anticipated from any conventional description of reorientational dynamics in a normal liquid. The feature was observed in several highly polar liquids, including water, and also in their solutions with non-polar liquids. High-resolution spectra of water [117] put an upper bound of $0.0002\,\mathrm{cm}^{-1}$ on the anomalous peak, which corresponds to a relaxation on a timescale longer than 26 ns.

As Shelton has pointed out, the simplistic discussion of the spectrum needs to be extended. The first-rank component of the hyperpolarizability will behave like the molecular dipole moment and long-range correlations between dipoles in polar liquids can never be neglected, which

means that the $\Delta\mathbf{k}$-dependence of the correlation function cannot be ignored. We should therefore discuss the influence of these dipolar correlations in the context of dielectric theory and distinguish between the relaxation of the longitudinal and transverse dipole densities $\mathbf{M}_{\mathrm{L}}(\mathbf{k},t)$ and $\mathbf{M}_{\mathrm{T}}(\mathbf{k},t)$ [120]:

$$\mathbf{M}_{\mathrm{L}}(\mathbf{k},t) = \sum_{i}^{N} \hat{\mathbf{k}}\hat{\mathbf{k}} \cdot \boldsymbol{\mu}^{i}(t) \exp(i\mathbf{k} \cdot \mathbf{r}^{i}(t)), \tag{9.2a}$$

$$\mathbf{M}_{\mathrm{T}}(\mathbf{k},t) = \sum_{i}^{N} (1 - \hat{\mathbf{k}}\hat{\mathbf{k}}) \cdot \boldsymbol{\mu}^{i}(t) \exp(i\mathbf{k} \cdot \mathbf{r}^{i}(t)), \tag{9.2b}$$

where the sums run over all molecules i with dipole moment $\boldsymbol{\mu}^{i}$ and position $\mathbf{r}^{i}$. Symmetry considerations indicate that the VH HRS spectrum contains a part which reflects the relaxation of the longitudinal dipole density (with $\mathbf{k} = \Delta\mathbf{k}$), whereas the other polarizations contain only the transverse part and Shelton has proposed that the slowly relaxing component observed in the VH HRS spectrum is associated with $\mathbf{M}_{\mathrm{L}}(\mathbf{k},t)$. The frequency dependent susceptibility observed in conventional dielectric spectroscopy reflects the transverse dipole density at *very* long wavelength.

This, in itself, does not resolve the problem. Theoretical considerations [121] indicate that, for a normal isotropic fluid, the long-time relaxation of the longitudinal dipole density is substantially *faster* than that of the transverse, with the latter on the same timescale as the normal single molecule dipole reorientation. If the most slowly relaxing parts of the longitudinal and transverse dipole densities were to be regarded as relaxing exponentially with time constants τ_{L} and τ_{T} respectively, then

$$\tau_{\mathrm{L}} = \frac{\tau_{\mathrm{T}}}{\epsilon}, \tag{9.3}$$

where ϵ is the dielectric constant of the material. For a normal polar liquid, where ϵ is large, the long-time relaxation of the longitudinal component should therefore be *much more rapid* than that of the transverse component which itself is on the timescale of molecular reorientation. So far as can be seen, the validity of these theoretical considerations has been borne out in computer simulations of acetonitrile [120] (at least with k at the smallest value normally accessed in a

simulation $\sim 0.3\,\text{Å}^{-1}$) and by the behaviour of the experimental dielectric spectrum [122].

Shelton has further suggested that the reason that these considerations do not account for his observation is that they are based upon an analysis of the relaxation of the dipole density in an *isotropic* polar liquid. He noted that the molecules on which his observations were made are sufficiently polar that the liquids obey the condition [115]

$$\frac{\mu^2\rho}{k_BT} \geq 9\epsilon, \tag{9.4}$$

where ρ is the molecular number density, which is the criterion for a dipolar hard-sphere or Stockmayer fluid to be ferroelectric. Recognising that the fluids of interest are not macroscopically ferroelectric, he has suggested that they form local ferroelectric domains with random orientations, whose size is smaller than $\frac{2\pi}{\Delta k}$. The slow, collective reorientation of these domains is then responsible for the narrow contribution to the HRS VH spectrum. From the relative intensities of the narrow and Lorentzian features in the spectrum he has suggested that the domain size could be of the order of one tenth of $\frac{2\pi}{\Delta k}$.

The reason why liquids like acetonitrile are believed not to be ferroelectric, whilst fulfilling the condition in Equation 9.4, is that the molecular shape encourages the molecules to pack locally in such a way as to frustrate the development of strong ferroelectric order [123]. The Kirkwood g-factor for acetonitrile [124], which measures the local dipole correlations, is close to unity meaning no net correlations, whereas that in water [125] is about 3. The measured dielectric constant of acetonitrile [126] is $\sim$ 35 and that of water [127] is $\sim$ 80. These values are much smaller than would be found in Stockmayer fluids at the same value of $\frac{\mu^2\rho}{k_BT}$.

Since the recording of an HRS spectrum is an experimental *tour de force* in which great care has been taken to eliminate spurious contributions to the signal, we have conducted a series of large scale computer simulations in order to re-examine the ideas which have been described above which themselves would suggest that Shelton's account of the origin of the narrow feature cannot be correct. We have studied the dipole density fluctuations in simulations containing close to 30,000 acetonitrile molecules and run the simulations for several nanoseconds. This allows for a simulation cell of length 133.8 Å, which will support fluctuations with wavevectors

as low as $0.047\,\text{Å}^{-1}$. This is still somewhat smaller than the Δk value in the experiments but it is substantially greater than the simulation cells which have been used in previous simulations of dipolar fluids and will allow us to detect if there is any build up of dipole correlations which have been missed in previous studies. We use a conducting ("tin-foil") Ewald treatment of the dipole correlations [128, 129] which should accentuate the tendency to build up dipolar correlations. The run lengths will enable us to calculate time correlation functions with acceptable statistics out to $\sim 1\,\text{ns}$ and detect if there are any weak long-lived correlations present. We have also carried out simulations of similar size and duration on a solution of acetonitrile in a non-polar solvent model; Shelton reported that the narrow feature was strengthened in these conditions compared to the pure acetonitrile. We also studied a molecule derived by morphing the acetonitrile model to a more spherical shape more closely resembling a Stockmayer fluid but whilst retaining the same value of $\frac{\mu^2\rho}{k_BT}$. This will enable us to check how ferroelectric behaviour is manifested in the simulations and to examine the consequence of the development of long-range order for the relaxation of the dipole density.

9.2 The simulations

A 3-site model of acetonitrile is used: one site representing the methyl group, and one site on each of the atoms of the nitrile group. The potential model consists of suitably parameterized Lennard-Jones functions and point charge interactions:

$$u_{ij} = \sum_{\alpha=1}^{3}\sum_{\beta=1}^{3}\left[4\epsilon_{\alpha\beta}\left\{\left(\frac{\sigma_{\alpha\beta}}{r_{i\alpha,j\beta}}\right)^{12} - \left(\frac{\sigma_{\alpha\beta}}{r_{i\alpha,j\beta}}\right)^{6}\right\} + \frac{q_\alpha q_\beta}{r_{i\alpha,j\beta}}\right], \tag{9.5}$$

where α and β label sites on molecules i and j. The parameter values initially used in this work are those of Edwards *et al.* [120], which are given in Table 9.1. This model was shown to yield reasonable predictions of the physical properties of liquid acetonitrile when run at the experimental density, and this has been confirmed in subsequent work [130]. The Lennard-Jones parameters for the cross interactions were taken from the usual mixing rules [131]. The point charges on the atomic sites in this model were chosen to reproduce the dipole moment

	$\epsilon_{\alpha\beta}$/K	$\sigma_{\alpha\beta}$ /Å	q_α/e
N	50	3.3	-0.398
C	50	3.4	0.129
Me	191	3.6	0.269

$r_{\mathrm{MeC}} = 1.46$ Å, $r_{\mathrm{MeN}} = 2.63$ Å.

Table 9.1: Parameters of the 3-site Edwards potential.

of an isolated MeCN molecule. The non-polar solvent molecule was created by replacing the N atom with a Me group.

The simulations were each run using the DL_POLY_2.15 molecular dynamics program [132] on the IBM BlueGene supercomputer at Edinburgh University. The electrostatic interactions are calculated using the Ewald sum technique using tin-foil outer boundary conditions. Each run was made at a molar volume of 52.18 cm^3 appropriate to MeCN at atmospheric pressure and 293 K. The initial configuration consists of a $24 \times 24 \times 24$ bcc lattice, each cube containing 2 molecules, so that in total there are 27,648 acetonitrile molecules in the sample volume. In the previous examination of the dielectric properties with this model only 500 molecules were used [120, 133]. This means that in the present calculations the simulation cell side is $L = 13.38$ nm, which determines the size $\left(\frac{2\pi}{L}\right)$ of the smallest wavevector accessible in the simulations, and may be contrasted with the experimental value of $\frac{2\pi}{\Delta k} = 280$ nm. The simulations cannot therefore reach the lengthscales probed in the experiments; on the other hand, the simulation cell size is comparable to Shelton's estimate of the size of the ferroelectric domains and should suffice to detect any longer range correlations whose influence was not noticed in the previous calculations with considerably smaller simulation cells.

The cut-off distance for the short-range interactions was 16 Å. To avoid biasing the dipolar order of the simulations, the charges were initially omitted from the simulation and a run of about 0.1 ns conducted during which the bcc lattice melted to produce a totally isotropic non-polar liquid. The charges were then introduced and the system equilibrated for 0.5 ns. The production run was for a further 1.5 ns. A timestep of 5×10^{-15} s was used.

	$\epsilon_{\alpha\beta}$/K	$\sigma_{\alpha\beta}$ /Å	q_α/e
N	50	3.3	-0.663
C	50	4.9	0.215
Me	191	3.6	0.448

$r_{\mathrm{MeC}} = 0.876$ Å, $r_{\mathrm{MeN}} = 1.578$ Å.

Table 9.2: Parameters of the 3-site Stockmayer-like liquid.

We also carried out simulations with a modified potential model in order to examine how far the shape of the acetonitrile molecules, as expressed in the original potential model, had to be changed before the fluid began to exhibit long-range dipole correlations. A Stockmayer fluid consists of Lennard-Jones particles with an embedded point dipole. Computer simulations of strongly dipolar spheres have shown that, at sufficiently low temperature and high pressure, the fluid can spontaneously break its symmetry and form an orientationally ordered liquid phase characterized by a spontaneous polarization [134, 135]. The model of acetonitrile can be transformed into a Stockmayer-like model with the same dipole density by effecting the following:

- an increase in the Lennard-Jones parameter σ_{CC} on the central carbon atom;
- a reduction in the Me—C and C—N bond lengths;
- a change in the atomic charges to leave the dipole moment unchanged.

The parameter values used are given in Table 9.2 (cf. Table 9.1). We used the same simulation protocol, density and temperature as for the original acetonitrile model.

9.3 Dipole correlations for the acetonitrile model

The nature of the mean dipole correlations between the acetonitrile molecules is illustrated in Figure 9.1. In this polar plot, we show the mean value of the scalar product $\cos \mathrm{B} = \mathbf{e}_i \cdot \mathbf{e}_j$ of unit vectors ($\mathbf{e}_i$ and $\mathbf{e}_j$) along the axes of a pair of molecules as a function of r, the distance of separation of their centres of mass (*i.e.* $|\mathbf{r}_{ij}|$), and $\cos \mathrm{A} = \mathbf{e}_i \cdot \mathbf{r}_{ij}$ which gives the orientation of

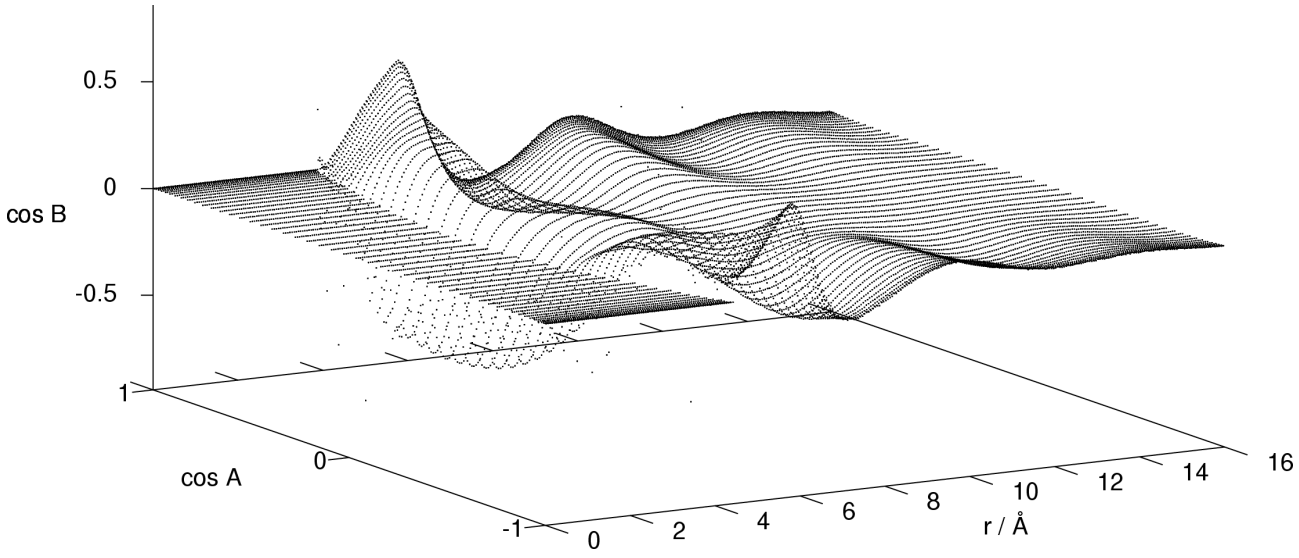

Figure 9.1: An illustration of the mean dipole correlations in acetonitrile.

the intermolecular vector with respect to the polar axis of one molecule. The figure indicates a strong tendency (large values of $\cos \mathrm{B}$) for parallel orientation of a neighbouring molecule lying at the head or tail of the reference molecule (*i.e.* for the regions of the graph where $|\cos \mathrm{A}|$ is close to one and for small values of r), and a similarly strong tendency for antiparallel alignment of neighbouring molecules lying side by side. This type of structure was discussed in the original simulation work [120, 123]. The figure also indicates that the dipole correlations die away for distances r greater than about 15 Å. The calculations are consistent with the previous ones in this regard: the competition between the tendencies for parallel and antiparallel alignments means that the dipole correlations do not build up in the manner which would be found for a Stockmayer fluid with the same dipole density. Integrating the dipole correlations out to large separations gives a value for the Kirkwood g-parameter, g^{S}, using

$$\lim_{k \to 0} g^{\mathrm{S}} = 1 + \sum_{j} \langle \mathbf{e_1} \cdot \mathbf{e_j} \rangle. \tag{9.6}$$

The dielectric constant can then be calculated using

$$\frac{(\epsilon - 1)(2\epsilon + 1)}{\epsilon} \; = \; \frac{\mu^2 \rho}{k_{\mathrm{B}} T \epsilon_0} g^{\mathrm{S}}, \tag{9.7}$$

which gives $\epsilon = 27$, as recorded in the final column of Table 9.3.

$k/k_{\min}$	$\Phi_{\mathrm{T}}(k,\omega=0)/\mathrm{ps}$	$\Phi_{\mathrm{L}}(k,\omega=0)/\mathrm{ps}$	$\Phi_{\mathrm{T}}/\Phi_{\mathrm{L}}$	$\epsilon^{\mathrm{static}}$	$\epsilon^{\mathrm{struc}}$
1	0.14	4.23	30	26	
2	0.14	4.28	31	27	27
3	0.14	4.14	30	25	

Table 9.3: Dielectric constant of acetonitrile.

The time-dependent longitudinal and transverse dipole density correlation functions,

$$C_{\mathrm{L}}(k,t) = \langle \mathbf{M}_{\mathrm{L}}(\mathbf{k},t) \cdot \mathbf{M}_{\mathrm{L}}(\mathbf{k},0)^{*} \rangle, \tag{9.8}$$

and

$$C_{\mathrm{T}}(k,t) = \langle \mathbf{M}_{\mathrm{T}}(\mathbf{k},t) \cdot \mathbf{M}_{\mathrm{T}}(\mathbf{k},0)^{*} \rangle, \tag{9.9}$$

were calculated for the three smallest values of k available in the simulation ($k_{\min}$, $\sqrt{2}k_{\min}$, and $\sqrt{3}k_{\min}$). Since no systematic differences were noted for the correlations calculated for different $\mathbf{k}$ vectors of a given length, as expected for an isotropic fluid, we averaged over them to improve the statistics. At sufficiently low k (*i.e.* where $\frac{2\pi}{k}$ is large compared to the range of the correlations in $\langle \mathbf{e}_i \cdot \mathbf{e}_j \rangle$) their $t = 0$ values are related to the dielectric constant ϵ by [121]

$$C_{\mathrm{T}}(k,0) = \epsilon C_{\mathrm{L}}(k,0), \tag{9.10}$$

and the values of ϵ extracted from this expression are collected in the penultimate column of Table 9.3. The ϵ values are k-independent, within the statistical significance of the calculations, and consistent with values obtained in previous simulations with this model. We can use the mean value for ϵ to calculate the Kirkwood g-parameter for the simulated fluid, using Equation 9.7. The value obtained is 0.88 which, being close to unity, indicates no net correlations in $\langle \mathbf{e}_i \cdot \mathbf{e}_j \rangle$ as anticipated above. The experimental value for the dielectric constant of acetonitrile is 35.8 from which we should extract a Kirkwood parameter from a modified Equation 9.7:

$$\frac{(\epsilon - \epsilon_\infty)(2\epsilon + \epsilon_\infty)}{\epsilon} = \left(\frac{\epsilon_\infty + 2}{3}\right)^2 \frac{\mu^2 \rho}{k_{\mathrm{B}} T \epsilon_0} g, \tag{9.11}$$

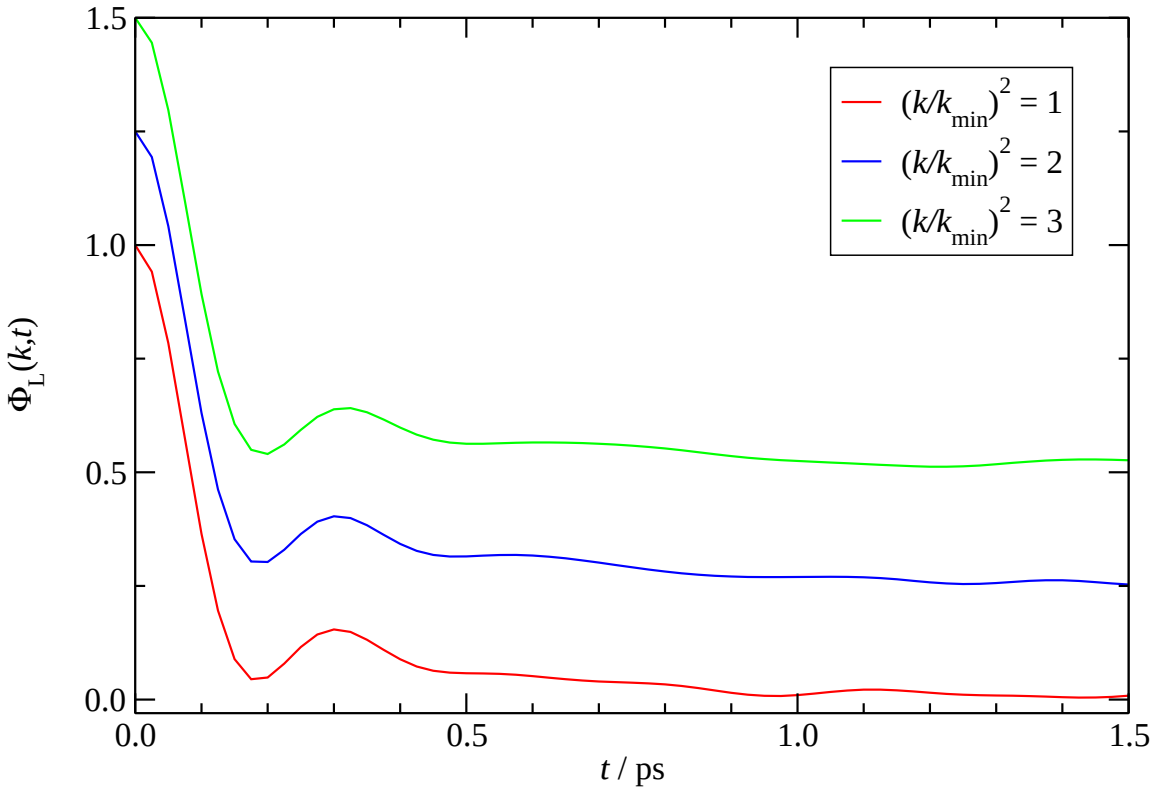

Figure 9.2: The collective longitudinal dipole density correlation functions for $(k/k_{\min})^2 = 1, 2,$ and 3. The functions are offset along the vertical axis by 0.25 units, for clarity.

which allows for the fact that the real fluid is polarizable. This gives a value of $g = 1.03$ when we use the gas-phase value of the dipole moment for μ and the experimental value of 1.25 for ϵ_∞, which indicates that the strength of the dipole correlations is *slightly* stronger in the real fluid than in the simulated one. The simulation model could be improved by enhancing the atomic charges to increase the dipole moment to capture the reaction-field induced component of the dipole, as has become standard practice in simulations of water [136], for example. We conclude that the static dipole correlations in the simulation model are similar to those in the real liquid and do not suggest there is ferroelectric order on a mesoscopic length scale.

The normalized, time-dependent correlation functions $\Phi_{\mathrm{L,T}}(k,t) = \frac{C_{\mathrm{L,T}}(k,t)}{C_{\mathrm{L,T}}(k,0)}$ (cf. Equations 9.8 and 9.9) at $k_{\min}$, $\sqrt{2}k_{\min}$ and $\sqrt{3}k_{\min}$ are shown in Figures 9.2 and 9.3. There is little k-

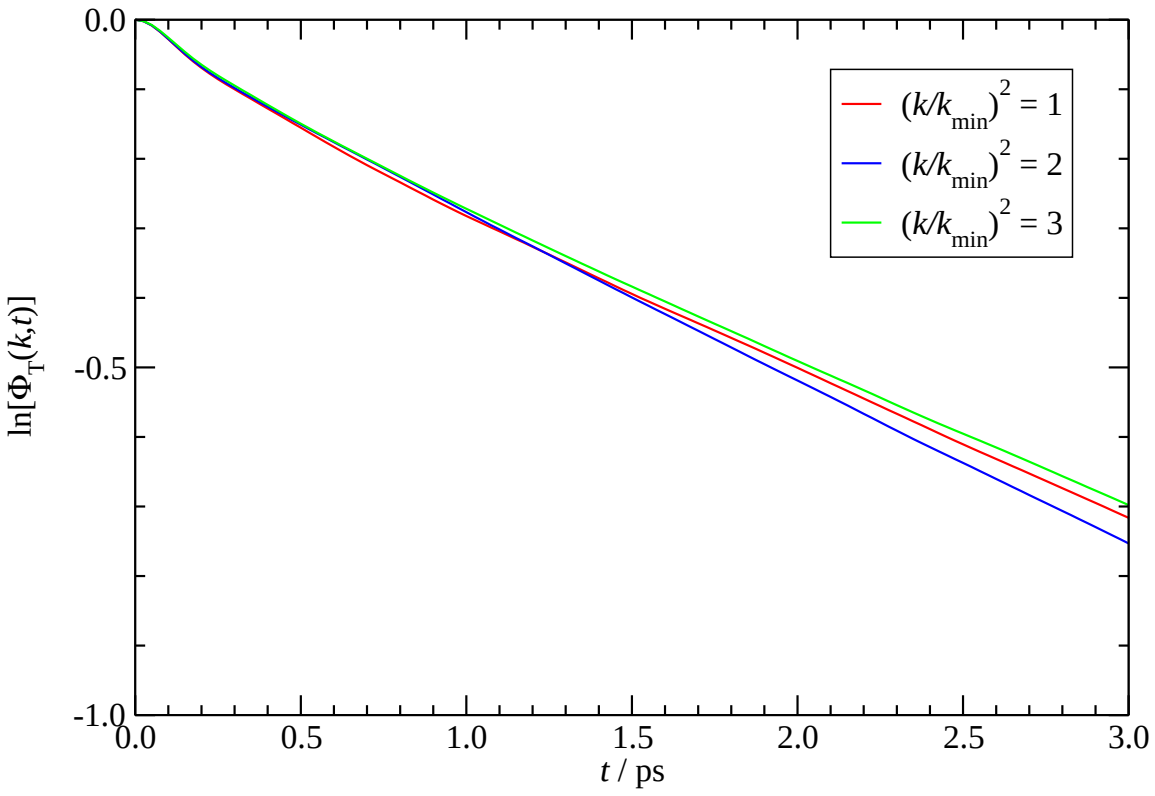

Figure 9.3: The collective transverse dipole density correlation functions for $(k/k_{\min})^2 = 1, 2,$ and 3.

dependence in either function at these values of k, showing that the dynamical behaviour they capture is that of fluctuations with wavelengths longer than the range of the dipole correlations in $\langle \mathbf{e}_i \cdot \mathbf{e}_j \rangle$. The transverse correlation function $\Phi_{\mathrm{T}}(k,t)$ is almost exponential with a decay constant of about 4 ps, which is similar to the molecular reorientation time. The longitudinal correlation function $\Phi_{\mathrm{L}}(k,t)$ exhibits a rapid initial decay followed by a pronounced oscillatory feature. The origin of the vastly different relaxation behaviour of these two functions and the origin of the oscillations in C_{L} were discussed in reference [121].

To test Shelton's suggestion that the narrow spectral feature is associated with the longitudinal correlation function is demanding. It is expected to be a very slowly relaxing part of the correlation function (the estimate suggests it is on the nanosecond timescale): it will therefore appear as a constant background on a normal simulation timescale. Furthermore, its amplitude will also be extremely low as the observations show that the narrow spectral feature is only of similar intensity at zero frequency to the broad (reorientational) Lorentzian. If the correlation function were modelled as consisting of two exponentials,

$$\Phi(t) \;=\; (1-A)\exp\left(-t/\tau_r\right) \;+\; A\exp\left(-t/\tau_s\right), \tag{9.12}$$

with τ_r the reorientational relaxation time and τ_s that of the slow mode and $\tau_s \gg \tau_r$, then the observation of equal intensities at zero frequency implies that

$$\frac{A}{1-A} \;=\; \frac{\tau_r}{\tau_s} \;\ll\; 1\ , \tag{9.13}$$

i.e. that the height of the "constant background" in the time correlation function will be very small compared to the amplitude of the initial reorientational decay and very difficult to detect directly. Examining the spectrum itself, by numerically transforming the correlation function, is not much better, since we will only pick up the full amplitude of the contribution from the background if we are able to complete the numerical integral over a timescale longer than τ_s; and at these long times the correlation function will be very noisy.

In Figure 9.4 we show the spectral densities $\hat{\Phi}^{T}_{\mathrm{L,T}}(k,\omega)$ obtained by numerically transforming

the correlation functions over different time windows

$$\hat{\Phi}^T_{\mathrm{L,T}}(k,\omega) \;=\; \int_0^T dt\, \cos(\omega t)\Phi_{\mathrm{L,T}}(k,t). \tag{9.14}$$

We see that $\hat{\Phi}^T_{\mathrm{L}}(k,0)$ is much smaller than $\hat{\Phi}^T_{\mathrm{T}}(k,0)$. The generalization of Equation 9.3 to non-exponential decay gives $\hat{\Phi}^\infty_{\mathrm{T}}(k,0) \;=\; \epsilon\hat{\Phi}^\infty_{\mathrm{L}}(k,0)$. Values of ϵ obtained from this expression (using $T = 62.5\,\mathrm{ps}$) are listed in the antepenultimate column of Table 9.3; we find reasonable consistency with those obtained from the static correlation. Furthermore, as the upper limit of integration T is extended to larger times we see no systematic tendency to develop a zero frequency feature in $\hat{\Phi}_{\mathrm{L}}(k,\omega)$, which would be the case if the correlation functions carried a weak constant background: we simply pick up more and more statistical noise. In order to minimize the noise we calculated spectra from the correlation functions averaged over the three lowest k values. We conclude that the low frequency feature cannot be detected in the simulations of acetonitrile.

We also carried out calculations on a 50% solution of acetonitrile in a non-polar solvent, a case where Shelton has reported an increase in the amplitude of the low frequency feature relative to the pure liquid. The model non-polar solvent was obtained from the acetonitrile model by replacing the N-site by another Me-site and equalizing the bond lengths. Figure 9.5 shows $\Phi_{\mathrm{L}}(k,t)$ and $\Phi_{\mathrm{T}}(k,t)$ for 50% concentration acetonitrile. We obtained qualitatively similar results to those described above for the pure liquid. The acetonitrile molecules relax more slowly when in the presence of slowly-relaxing neighbouring solvent molecules, as found in the experiments [115].

Overall, the results we obtain for the simulations of acetonitrile are in good accord with the expectations of dielectric theory and provide no suggestion of ferroelectric order on mesoscopic lengthscales or of a slowly relaxing component to the longitudinal dipole density correlation function.

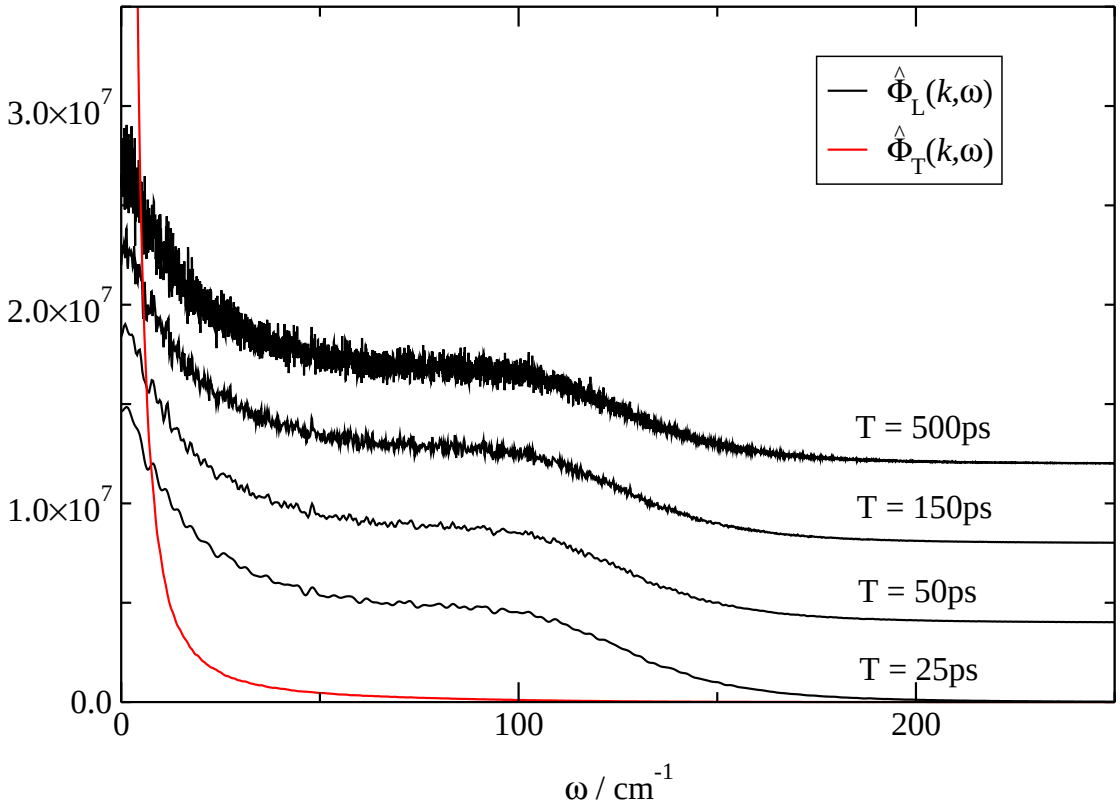

Figure 9.4: Fourier transforms of the longitudinal and transverse dipole density correlation functions shown in Figures 9.2 and 9.3. The $\hat{\Phi}_{\mathrm{L}}^{T}(k,\omega)$ transforms are offset for clarity.

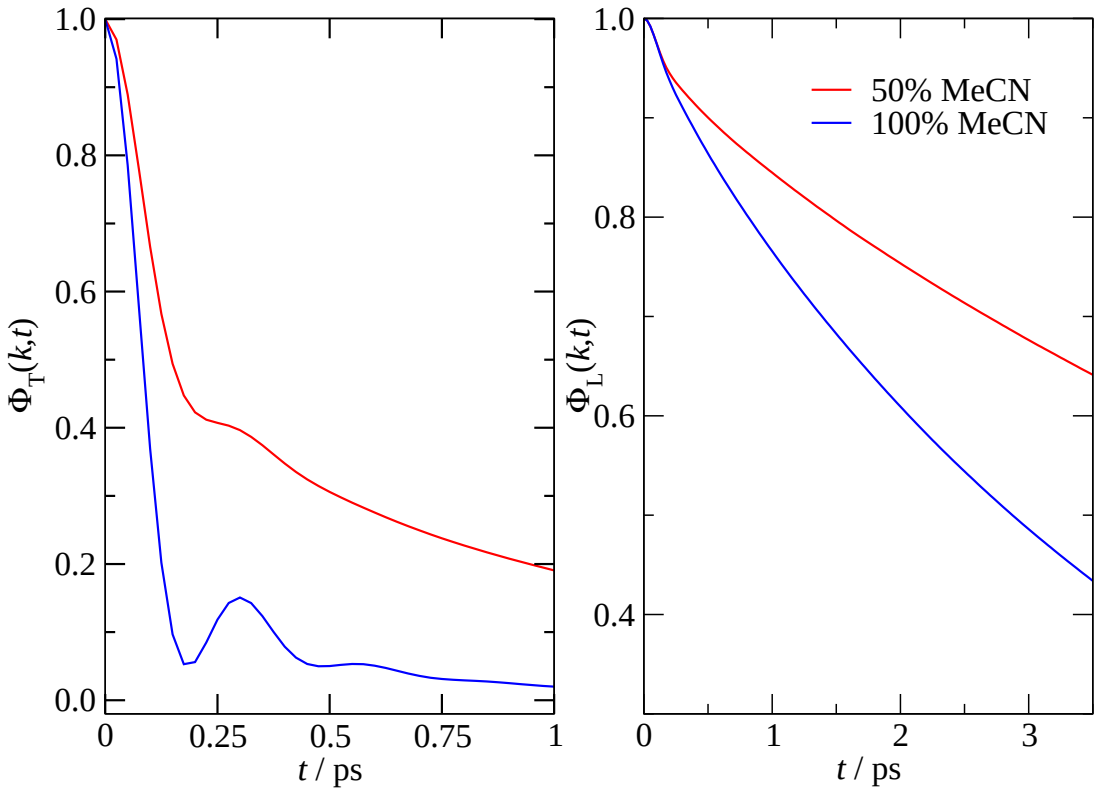

Figure 9.5: Comparison of the longitudinal (left panel) and transverse (right panel) dipole density correlation functions for pure MeCN and the 50% mixture of MeCN with a non-polar fluid.

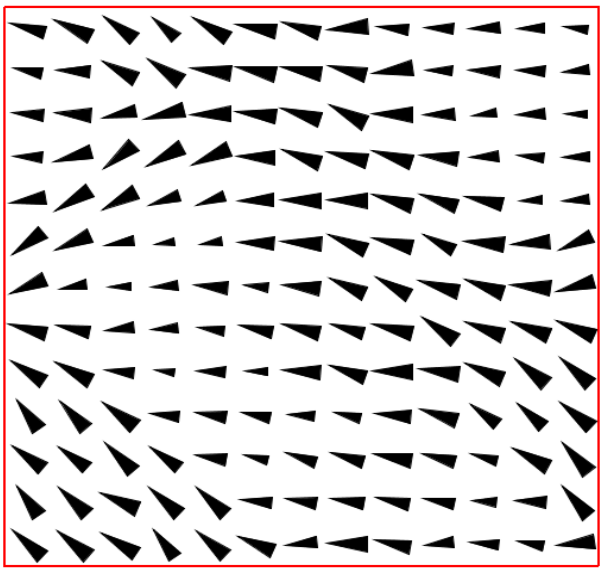

Figure 9.6: A two-dimensional snapshot of the simulation cell. The picture is coarse-grained, such that each arrow represents the molecular dipoles in a 10 Å × 10 Å box.

9.4 Dipole relaxation in the ferroelectric régime

In order to examine how the existence of ferroelectric order would affect the longitudinal dipole density correlation function we carried out simulations with the transmuted potential model described in Section 9.2.

Figure 9.6 shows a slice of a coarse-grained representation of the dipole density through the simulation cell at the end of the 2 ns simulation. In this figure each arrow represents the net dipole moment of the molecules in a 10 Å × 10 Å subcell centred on the position at which the arrow is drawn. Such a cell will on average contain about ten molecules. There is clear long-range ordering of the dipole density; recall that the simulation was initiated in such a way as to have no dipolar order, so we can conclude that a partially relaxed ferroelectric structure has emerged on the simulation timescale. This partially relaxed structure exhibits the same kind of structure of domains with well-defined internal orientations as envisaged by Shelton in his suggestion for the origin of the low frequency spectral spike. Ultimately, we would expect the domain structure to anneal out under these simulation conditions, leading to a uniform mean direction of polarization, but the timescale on which this will happen is very long compared to

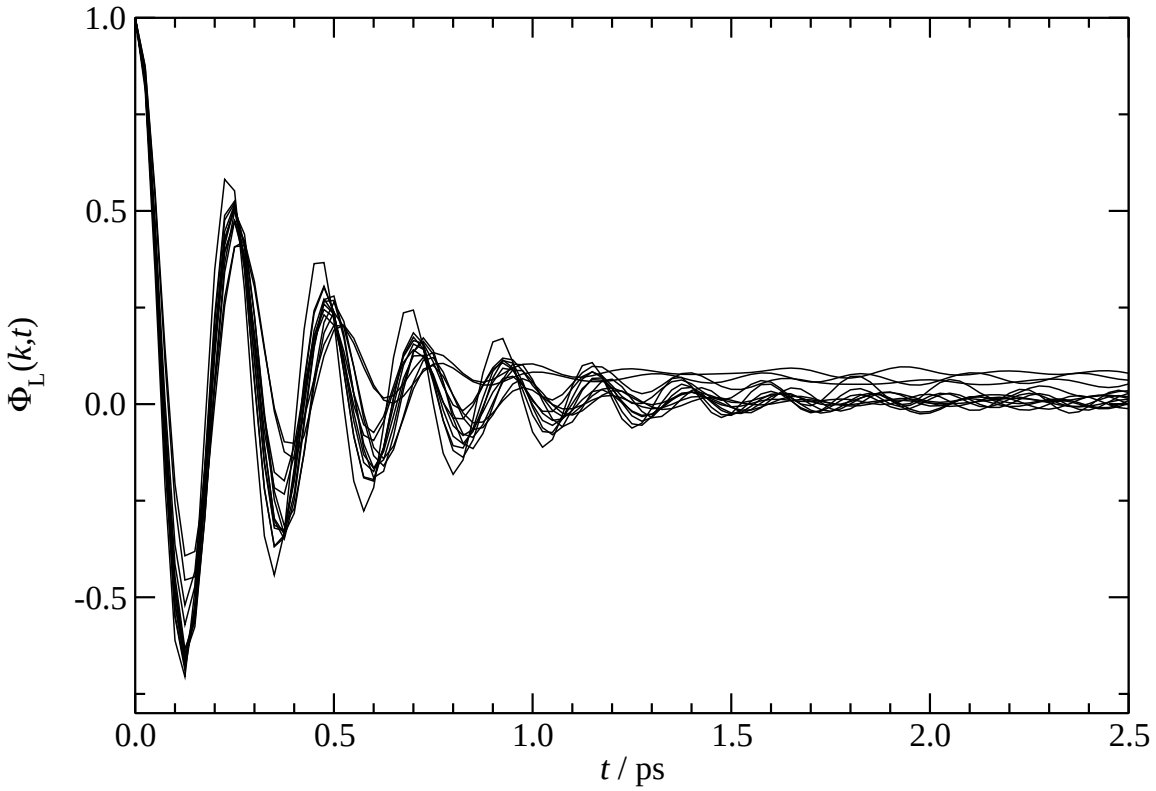

Figure 9.7: The collective longitudinal dipole density correlation function for the Stockmayer-like fluid with no k-averaging.

the simulation timescale. However, the type of disordered structure seen in the figure seems well suited to our purpose of examining the character of the relaxation of the dipole density in a system with the kind of domain structure envisaged by Shelton.

Figures 9.7 and 9.8 show respectively the longitudinal (Φ_{L}) and transverse (Φ_{T}) dipole density correlation functions for the Stockmayer-like fluid. In these figures, we have shown the correlation functions for the thirteen different wavevectors $\mathbf{k}$ belonging to the smallest k value (k_{min}). Unlike the isotropic fluid case, because the system now has a preferred direction of polarization for the duration of the run, the correlation functions have a strong dependence on the orientation of the wavevector with respect to this direction and we see slow relaxation in both the transverse and longitudinal functions.

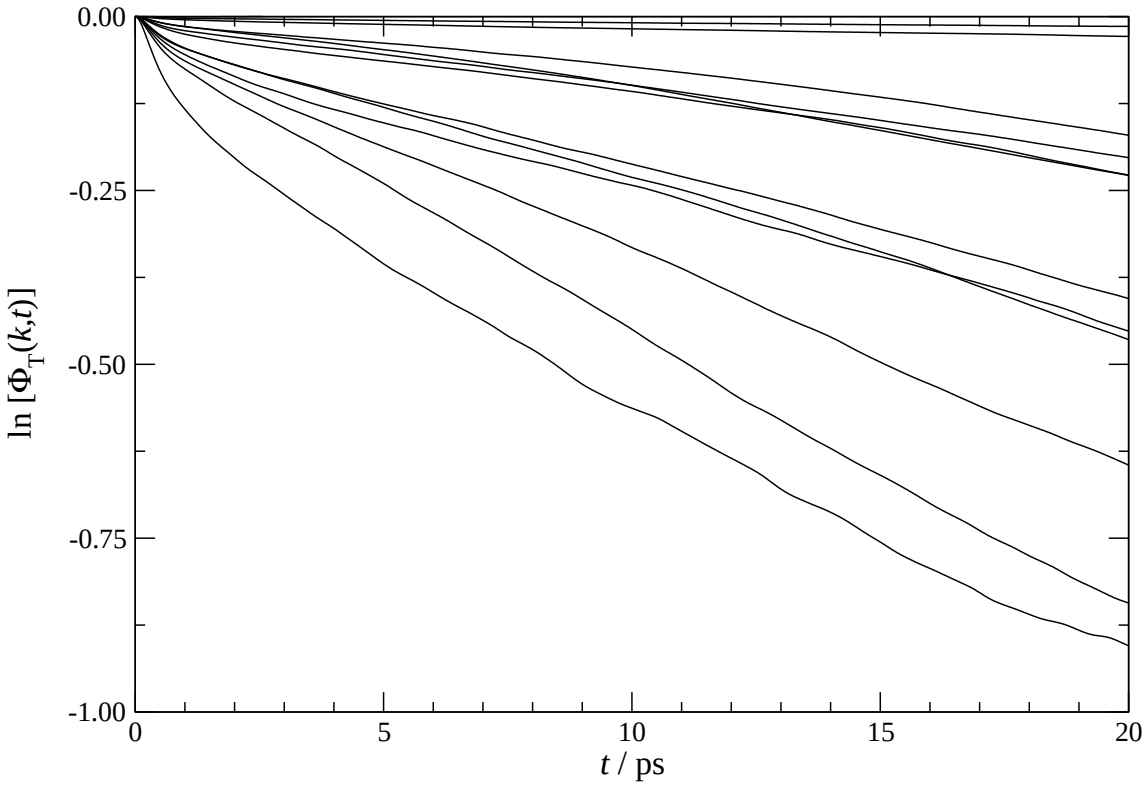

Figure 9.8: The collective transverse dipole density correlation function for the Stockmayer-like fluid with no k-averaging.

Figure 9.9 shows the spectral density of the longitudinal correlation function Φ_{L} obtained by averaging over the spectra of all the longitudinal correlation functions above. This samples the effect of averaging over several domains with different preferred directions for the polarization. The spectrum shows two prominent features:

- A near-zero frequency spike attributed to slowly relaxing ferroelectric domains; the origin of this feature in the spectrum is the same as that invoked by Shelton to explain the low frequency feature seen in the experimental HRS spectrum. However, as is evident from Figure 9.8, the transverse correlation function also shows slow relaxation on a similar timescale to the longitudinal function, and we would therefore anticipate that a narrow feature would appear in the HRS spectrum for other polarizations besides the VH one.

- A broad, higher-frequency peak, attributed to the librational motion of the molecular dipoles about the local direction of spontaneous polarization. The origin of this feature seems to be the same type of motion observed by Murashov *et al.* in simulations of dipolar spheres [137] in the ferroelectric régime (see below); as they discuss, the development of long-range order in the system is responsible for a splitting in the timescales of reorientational motion. As is clear from Figure 9.7, the frequency of this oscillatory motion does not show a systematic dispersion in k. We would therefore predict that if the low frequency spike in the VH HRS spectrum were associated with the behaviour of the longitudinal dipole density in a system with local ferroelectric order there should be a relatively high frequency ($\sim 80 - 150\,\mathrm{cm}^{-1}$) peak in the spectrum associated with the oscillatory motion. The published spectra do not show this frequency range.

Murashov *et al.* [137] considered a chain of point dipoles separated by a hard-core diameter, and derived an expression for the dipole oscillation frquency, ω_0:

$$\omega_0 = \sqrt{4\zeta(3)\mu^2\langle\cos\gamma\rangle/I\sigma^3}, \tag{9.15}$$

where $\zeta(3)\langle\cos\gamma\rangle \approx 1$, I is the moment of inertia, and σ is the hard-core diameter of the molecule (the position of the first peak in the centre-centre radial distribution function is used). This

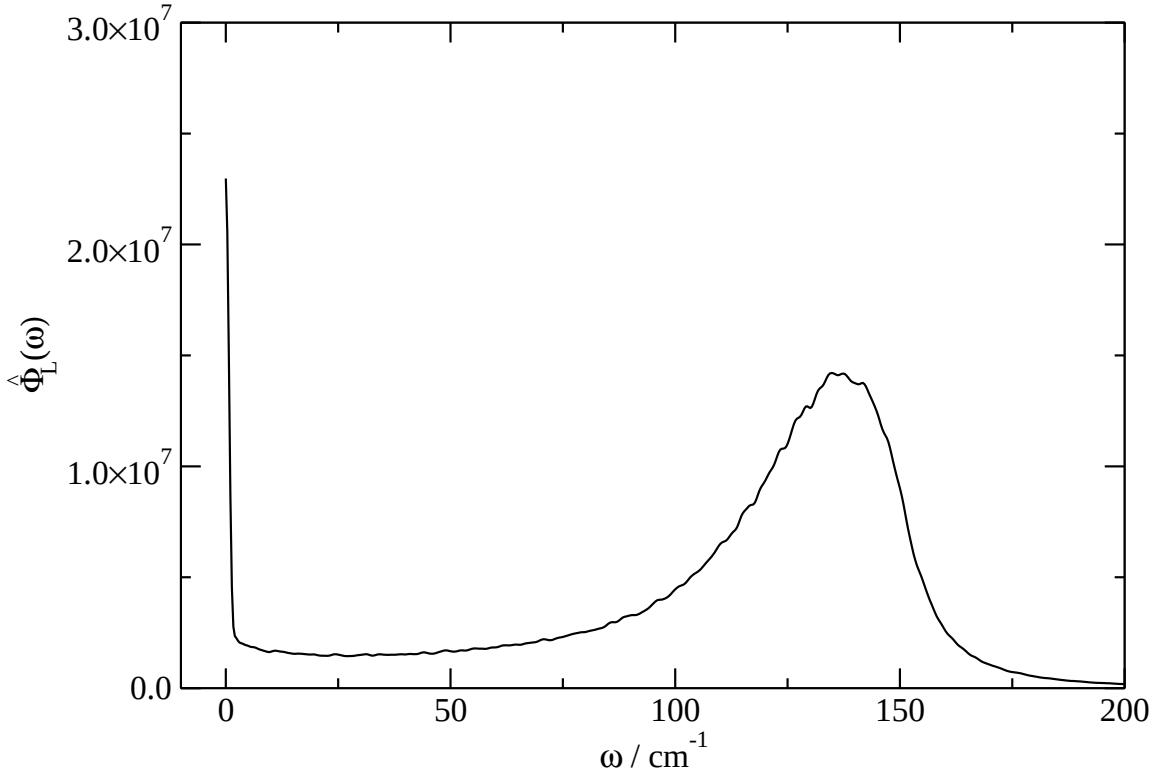

Figure 9.9: Fourier transform of the longitudinal dipole density correlation function for the Stockmayer-like liquid.

gives $\omega_0 = 76\,\mathrm{cm}^{-1}$ for acetonitrile, and the corresponding feature seen in Figure 9.9 is at $\sim 135\,\mathrm{cm}^{-1}$. Were the model changed to incorporate three point charges per sphere, it is envisaged that the close proximity of opposite charges on adjacent molecules would increase the restoring force experienced by each dipole, and thus effect a higher oscillation frequency.

9.5 Summary

This work was motivated by hyper-Rayleigh scattering spectra of acetonitrile: in common with several other polar liquids the VH spectrum contained a strong narrow peak but the HV spectrum did not, suggesting slowly relaxing *longitudinal* dipole density relaxation. The absence of macroscopic polarization (despite the observation that the dipole density of acetonitrile would be high enough to give a ferroelectric fluid were the molecules to be dipolar spheres) led to the hypothesis that acetonitrile had a slowly relaxing domain structure. We measured the longitudinal and transverse components of the molecular dipole density correlation functions in a molecular dynamics simulation of $\sim$ 28000 molecules, and found no slowly relaxing longitudinal orientation mode. Indeed, the transverse relaxation time was found to be larger than the longitudinal by a factor equal to the static dielectric constant, ϵ, consistent with current molecular dielectric theory. Furthermore, a simulation of a Stockmayer-like fluid at the same dipole density *which resulted in a ferroelectric phase* highlighted discrepancies with the experimental spectra: (i) slow longitudinal *and* transverse orientation modes were observed which would influence both VH and HV HRS spectra; (ii) a spectral feature was present at $\sim 135\,\mathrm{cm}^{-1}$ due to a librational motion of the dipoles within a domain; no such feature was reported in the experimental spectrum.

Our conclusion is that the low frequency feature observed in the VH HRS spectra of acetonitrile is not associated with slow relaxation of the longitudinal dipole density and that acetonitrile does not exhibit local ferroelectric order. Since great care has been taken to eliminate the obvious artifacts which might be responsible for the observation from the experimental spectrum, we conclude that the observed low frequency spike must be due to a non-linear effect not expressed by the time correlation function shown in Equation 9.1.

Bibliography

[1] P. W. Atkins. *Physical Chemistry*. Oxford University Press, sixth edition, (1998).

[2] A. C. Fisher. *Electrode Dynamics*. Oxford University Press, (1996).

[3] S. Kuznetsov, L. Rycerz and M. Gaune-Escard. *Journal of Nuclear Materials*, **344**, 152 (2005).

[4] A. J. Bard and L. R. Faulkner. *Electrochemical Methods. Fundamental and Applications*. Wiley, (2001).

[5] H. L. F. von Helmholtz. *Ann. Physik*, **165**, 211 (1853).

[6] G. Quincke. *Pogg. Ann.*, **113**, 513 (1861).

[7] H. L. F. von Helmholtz. *Ann. Physik*, **243**, 337 (1879).

[8] G. Gouy. *J. Phys. Radium*, **9**, 457 (1910).

[9] G. Gouy. *Compt. Rend.*, **149**, 654 (1910).

[10] D. L. Chapman. *Phil. Mag.*, **25**, 475 (1913).

[11] A. J. Bard and L. R. Faulkner. *Electrochemical Methods. Fundamental and Applications. Student Solutions Manual*. Wiley, (2002).

[12] O. Stern. *Z. Elektrochem.*, **30**, 508 (1924).

[13] G. M. Torrie and J. P. Valleau. *Chem. Phys. Lett.*, **65**, 343 (1979).

[14] G. M. Torrie and J. P. Valleau. *J. Phys. Chem.*, **86**, 3251 (1982).

[15] D. Boda, W. R. Fawcett, D. Henderson and S. Sokolowski. *J. Chem. Phys.*, **116**, 7170 (2002).

[16] K. R. Painter, P. Ballone, M. P. Tosi, P. J. Grout and N. H. March. *Surf. Sci.*, **133**, 89 (1983).

[17] A. Hamelin, S. Rottgermann and W. Schmickler. *J. Electroanal. Chem.*, **230**, 281 (1987).

[18] D. Henderson and D. Boda. *Phys. Chem. Chem. Phys.*, **11**, 3822 (2009).

[19] J. Pelta, D. Durand, J. Doucet and F. Livolant. *Biophys. J.*, **71**, 48 (1996).

[20] V. Lobaskin and K. Qamhieh. *J. Phys. Chem. B*, **107**, 8022 (2003).

[21] B. Jönsson, H. Wennerström, A. Nonat and B. Cabane. *Langmuir*, **20**, 6702 (2004).

[22] A. P. Lyubartsev, J. X. Tang, P. A. Janmey and L. Nordenskiöld. *Phys. Rev. Lett.*, **81**, 5465 (1998).

[23] E. Allahyarov, G. Gompper and H. Löwen. *J. Phys.: Condens. Matter*, **17**, S1827 (2005).

[24] O. J. Lanning and P. A. Madden. *J. Phys. Chem. B*, **108**, 11069 (2004).

[25] C. Pinilla, M. G. D. Popolo, J. Kohanoff and R. M. Lynden-Bell. *J. Phys. Chem. B*, **111**, 4877 (2007).

[26] S. K. Reed, O. J. Lanning and P. A. Madden. *J. Chem. Phys.*, **126**, 084704 (2007).

[27] M. V. Fedorov and A. A. Kornyshev. *Electrochimica Acta*, **53**, 6835 (2008).

[28] M. V. Fedorov and A. A. Kornyshev. *J. Phys. Chem. B*, **112**, 11868 (2008).

[29] M. F. Toney, J. N. Howard, J. Richer, G. L. Borges, J. G. Gordon, O. Melroy, D. Wiesler, D. Yee and L. Sorensen. *Surf. Sci.*, **335**, 326 (1995).

[30] J. Israelachvili. *Intermolecular and Surface Forces.* Academic Press, New York, (1991).

[31] D. C. Grahame. *Chem. Rev.*, **41**, 441 (1947).

[32] R. Parsons. *Chem. Rev.*, **90**, 813 (1990).

[33] C. Nanjundiah, S. F. McDevitt and V. R. Koch. *J. Electrochem. Soc.*, **144**, 3392 (1997).

[34] M. M. Islam, M. T. Alam and T. Ohsaka. *J. Phys. Chem. C*, **112**, 16568 (2008).

[35] A. A. Kornyshev. *J. Phys. Chem. B*, **111**, 5545 (2007).

[36] T. Welton. *Chem. Rev.*, **99**, 2071 (1999).

[37] F. Bresme and J. Alejandre. *J. Chem. Phys.*, **118**, 4134 (2003).

[38] M. Blander. *Molten Salt Chemistry.* Interscience, (1964).

[39] H. Taube. *Electron transfer reactions of complex ions in solution.* Academic, New York, (1970).

[40] C. J. Chen. *Introduction to scanning tunneling microscopy.* Oxford University Press, New York, (1993).

[41] A. Nitzan. *Chemical Dynamics in Condensed Phases.* Oxford University Press, (2006).

[42] R. A. Marcus. *J. Chem. Phys.*, **43**, 679 (1965).

[43] R. A. Marcus. *J. Phys. Chem.*, **94**, 1050 (1990).

[44] F. Hutchinson, M. Wilson and P. Madden. *Mol. Phys.*, **99**, 811 (2001).

[45] W. Glover and P. Madden. *J. Chem. Phys.*, **121**, 7293 (2004).

[46] P. Madden and M. Wilson. *J. Phys.: Condens. Matter*, **12**, A95 (2000).

[47] M. Wilson and P. Madden. *Mol. Phys.*, **92**, 197 (1997).

[48] M. Wilson and M. Ribeiro. *Mol. Phys.*, **96**, 867 (1999).

[49] M. Salanne, C. Simon, P. Turq and P. A. Madden. *J. Phys. Chem. B*, **112**, 1177 (2008).

[50] K. T. Tang and J. P. Toennies. *J. Chem. Phys.*, **80**, 3726 (1984).

[51] P. A. Madden and M. Wilson. *Chem. Soc. Review*, **25**(5), 339 (1996).

[52] M. P. Allen and D. J. Tildesley. *Computer Simulation of Liquids*. Oxford Science Publications, (1989).

[53] L. Verlet. *Phys. Rev.*, **159**, 98 (1967).

[54] S. Nosé. *Mol. Phys.*, **52**, 255 (1984).

[55] W. G. Hoover. *Phys. Rev. A*, **31**, 1695 (1985).

[56] G. J. Martyna, M. E. Tuckerman and M. L. Klein. *J. Chem. Phys.*, **97**, 2635 (1992).

[57] G. J. Martyna, D. J. Tobias and M. L. Klein. *J. Chem. Phys.*, **101**, 4177 (1994).

[58] J. W. Halley, A. Mazzolo, Y. Zhou and D. Price. *J. Electroanal. Chem.*, **450**, 273 (1998).

[59] S. Izvekov, A. Mazzolo, K. VanOpdorp and G. A. Voth. *J. Chem. Phys.*, **114**, 3248 (2001).

[60] E. Spohr. *Electrochim. Acta*, **44**, 1697 (1999).

[61] W. Schmickler. *Chem. Rev.*, **96**, 3177 (1996).

[62] J. I. Siepmann and M. Sprik. *J. Chem. Phys.*, **102**, 511 (1995).

[63] S. K. Reed, P. A. Madden and A. Papadopoulos. *J. Chem. Phys*, **128**, 124701 (2008).

[64] P. P. Ewald. *Ann. Phys.*, **64**, 253 (1921).

[65] A. Aguado and P. Madden. *J. Chem. Phys.*, **119**, 7471 (2003).

[66] I. C. Yeh and M. Berkowitz. *J. Chem. Phys.*, **111**, 3155 (1999).

[67] D. E. Parry. *Surf. Sci.*, **49**, 433 (1975).

[68] D. M. Heyes, M. Barber and J. H. R. Clarke. *J. Chem. Soc., Faraday Trans. 2*, **73**, 1485 (1977).

[69] S. de Leeuw and J. Perram. *Mol. Phys.*, **37**, 1313 (1979).

[70] M. Kawata and M. Mikami. *Chem. Phys. Lett.*, **340**, 157 (2001).

[71] A. Stone. *Theory of Intermolecular Forces*. Oxford University Press, (1996).

[72] M. Wilson, B. Costa-Cabral and P. Madden. *J. Phys. Chem.*, **100**, 1227 (1996).

[73] A. Aguado, M. Wilson and P. A. Madden. *J. Chem. Phys.*, **115**, 8603 (2001).

[74] A. Aguado, W. Scott and P. A. Madden. *J. Chem. Phys.*, **115**, 8612 (2001).

[75] A. Aguado and P. A. Madden. *J. Chem. Phys.*, **117**, 7659 (2002).

[76] E. Spohr. *J. Chem. Phys.*, **107**, 6342 (1997).

[77] C. Wick, L. Dang and P. Jungwirth. *J. Chem. Phys.*, **125**, 24706 (2006).

[78] M. Salanne, C. Simon, P. Turq and P. Madden. *C. R. Chim.*, **10**, 1131 (2007).

[79] A. Warshel. *J. Phys. Chem.*, **86**, 2218 (1982).

[80] J. Blumberger and M. Sprik, in *Lecture Notes in Physics*, edited by M. Ferrario, G. Ciccotti, and K. Binder (Springer, Berlin, 2006), Vol. 704, p. 481.

[81] `http://www.webelements.com`.

[82] C. G. Guymon, R. L. Rowley, J. N. Harb and D. R. Wheeler. *Condensed Matter Physics*, **8**, 335 (2005).

[83] `http://plasma-gate.weizmann.ac.il/Grace/`.

[84] D. M. Heyes and J. H. R. Clarke. *J. Chem. Soc., Faraday Trans. 2*, **77**, 1089 (1981).

[85] R. M. Esnouf and P. J. Grout. *Philos. Mag. A*, **58**, 27 (1988).

[86] J. O. Bockris, A. K. N. Reddy and M. Gamboa-Aldeco. *Modern Electrochemistry 2A*. Kluwer, New York, (2000).

[87] M. J. Booth and A. D. J. Haymet. *Mol. Phys.*, **99**, 1817 (2001).

[88] A. Kisza. *Electrochim. Acta.*, **51**, 2315 (2006).

[89] A. P. Willard, S. K. Reed, P. A. Madden and D. Chandler. *Faraday Discuss.*, **141**, 423 (2009).

[90] M. Sprik and G. Ciccotti. *J. Chem. Phys*, **109**, 7737 (1998).

[91] D. A. Rose and I. Benjamin. *J. Chem. Phys.*, **100**, 3545 (1994).

[92] R. M. Lynden-Bell. *J. Phys. Chem. B*, **111**, 10800 (2007).

[93] J. Blumberger and G. Lamoureux. *Mol. Phys.*, **106**, 1597 (2008).

[94] R. G. Compton and C. E. Banks. *Understanding Voltammetry*. World Scientific, London, (2007).

[95] S. A. Kuznetsov and M. Gaune-Escard. *Z. Naturforsch*, **57a**, 85 (2002).

[96] B. G. Dick and A. W. Overhauser. *Phys. Review*, **112**, 90 (1958).

[97] A. Laio, S. Bernard, G. L. Chiarotti, S. Scandolo and E. Tosatti. *Science*, **287**, 102 (2000).

[98] A. Aguado, L. Bernasconi, S. Jahn and P. A. Madden. *Faraday Discuss.*, **124**, 171 (2003).

[99] N. Marzari and D. Vanderbilt. *Phys. Rev. B*, **56**, 12847 (1997).

[100] R. Car and M. Parrinello. *Phys. Rev. Lett.*, **55**, 2471 (1985).

[101] W. H. Press, B. P. Flannery, S. A. Teukolski and W. T. Vetterling. *Numerical Recipes*. Cambridge University Press, 2nd edition, (1992).

[102] N. Troullier and J. L. Martins. *Phys. Rev. B*, **43**, 1993 (1991).

[103] P. L. Silvestrelli, N. Marzari, D. Vanderbilt and M. Parrinello. *Solid State Commun.*, **107**, 7 (1998).

[104] P. L. Silvestrelli. *Phys. Rev. B*, **59**, 9703 (1999).

[105] E. Hult, H. Rydberg, B. I. Lundqvist and D. C. Langreth. *Phys. Rev. B*, **59**, 4708 (1999).

[106] R. G. Gordon and R. LeSar. *Adv. Quantum Chemistry*, **21**, 341 (1990).

[107] D. L. Price and J. W. Halley. *J. Chem. Phys.*, **102**, 6603 (1995).

[108] G.-B. Pan and W. Freyland. *Chem. Phys. Lett.*, **427**, 96 (2006).

[109] W. Freyland. *Phys. Chem. Chem. Phys.*, **10**, 923 (2007).

[110] J. W. Halley and J. Hautman. *Phys. Rev. B*, **38**, 11704 (1988).

[111] N. S. Hush. *J. Chem. Phys.*, **28**, 962 (1958).

[112] H. O. Finklea. *Electroanal. Chem.*, **19**, 109 (1996).

[113] D. M. Kolb. Surface reconstruction at metal-electrolyte interfaces. In J. Lipkowski and P. N. Ross, editors, *Structure of Electrified Interfaces*. VCH, New York, (1993).

[114] D. M. Kolb and J. Schneider. *Electrochim. Acta*, **31**, 929 (1986).

[115] D. P. Shelton. *J. Chem. Phys.*, **123**, 084502 (2005).

[116] D. P. Shelton. *J. Chem. Phys.*, **117**(20), 9374–9382 (2002).

[117] D. P. Shelton. *Phys. Rev. B*, **72**, 020201 (2005).

[118] D. P. Shelton. *J. Chem. Phys.*, **123**, 111103 (2005).

[119] D. P. Shelton. *J. Chem. Phys.*, **124**(12), 124509 (2006).

[120] D. M. F. Edwards, P. A. Madden and I. R. McDonald. *Mol. Phys.*, **51**(5), 1141–1161 (1984).

[121] P. Madden and D. Kivelson. A molecular treatment of dielectric phenomena. In *Adv. Chem. Phys.*, volume LVI. John Wiley & Sons, (1984).

[122] K. Arnold and J. Yarwood. *Mol. Phys.*, **48**, 451 (1983).

[123] H. J. Bohm, I. R. McDonald and P. A. Madden. *Mol. Phys.*, **49**, 347 (1983).

[124] A. Buckingham. *Discuss. Faraday Soc.*, **43**, 205 (1967).

[125] T. Lazaridis and M. Karplus. *J. Chem. Phys.*, **105**, 4294 (1996).

[126] J. Macdonald and S. Kenkel. *J. Phys. D: Appl. Phys.*, **16**, L195 (1983).

[127] L. Duvillaret, F. Garet and J.-L. Coutaz. *IEEE J. Sel. Top. Quantum Electron*, **2**, 739 (1996).

[128] S. D. Leeuw, J. Perram and E. Smith. *Proc. R. Soc. A*, **373**, 27 (1980).

[129] B. Felderhof. *Physica A*, **101**, 275 (1980).

[130] P. J. Gee and W. F. van Gunsteren. *Mol. Phys.*, **104**(3), 477–483 (2006).

[131] G. Maitland, M. Rigby, E. Smitha and W. Wakeham. *Intermolecular Forces*. Clarendon Press, (1981).

[132] W. Smith and T. Forester. *J. Molec. Graphics*, **14**, 136 (1996).

[133] D. M. F. Edwards and P. A. Madden. *Mol. Phys.*, **51**(5), 1163–1179 (1984).

[134] J. Weis and D. Levesque. *Phys. Rev. E.*, **48**, 3728 (1993).

[135] S. Klapp and M. Schoen. *J. Chem. Phys.*, **117**, 8050 (2002).

[136] K. Watanabe and D. Klein. *Chem. Phys.*, **131**, 157 (1989).

[137] V. V. Murashov, P. J. Camp and G. N. Patey. *J. Chem. Phys.*, **116**, 6731 (2002).

[138] A. Szabo and N. Ostlund. *Modern Quantum Chemistry: Introduction to Advanced Electronic Structure Theory*. MacMillan Publishing Co., (1982).

A

Derivation of the Ewald summation in 2D periodicity

This derivation follows that in reference [26], albeit with minor emendations.

The Coulomb energy of a system which is periodic in 2 dimensions is

$$U_c = \frac{1}{2}\sum_{i,j}\sum_{k,l=-\infty}^{\infty}\int\int \frac{\rho_i(\mathbf{r}')\rho_j(\mathbf{r}'')\,\mathrm{d}\mathbf{r}'\mathrm{d}\mathbf{r}''}{|\mathbf{r}_{ij}+\mathbf{r}'-\mathbf{r}''+k\mathbf{a}+l\mathbf{b}|}, \tag{A.1}$$

where ρ_i is the charge distribution associated with particle i, $\mathbf{r}_{ij} = \mathbf{r}_i - \mathbf{r}_j$, and $\mathbf{a}$ and $\mathbf{b}$ are elementary lattice vectors in the periodic directions.

In the system we are currently interested in, some of the particles (the melt ions) have point charge distributions while the others (electrode atoms) have Gaussian charge distributions. The following derivation for the Ewald summation for such a mixed system is performed along the lines of the derivation for a system of pure point charges by de Leeuw and Perram [69]. Some of the procedure however makes use of the Gaussian integrals in the appendix of ref. [138], whilst the final form is obtained with help from the work of Kawata and Mikami [70].

Equation A.1 may be split into three parts. The first part gives the Coulomb energy of the point charge subsystem, the second part gives the energy of the subsystem with Gaussian charge distributions, whilst the third and final part gives the interaction energy of the point charges interacting with the Gaussian charge distributions. The first part is clearly the same

as the result found previously [69, 70]. The derivation of the third part is essentially the same as but slightly less complicated than the derivation of the second part. We therefore restrict our proof to that for a pure Gaussian system but give the general result for the mixed system at the end.

The Gaussian charge density for particle j is given by

$$\rho_j(\mathbf{r}) = q_j A \exp(-|\mathbf{r} - \mathbf{r}_j|^2 \eta^2), \tag{A.2}$$

where $A = \eta^3 \pi^{3/2}$ is the normalization constant, q_j is the integrated charge, and the Gaussian is of fixed width η. Incorporating this into Equation A.1 gives

$$U_c = \frac{A^2}{2} \sum_{i,j} \sum_{k,l=-\infty}^{\infty} \int\int \frac{q_i \exp\left(-\left|\mathbf{r}' - \mathbf{r}_i\right|^2 \eta^2\right) q_j \exp\left(-\left|\mathbf{r}'' - \mathbf{r}_j\right|^2 \eta^2\right) \, \mathrm{d}\mathbf{r}' \mathrm{d}\mathbf{r}''}{|\mathbf{r}_{ij} + \mathbf{r}' - \mathbf{r}'' + k\mathbf{a} + l\mathbf{b}|} \, . \tag{A.3}$$

We then use the identities

$$r^{-1} = \frac{1}{\sqrt{\pi}} \int_0^\infty t^{-1/2} \exp(-r^2 t) \mathrm{d}t \, , \tag{A.4}$$

$$\exp\left(-z^2 t\right) = \frac{1}{2\sqrt{\pi t}} \int_{-\infty}^{\infty} \exp\left(-\frac{u^2}{4t} + iuz\right) \mathrm{d}u \, , \tag{A.5}$$

and

$$\exp\left(-|\mathbf{r}|^2 \eta^2\right) = (2\pi)^{-3} \frac{\pi^{3/2}}{\eta^3} \int_{-\infty}^{\infty} \exp\left(-\frac{|\mathbf{v}|^2}{4\eta^2} + i\mathbf{v}.\mathbf{r}\right) \mathrm{d}v \, , \tag{A.6}$$

and Jacobi's imaginary transformation,

$$\sum_{k=-\infty}^{\infty} \exp\left[-(x + ka)^2 t\right] = \frac{1}{a} \left(\frac{\pi}{t}\right)^{1/2} \sum_{k=-\infty}^{\infty} \exp\left[-\frac{\pi^2 k^2}{a^2 t} + \frac{i2\pi kx}{a}\right] \, , \tag{A.7}$$

with $i = \sqrt{-1}$ to get

$$\begin{aligned} U_c = \frac{1}{4ab(2\pi)^6} \sum_{i,j} q_i q_j \sum_{k=-\infty}^{\infty} \sum_{l=-\infty}^{\infty} \int t^{-2} \exp\left[-\frac{\pi^2 k^2}{a^2 t} + \frac{i2\pi k}{a} \left(x'' + x_{ij} - x' \right) \right] \\ \times \exp\left[-\frac{\pi^2 l^2}{b^2 t} + \frac{i2\pi l}{b} \left(y'' + y_{ij} - y' \right) \right] \exp\left[-\frac{u^2}{4t} + iu \left(z'' + z_{ij} - z' \right) \right] \\ \times \exp\left(-\frac{|\mathbf{v}|^2}{4\eta^2} + i\mathbf{v}.\mathbf{r}' \right) \exp\left(-\frac{|\mathbf{w}|^2}{4\eta^2} + i\mathbf{w}.\mathbf{r}'' \right) \mathrm{d}u \, \mathrm{d}\mathbf{v} \, \mathrm{d}\mathbf{w} \, \mathrm{d}t \, \mathrm{d}\mathbf{r}' \, \mathrm{d}\mathbf{r}'' \, . \end{aligned} \tag{A.8}$$

Next collecting terms with single and double primes and noting that, for example,

$$(2\pi)^{-1} \int \exp\left[ix' \left(v_x - \frac{2\pi k}{a} \right) \right] \mathrm{d}x' = \delta\left(v_x - \frac{2\pi k}{a} \right) , \tag{A.9}$$

where δ is the Kronecker delta function [138], we get

$$\begin{aligned} U_c = \frac{1}{4ab} \sum_{i,j} q_i q_j \sum_{k=-\infty}^{\infty} \sum_{l=-\infty}^{\infty} \int t^{-2} \exp\left(-\frac{|\mathbf{v}|^2 + |\mathbf{w}|^2}{4\eta^2} \right) \\ \times \exp\left[-\frac{\pi^2 k^2}{a^2 t} + \frac{i2\pi k x_{ij}}{a} \right] \exp\left[-\frac{\pi^2 l^2}{b^2 t} + \frac{i2\pi l y_{ij}}{b} \right] \exp\left[-\frac{u^2}{4t} + iuz_{ij}) \right] \\ \times \delta\left(v_x - \frac{2\pi k}{a} \right) \delta\left(v_y - \frac{2\pi l}{b} \right) \delta\left(v_z - u \right) \\ \times \delta\left(w_x + \frac{2\pi k}{a} \right) \delta\left(w_y + \frac{2\pi l}{b} \right) \delta\left(w_z + u \right) \\ \times \mathrm{d}u \, \mathrm{d}\mathbf{v} \, \mathrm{d}\mathbf{w} \, \mathrm{d}t \, . \end{aligned} \tag{A.10}$$

Integrating with respect to $\mathbf{v}$ and $\mathbf{w}$ over the delta functions chooses: $v_x = 2\pi k/a$, $v_y = 2\pi l/b$, $v_z = u$, $w_x = -2\pi k/a$, $w_y = -2\pi l/b$ and $w_z = -u$. On rearrangement, this gives

$$\begin{aligned} U = \frac{1}{4ab} \sum_{i,j} q_i q_j \sum_{k=-\infty}^{\infty} \sum_{l=-\infty}^{\infty} \int_{t=0}^{\infty} \int_{u=-\infty}^{\infty} t^{-2} \exp\left[-\frac{\pi^2 k^2}{a^2} \left(\frac{1}{t} + \frac{2}{\eta^2} \right) + \frac{i2\pi k x_{ij}}{a} \right] \\ \times \exp\left[-\frac{\pi^2 l^2}{b^2} \left(\frac{1}{t} + \frac{2}{\eta^2} \right) + \frac{i2\pi l y_{ij}}{b} \right] \exp\left[-\frac{u^2}{4} \left(\frac{1}{t} + \frac{2}{\eta^2} \right) + iuz_{ij} \right] \mathrm{d}u \, \mathrm{d}t \, . \end{aligned} \tag{A.11}$$

Next we split the integral over t into two parts, from 0 to α^2 and from α^2 to ∞. To begin with, consider only the upper part. After reversing the Jacobi transformations and the identity

from Equation A.5 and making a change of variable $v^2 = r^2 t\eta^2/(\eta^2 + 2t)$, we arrive at

$$U_I = \frac{1}{2}\sum_{i,j} q_i q_j \sum_{k=-\infty}^{\infty}\sum_{l=-\infty}^{\infty} \frac{1}{r_{ijkl}} \frac{2}{\sqrt{\pi}} \int_{v_0^2}^{\infty} \exp -v^2 \mathrm{d}u \,, \tag{A.12}$$

where $r_{ijkl} = \left\{(x_{ij} + ka)^2 + (y_{ij} + lb)^2 + z_{ij}^2\right\}^{1/2}$. The complimentary error function is defined as

$$\mathrm{erfc}(v_0) = \frac{2}{\sqrt{\pi}} \int_{v_0^2}^{\infty} \exp(-v^2) \mathrm{d}v \,, \tag{A.13}$$

so the final expression for the contribution of the upper part of the integral to the energy is

$$U_I = \frac{1}{2}\sum_{i,j} q_i q_j \sum_{k=-\infty}^{\infty}\sum_{l=-\infty}^{\infty} \frac{1}{r_{ijkl}} \mathrm{erfc}\left(r_{ijkl}\beta\right) \ . \tag{A.14}$$

where $\beta = \eta\alpha\left(\eta^2 + 2\alpha^2\right)^{-1/2}$. In practice, the parameter α is usually chosen so that the complimentary error function has decayed to zero within half the length of the smallest dimension of the system, in which case the sum over k and l may be ignored.

Now we consider the lower part of the integral over t in Equation A.11. The integral with respect to t diverges when $k = l = 0$. This term can be subtracted and then added on separately:

$$\begin{aligned} U_{II} =& \frac{1}{4ab}\sum_{i,j} q_i q_j \sum_{k=-\infty}^{\infty}\sum_{l=-\infty}^{\infty}{}' \int_{t=0}^{\alpha^2}\int_{u=-\infty}^{\infty} t^{-2} \exp\left[i2\pi\left(\frac{kx_{ij}}{a} + \frac{ly_{ij}}{b}\right)\right] \exp\left(iuz_{ij}\right) \\ & \times \exp\left[-\left(\frac{\eta^2 + 2t}{\eta^2 t}\right)\left(\frac{\pi^2 k^2}{a^2} + \frac{\pi^2 l^2}{b^2} + \frac{u^2}{4}\right)\right] \mathrm{d}u\,\mathrm{d}t \\ & + \frac{1}{4ab}\sum_{\substack{i,j \\ i\neq j}} q_i q_j \int_{t=0}^{\alpha^2}\int_{u=-\infty}^{\infty} t^{-2} \exp\left[-\frac{u^2}{4}\left(\frac{\eta^2 + 2t}{\eta^2 t}\right) + iuz_{ij}\right] \mathrm{d}u\,\mathrm{d}t \,, \end{aligned} \tag{A.15}$$

where the prime indicates that the $k = l = 0$ term is excluded from the summation. After removing the identity of Equation A.5, the $k = l = 0$ term in Equation A.15 may be written as

$$U_{II}^0 = \frac{\sqrt{\pi}}{2ab}\sum_{\substack{i,j \\ i\neq j}} q_i q_j \int_{t=0}^{\alpha^2} t^{-2}\left(\frac{t\eta^2}{\eta^2 + 2t}\right)^{1/2} \exp\left[-z^2\frac{t\eta^2}{\eta^2 + 2t}\right] \mathrm{d}t \,. \tag{A.16}$$

Changing the variable again in a similar way to before gives

$$U_{II}^{0} = \frac{\sqrt{\pi}}{ab} \sum_{\substack{i,j \\ i \neq j}} q_i q_j \int_0^{u_o^2} \frac{1}{u^2} \exp\left(-z_{ij}^2 u^2\right) \mathrm{d}u \,. \tag{A.17}$$

This can be integrated by parts to get

$$\begin{aligned} U_{II}^{0} = \frac{-\sqrt{\pi}}{ab} \sum_{\substack{i,j \\ i \neq j}} q_i q_j \Bigg\{ & \frac{\sqrt{\eta^2 + 2\alpha^2}}{\eta\alpha} \exp\left(-\frac{z_{ij}^2 \eta^2 \alpha^2}{\eta^2 + 2\alpha^2}\right) \\ & + z_{ij}\sqrt{\pi}\mathrm{erf}\left(\frac{z_{ij}\eta\alpha}{\sqrt{\eta^2 + 2\alpha^2}}\right) - \lim_{t \to 0} \frac{\sqrt{2 + \eta^2/t}}{\eta} \Bigg\} \,. \end{aligned} \tag{A.18}$$

As η^2/t becomes large, the limit may be written as $\lim_{t\to 0}\ t^{-1/2}$. As this is independent of α and η, this term disappears if the system as a whole is neutral. The final expression for the U_{II}^{0} is therefore

$$U_{II}^{0} = \frac{-\sqrt{\pi}}{ab} \sum_{\substack{i,j \\ i \neq j}} q_i q_j \left\{ \frac{1}{\beta} \exp\left(-z^2\beta^2\right) + z\sqrt{\pi}\mathrm{erf}\left(z\beta\right) \right\} , \tag{A.19}$$

where β is defined after Equation A.14.

Finally we return to the lower part of the integral in Equation A.11, but when k and l are not both equal to zero. After rearranging Equation A.11 and setting $v = t\eta^2/(\eta^2 + 2t)$ we obtain

$$\begin{aligned} U_{II}^{*} = \frac{1}{4ab} \sum_{i,j} q_i q_j \sum_{k=-\infty}^{\infty} \sum_{l=-\infty}^{\infty} \int_{v=0}^{v_0} \int_{u=-\infty}^{\infty} & v^{-2} \exp\left[i2\pi\left(\frac{kx_{ij}}{a} + \frac{ly_{ij}}{b} + \frac{uz_{ij}}{2\pi}\right)\right] \\ & \times \exp\left[-\frac{1}{v}\left(\frac{\pi^2 k^2}{a^2} + \frac{\pi^2 l^2}{b^2} + \frac{u^2}{4}\right)\right] \mathrm{d}u\mathrm{d}v \,. \end{aligned} \tag{A.20}$$

The integral with respect to v is straightforward and we get

$$\begin{aligned} U_{II}^{*} = \frac{1}{4ab} \sum_{i,j} q_i q_j \sum_{k=-\infty}^{\infty} \sum_{l=-\infty}^{\infty} & \exp\left[i2\pi\left(\frac{kx_{ij}}{a} + \frac{ly_{ij}}{b}\right)\right] \exp\left[-\pi^2\beta^2\left(\frac{k^2}{a^2} + \frac{l^2}{b^2}\right)\right] \\ & \times \int_{-\infty}^{\infty} \frac{\exp\left[-\frac{u^2}{4\beta^2} + iuz_{ij}\right]}{\left(\frac{\pi^2 k^2}{a^2} + \frac{\pi^2 l^2}{b^2} + \frac{u^2}{4}\right)} \mathrm{d}u \,. \end{aligned} \tag{A.21}$$

This is essentially Equation 9 of de Leeuw and Perram with $\beta^2 = \alpha^2\eta^2/(\eta^2 + 2\alpha^2)$ instead of α^2. According to de Leeuw and Perram, this can then be written as

$$U_{II}^* = \frac{1}{4ab}\sum_{i,j} q_i q_j \sum_{k=-\infty}^{\infty}\sum_{l=-\infty}^{\infty} \exp\left[i2\pi\left(\frac{kx_{ij}}{a} + \frac{ly_{ij}}{b}\right)\right]\left(\frac{k^2}{a^2} + \frac{l^2}{b^2}\right)^{-1/2} F_{kl}\left(z_{ij}\right) , \tag{A.22}$$

where

$$F_{kl}\left(z_{ij}\right) = \exp\left(-2\pi|\mathbf{k}|z\right)\operatorname{erfc}\left(\frac{\pi|\mathbf{k}|}{\beta} - z_{ij}\beta\right) + \exp\left(2\pi|\mathbf{k}|z\right)\operatorname{erfc}\left(\frac{\pi|\mathbf{k}|}{\beta} + z_{ij}\beta\right) , \tag{A.23}$$

with

$$|\mathbf{k}| = \left(\frac{k^2}{a^2} + \frac{l^2}{b^2}\right)^{1/2} . \tag{A.24}$$

Kawata and Mikami [70] noted that this can be rewritten using a Fourier integral

$$\begin{aligned}\frac{1}{4|\mathbf{k}|}\exp\left(\frac{\pi^2|\mathbf{k}|^2}{\beta^2}\right)\left[\mathrm{e}^{-2\pi|\mathbf{k}|z}\operatorname{erfc}\left(\frac{\pi|\mathbf{k}|}{\beta} - \beta z_{ij}\right) + \mathrm{e}^{2\pi|\mathbf{k}|z}\operatorname{erfc}\left(\frac{\pi|\mathbf{k}|}{\beta} + \beta z_{ij}\right)\right] \\ = \int_{-\infty}^{\infty}\mathrm{d}h\mathrm{e}^{ihz_{ij}}\frac{1}{4\pi^2|\mathbf{k}|^2 + h^2}\exp\left(-\frac{\mathbf{h}^2}{4\beta^2}\right) ,\end{aligned} \tag{A.25}$$

to get

$$\begin{aligned}U_{II}^* = \frac{1}{ab}\sum_{i,j} q_i q_j \sum_{k=-\infty}^{\infty}\sum_{l=-\infty}^{\infty} \exp\left[i2\pi\left(\frac{kx_{ij}}{a} + \frac{ly_{ij}}{b}\right)\right] \\ \times \int_{-\infty}^{\infty}\mathrm{d}h\mathrm{e}^{ihz_{ij}}\frac{1}{4\pi^2|\mathbf{k}|^2 + h^2}\exp\left(-\frac{|4\pi^2\mathbf{k}|^2 + h^2}{4\beta^2}\right) .\end{aligned} \tag{A.26}$$

Defining the structure factor $S(\mathbf{k}, h)$ as

$$S(\mathbf{k}, h) = \exp\left(-\frac{4\pi^2k^2 + h^2}{4\eta^2}\right)\sum_i q_i \exp\left[i\left(2\pi\mathbf{k}.\mathbf{r}_i' + hz_i\right)\right] , \tag{A.27}$$

with $\mathbf{r}_i' = (x_i, y_i)$ and $\mathbf{k} = (k/a, l/b)$, we can rewrite U_{II}^* as

$$U_{II}^* = \frac{1}{ab}\sum_{k=-\infty}^{\infty}\sum_{l=-\infty}^{\infty}\int_{-\infty}^{\infty}\mathrm{d}h\frac{1}{4\pi^2|\mathbf{k}|^2 + h^2}\exp\left(-\frac{4\pi^2|\mathbf{k}|^2 + h^2}{4\alpha^2}\right)|S(\mathbf{k}, h)|^2 . \tag{A.28}$$

U_{II} erroneously includes part of the interaction of the particle with itself. This contribution, which needs to be subtracted, may be determined by considering $U - U_I$ for a single particle:

$$\lim_{r_{ij}\to 0}\left\{\frac{q_i q_j}{2r_{ij}} - \frac{q_i q_j \operatorname{erfc}(\beta r_{ij})}{2r_{ij}}\right\} = \frac{q_i^2\beta}{\sqrt{\pi}}\,. \tag{A.29}$$

For the Gaussian charge distribution, the full self term which needs to be added is

$$\begin{aligned} U_{\text{self}} &= \frac{1}{2}\int\int \frac{1}{|\mathbf{r}-\mathbf{r}'|}\frac{\eta^6}{\pi^3}\exp(-r^2\eta^2)\exp(-r'^2\eta^2)\mathrm{d}\mathbf{r}\mathrm{d}\mathbf{r}' \\ &= \frac{q_i^2\eta}{\sqrt{2\pi}}\,. \end{aligned} \tag{A.30}$$

The total Coulomb energy for a system of Gaussian charge distributions is therefore

$$U_c = U_I + U_{II}^* + U_{II}^0 - \frac{q_i^2\beta}{\sqrt{\pi}} + \frac{q_i^2\eta}{\sqrt{2\pi}}\,. \tag{A.31}$$

These equations are almost the same as those for a system of point charges derived previously [69, 70], apart from the redefinition of the structure factor, the Gaussian self interaction term, and the inclusion of β rather than just α.

The derivation of the equations for the Coulomb energy of a system of point charges interacting with a system of Gaussian charges is virtually the same as for the Gaussian–Gaussian Coulomb energy except that the initial factor of two is not present because the particles have either a point or Gaussian charge distribution, and so there is no double counting. As one of the charge distributions becomes a delta function, one of the integrals in Equation A.3 disappears. Also, β becomes $\gamma = \eta\alpha(\eta^2+\alpha^2)^{-1/2}$ and there is no self interaction correction. The incorporation of η into the structure factor as in Equation A.27 is not quite so clean. This is resolved however when we consider the complete system with both Gaussian and point charges.

The total Coulomb energy for a system comprising both point and Gaussian charges is simply the sum of the original point-point interaction terms, the Gaussian–Gaussian terms, and the cross term which is again very similar. If there are n_p point charges and n_g Gaussian

charges, the final expression for the Coulomb energy is

$$
\begin{aligned}
U_c = & \frac{1}{2}\sum_{i,j}^{n_p} q_i q_j \frac{1}{r_{ij}} \operatorname{erfc}(\alpha r_{ij}) \\
& + \sum_{i}^{n_p}\sum_{j}^{n_g} q_i q_j \frac{1}{r_{ij}} \operatorname{erfc}(\gamma r_{ij}) \\
& + \frac{1}{2}\sum_{i,j}^{n_g} q_i q_j \frac{1}{r_{ij}} \operatorname{erfc}(\beta r_{ij}) \\
& + \frac{1}{ab}\sum_{k=-\infty}^{\infty}\sum_{l=-\infty}^{\infty}\int_{-\infty}^{\infty} \frac{1}{4\pi^2|\mathbf{k}|^2 + h^2} \\
& \quad \times \exp\left(-\frac{4\pi^2|\mathbf{k}|^2 + h^2}{4\alpha^2}\right) |S(\mathbf{k},h)|^2 \,\mathrm{d}h \\
& - \frac{1}{ab}\sum_{i,j}^{n_p} q_i q_j \left\{\frac{\sqrt{\pi}}{\alpha}\exp\left(-z_{ij}^2\alpha^2\right) + z_{ij}\,\pi\operatorname{erf}(z_{ij}\alpha)\right\} \\
& - \frac{2}{ab}\sum_{i}^{n_p}\sum_{j}^{n_g} q_i q_j \left\{\frac{\sqrt{\pi}}{\gamma}\exp\left(-z_{ij}^2\gamma^2\right) + z\,\pi\operatorname{erf}(z\gamma)\right\} \\
& - \frac{1}{ab}\sum_{i,j}^{n_g} q_i q_j \left\{\frac{\sqrt{\pi}}{\beta}\exp\left(-z_{ij}^2\beta^2\right) + z_{ij}\,\pi\operatorname{erf}(z_{ij}\beta)\right\} \\
& - \sum_{i}^{n_p}\frac{\alpha q_i^2}{\sqrt{\pi}} - \sum_{i}^{n_g}\frac{\beta q_i^2}{\sqrt{\pi}} + \sum_{i}^{n_g}\frac{\eta q_i^2}{\sqrt{2\pi}}\,,
\end{aligned}
\tag{A.32}
$$

where we have redefined the structure factor again, this time as

$$
\begin{aligned}
S(\mathbf{k},h) = & \sum_{i=1}^{n_p} q_i \exp\left[i\left(2\pi\mathbf{k}.\mathbf{r}_i' + hz_i\right)\right] \\
& + \exp\left(-\frac{4\pi^2k^2 + h^2}{4\eta^2}\right)\sum_{j=1}^{n_g} q_j \exp\left[i\left(2\pi\mathbf{k}.\mathbf{r}_j' + hz_j\right)\right]\,,
\end{aligned}
\tag{A.33}
$$

with $\mathbf{r}_i' = (x_i, y_i)$, $\mathbf{k} = (k/a, l/b)$, $\beta = \eta\alpha(\eta^2 + 2\alpha^2)^{-1/2}$ and $\gamma = \eta\alpha(\eta^2 + \alpha^2)^{-1/2}$. By dropping the sums over k and l for the so-called real-space terms involving α, β, and γ, it has been

assumed that α is chosen such that $\mathrm{erfc}(\alpha r)$ decays to zero within half the smallest dimension of the cell.

B

Multipole interaction tensors

The T multipole interaction tensors employed in the real space sums have the following expressions: [71]

$$T_{ij} = \frac{1}{r_{ij}} \tag{B.1}$$

$$T_{ij}^{\alpha} = \nabla_{\alpha} T_{ij} \quad = -\frac{r_{ij,\alpha}}{r_{ij}^3} \tag{B.2}$$

$$T_{ij}^{\alpha\beta} = \nabla_{\alpha} T_{ij}^{\beta} \quad = \frac{3r_{ij,\alpha}r_{ij,\beta} - r_{ij}^2\delta_{\alpha\beta}}{r_{ij}^5} \tag{B.3}$$

$$T_{ij}^{\alpha\beta\gamma} = \nabla_{\alpha} T_{ij}^{\beta\gamma} \quad = -\frac{1}{r_{ij}^7}[15r_{ij,\alpha}r_{ij,\beta}r_{ij,\gamma} - 3r_{ij}^2(r_{ij,\alpha}\delta_{\beta\gamma} + r_{ij,\beta}\delta_{\alpha\gamma} + r_{ij,\gamma}\delta_{\alpha\beta})] \tag{B.4}$$

Apart from the usual T multipole tensors, an additional tensor is used in the real space formulas:

$$D_{ij}^{\alpha\beta} = r_{ij,\alpha}r_{ij,\beta} \tag{B.5}$$

C

Screening functions

The screening functions $f_i(r_{ij})$ employed in the real space energy expressions [Equations 3.15 to 3.17] are given by the following expressions:

$$f_0(r) = \mathrm{erfc}(A_{ij}r)\,, \tag{C.1}$$

$$f_1(r) = \frac{2A_{ij}r}{\sqrt{\pi}} + e^{-A_{ij}^2 r^2} + f_0(r)\,, \tag{C.2}$$

$$f_2(r) = \frac{4A_{ij}^3}{\sqrt{\pi}} \frac{e^{-A_{ij}^2 r^2}}{r^2}\,, \tag{C.3}$$

where A_{ij} is defined by Equation 3.13.

D
Published papers

Ion adsorption at a metallic electrode: an *ab initio*-based simulation study
M. Pounds, S. Tazi, M. Salanne and P. A. Madden
J. Phys.: Condens. Matter, **21**, 424109 (2009)

This paper covers the material in Chapter 7 of this thesis.

Are dipolar liquids ferroelectric? Simulation studies
M. Pounds and P. A. Madden
J. Chem. Phys., **126**, 104506 (2007)

This paper is reproduced verbatim in Chapter 9.